

Ministry of Education and Science of the Russian Federation
Saint Petersburg National Research University of Information
Technologies, Mechanics, and Optics

NANOSYSTEMS:
PHYSICS, CHEMISTRY, MATHEMATICS

2015, volume 6(6)

Special Issue

INTERNATIONAL CONFERENCE
“SECOND DYNAMICS DAYS CENTRAL ASIA”

Наносистемы: физика, химия, математика

2015, том 6, № 6



NANOSYSTEMS:

PHYSICS, CHEMISTRY, MATHEMATICS

ADVISORY BOARD MEMBERS

Chairman: V.N. Vasiliev (*St. Petersburg, Russia*),
V.M. Ievlev (*Voronezh*), P.S. Kop'ev (*St. Petersburg, Russia*), N.F. Morozov (*St. Petersburg, Russia*), V.N. Parmon (*Novosibirsk*), A.I. Rusanov (*St. Petersburg, Russia*),

EDITORIAL BOARD

Editor-in-Chief: I.Yu. Popov (*St. Petersburg, Russia*)

Section Co-Editors:

Physics – V.M. Uzdin (*St. Petersburg, Russia*),
Chemistry, material science – V.V. Gusarov (*St. Petersburg, Russia*),
Mathematics – I.Yu. Popov (*St. Petersburg, Russia*).

Editorial Board Members:

V.M. Adamyan (*Odessa, Ukraine*); O.V. Al'myasheva (*St. Petersburg, Russia*);
A.P. Alodjants (*Vladimir, Russia*); S. Bechta (*Stockholm, Sweden*); J. Behrndt (*Graz, Austria*);
M.B. Belonenko (*Volgograd, Russia*); V.G. Bepalov (*St. Petersburg, Russia*); J. Brasche (*Clausthal, Germany*);
A. Chatterjee (*Hyderabad, India*); S.A. Chivilikhin (*St. Petersburg, Russia*); A.V. Chizhov (*Dubna, Russia*);
A.N. Enyashin (*Ekaterinburg, Russia*), P.P. Fedorov (*Moscow, Russia*); E.A. Gudilin (*Moscow, Russia*); V.K. Ivanov (*Moscow, Russia*),
H. Jónsson (*Reykjavik, Iceland*); A.A. Kiselev (*Madison, USA*); Yu.S. Kivshar (*Canberra, Australia*);
S.A. Kozlov (*St. Petersburg, Russia*); P.A. Kurasov (*Stockholm, Sweden*); A.V. Lukashin (*Moscow, Russia*);
V.A. Margulis (*Saransk, Russia*); I.V. Melikhov (*Moscow, Russia*); G.P. Miroshnichenko (*St. Petersburg, Russia*);
I.Ya. Mittova (*Voronezh, Russia*); H. Neidhardt (*Berlin, Germany*); K. Pankrashkin (*Orsay, France*); B.S. Pavlov (*Auckland, New Zealand*);
A.V. Ragulya (*Kiev, Ukraine*); V. Rajendran (*Tamil Nadu, India*); A.A. Rempel (*Ekaterinburg, Russia*);
V.Ya. Rudyak (*Novosibirsk, Russia*); D Shoikhet (*Karmiel, Israel*); P Stovicek (*Prague, Czech Republic*); V.M. Talanov (*Novocherkassk, Russia*);
A.Ya. Vul' (*St. Petersburg, Russia*); V.A. Zagrebnov (*Marseille, France*).

Editors:

I.V. Blinova; A.I. Popov; A.I. Trifanov; E.S. Trifanova (*St. Petersburg, Russia*),
R. Simoneaux (*Philadelphia, Pennsylvania, USA*).

Address: University ITMO, Kronverkskiy pr., 49, St. Petersburg 197101, Russia.

Phone: +7(812)232-67-65, **Journal site:** <http://nanojournal.ifmo.ru/>,

E-mail: popov1955@gmail.com

AIM AND SCOPE

The scope of the journal includes all areas of nano-sciences. Papers devoted to basic problems of physics, chemistry, material science and mathematics inspired by nanosystems investigations are welcomed. Both theoretical and experimental works concerning the properties and behavior of nanosystems, problems of its creation and application, mathematical methods of nanosystem studies are considered.

The journal publishes scientific reviews (up to 30 journal pages), research papers (up to 15 pages) and letters (up to 5 pages). All manuscripts are peer-reviewed. Authors are informed about the referee opinion and the Editorial decision.

Content

FROM THE EDITORIAL BOARD

International conference “Second Dynamics Days Central Asia” 741

PAPERS, PRESENTED AT THE CONFERENCE

M. Salerno, F.Kh. Abdullaev

Matter wave compactons in deep optical lattices with strong nonlinearity management 742

G.F. Dell'Antonio, A. Michelangeli

From "fat" graphs to metric graphs: the problem of boundary conditions 751

Z.A. Sobirov, M.I. Akhmedov, O.V. Karpova, B. Jabbarova

Linearized KdV equation on a metric graph 757

K.K. Sabirov, U.A. Aminov, Kh.Sh. Saparov,
M.K. Karimov, Kh. Abdikarimov

The Green function for simplest quantum graphs 762

S. Rakhmanov, O. Karpova, D.R. Rakhimboeva,
F. Khashimova, D. Babajanov

Quantum dynamics of hydrogen-like atom in one-dimensional box with oscillating walls 767

J. Yusupov, V. Eshniyozov, O. Karpova, D.Sh. Saidov

Kicked particle dynamics in quantum graphs 773

V.E. Eshniyazov, B.Kh. Eshchanov, D.B. Yusupov,
Q.Ya. Ergashev, U.K. Sapaev

On theory of second harmonic generation in 2D nonlinear photonic crystals with arbitrary structures 779

A. Tanaka, T. Cheon

A topological formulation for exotic quantum holonomy 786

M. Aripov, Sh. Sadullaeva

An asymptotic analysis of a self-similar solution for the double nonlinear reaction-diffusion system 793

B. Abdullaev, D.B. Abdullaev, C.-H. Park, M.M. Musakhanov

Intra pseudogap and superconductivity pair spin and charge fluctuations and underdome metal-insulator (fermion-boson) – crossover phenomena as keystone of curate physics 803

B.L. Oksengendler, S.E. Maksimov, M.B. Marasulov Degradation of perovskites and Dexter-Varley paradox	825
Kh.B. Ashurov, M.M. Adilov, S.E. Maksimov, B.L. Oksengendler Influence of the radius of the quantum dot and the non-equilibrium degree on the conversion efficiency of light emitting diodes	833
A.E. Atamuratov, U.A. Aminov, Z.A. Atamuratova, M. Halillaev, A. Abdikarimov, H. Matyakubov The lateral capacitance of nanometer MNOSFET with a single charge trapped in oxide layer or at SiO₂ - Si₃N₄	837
<u>REGULAR PAPERS</u>	
A.A. Lobinsky, V.P. Tolstoy Red-ox reactions in aqueous solutions of Co(OAc)₂ and K₂S₂O₈ and synthesis of CoOOH nanolayers by the SILD method	843
A.V. Lukashin, N.S. Falaleev, N.I. Verbitskiy, A.A. Volykhov, I.I. Verbitskiy, L.V. Yashna, A.S. Kumskov, N.A. Kiselev, A.A. Eliseev Quasi free-standing one-dimensional nanocrystals of PbTe grown in 1.4 nm SWNTs	850
G.P. Miroshnichenko Parameterization of an interaction operator of optical modes in a single-mode optical fiber	857
V.I. Popkov, O.V. Almjasheva, V.N. Nevedomskiy, V.V. Sokolov, V.V. Gusarov Crystallization behavior and morphological features of YFeO₃ nanocrystallites obtained by glycine-nitrate combustion	866
S. Saeid Influence of the oxidation of GaAs on the work of light-emitting spintronic diodes with InGaAs/GaAs quantum wells	875
Satya Pal Singh First observations of entropy vs free energy for lattice based Ising model for spin coarsening in conserved and non-conserved binary mixtures: a phenomenological study of phase transitions in 2D thin films	882
Information for authors	896

International conference “Second Dynamics Days Central Asia”

This issue contains contributions to the international conference “Second Dynamics Days Central Asia” held in May 25-27, 2015 in Khiva (Uzbekistan). The talks presented at this conference were mainly focused on such topics as nonlinear evolution equations, particle and wave dynamics in networks and branched structures, quantum transport in low-dimensional systems and other issues of nonlinear dynamics.

Particle and wave transports in low-dimensional nanoscale and mesoscopic systems have practical applications in broad variety of problems in physics, chemistry, biology and rapidly emerging area, nanotechnology. Many nanoscale devices and materials can be effectively modeled using the nonlinear evolution equations on low-dimensional systems and metric graphs.

The conference aimed at bringing together various ideas, problems and expertise on the applications of nonlinear evolution equations and quantum mechanical wave equations to a wide spectrum of systems from mesoscopic physics, cold atoms, nonlinear optics and condensed matter physics. Invited lectures covered such topics as nonlinear evolution equations on branched and confined domains, quantum transport in networks, wave dynamics in condensed media, matter waves and charge generation in low-dimensional structures.

A total 32 talks have been presented at the meeting, with 20 invited and 12 short plenary talks.

Panel discussions has attracted broad auditorium experts and young researchers working on different issues of physics, mathematics and chemistry.

We would like to thank members of organizing Committee, Workshop Secretary, Dr. Olga Karpova and the sponsors of the meeting, Abdus Salam International Center for Theoretical Physics, Volkswagen Foundation and Physical Society of Uzbekistan.

Davron Matrasulov

Matter wave compactons in deep optical lattices with strong nonlinearity management

M. Salerno¹, F. Kh. Abdullaev²

¹ Dipartimento di Fisica “E.R. Caianiello”, CNISM and INFN - Gruppo Collegato di Salerno, Università di Salerno, Via Giovanni Paolo II, 84084 Fisciano (SA), Italy

²Department of Physics, Kulliyyah of Science, International Islamic University Malaysia, 25200 Kuantan, Pahang, Malaysia

salerno@sa.infn.it

PACS 42.65.-k, 42.81.Dp, 03.75.Lm DOI 10.17586/2220-8054-2015-6-6-742-750

Compacton matter waves are considered in Bose-Einstein condensates (BEC) and in binary BEC mixtures, trapped in deep optical lattices in the presence of strong and rapid periodic time modulations of the atomic scattering length, are considered. For this, we derive vector averaged discrete nonlinear Schrödinger equations (DNLSE) and show that compacton solutions of different types can exist as stable excitations. Stability properties are studied by linear analysis and by direct numerical integrations of the DNLSE system.

Keywords: Bose-Einstein condensates, wave compactons, solitons, nonlinear Schrödinger equation.

Received: 1 November 2015

1. Introduction

Periodic management of nonlinear wave system parameters is a very attractive technique for the generation of solitons with new types of properties [1]. Examples of the management technique in continuous systems are the dispersion management of solitons in optical fibers which allows one to improve communication capacities [2], and the nonlinearity management of 2D and 3D Bose-Einstein condensates (BEC) or optically layered media which provides partial stabilization against collapse in the case of attractive interatomic interactions [3]. In discrete systems, the diffraction management technique was used to generate spatially discrete solitons with novel properties [4, 5] which have recently been observed in experiments [5]. The suppression of the inter-well tunneling was experimentally observed for light propagation in waveguide arrays [6] and for BEC's in strongly driven optical lattices [7]. In these cases, however, the system is typically subjected either to resonant modulations of the dispersion (coupling between waveguides for the case of light propagation) or to external linear forces (optical lattice shaking in the BEC case). The inhibition of the inter-well tunneling, however, may also become possible in the presence of fast periodic time variations in the nonlinearity, the so called *strong nonlinearity management* (SNLM). In this case, new phenomena can arise, such as strong localization and formation of (discrete counterparts to) the so called *compactons* [8] e.g. localized nonlinear waves with compact support.

The aim of the present work is investigate discrete compactons solutions of the discrete nonlinear Schrödinger equation (DNLS) system [9] subjected to SNLM both for single component BEC and for vectorial (binary) BEC mixtures. Contrary to ordinary solitons, the amplitude of a compacton was shown to reduce exactly to zero outside of the localizing domain, implying the total suppression of the inter-well tunneling at the compacton edges. For this, we derive the averaged DNLSE and show that compacton solutions of different

types can exist as stable excitations [10]. The stability properties are studied by linear analysis and by direct numerical integrations of the DNLSE system. Similar results will also be derived for arrays of binary BEC mixtures described by the vector DNLSE equation in the presence of inter-species scattering length SNLM.

2. The model

The dynamical lattice considered here is the well known DNLSE [9]:

$$i\dot{u}_n + \kappa(u_{n+1} + u_{n-1}) + (\gamma_0 + \gamma(t))|u_n|^2 u_n = 0, \quad (1)$$

which serves as a prototypical model for both matter waves in BEC arrays and for light propagation in arrays of optical waveguides. In the BEC context, κ quantifies the coupling (tunneling of matter) between adjacent wells of the optical lattice, t represents the time and γ_0 and $\gamma(t)$ represent the constant and the modulated part of the interatomic interaction (nonlinearity), respectively. In this case the management corresponds to the periodically variable in time the atomic scattering length which can be achieved by the Feshbach resonance technique. In the optical context, the time t should be replaced by the propagation distance z , κ quantifies the coupling between adjacent waveguides, and the nonlinear management consists of a periodic spatially variable Kerr nonlinearity around a constant value γ_0 . In the following, we shall refer to the BEC context and assume $\gamma(t)$ to be a periodic, $\gamma(t) = \gamma(t + T)$, and rapidly varying function of time of the form: $\gamma(t) = \frac{\gamma_1}{\epsilon} \cos(\Omega \frac{t}{\epsilon})$, with $\epsilon \ll 1$ and $T = 2\pi/\Omega$ the period.

To investigate the existence of discrete compacton solitons in this model, we shall derive averaged equations over rapid modulations, using the method developed in [11]. Following this approach, we introduce the new variables v_n related to the field u_n as:

$$u_n(t) = v_n(t) e^{i\Gamma(t)|v_n|^2(t)}, \quad \Gamma(t) = \frac{1}{\epsilon} \int_0^t dt \gamma_1 \left(\frac{t}{\epsilon}\right). \quad (2)$$

Substituting this expression into Eq.(1) and averaging the resulting equation over the period of the rapid modulation, we obtain:

$$i v_{n,t} = -\alpha \kappa v_n [(v_{n+1} v_n^* + v_{n+1}^* v_n) J_1(\alpha \theta_+) + (v_{n-1} v_n^* + v_{n-1}^* v_n) J_1(\alpha \theta_-)] - \kappa [v_{n+1} J_0(\alpha \theta_+) + v_{n-1} J_0(\alpha \theta_-)] - \gamma_0 |v_n|^2 v_n, \quad (3)$$

where $J_n(x)$ is the Bessel function of order n , $\theta_{\pm} = |v_{n\pm 1}|^2 - |v_n|^2$ and $\alpha = \gamma_1/K$. This modified DNLSE has essentially nonlinear neighbor-neighbor interactions and can be put in Hamiltonian form $i\dot{v}_n = \frac{\delta H}{\delta v_n^*}$, with the following Hamiltonian:

$$H_{av} = - \sum_n \{ \kappa J_0(\alpha \theta_+) [v_{n+1} v_n^* + v_{n+1}^* v_n] + \frac{\gamma_0}{2} |v_n|^4 \}.$$

For small $\alpha \theta_+$ the function J_0 can be expanded in a series giving the same averaged Hamiltonian for the DNLSE obtained in [12] in the limit of *weak* nonlinearity management.

3. Compactly-supported localized modes

In this section, we demonstrate the existence of exact compactons in this averaged system. We remark that compacton solutions were initially reported as a ‘‘mathematical curiosity’’ of somewhat artificial variants of the DNLSE where linear dispersion is absent [13], by analogy to their continuum siblings [8]. The present setting, however, is in some sense unique in that linear dispersion is not, generally speaking, absent. In fact, there is a linear spectrum for the background state in the linearization of even these compact solutions and

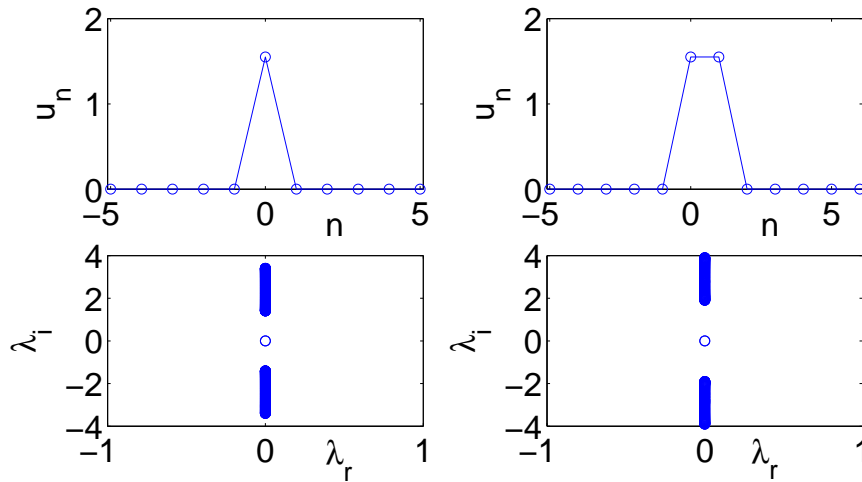


FIG. 1. Typical examples for $\kappa = 0.5$, $\alpha = 1$ of compact localized mode solutions of Eq. (4) (top panels) and of the spectral plane (λ_r, λ_i) of their linearization eigenvalues $\lambda = \lambda_r + i\lambda_i$. 1st column: on-site, 2nd column: inter-site in-phase compacton. Remarkably, all solutions are spectrally stable.

can be analytically shown to extend from $[-\mu - 2\kappa, -\mu + 2\kappa]$ and from $[\mu - 2\kappa, \mu + 2\kappa]$. Yet, there exist particular amplitude values which, in essence, completely *inhibit* the inter-well tunneling to the nearest neighbors and hence, enable the formation of such compact structures.

In this regard, we seek stationary solutions of the form $v_n = A_n e^{-i\mu t}$, for which Eq. (4) becomes:

$$\begin{aligned} \mu A_n + \gamma_0 A_n^3 + \kappa(A_{n+1} J_0(\alpha\theta_+) + A_{n-1} J_0(\alpha\theta_-)) + \\ 2\alpha\kappa A_n [A_{n+1} A_n J_1(\alpha\theta_+) + A_{n-1} A_n J_1(\alpha\theta_-)] = 0, \end{aligned} \tag{4}$$

and for conditions of tunneling suppression at the last site of vanishing amplitude (edge of the compacton) denoted as n_0 below. In the setting of Eq. (4), this directly establishes that:

$$J_0(\alpha|u_{n_0+1}|^2) = 0 \Rightarrow |u_{n_0+1}|^2 = 2.4048/\alpha, \tag{5}$$

which yields the solution based on the first zero of the Bessel function for the “boundary” of the compactly supported site. Then, for $\mu = -\gamma_0|u_{n_0+1}|^2$, both the condition for compact support at $n_0 \pm 1$, and the equation for $n = n_0$ are satisfied. Hence, Eq. (5) yields a single-site discrete compacton, which linearization illustrates to be stable (both the solution and its typical linearization are shown in Fig.1).

One can then generalize this type of consideration to two-sites, which are either in phase (2nd column of Fig.1) or out-of-phase (the so-called twisted modes of the 1st column of Fig.2). The only thing that changes here is that in order to satisfy the equation at the non-vanishing sites,

$$\mu = -\kappa - \gamma_0|u_{n_0+1}|^2 \quad \mu = \kappa - \gamma_0|u_{n_0+1}|^2, \tag{6}$$

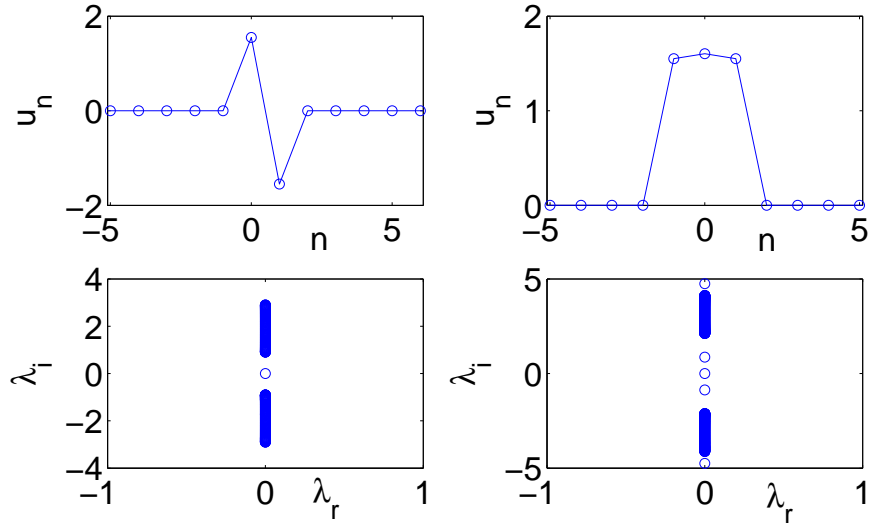


FIG. 2. Compacton solutions of Eq.(4) 1st column: inter-site out-of-phase mode , 2nd column: symmetric 3-site compacton.

respectively for the in-phase and out-of-phase two-site modes. We stress that these are *exact solutions* for the reduced system. Surprisingly, and completely contrary to what is the case for the DNLSE, *both* of these solutions are spectrally stable, as shown in Fig.2.

Moreover, with some additional effort, one can generalize these considerations to an arbitrary number of sites. As a typical example, a 3 site mode with amplitudes $(\dots, 0, A_1, A_2, A_1, 0, \dots)$ will satisfy, in addition to the “no tunneling condition” $J_0(\alpha A_1) = 0$, the constraints:

$$\begin{aligned} & \mu A_1 + \kappa A_2 J_0(\alpha(A_2^2 - A_1^2)) + \\ & 2\alpha\kappa A_1^2 A_2 J_1(\alpha(A_2^2 - A_1^2)) + \gamma_0 A_1^3 = 0, \\ & \mu A_2 + \kappa A_1 J_0(\alpha(A_1^2 - A_2^2)) + \\ & 4\alpha\kappa A_2^2 A_1 J_1(\alpha(A_1^2 - A_2^2)) + \gamma_0 A_2^3 = 0 \end{aligned}$$

which can be easily solved to yield a solution as the one shown in the 2nd column of Fig.2. Even such more complex solutions which would be highly unstable in the DNLSE are dynamically robust in the present setting. To examine the full nonlinear dynamical stability of these solutions, we considered them as initial conditions both in the averaged Eq. (4), as well as in the full Eq. (1). The results are shown in Fig.3. The single-site results are shown (similar findings were obtained for other modes). The top panel (of large color-bar amplitude) shows the space-time contour map of the solution modulus, while the bottom panel (of small colorbar amplitude) illustrates the deviation from the original solution. To further ensure robustness, a uniformly-distributed random perturbation of small amplitude was added to the original solution. It can clearly be seen that in *all* cases, both in the averaged equation and in the original system of Eq. (1), the relevant perturbation stays uniformly bounded and never exceeds 2% of the solution amplitude. The waveforms remain remarkably localized in their compact shape (after a transient stage of shedding off small

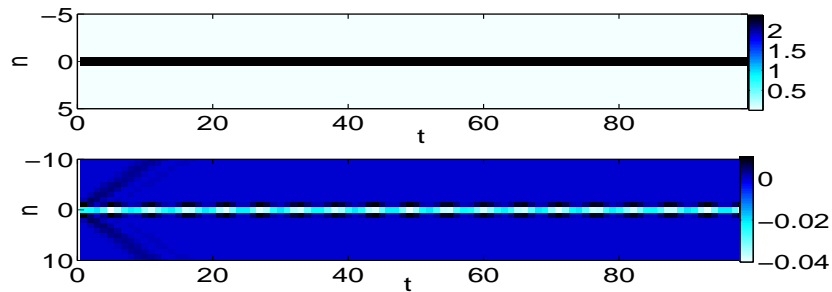


FIG. 3. Time evolution of single-site compacton solution. The top panel shows the evolution obtained from the averaged equation in Eq. (4), while the bottom panel refers to the numerical integration of the original DNLSE system in Eq. (1).

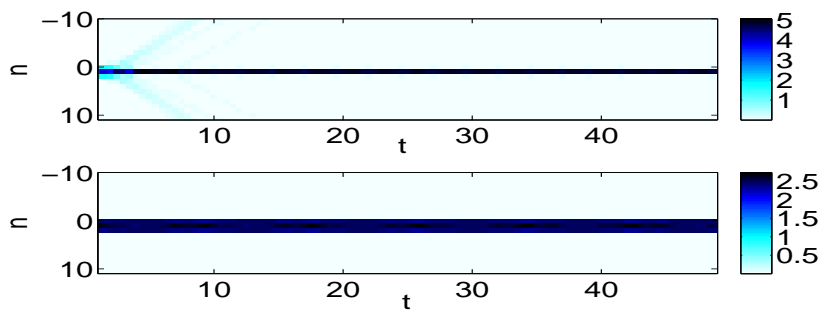


FIG. 4. Time evolution of a perturbed 3-site compacton for $\kappa = 1$ decaying into a single-site compacton for $\epsilon = 0.1$ (top panel) and remaining stable for $\epsilon = 0.025$ (bottom panel).

amplitude wavepackets). Notice that for Eq. (1), $\gamma(t) = 1 + \frac{1}{\epsilon} \cos(t/\epsilon)$, with $\epsilon = 0.1$ was used.

It should, however, be noted that if one departs from the regime of averaging validity of the averaging, an interesting deviation from the above behavior (and stability) may ensue. An example of this is shown in the panels of Fig. 4. In this case, the 3-site solution was initialized in Eq. (1) with $\epsilon = 0.1$ in the top panel, while $\epsilon = 0.025$ in the bottom one. While in the latter case, the above-argued robustness of the averaged modes was observed, in the former one, the apparent lack thereof was clearly due to the use of an ϵ outside of the regime of applicability for averaging approximation. Nevertheless, the resulting evolution confirms the general preference of the system towards settling in compact modes, since despite the large coupling $\kappa = 1$ used in this case, the evolution asymptotes to an essentially single-site solution.

4. Discrete compactons of binary BEC mixtures under SNLM

The above results can be extended to the case of two-component atomic BEC in a deep OL. In this case, the tight binding approximation leads to the following vector DNLSE [14]:

$$\begin{aligned} i\dot{u}_n &= -\kappa_1(u_{n+1} + u_{n-1}) - (\gamma_1|u_n|^2 + \gamma_{12}|v_n|^2)u_n, \\ i\dot{v}_n &= -\kappa_2(v_{n+1} + v_{n-1}) - (\gamma_{12}|u_n|^2 + \gamma_2|v_n|^2)v_n, \end{aligned} \quad (7)$$

where the overdot stands for time derivative, the coefficients κ_i , $i = 1, 2$, are related to the tunneling rates of atoms between neighboring wells of the optical lattice and γ_{12} , γ_i , $i = 1, 2$ are nonlinear coefficients related to the inter-species (a_{12}) and intra-species (a_{ii} , $i = 1, 2$) scattering lengths, respectively. Eq. (7) also arises in nonlinear optics where it models the propagation of an electric field in an array of optical waveguides with variable Kerr nonlinearity. In this context, the roles of the nonlinear coefficients γ_{ij} correspond to self- and cross-phase modulations of the electric field components, respectively [15, 16]. Notice that the above two component DNLSE has the Hamiltonian form $\dot{\chi}_n = \delta H / \delta \chi_n^*$ with $\chi_n = u_n, v_n$ and the Hamiltonian H given by:

$$H = - \sum_n \left[(\kappa_1 u_{n+1} u_n^* + \kappa_2 v_{n+1} v_n^* + c.c.) + \frac{1}{2} (\gamma_1 |u_n|^4 + \gamma_2 |v_n|^4) + \gamma_{12} |u_n|^2 |v_n|^2 \right]. \quad (8)$$

Here, the $*$ stands for the complex conjugation and *c.c.* denotes the complex conjugate of the expression in the parenthesis. Also, notice that the number of atoms $N_i = \sum_n |\chi_n|^2$, $\chi_n = u_n, v_n$ is conserved for each component. Below, we concentrate on the case of BEC mixtures with fixed (not necessarily equal) intra-species nonlinearities and subjected to strong nonlinear inter-species management of the form:

$$\gamma_{12}(t) \equiv \gamma_{12}^{(0)} + \gamma_{12}^{(1)}(t) = \gamma_{12}^{(0)} + \frac{\gamma_{12}^{(1)}}{\epsilon} \cos(\Omega \frac{t}{\epsilon}), \quad (9)$$

with $\gamma_{12}^{(0)}, \gamma_{12}^{(1)}$ real constants and ϵ a small parameter controlling the strength of the modulation as before (strong nonlinearity management corresponding to $\epsilon \ll 1$ with Ω , $\gamma_{12}^{(1)} \sim O(1)$). We remark that although we have considered for simplicity in Eq. (9) a sinusoidal modulation of period $T = 2\pi/\Omega$ in the fast time variable $\tau = t/\epsilon$, results can be extended easily to other types of periodic $\gamma_{12}^{(1)}(t)$ functions. This management setting appears to be quite convenient in experiments since it involves changing only one parameter (for the case of intra-species SNLM see [17]). Moreover, the averaged equations obtained in this case are physically more interesting because nonlinear dispersion terms that involve both components

could lead, in principle, to novel types of binary compactons. Analogously to what was done for the single component case above, we use the averaging method to eliminate the fast time, $\tau = t/\epsilon$, dependence. In this respect, we perform the following transformation:

$$u_n = U_n e^{i\Gamma|V_n|^2}, \quad v_n = V_n e^{i\Gamma|U_n|^2}, \quad (10)$$

where Γ denotes the antiderivatives of $\gamma_{12}^{(1)(t)}$, e.g. $\Gamma_{12}(\tau) = \frac{\gamma_{12}^{(1)}}{\epsilon} \int_0^\tau \cos(\Omega\tau') d\tau'$. By substituting Eq.(10) into Eqs.(7) we obtain:

$$i\dot{U}_n = i\kappa_2\Gamma(\tau)U_n[V_n^*X_1 - V_nX_1^*] - \kappa_1X_2 - (\gamma_1|U_n|^2 + \gamma_{12}^0|V_n|^2)U_n, \quad (11)$$

$$i\dot{V}_n = i\kappa_1\Gamma(\tau)V_n[U_n^*X_2 - U_nX_2^*] - \kappa_2X_1 - (\gamma_2|V_n|^2 + \gamma_{12}^{(0)}|U_n|^2)V_n, \quad (12)$$

where $X_1 = U_{n+1}e^{i\Gamma\theta_1^+} + U_{n-1}e^{i\Gamma\theta_1^-}$, $X_2 = V_{n+1}e^{i\Gamma\theta_2^+} + V_{n-1}e^{i\Gamma\theta_2^-}$ and with θ_i^\pm denoting the quantities:

$$\theta_1^\pm = |U_{n\pm 1}|^2 - |U_n|^2, \quad \theta_2^\pm = |V_{n\pm 1}|^2 - |V_n|^2. \quad (13)$$

The average over the rapid modulation in these equations can easily be done with the help of the relations:

$$\begin{aligned} \langle e^{\pm i\Gamma(\tau)\theta^\pm} \rangle &= J_0(\alpha\theta^\pm) \\ \langle \Gamma(\tau)e^{\pm i\Gamma(\tau)\theta^\pm} \rangle &= \pm i\alpha J_1(\alpha\theta^\pm), \end{aligned} \quad (14)$$

where the angular bracket $\langle \cdot \rangle$ denotes the average with respect to the fast time, e.g. $\langle F \rangle \equiv (1/T) \int_0^T F d\tau$, while J_0, J_1 are Bessel functions [18] of the first kind for the zero-th and first order respectively, and the parameter α is given by:

$$\alpha = \gamma_{12}^{(1)}/\Omega. \quad (15)$$

The system of averaged equations is then obtained as:

$$\begin{aligned} i\dot{U}_n &= -\alpha\kappa_2U_n \left[J_1(\alpha\theta_1^+) (V_n^*V_{n+1} + V_nV_{n+1}^*) + J_1(\alpha\theta_1^-) (V_n^*V_{n-1} + V_nV_{n-1}^*) \right] \\ &\quad - \kappa_1 [U_{n+1}J_0(\alpha\theta_2^+) + U_{n-1}J_0(\alpha\theta_2^-)] - [\gamma_1|U_n|^2 + \gamma_{12}^{(0)}|V_n|^2] U_n, \end{aligned} \quad (16)$$

$$\begin{aligned} i\dot{V}_n &= -\alpha\kappa_1V_n \left[J_1(\alpha\theta_2^+) (U_n^*U_{n+1} + U_nU_{n+1}^*) + J_1(\alpha\theta_2^-) (U_n^*U_{n-1} + U_nU_{n-1}^*) \right] \\ &\quad - \kappa_2 [V_{n+1}J_0(\alpha\theta_1^+) + V_{n-1}J_0(\alpha\theta_1^-)] - [\gamma_2|V_n|^2 + \gamma_{12}^{(0)}|U_n|^2] V_n. \end{aligned} \quad (17)$$

Here, we only report on some interesting consequences implied by these equations for the simplest case of a bright-bright compacton, which can be searched in the form of for stationary states:

$$U_n = A_n e^{-i\mu_u t}, \quad V_n = B_n e^{-i\mu_v t}, \quad (18)$$

with μ_u, μ_v chemical potentials of the two atomic species. Substituting these expressions into Eq. (16,17), one gets the following stationary equations:

$$\begin{aligned} \mu_u A_n + (\gamma_1 A_n^3 + \gamma_{12}^{(0)} B_n^2 A_n) + \kappa_1 [A_{n+1} J_0(\alpha\theta_2^+) + \\ A_{n-1} J_0(\alpha\theta_2^-)] + 2\alpha\kappa_2 A_n B_n [B_{n+1} J_1(\alpha\theta_1^+) + \\ B_{n-1} J_1(\alpha\theta_1^-)] = 0, \end{aligned} \quad (19)$$

$$\begin{aligned} \mu_v B_n + (\gamma_2 B_n^3 + \gamma_{12}^{(0)} A_n^2 B_n) + \kappa_2 [B_{n+1} J_0(\alpha\theta_1^+) + \\ B_{n-1} J_0(\alpha\theta_1^-)] + 2\alpha\kappa_1 A_n B_n [A_{n+1} J_1(\alpha\theta_2^+) + \\ A_{n-1} J_1(\alpha\theta_2^-)] = 0, \end{aligned} \quad (20)$$

to be solved for the chemical potentials and amplitudes A_n, B_n of the compacton modes. The compact nature of the solution ($A_i, B_i = 0$ outside a finite (small) range of sites), allows one to truncate the above infinite system into a finite number of relations between the above variables, which can be solved exactly.

4.1. Bright-Bright compactons

To search for bright-bright (B-B) compacton solutions we need to look for the last sites of vanishing amplitude, i.e. $n_0 \pm 1$, where the vanishing of the tunneling rate is realized. For a single site B-B compacton, we assume $A_{n_0} = a, B_{n_0} = b, A_{n_0 \pm j} = 0, B_{n_0 \pm j} = 0$ for all $j \geq 1$. Substituting this ansatz in Eqs.(19,20), we obtain the corresponding condition for the compacton existence as:

$$\begin{aligned} J_0(\alpha a^2) &= 0, \quad a^2 = \xi_1/\alpha, \\ J_0(\alpha_2 b^2) &= 0, \quad b^2 = \xi_2/\alpha \end{aligned} \quad (21)$$

where ξ_1, ξ_2 are zeros (not necessary equal) of the Bessel function J_0 . This condition, together with:

$$\mu_u = -\gamma_1 a^2 - \gamma_{12} b^2, \quad \mu_v = -\gamma_2 b^2 - \gamma_{12} a^2, \quad (22)$$

gives us the single site B-B compacton pair.

Notice that these equations are the same as for intra-species management case. A big difference with the intra-species management case, however, is the fact that now, the numbers of atoms in the two components of a single site compacton cannot be arbitrary but must be related as follows:

$$\frac{N_1}{N_2} = \frac{\xi_1}{\xi_2}. \quad (23)$$

This relation implies that for a given number of particles in the first component $N_1 = a^2$ (controlled by the parameter α), only a discrete set of values for N_2 are permitted. It is interesting to see if such a state can emerge from generic initial conditions (for example Gaussians). Further research is currently underway to see if this approach is feasible.

5. Conclusions

In conclusion, we have shown that in the SNLM limit stable discrete compactons can exist both in one-dimensional BEC trapped in deep optical lattices and in binary BEC mixtures. In this last case, the variety of the compact excitations is larger and includes also dark components in the form of stable bright-dark or dark-dark compactons. The lack of interacting tails in these excitations could be of interest for practical applications. In particular, in the field of nonlinear optics, this could permit one to achieve a maximum rate of information transfer signal in waveguide arrays without disturbing interferences. The solutions considered herein could also lead to experimental observation of discrete compactons both in BEC arrays and in arrays of binary BEC mixtures subjected to SNLM.

Acknowledgements

MS acknowledges partial support from the Ministero dell'Istruzione, dell'Università e della Ricerca (MIUR) through a PRIN (Programmi di Ricerca Scientifica di Rilevante Interesse Nazionale) 2010 – 2011 initiative (grant # 2010HXAW77-005).

References

- [1] B.A. Malomed, *Soliton management in periodic systems*, Springer-Verlag, Berlin, 2007.
- [2] N.J. Smith *et al.* Enhanced power solitons in optical fibres with periodic dispersion management. *Electron. Lett.*, 1996, **32**, P. 54;
I. Gabitov, S.K. Turytsin. Averaged pulse dynamics in a cascaded transmission system with passive dispersion compensation. *Optics Lett.*, 1996, **21**, P. 327.
- [3] H. Saito and M. Ueda. Dynamically Stabilized Bright Solitons in a Two-Dimensional Bose-Einstein Condensate. *Phys. Rev. Lett.*, 2003, **90**, P. 040403;
F.Kh. Abdullaev *et al.* Adiabatic Dynamics of Periodic Waves in Bose-Einstein Condensates with Time Dependent Atomic Scattering Length. *Phys. Rev. Lett.*, 2003, **90**, P. 230402.
- [4] M.J. Ablowitz and Z.H. Musslimani. Discrete Diffraction Managed Spatial Solitons. *Phys. Rev. Lett.*, 2001, **87**, P. 254102.
- [5] I.L. Garanovich, A.A. Sukhorukov, and Yu.S. Kivshar. Nonlinear diffusion and beam self-trapping in diffraction-managed waveguide arrays. *Opt. Express*, 2007, **15**, P. 9547.
- [6] A. Szameit, *et al.* Inhibition of Light Tunneling in Waveguide Arrays. *Phys. Rev. Lett.*, 2009, **102**, P. 153901.
- [7] H. Lignier *et al.* Dynamical Control of Matter-Wave Tunneling in Periodic Potentials. *Phys. Rev. Lett.*, 2007, **99**, P. 220403.
- [8] P. Rosenau, J.M. Hyman. Compactons: Solitons with finite wavelength. *Phys. Rev. Lett.*, 1993, **70**, P. 564;
P. Rosenau. Compact and noncompact dispersive structures. *Phys. Lett. A*, 2000, **275**, P. 193.
- [9] P.G. Kevrekidis, *The discrete nonlinear Schrödinger equation*, Springer-Verlag, Heidelberg, 2009.
- [10] F. Kh. Abdullaev, P. G. Kevrekidis, and M. Salerno. Compactons in Nonlinear Schrödinger Lattices with Strong Nonlinearity Management. *Phys. Rev. Lett.*, 2010, **105**, P. 113901.
- [11] D.E. Pelinovsky *et al.* Hamiltonian averaging for solitons with nonlinearity management. *Phys. Rev. E*, 2004, **70**, P. 047604.
- [12] F.Kh. Abdullaev *et al.* Intrinsic localized modes in arrays of atomic-molecular Bose-Einstein condensates. *Phys. Rev. A*, 2003, **67**, P. 013605.
- [13] P.G. Kevrekidis, V.V. Konotop. Bright compact breathers. *Phys. Rev. E*, 2002, **65**, P. 066614.
- [14] U. Shrestha, J. Javanainen, and J. Ruostekoski. Pulsating and Persistent Vector Solitons in a Bose-Einstein Condensate in a Lattice upon Phase Separation Instability. *Phys.Rev.Lett.*, 2009, **103**, P. 190401.
- [15] A. Kobayakov, S. Darmanyan, F. Lederer, E. Schmidt. Dark Spatial Solitons in Discrete Cubic Media with Self- and Cross-Phase-Modulation. *Optical and Quantum Electronics*, 1998, **30**, P. 795.
- [16] Gaetano Assanto, Luis A. Cisneros, Antonmaria A. Minzoni, Benjamin D. Skuse, Noel F. Smyth, and Annette L. Worthy. Soliton Steering by Longitudinal Modulation of the Nonlinearity in Waveguide Arrays. *Phys.Rev.Lett.*, 2010, **104**, P. 053903.
- [17] F. Kh. Abdullaev, M. S.A. Hadi, M. Salerno, and B. Umarov. Compacton matter waves in binary Bose gases under strong nonlinear management. *Phys. Rev. A*, 2014, **90**, P. 063637.
- [18] M. Abramowitz and I. A. Stegun, *Handbook of Mathematical Functions*, National Bureau of Standards, Washington, 1964.

From “fat” graphs to metric graphs: the problem of boundary conditions

G. F. Dell’Antonio¹, A. Michelangeli²

¹Sapienza, Rome, Italy and

SISSA, Via Bonomea 265, 34136, Trieste, Italy

²SISSA, Via Bonomea 265, 34136, Trieste, Italy and

Center for Advanced Studies, Ludwig-Maximilians-Universität München,

Geschwister-Scholl-Platz, 1, 80539, Munich, Germany

gianfa@sissa.it

PACS 03.65.Ge, 02.30.Jr

DOI 10.17586/2220-8054-2015-6-6-751-756

We discuss how the vertex boundary conditions for the dynamics of a quantum particle on a metric graph emerge when the dynamics is regarded as a limit of the dynamics in a tubular region around the graph. We give evidence for the fact that the boundary conditions are determined by the possible presence of a zero-energy resonance. Therefore, the boundary conditions depend on the shape of the fat graph near the vertex. We also give evidence, by studying the case of the half-line, for the fact that on the contrary, in general, adding on a graph a shrinking support potentials at the vertex either does not alter the boundary condition or does not produce a self-adjoint dynamics. Convergence, throughout, is meant in the sense of strongly resolvent convergence.

Keywords: quantum billiards, Schrödinger equation.

Received: 1 November 2015

1. Introduction

We consider in \mathbb{R}^3 a star graph Γ with vertex at the origin and N “rays” (half-lines) $K^{(n)}$, $n = 1 \dots N$. We consider also a suitable vicinity of Γ (“fat graph”), denoted by Γ_ε , whose “width” is proportional to $\varepsilon > 0$. More concretely, we consider Γ_ε as consisting of a junction region contained in a ball B_ε of radius $C \cdot \varepsilon$ ($C > 1$), attached to which there are N tubes” $K_\varepsilon^{(n)}$, $n = 1, \dots, N$, namely N non-intersecting infinite half-cylinders with transversal radius ε , whose axes are the rays $K^{(n)}$.

The limit $\varepsilon \rightarrow 0$ that we have in mind is a homotetic shrinking of Γ_ε to its skeleton Γ .

The internal region may be arbitrary and need not be connected; it may also be fragmented. In the case of graphene, the image in an electronic microscope shows that the density of conducting electrons is essentially localized in a spherical corona of width approximately equal to the diameter of the cylinders.

This may be considered as a result of the combined action of the attraction to the nucleus and of the presence near the nucleus of the valence electrons.

Let $\Delta_{\Gamma_\varepsilon}$ be the Laplacian on Γ_ε with Dirichlet boundary conditions at $\partial\Gamma_\varepsilon$.

We denote by $\lambda_\varepsilon > 0$ and $\xi_\varepsilon^{(1)}$, respectively, the lowest eigenvalue and the corresponding normalized eigenfunction of the two-dimensional negative Laplacian on a disk with Dirichlet boundary conditions. By scaling $\lambda_\varepsilon \sim \varepsilon^{-2}\lambda$.

We define the following:

$$H_\varepsilon := -\Delta_{\Gamma_\varepsilon} - \lambda_\varepsilon \mathbf{1}.$$

We have thus obtained a self-adjoint operator on the fat graph Γ_ε . Depending on the shape of Ω_ε for all values of $\varepsilon > 0$, H_ε may possibly have a negative point spectrum and an absolutely continuous spectrum coinciding with \mathbb{R}^+ .

It turns out that a deep understanding of the structure of the limit $\varepsilon \rightarrow 0$ is achieved by means of the notion of *zero energy resonance*. For the present purposes, we define a zero energy resonance of H_ε as a singularity of the spectral measure of H_ε at the bottom of the continuous spectrum, equivalently, as a singularity in k^2 at $k = 0$ of the resolvent $(H_\varepsilon - k^2)^{-1}$.

If the boundary $\partial\Gamma_\varepsilon$ is smooth, the singularity at the bottom of the continuous spectrum is of the type $\frac{1}{|k|}$. This corresponds, in our case, due to the special form of the domain Γ_ε , to a generalized (i.e., distributional) solution Φ_ε to $H_\varepsilon\Phi_\varepsilon = 0$ which is only square-integrable locally.

There is in fact a **one-to-one correspondence** between the possible singularities at zero of the resolvent of H_ε , due to **resonances**, and the singularities at zero of the resolvents of each self-adjoint Laplacian on the star graph. The former are non square-integrable functions that on each cylinder behave, axially, as a constant plus linear function $a_n + b_n z_n$ (z_n is the axial coordinate on the n -th cylinder); the latter have the very same behavior on the corresponding rays of the star graph.

2. Setting the problem up

We want to study the effect of Ω_ε on the limit $\varepsilon \rightarrow 0$ by means of the associated problem – we shall call it “the internal region problem” – consisting of the negative Laplacian in the internal region Ω_ε with boundary conditions that are of some assigned type, denoted by α , on the bases of the cylinders, and are of the Dirichlet type on the rest of $\partial\Omega_\varepsilon$.

With this choice, we denote by $\mu_+(\Omega_\varepsilon)$ and $\mu_-(\Omega_\varepsilon)$, respectively, the lowest eigenvalue of the internal region problem when $\alpha = \text{Dirichlet}$ or $\alpha = \text{Neumann}$, and by $\mu_\alpha(\Omega_\varepsilon)$ the lowest eigenvalue with generic boundary condition α (recall that on the rest of $\partial\Omega_\varepsilon$ we always take Dirichlet boundary conditions). Clearly:

$$\mu_-(\Omega_\varepsilon) \leq \mu_\alpha(\Omega_\varepsilon) \leq \mu_+(\Omega_\varepsilon),$$

and each $\mu_\alpha(\Omega_\varepsilon)$ scales as ε^{-2} . We also note that by min-max, when one increases Ω_ε , both $\mu_-(\Omega_\varepsilon)$ and $\mu_+(\Omega_\varepsilon)$ decrease.

Suppose that the internal region problem with a given boundary condition α has a lowest-energy solution given by the eigenfunction $\phi_\varepsilon(\mathbf{x})$ and the eigenvalue $\mu_\alpha(\Omega_\varepsilon)$, where \mathbf{x} is the three-dimensional coordinate in Ω_ε .

Correspondingly, prolonging ϕ_ε by continuity of the function and its derivatives, to a function Φ_ε , also defined also on the external cylinders in such a way that, if (x_n, y_n) are the transversal coordinates and z_n is the axial coordinate in $K_\varepsilon^{(n)}$, then:

$$\Phi_\varepsilon(x_1, y_1, z_1, \dots, x_N, y_N, z_N) = \prod_{n=1}^N \xi_\varepsilon^{(1)}(x_n, y_n)(a_n + b_n z_n), \quad z_n \geq 0,$$

Fundamental observation: a zero energy resonance for H_ε on Γ_ε can occur only if for the associated internal region problem there exists a boundary condition α at the bases of the cylinders such that the first eigenvalue $\mu_\alpha(\Omega_\varepsilon)$ of the internal region problem (namely the negative Laplacian inside Ω_ε with boundary condition α at the bases of the cylinders and Dirichlet boundary conditions on the remaining part of $\partial\Omega_\varepsilon$) **coincides** with the lowest

eigenvalue λ_ε of the negative Laplacian on the cylinders transversal section, namely if

$$\mu_-(\Omega_\varepsilon) \leq \lambda_\varepsilon \leq \mu_+(\Omega_\varepsilon).$$

Decomposition:

$$L^2(\Gamma_\varepsilon) \cong L^2(\Omega_\varepsilon) \oplus \left(\bigoplus_{n=1}^N L^2(K_\varepsilon^{(n)}) \right)$$

(Ω_ε = the central region, $K_\varepsilon^{(n)}$ = the cylinders). In turn,

$$\begin{aligned} L^2(K_\varepsilon^{(n)}) &\cong L^2(K^{(n)}) \otimes L^2(D_\varepsilon) \\ &\cong \left(L^2(\mathbb{R}^+) \otimes \text{Span}\{\xi_\varepsilon^{(1)}\} \right) \oplus \left(L^2(\mathbb{R}^+) \otimes \left(\bigoplus_{k=2}^\infty \text{Span}\{\xi_\varepsilon^{(k)}\} \right) \right); \end{aligned}$$

($K^{(n)}$ = corresponding ray of the star graph Γ) (hence $L^2(K^{(n)}) \cong L^2(\mathbb{R}^+)$), D_ε is the disk in \mathbb{R}^2 centered at the origin and with radius ε , and $\{\xi_\varepsilon^{(k)} | k \in \mathbb{N}\}$ is the o.n.b. of $L^2(D_\varepsilon)$ consisting of all Dirichlet Laplacian eigenfunctions.

We note that this decomposition *is not left invariant* by the flow of H_ε .

Consider the natural map:

$$\Pi_\varepsilon : L^2(\Gamma_\varepsilon) \rightarrow L^2(\Gamma)$$

which “crushes” the square integrable functions on the fat graph to square integrable functions on the star graph by first taking only the part of the function existing on the cylinders $K_\varepsilon^{(n)}$ ’s and neglecting the part supported on the vertex region Ω_ε , and then on each cylinder projecting the transversal part of the wave-function onto $\xi_\varepsilon^{(1)}$.

We want to investigate the limit of the “squeezed resolvent”:

$$\Pi_\varepsilon (H_\varepsilon - k^2)^{-1} \Pi_\varepsilon^* \xrightarrow{\varepsilon \rightarrow 0} ?$$

2.1. Resonant case

Resonant case: \exists a zero energy resonance Φ_ε for H_ε :

$$\begin{aligned} \Phi_\varepsilon &\in L^2_{\text{loc}}(\Gamma_\varepsilon) \setminus L^2(\Gamma_\varepsilon) \\ H_\varepsilon \Phi_\varepsilon &= 0 \quad \text{distributionally.} \end{aligned}$$

on the n -th cylinder, $K_\varepsilon^{(n)}$ it has the form

$$\left(\Phi_\varepsilon \Big|_{K_\varepsilon^{(n)}} \right) (x_n, y_n, z_n) = \xi_\varepsilon^{(1)}(x_n, y_n) (a_n + b_n z_n).$$

Each self-adjoint Laplacian $\Delta_{A,B}$ on the star graph Γ is identified by a vertex boundary condition on each $f \equiv (f^{(1)}, \dots, f^{(N)})$

$$A \begin{pmatrix} f^{(1)}(0) \\ \vdots \\ f^{(N)}(0) \end{pmatrix} + B \begin{pmatrix} f^{(1)'}(0) \\ \vdots \\ f^{(N)'}(0) \end{pmatrix} = 0$$

for suitable $N \times N$ matrices A and B [Kostykin-Schrader]. Each $\Delta_{A,B}$ admits a zero-energy resonance in $L^2_{\text{loc}}(\Gamma) \setminus L^2(\Gamma)$, that on each ray $K^{(n)}$, $n = 1, \dots, N$, behaves as $\alpha_n + \beta_n z_n$ for certain coefficient pairs (α_n, β_n) determined by A and B .

There is an evident **one-to-one correspondence** between the set of parameters qualifying a **resonance on the fat graph** and the set of parameters qualifying a **resonance on a star graph**, an observation that we now intend to develop further.

Let $-\Delta_{A,B}$ be that Laplacian whose resonance’s behavior is given by $\alpha_n = a_n, \beta_n = b_n$.

It can be argued that if $\Pi_\varepsilon H_\varepsilon \Pi_\varepsilon - (-\Delta_{A,B})$ has no further resonance, and if the resolvent convergence has suitable distributional properties then the limit exists and corresponds to a Laplacian $-\Delta_{A,B}$ i.e. $\Pi_\varepsilon H_\varepsilon - k^2) \Pi_\varepsilon^* \xrightarrow{\varepsilon \rightarrow 0} (-\Delta_{A,B} - k^2)^{-1}$

“the limit is selected by the resonance of H_ε ”.

Note that this claim is well-posed, for the resonance function of H_ε is scale invariant.

The claim is proved by the following argument. Let $H_0 \equiv \Pi_\varepsilon H_\varepsilon \Pi_\varepsilon$ and let $V_\varepsilon W_\varepsilon^* = H_0 + \Delta_{A,B}$. One has:

$$\frac{1}{H_0 + V_\varepsilon W_\varepsilon^* - z} - \frac{1}{H_0 + z} = \frac{1}{H_0 - z} V_\varepsilon C_\varepsilon W_\varepsilon^* \frac{1}{H_0 - z}$$

$$C_\varepsilon \equiv \frac{1}{1 - W_\varepsilon^* \frac{1}{H_0 - z} V_\varepsilon}$$

If V_ε and W_ε are H_0 -compact and converge weakly to zero when $\varepsilon \rightarrow 0$ and if H_0 and $\Delta_{A,B}$ have the same zero-energy resonances, then C_ε vanishes in the limit $\varepsilon \rightarrow 0$.

2.2. Non-resonant case

Non-resonant case: no zero-resonance for H_ε .

Two subcases:

First case: $\lambda_\varepsilon < \mu_-(\Omega_\varepsilon)$.

In this case, the energy threshold for the internal region is high (compared to λ_ε), which means that the domain Ω_ε has to be “very small” (in order for the spectrum of the internal region problem to have such a high bottom). Functions that belong to the continuous spectrum of H_ε have a component in Ω_ε vanishing in the sup-norm as $\varepsilon \rightarrow 0$, in order for their H^2 -norm to stay finite. Therefore, the functions in the domain of any limit operator on the graph must be zero at the vertex.

\Rightarrow The limit is the Dirichlet Laplacian.

Second case: $\lambda_\varepsilon > \mu_+(\Omega_\varepsilon)$.

Now the energy threshold for the internal region is low (compared to λ_ε) and the argument above does not apply. We expect that the projection Π_ε “kills” in the limit the wave function (the fast transversal oscillations average to zero).

Therefore, in this case too, we expect that if the limit dynamics on the star graph exists they are Dirichlet-based.

But consider that strong convergence of the resolvents as bounded operators in the Hilbert space does not imply that the limit be the resolvent of a self-adjoint operator even if the convergence is strong and the resolvent identities are satisfied. The limit must be analytic away from the real axis and strong convergence need not preserve analyticity. We shall later give a simple example.

We expect that in the limit $\Pi_\varepsilon (H_\varepsilon - k^2)^{-1} \Pi_\varepsilon^*$ becomes analytic for $Imk^2 > 0$ and regular at $k^2 \rightarrow 0$ as $\varepsilon \rightarrow 0$, because on the star graph, the Dirichlet Laplacian is the *only* self-adjoint Laplacian whose spectral measure is regular at zero [Kostyrykin-Schrader].

A *removal of singularity* of the resolvent must therefore take place in the limit $\varepsilon \rightarrow 0$. This is typical of this second sub-case: in the first sub-case $\lambda_\varepsilon < \mu_-(\Omega_\varepsilon)$, instead, the resolvent of H_ε is regular at $k^2 = 0$ uniformly in $\varepsilon > 0$ and hence also in the limit.

A way to monitor this *removal of singularity* for the limiting resolvent is to compare (the resolvent of) H_ε with the second operator:

$$H_\varepsilon + V_\varepsilon \quad V_\varepsilon := C\varepsilon^{-2}\mathbf{1}_{\Omega_\varepsilon}$$

We choose $C > 0$, which is always possible, so that the “modified internal region problem” $-\Delta + V_\varepsilon$ on Ω_ε , with a given boundary condition α at the bases of the cylinders and, as usual, Dirichlet boundary conditions on the remaining part of $\partial\Omega_\varepsilon$, has the lowest eigenvalue that precisely coincides with λ_ε (the role of V_ε is therefore merely to lift the bottom of the spectrum of the internal region problem up to the desired level λ_ε). For convenience, we denote by φ_ε the corresponding lowest energy eigenfunction, that is, $(-\Delta + V_\varepsilon)\varphi_\varepsilon = \lambda_\varepsilon\varphi_\varepsilon$ in Ω_ε with Dirichlet boundary conditions on the whole $\partial\Omega_\varepsilon$.

The internal region problem, consisting now of the negative Laplacian plus the potential V_ε with a given boundary condition α , has the lowest eigenvalue that can be lifted up by means of a suitable choice of the constant C so as to precisely match the value λ_ε . This does *not* alter, but for an overall phase factor, the solutions to the internal region problem and hence the matching conditions at the bases of the cylinders.

Notice:

$$\sigma(H_\varepsilon + V_\varepsilon) = [0, +\infty)$$

$H_\varepsilon + V_\varepsilon$ admits a zero energy resonance.

We thus have two operators on $L^2(\Gamma_\varepsilon)$, namely H_ε and $H_\varepsilon + V_\varepsilon$, where the latter is a perturbation of the former and it is zero-resonant.

This is the input for a well-established scheme developed by Kato, Konno, and Kuroda that allows one to re-write:

$$(H_\varepsilon + V_\varepsilon - \lambda)^{-1} - (H_\varepsilon - \lambda)^{-1},$$

in a way that is well suited for taking the limit $\varepsilon \rightarrow 0$ and for taking advantage of the existence of a zero-energy resonance.

For instance:

$$\begin{aligned} \Pi_\varepsilon \left((H_\varepsilon^N + V_\varepsilon - \lambda)^{-1} - (H_\varepsilon^N - \lambda)^{-1} \right) \Pi_\varepsilon^* &\xrightarrow{\varepsilon \rightarrow 0} \\ &\xrightarrow{\varepsilon \rightarrow 0} (-\Delta^N - \lambda)^{-1} + C(k)P_{N,k} \end{aligned}$$

where $P_{N,k}$ is the projection onto the vector $|G_k^N(\cdot, 0)\rangle$.

Using the explicit form of the resolvents on a graph given e.g. in [1], one verifies that the last term is:

$$\left((-\Delta^D - \lambda)^{-1} - (-\Delta^N - \lambda)^{-1} \right)$$

and therefore \Rightarrow The limit is the resolvent of the Dirichlet Laplacian.

Notice: V_ε is added in the *internal region* Ω_ε and this can be done only in the case of a fat graph Γ_ε . This procedure has no counterpart on the graph Γ (because there is no internal region).

One may hope to obtain similar results by adding directly in the graph a potential V_ε supported around the vertex of the graph and taking the limit when the support shrinks to the vertex.

Prototype: a “star graph” with one edge only. The corresponding fat graph has the shape of a safety match.

By choosing suitably the shape of the head of the safety match, one can produce in the limit any boundary condition at the vertex.

We can now try to change boundary conditions at the vertex of the graph by adding a

potential shrinking around the origin

We introduce the Hamiltonian on $L^2(\mathbb{R}^+)$:

$$H_\varepsilon^{(\nu)} = -\Delta_\nu + V_\varepsilon, \quad \mathcal{D}(H_\varepsilon^{(\nu)}) = \mathcal{D}(-\Delta_\nu),$$

$$V_\varepsilon(x) := \frac{1}{\varepsilon^{1+\gamma}} V\left(\frac{x}{\varepsilon}\right),$$

where

→ V is real-valued, $V \in L^1(\mathbb{R}^+) \cap L^\infty(\mathbb{R}^+)$

→ self-adjoint boundary condition at the origin

$$f(0) \sin \nu = f'(0) \cos \nu \quad \nu \in \left(-\frac{\pi}{2}, \frac{\pi}{2}\right]$$

→ $\gamma < 0$ weak scaling, $\gamma = 0$ canonical, $\gamma > 0$ strong

The problem is simple enough to allow an explicit solution.

For $k^2 \in \mathbb{C}$ with $\text{im } k \neq 0$, we find that

$$(-\Delta_\nu + V_\varepsilon - k^2)^{-1} \xrightarrow{\varepsilon \rightarrow 0} (-\Delta_\nu - k^2)^{-1} + \Theta_{\nu, V, k}(\gamma) |\eta_{\nu, k}\rangle \langle \overline{\eta_{\nu, k}}|$$

in the norm operator sense, where

$$\eta_{\nu, k}(x) := (\tan \nu - k)^{-1} e^{ikx}, \quad x \in [0, +\infty),$$

$$\Theta_{\nu, V, k}(\gamma) = \begin{cases} 0 & \text{if } \gamma < 0 \text{ (weak scaling)} \\ -\frac{(\int_{\mathbb{R}^+} V)}{1 + (\tan \nu - ik)^{-1}(\int_{\mathbb{R}^+} V)} & \text{if } \gamma = 0 \text{ (canonical scaling)} \\ -(\tan \nu - ik) & \text{if } 0 < \gamma < 1 \text{ (strong scaling).} \end{cases}$$

The convergence being in operator norm, the limit operator R_k satisfies the resolvent identity.

In the weak scaling regime the boundary conditions are not changed.

In the canonical or strong scaling, in general R_k is not the resolvent of a self-adjoint operator (in particular the limit does not produce new boundary conditions at $x = 0$), because R_k is not holomorphic in k^2 :

in fact $R_k = (-\Delta_D - k^2)^{-1}$ for all $k^2 \in (-\infty, 0)$,

but $R_k \neq (-\Delta_D - k^2)^{-1}$ for some values $k^2 \in \mathbb{C} \setminus (-\infty, 0)$

Exceptions:

→ $\int_{\mathbb{R}^+} V = 0$ in the canonical scaling ($\gamma = 0$)

→ Dirichlet boundary conditions are preserved in any scaling

This phenomenon can be proved for a general metric graph as well.

Remarkably, the only exception is a “fake” star graph consisting of the real line \mathbb{R} regarded as the union of the two rays \mathbb{R}^+ and \mathbb{R}^- .

In this case one can add to the self-adjoint Laplacian on \mathbb{R} a potential $\varepsilon^{-1} \mathbf{1}_{\{|x| \leq \varepsilon\}}$ at the “vertex” of the graph so to obtain in the limit $\varepsilon \rightarrow 0$ a so-called “point interaction” at the origin, namely a self-adjoint operator with certain boundary conditions at the origin [2].

References

- [1] K. Kostykin, S. Schrader. Kirchhoff’s rule for quantum wires. *J. Phys. A: Math. Gen.*, 1999, **32**, P. 595–630.
- [2] S. Albeverio, R. Høegh-Krohn. Perturbation of resonances in quantum mechanics. *J. Math. Anal. Appl.*, 1984, **101**(2), P. 491-513.

Linearized KdV equation on a metric graph

Z. A. Sobirov^{1,2}, M. I. Akhmedov², O. V. Karpova^{3,4}, B. Jabbarova⁵

¹Faculty of Mechanics and Mathematics, National University of Uzbekistan, Vuzgorodok, 100047 Tashkent, Uzbekistan

²Applied Mathematics Department of Tashkent Financial Institute, 100000 Tashkent, Uzbekistan

³Faculty of Physics, National University of Uzbekistan, Vuzgorodok, 100047 Tashkent, Uzbekistan

⁴Turin Polytechnic University in Tashkent, Uzbekistan

⁵Urganch State University, Urganch, Uzbekistan
sobirovzar@gmail.com, ola_july@mail.ru

PACS 02.30.Ik, 05.45.Yv

DOI 10.17586/2220-8054-2015-6-6-757-761

We address a linearized KdV equation on metric star graphs with one incoming finite bond and two outgoing semi-infinite bonds. Using the theory of potentials, we reduce the problem to systems of linear integral equations and show that they are uniquely solvable under conditions of the uniqueness theorem.

Keywords: KdV, IBVP, PDE on metric graphs, exact solution, third order differential equations.

Received: 1 November 2015

Introduction

The Korteweg – de Vries (KdV) equation is of importance for many problems of physics and related fields. In particular, soliton solutions of KdV equation have found applications in fluid mechanics [1-11]. A pioneering study of KdV equation dates back to Scott Russell, who was able to model the propagation of solitary wave on the water surface in 1834. The linearized KdV provides an asymptotic description of linear, weakly dispersive long waves, such as, e.g., shallow water waves. Earlier, it was proven that via the normal form transforms the solution of the KdV equation can be reduced to the solution of the linear KdV equation [12]. Namely, Belashov and Vladimirov [12] numerically investigated evolution of a single disturbance $u(0, x) = u_0 \exp(-x^2/l^2)$ and showed that in the limit $l \rightarrow 0$, $u_0 l^2 = const$, the solution of the KdV equation is qualitatively similar to that of the linearized KdV equation. The boundary value problems for KdV equation on half lines are considered in [2,5,7].

In this paper, we address the linearized KdV equation on a star graph Γ with one bounded bond and two semi-infinite bonds connected at one point, called the vertex. The bonds are denoted by B_j , $j = 1, 2, 3$, the coordinate x_1 on B_1 is defined from -1 to 0 , and coordinates x_2 and x_3 on the bonds B_2 and B_3 are defined from 0 to such that on each bond the vertex corresponds to 0 . On each bond we consider the linear equation:

$$\left(\frac{\partial}{\partial t} - \frac{\partial^3}{\partial x_j^3} \right) u_j(x_j, t) = f_j(x, t), \quad t > 0, x_j \in B_j, \quad j = 1, 2, 3. \quad (1)$$

Below, we will also use the notation x instead of x_j ($j = 1, 2, 3$). We treat a boundary value problem and using the method of potentials, reduce it to a system of integral equations. The solvability of the obtained system of integral equations is proven.

1. Formulation of the problems

To solve the linear KdV equation on an interval, one needs to impose three boundary conditions (BC): two on the left end of the x -interval and one on the right end, (see, e.g., [5-6] and references therein). For the above star graph, we need to impose 5 BCs at the vertex point, which should provide also connection between the bonds and 2 BCs at the left side of B_1 . In detail, we require:

$$u_1(-1; t) = \phi_0(t), \quad u_{1x}(-1; t) = \phi_1(t), \tag{2}$$

$$u_1(0, t) = a_2 u_2(0, t) = a_3 u_3(0, t), \tag{3}$$

$$u_{1x}(0; t) = b_2 u_{2x}(0; t) = b_3 u_{3x}(0; t), \tag{4}$$

$$u_{1xx}(0; t) = a_2^{-1} u_{2xx}(0; t) + a_3^{-1} u_{3xx}(0; t), \tag{5}$$

for $0 < t < T$, $T = const$.

Furthermore, we assume that the functions $f_j(x, t)$, $j = 1, 2, 3$, are smooth enough and bounded. The initial conditions are given by:

$$u_j(x, 0) = 0, \quad x \in \overline{B_j}, \quad (j = 1, 2, 3). \tag{6}$$

It should be noted that the above vertex conditions are not the only possible ones. The main motivation for our choice is caused by the fact that they guarantee uniqueness of the solution and, if the solutions decay (to zero) at infinity, the norm (energy) conservation.

2. Existence and uniqueness of solutions

Lemma 1. *Let $\frac{1}{b_2^2} + \frac{1}{b_3^2} \leq 1$. Then the problem (1)-(6) has at most one solution.*

Proof of Lemma 1. Using the equation (1) one can easily get:

$$\frac{d}{dt} \int_a^b u_j^2(x, t) dx = (2u_j u_{jxx} - u_{jx}^2) \Big|_{x=a}^{x=b} + 2 \int_a^b f_j(x, t) u_j(x, t) dx,$$

for appropriate values of constants a and b on each bond. We put $\phi_0(t) \equiv 0$. Then, the above equalities and vertex conditions (2)-(5) yield:

$$\frac{d}{dt} (e^{-\varepsilon t} \|u\|^2) \leq e^{-\varepsilon t} \left(\frac{1}{\varepsilon^2} \|f\|^2 + \phi_1^2(t) \right),$$

$$\|u\|^2 \leq \int_0^t e^{-\varepsilon(t-\tau)} \left(\frac{1}{\varepsilon^2} \|f(\cdot, \tau)\|^2 + \phi_1^2(\tau) \right) d\tau, \tag{7}$$

where $(u, v) = \int_{-1}^0 u_1 v_1 dx_1 + \int_0^{+\infty} u_2 v_2 dx_2 + \int_0^{+\infty} u_3 v_3 dx_3$, $\|u\| = \sqrt{(u, u)}$ are L_2 scalar product and norm defined on graph, ε is an arbitrary positive number.

Uniqueness of the solution follows from (7).

Theorem 1. *Let $a_2^2 + a_3^2 + a_2^2 a_3^2 + \frac{a_2}{b_3} + \frac{a_3}{b_2} \neq 0$, $\frac{1}{b_2^2} + \frac{1}{b_3^2} \leq 1$, $\phi_0(t) \in C^2[0, T]$, $\phi_1(t) \in C^1[0, T]$. Then the problem (1) – (6) has a unique solution in $C^1([0, T], C^3(\Gamma))$.*

Proof of Theorem 1.

To prove the theorem, we use the following functions are called fundamental solutions of the equation $u_t - u_{xxx} = 0$ (see [1, 3, 5, 12, 16]):

$$U(x, t; \xi, \eta) = \begin{cases} \frac{1}{(t-\eta)^{1/3}} f\left(\frac{x-\xi}{(t-\eta)^{1/3}}\right), & t > \eta, \\ 0 & t \leq \eta, \end{cases}$$

$$V(x, t; \xi, \eta) = \begin{cases} \frac{1}{(t-\eta)^{1/3}} \varphi\left(\frac{x-\xi}{(t-\eta)^{1/3}}\right), & t > \eta, \\ 0 & t \leq \eta, \end{cases}$$

where $f(x) = \frac{\pi}{3^{1/3}} Ai\left(-\frac{x}{3^{1/3}}\right)$, $\varphi(x) = \frac{\pi}{3^{1/3}} Bi\left(-\frac{x}{3^{1/3}}\right)$ for $x \geq 0$, $\varphi(x) = 0$ for $x < 0$ and $Ai(x)$ and $Bi(x)$ are the Airy functions. The functions $f(x)$ and $\varphi(x)$ are integrable and $\int_{-\infty}^0 f(x)dx = \frac{\pi}{3}$, $\int_0^{+\infty} f(x)dx = \frac{2\pi}{3}$, $\int_0^{+\infty} \varphi(x)dx = 0$.

Below, we also use fractional integrals [9]:

$$J_{(0,t)}^\alpha f(t) := \frac{1}{\Gamma(\alpha)} \int_0^t (t-\tau)^{\alpha-1} f(\tau) d\tau, \quad 0 < \alpha < 1,$$

and the inverse of this operator, i.e. the Riemann-Liouville fractional derivatives [8, 9] defined by:

$$D_{(0,t)}^\alpha f(t) := \frac{1}{\Gamma(1-\alpha)} \frac{d}{dt} \int_0^t (t-\tau)^{-\alpha} f(\tau) d\tau, \quad 0 < \alpha < 1.$$

We look for solution in the form:

$$u_1(x, t) = \int_0^t U(x, t; 0, \eta) \varphi_1(\eta) d\eta + \int_0^t U(x, t; -1, \eta) \alpha(\eta) d\eta + \int_0^t V(x, t; -1, \eta) \beta(\eta) d\eta + F_1(x, t),$$

$$u_2(x, t) = \int_0^t U(x, t; 0, \eta) \varphi_2(\eta) d\eta + \int_0^t V(x, t; 0, \eta) \psi_2(\eta) d\eta + F_2(x, t), \tag{8}$$

$$u_3(x, t) = \int_0^t U(x, t; 0, \eta) \varphi_3(\eta) d\eta + \int_0^t V(x, t; 0, \eta) \psi_3(\eta) d\eta + F_3(x, t), \tag{9}$$

where $F_k(x, t) = \frac{1}{\pi} \int_0^t \int_{B_k} U(x, t; \xi, \eta) f_k(\xi, \eta) d\xi d\eta$, $k = 1, 2, 3$.

Satisfying the conditions (2) - (4), we have:

$$f(0)\alpha(t) + \varphi(0)\beta(t) + D_{(0,t)}^{2/3} \int_0^t \varphi_1(\eta) f\left(-\frac{1}{(t-\eta)^{1/3}}\right) dt = \frac{1}{\Gamma(\frac{1}{3})} D_{(0,t)}^{2/3} [\phi_0(t) - F_1(0, t)], \tag{10}$$

$$f'(0)\alpha(t) + \varphi'(0)\beta(t) + D_{(0,t)}^{1/3} \int_0^t \varphi_1(\eta) f'\left(-\frac{1}{(t-\eta)^{1/3}}\right) dt = \frac{1}{\Gamma(\frac{2}{3})} D_{(0,t)}^{1/3} [\phi_1(t) - F_{1x}(0, t)], \tag{11}$$

$$\begin{aligned} & f(0)\varphi_1(t) - a_2 f(0)\varphi_2(t) - a_2 \varphi(0)\psi_2(t) + \int_0^t K_1 \alpha(\eta) d\eta + \int_0^t K_2 \beta(\eta) d\eta = \\ & = \frac{1}{\Gamma(\frac{1}{3})} D_{(0,t)}^{2/3} [F_2(0, t) - F_1(0, t)], \end{aligned} \tag{12}$$

$$\begin{aligned} & f(0)\varphi_1(t) - a_3 f(0)\varphi_3(t) - a_3 \varphi(0)\psi_3(t) + \int_0^t K_1 \alpha(\eta) d\eta + \int_0^t K_2 \beta(\eta) d\eta = \\ & = \frac{1}{\Gamma(\frac{1}{3})} D_{(0,t)}^{2/3} [F_3(0, t) - F_1(0, t)]. \end{aligned} \tag{13}$$

We take derivatives from (10) – (11) to obtain:

$$f(0)\alpha'(t) + \varphi(0)\beta'(t) + \frac{1}{\Gamma(\frac{1}{3})} \int_0^t K_3 \varphi_1(\eta) d\eta = \frac{1}{\Gamma(\frac{1}{3})} D_{(0,t)}^{2/3} \frac{d}{dt} [\phi_0(t) - F_1(0, t)], \quad (14)$$

$$f'(0)\alpha'(t) + \varphi'(0)\beta'(t) + \frac{1}{\Gamma(\frac{2}{3})} \int_0^t K_4 \varphi_1(\eta) d\eta = \frac{1}{\Gamma(\frac{2}{3})} D_{(0,t)}^{1/3} \frac{d}{dt} [\phi_1(t) - F_{1x}(0, t)]. \quad (15)$$

From conditions (4) and (5), it follows:

$$\begin{aligned} f'(0)\varphi_1(t) + b_2 f'(0)\varphi_2(t) - b_2 \varphi'(0)\psi_2(t) + \frac{1}{\Gamma(\frac{2}{3})} \int_0^t K_5 \alpha(\eta) d\eta + \frac{1}{\Gamma(\frac{2}{3})} \int_0^t K_6 \beta(\eta) d\eta = \\ = \frac{1}{\Gamma(\frac{2}{3})} D_{(0,t)}^{1/3} [b_2 F_{2x}(0, t) - F_{1x}(0, t)], \end{aligned} \quad (16)$$

$$\begin{aligned} f'(0)\varphi_1(t) + b_3 f'(0)\varphi_3(t) - b_3 \varphi'(0)\psi_3(t) + \frac{1}{\Gamma(\frac{2}{3})} \int_0^t K_5 \alpha(\eta) d\eta + \frac{1}{\Gamma(\frac{2}{3})} \int_0^t K_6 \beta(\eta) d\eta = \\ = \frac{1}{\Gamma(\frac{2}{3})} D_{(0,t)}^{1/3} [b_3 F_{3x}(0, t) - F_{1x}(0, t)], \end{aligned} \quad (17)$$

$$\begin{aligned} -\frac{\pi}{3} \varphi_1(t) - \frac{1}{a_2} \frac{2\pi}{3} \varphi_2(t) - \frac{1}{a_3} \frac{2\pi}{3} \varphi_3(t) + \int_0^t K_7 \alpha'(\eta) d\eta + \int_0^t K_8 \beta'(\eta) d\eta = \\ = \frac{1}{a_2} F_{2xx}(0, t) + \frac{1}{a_3} F_{3xx}(0, t) - F_{1xx}(0, t), \end{aligned} \quad (18)$$

where the kernels of integral operators defined as:

$$\begin{aligned} K_1 &= \int_{\eta}^t \frac{1}{(t-\tau)^{2/3}(\tau-\eta)^{1/3}} f' \left(-\frac{1}{(\tau-\eta)^{1/3}} \right) d\tau, \\ K_2 &= \int_{\eta}^t \frac{1}{(t-\tau)^{2/3}(\tau-\eta)^{1/3}} \varphi' \left(-\frac{1}{(\tau-\eta)^{1/3}} \right) d\tau, \\ K_3 &= \int_{\eta}^t \frac{1}{(t-\tau)^{2/3}(\tau-\eta)^{2/3}} f'' \left(-\frac{1}{(\tau-\eta)^{1/3}} \right) d\tau, \\ K_4 &= \int_{\eta}^t \frac{1}{(t-\tau)^{1/3}(\tau-\eta)^{2/3}} f''' \left(-\frac{1}{(\tau-\eta)^{1/3}} \right) d\tau, \\ K_5 &= \int_{\eta}^t \frac{1}{(t-\tau)^{1/3}(\tau-\eta)^{1/3}} f'' \left(-\frac{1}{(\tau-\eta)^{1/3}} \right) d\tau, \\ K_6 &= \int_{\eta}^t \frac{1}{(t-\tau)^{1/3}(\tau-\eta)^{1/3}} \varphi'' \left(-\frac{1}{(\tau-\eta)^{1/3}} \right) d\tau, \\ K_7 &= \int_0^x U(y+1; t-\eta) dy \quad , \quad K_8 = \int_0^x V(y+1; t-\eta) dy. \end{aligned}$$

We obtained the system of integral equations (12) – (18) with respect to unknowns $(\alpha'(t), \beta'(t), \varphi_1(t), \varphi_2(t), \varphi_3(t), \psi_2(t), \psi_3(t))$. The matrix of the coefficients M of these unknowns on the off integral part of the system has a determinant:

$$\det M = \frac{\pi^4 b_2 b_3}{81 a_2 a_3} \left(a_2^2 + a_3^2 + a_2^2 a_3^2 + \frac{a_2}{b_3} + \frac{a_3}{b_2} \right).$$

Under conditions of the theorem this determinant is not singular.

According to the asymptotes of Airy functions the kernels of the integral operators are integrable (see [14, 15]). Hence, it follows from the uniqueness theorem and Fredholm alternatives that the system of equations has a unique solution. Thus the solvability of the problem is proved.

Acknowledgments

This work is partly supported by a grant of the Volkswagen Foundation.

References

- [1] S. Abdinazarov. The general boundary value problem for the third order equation with multiple characteristics (in Russian). *Differential Equations*, 1881, **3**(1), P. 3–12.
- [2] J.L. Bona and A.S. Fokas. Initial-boundary-value problems for linear and integrable nonlinear dispersive partial differential equations. *Nonlinearity*, 2008, **21**, P. 195–203.
- [3] L. Cattabriga. Unproblema al contorno per un'equazione parabolica di ordine dispari. *Annali della Scuola Normale Superiore di Pisa a mat., Serie III*, **13**(2), 1959.
- [4] J. E. Colliander, C. E. Kenig. The generalized Korteweg-de Vries equation on the half line. *Commun. Partial Differ. Equations*, 2002, **27**(11-12), P. 2187–2266.
- [5] T. D. Djuraev. *Boundary value problems for mixed and mixed-composite type equations*, (in Russian). Fan, Tashkent, 1979.
- [6] A. V. Faminskii, N. A. Larkin. Initial-boundary value problems for quasilinear dispersive equations posed on a bounded interval. *Electron. J. Differ. Equ.*, 2010, **2010**(20).
- [7] A.S. Fokas and L.Y. Sung. Initial boundary value problems for linear dispersive evolution equations on the half line. Technical report of Industrial Mathematics Institute at the University of South Carolina, 1999.
- [8] M. Rahimy. Applications of fractional differential equations. *Applied Mathematical Sciences*, 2010, **4**(50), P. 2453–2461.
- [9] R. Gorenflo, F. Mainard. Fractional calculus: Integral and differential equations of fractional order. arXiv:0805.3823v1, 2008.
- [10] E. Taffin. Analytic linearization of the Korteweg-De Vries equation. *Pacific Journal of Mathematics*, 1983, **108**(1).
- [11] V. Belashov, S. Vladimirov. *Solitary waves in dispersive complex media: theory, simulation, application*. Springer, 2005.
- [12] G.B. Whitham. *Linear and nonlinear waves*. Pure and Applied Mathematics, Wiley-Interscience., 1974.
- [13] Z.A. Sobirov, H. Uecker, M. Akhmedov. Exact solutions of the Cauchy problem for the linearized KdV equation on metric star graphs. *Uz. Math. J.*, 2015, **3**.
- [14] A. R. Khashimov. Some properties of the fundamental solutions of non-stationary third order composite type equation in multidimensional domains. *Journal of Nonlinear Evolution Equations and Applications*, January 2013, **2013**(1), P. 1–9.
- [15] A.R. Khashimov, S. Yakubov. On some properties of cauchy problem for non-stationary third order composite type equation. *Ufa Mathematical Journal*, 2014, **6**(4), P. 135–144.
- [16] Z. A. Sobirov, M. I. Akhmedov, H. Uecker. Cauchy problem for the linearized KdV equation on general metric star graphs. *Nanosystems: Physics, Chemistry, Mathematics*, 2015, **6**(1), P. 198–204.

The Green function for simplest quantum graphs

K. K. Sabirov¹, U. A. Aminov², Kh. Sh. Saparov², M. K. Karimov², Kh. Abdikarimov²

¹ Physics Faculty, National University of Uzbekistan, Tashkent, Uzbekistan

²Urganch State University, Urganch, Uzbekistan

karimjonsabirov@yahoo.com

PACS 03.65.Ge, 02.30.Ik

DOI 10.17586/2220-8054-2015-6-6-762-766

We treat the problem of the Green function for quantum graphs by focusing on such topologies as star and tree graphs. The exact Green function for the Schrödinger equation on primary star graphs is derived in the form of 3×3 - matrix using the vertex boundary conditions providing continuity and current conservation. Extension of the approach for the derivation for the Green function on tree graph is presented. Possible practical applications of the obtained results are discussed.

Keywords: quantum graphs, Green function, vertex boundary conditions.

Received: 1 November 2015

1. Introduction

Particle and wave transport in branched systems has attracted much attention in different topics of physics such as optics, polymer and cold atom physics, condensed matter and biophysics. In most cases, such transport can be modeled by evolution equations on so-called metric graphs. The latter is called quantum graphs for nanometer scales and has become a rapidly developing subject over the last three decades (see, e.g., reviews [1-3] and references therein). In this case, one deals with the Schrödinger equation for which the boundary conditions on graph vertices graphs are imposed [1].

The simplest case for propagation of linear waves in branched optical structures is described by the Helmholtz equation on graphs. Formally, it coincides with the Schrödinger equation, which was extensively studied in the context of quantum chaos theory [1-10]. Linear waves in optical waveguide networks provide experimental realization of quantum graphs [11].

The Schrödinger equation on graphs was first introduced by Pavel Exner in [5, 6]. Strict mathematical formulation of Schrödinger equation on graphs was given by Kostykin and Schrader in [7], who formulated general boundary conditions, providing the self-adjointness of the problem. Nonrelativistic particle dynamics in networks described by the Schrödinger equation on graphs has been studied in the context of quantum chaos in the Refs. [1-3]. Despite the progress made in the study Schrödinger equation on graphs, the Green function based approach to particle transport still remains undeveloped. The only attempts for treatment of Green function on metric graphs are those in Refs. [12-14]. In [12] the Green function is constructed for the regular Shturm-Liouville problem on the interval via different approaches. The Green function for the Schrödinger operator on the open star graph is studied by the multiscattering expansion in [13]. Schmidt, Cheng and da Luz [14] presented a recursive prescription to calculate the exact Green function for general quantum graphs via a scattering approach. However, these works do not provide an explicit form of the Green function, even for star graph.

In this paper, we address the problem of derivation of the exact Green function for the simplest quantum graphs in an explicit form using the Schrödinger equation with boundary conditions providing continuity and the current conservation at the graph's vertex. In quantum physics, the Green function is of importance for different problems, such as quantum transport, vacuum fluctuations, heat transport, and many others. In the case of quantum networks, knowledge of the Green function greatly facilitates transport phenomena in such systems and the Casimir effect in branched systems [15-19].

2. Schrödinger equation on metric graphs

Our task is to derive Green function for the Schrödinger equation on metric graphs. A graph represents system of bonds which are connected at one or more vertices (branching points). The connection rule is called the topology of a graph. When the bonds can be assigned a length, the graph is called a metric graph. The Schrödinger equation on a metric graph having N represents system of N – equations which are connected to each other via the vertex boundary conditions [1,7]. In the following we deal with the Schrödinger equation on the primary star graph (see 1) Γ having three bonds with the lengths L_j , $j = 1, 2, 3$ of finite bonds b_j , $j = 1, 2, 3$ given as:

$$-\frac{1}{2} \frac{d^2}{dx^2} \psi_j = E \psi_j. \quad (1)$$

The vertex boundary conditions for such graph can be written as:

$$\psi_1(0) = \psi_2(0) = \psi_3(0), \quad (2)$$

$$\left. \frac{\partial}{\partial x} \psi_1 \right|_{x=0} + \left. \frac{\partial}{\partial x} \psi_2 \right|_{x=0} + \left. \frac{\partial}{\partial x} \psi_3 \right|_{x=0} = 0, \quad (3)$$

$$\psi_j(L_j) = 0, \quad j = 1, 2, 3. \quad (4)$$

Eq.(1), together with the boundary conditions given by Eqs.(2)-(4), define the quantum

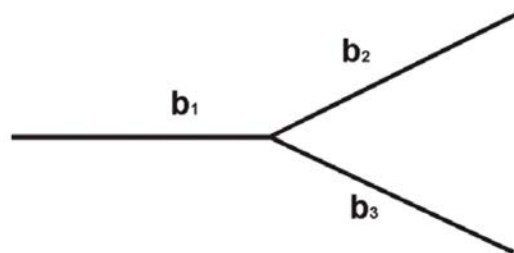


FIG. 1. Primary star graph consisting of 3 bonds connected at a vertex

mechanical problem of the quantum graph presented in Fig.1. Below, we will use Green function approach for this problem and derive explicit Green functions for this system.

2.1. The Green function for quantum star graph

The Green function for Schrödinger equation on star graph is defined as the solution of the following equation:

$$-\frac{d^2}{dx^2} G(x, x') - 2EG(x, x') = 2\delta(x - x')I_3, \quad (5)$$

(where I_3 is 3×3 the identity matrix) with the boundary conditions:

$$G_{1j}(0, x') = G_{2j}(0, x') = G_{3j}(0, x'), \quad j = 1, 2, 3, \quad (6)$$

$$\left. \frac{\partial}{\partial x} G_{1,j}(x, x') \right|_{x=0} + \left. \frac{\partial}{\partial x} G_{2,j}(x, x') \right|_{x=0} + \left. \frac{\partial}{\partial x} G_{3,j}(x, x') \right|_{x=0} = 0, \quad j = 1, 2, 3, \quad (7)$$

$$G_{j,m}(L_j, x') = 0, \quad j, m = 1, 2, 3, \quad (8)$$

$$G_{j,m}(x, x')|_{x=x'-0} = G_{j,m}(x, x')|_{x=x'+0}, \quad j, m = 1, 2, 3 \quad (9)$$

$$\left. \frac{\partial}{\partial x} G_{j,m}(x, x') \right|_{x=x'-0} - \left. \frac{\partial}{\partial x} G_{j,m}(x, x') \right|_{x=x'+0} = -2\delta_{j,m}, \quad j, m = 1, 2, 3. \quad (10)$$

Let us assume that equation:

$$-\frac{1}{2} \frac{d^2}{dx^2} \varphi_j(x) - E\varphi_j(x) = f_j(x), \quad (11)$$

obeys the boundary conditions given by Eqs.(2)-(4). Then the solution of Eq.(11) can be written as:

$$\varphi_j(x) = \sum_{m=1}^3 \int_0^{L_m} G_{jm}(x, x') f_m(x') dx'. \quad (12)$$

It is clear that from the boundary conditions (6)-(8), one can obtain boundary conditions (2)-(4), i.e. the solution of Eq. (12) satisfies the boundary conditions given by Eqs. (2)-(4).

Thus, the Green function for a star graph presented in Fig.1 can be written as:

$$G(x, x') = \frac{1}{i\sqrt{2E}} e^{i\sqrt{2E}|x-x'|} I_3 + \frac{1}{i\sqrt{2E}} \sin(\sqrt{2E}x) \cdot \mu^{(1)}(x') + \frac{1}{i\sqrt{2E}} \cos(\sqrt{2E}x) \cdot \mu^{(2)}(x'), \quad (13)$$

where I_3 is the 3×3 identity matrix, with $\mu^{(1)}, \mu^{(2)}$ are 3×3 are matrices, which obey the boundary conditions given by Eqs.(6)-(8):

$$\mu_{jm}^{(1)} = \begin{cases} \frac{1}{\Delta} \left[ie^{i\sqrt{2E}x'} \Delta_j - e^{i\sqrt{2E}(L_j-x')} \sum_{n \neq j} \Delta_{n,j} \right], & m = j, \\ \frac{1}{\Delta} \left[ie^{i\sqrt{2E}x'} \Delta_j + e^{i\sqrt{2E}(L_m-x')} \Delta_{j,m} \right], & m \neq j, \end{cases}$$

$$\mu_{jm}^{(2)} = -\frac{1}{\Delta} \left[ie^{i\sqrt{2E}x'} \prod_{n=1}^3 \sin(\sqrt{2E}L_n) + e^{i\sqrt{2E}(L_m-x')} \prod_{n \neq m} \sin(\sqrt{2E}L_n) \right],$$

here $\Delta_j = \cos(\sqrt{2E}L_j) \prod_{n \neq j} \sin(\sqrt{2E}L_n)$, $\Delta_{j,m} = \cos(\sqrt{2E}L_j) \prod_{n \neq j,m} \sin(\sqrt{2E}L_n)$, $\Delta = \sum_{j=1}^3 \Delta_j$, $j, m = 1, 2, 3$.

This Green function can be used for solving of the transport phenomena and vacuum effect such as Casimir effect on branched structures and networks [15-19].

3. Other simplest graph

Here, we briefly show that the above approach can be used to derive the Green function for other simple graphs, such as the tree graph presented in Fig.2. In the case of

the Schrödinger equation given by (1), one can impose the following boundary conditions:

$$\psi_1(0) = 0, \psi_{1mn}(L_{1mn}) = 0, m, n = 1, 2, \tag{14}$$

$$\psi_1(L_1) = \psi_{1m}(L_1), m = 1, 2, \tag{15}$$

$$\frac{\partial}{\partial x} \psi_1 \Big|_{x=L_1} + \sum_{m=1}^2 \frac{\partial}{\partial x} \psi_{1m} \Big|_{x=L_1} = 0, \tag{16}$$

$$\psi_{1m}(L_{1m}) = \psi_{1mn}(L_{1m}), m, n = 1, 2, \tag{17}$$

$$\frac{\partial}{\partial x} \psi_{1m} \Big|_{x=L_{1m}} + \sum_{n=1}^2 \frac{\partial}{\partial x} \psi_{1mn} \Big|_{x=L_{1m}} = 0. \tag{18}$$

The Green function for a tree graph having seven bonds, $G(x, x')$ is a 7×7 -matrix obeying

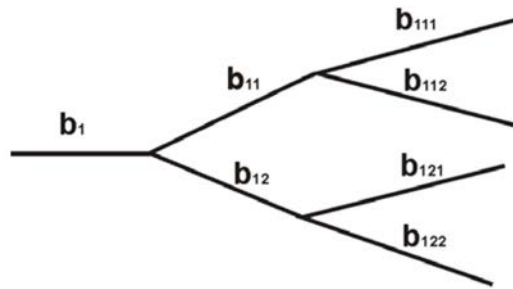


FIG. 2. Tree graph

the following conditions:

$$G_{1,b}(0, x') = 0, G_{1mn,b}(L_{1mn}, x') = 0, m, n = 1, 2, \tag{19}$$

$$G_{1,b}(L_1, x') = G_{1m,b}(L_1, x'), m = 1, 2, \tag{20}$$

$$\frac{\partial}{\partial x} G_{1,b}(x, x') \Big|_{x=L_1} + \sum_{m=1}^2 \frac{\partial}{\partial x} G_{1m,b}(x, x') \Big|_{x=L_1} = 0, \tag{21}$$

$$G_{1m,b}(L_{1m}, x') = G_{1mn,b}(L_{1m}, x'), m, n = 1, 2, \tag{22}$$

$$\frac{\partial}{\partial x} G_{1m,b}(x, x') \Big|_{x=L_{1m}} + \sum_{n=1}^2 \frac{\partial}{\partial x} G_{1mn,b}(x, x') \Big|_{x=L_{1m}} = 0, m = 1, 2, \tag{23}$$

($b \in \{1; 11; 12; 111; 112; 121; 122\}$) and the Green function can be written as:

$$G(x, x') = \frac{1}{i\sqrt{2E}} e^{i\sqrt{2E}|x-x'|} I_7 + \frac{1}{i\sqrt{2E}} \sin(\sqrt{2E}x) \cdot \mu^{(1)}(x') + \frac{1}{i\sqrt{2E}} \cos(\sqrt{2E}x) \cdot \mu^{(2)}(x'), \tag{24}$$

where I_7 - 7×7 is the unit matrix, $\mu^{(1)}, \mu^{(2)}$ are 7×7 - matrices, which obey the boundary conditions given by Eqs.(19)-(23). It is clear that a similar way can be used to obtain the Green function of a tree graph with arbitrary number of bonds as well as other simplest topologies.

4. Conclusion

In this paper, using the direct approach based on the definition of the Green function, we derived the explicit Green functions for the simplest graphs such as star and tree graphs.

The approach can be used for the derivation of the Green function of other simple topologies. The above results can be useful for the study of particle transport in quantum networks such as polymers, molecular chains, lattices and other discrete structures. An important problem where knowledge of the Green function on graphs is important is the problem of the Casimir effect on networks [15-19]. Using of the Green function approach for calculating the zero point energy is an effective tool, and in many cases, allows one to avoid divergencies [20].

References

- [1] T. Kottos and U. Smilansky. Periodic orbit theory and spectral statistics for quantum graphs, *Ann.Phys.*, 1999, **76**, P. 274.
- [2] S. Gnutzmann, U. Smilansky. Quantum graphs: Applications to quantum chaos and universal spectral statistics, *Adv.Phys.*, 2006, **55**, P. 527.
- [3] S. Gnutzmann J.P., Keating b, F. Pietet. Eigenfunction statistics on quantum graphs, *Ann.Phys.*, 2010, **325**, P. 2595.
- [4] L. Pauling. The Diamagnetic Anisotropy of Aromatic Molecules, *J. Chem. Phys.*, 1936, **4**, P. 673.
- [5] P. Exner, P. Seba, P. Stovicek. Quantum interference on graphs controlled by an external electric field. *J. Phys. A: Math. Gen.*, 1988, **21**, P. 4009–4019.
- [6] P. Exner, P. Seba. Free quantum motion on a branching graph, *Rep. Math. Phys.*, 1989, **28**, P. 7.
- [7] R. Kostykin, R. Schrader. Kirchhoff's rule for quantum wires, *J. Phys. A: Math. Gen.*, 1999, **32**, P. 595.
- [8] J. Boman, P. Kurasov. Symmetries of quantum graphs and the inverse scattering problem, *Adv. Appl. Math.*, 2005, **35**, P. 58.
- [9] T. Cheon, P. Exner, O. Turek. Approximation of a general singular vertex coupling in quantum graphs, *Ann.Phys.*, 2010, **325**, P. 548.
- [10] J.P. Keating. Fluctuation statistics for quantum star graphs. Quantum graphs and their applications, *Contemp. Math.*, 2006, **415**, P. 191.
- [11] O. Hul et al. Experimental simulation of quantum graphs by microwave networks, *Phys. Rev. E*, 2004, **69**, P. 056205.
- [12] W. J. Parnell. Greens functions, integral equations and applications, MATH 34032, Spring 2013.
- [13] F. Barra, P. Gaspard. Transport and dynamics on open quantum graphs, *Physical review E*, 2001, **65**, P. 016205.
- [14] A. G. M. Schmidt, B. K. Cheng, M.G.E. da Luz. Green function approach for general quantum graphs, *J. Phys. A: Math. Gen.*, 2003, **36**, P. L545L551.
- [15] P. Calabrese, M. Mintchev, E. Vicari. Entanglement entropy of quantum wire junctions, *J. Phys. A: Math. Theor.*, 2012, **45**, P. 105206.
- [16] B. Bellazzini, M. Burrello, M. Mintchev, P. Sorba. Quantum field theory on star graphs, *Proc. Symp. Pure Math.*, 2008, **77**, P. 639.
- [17] B. Bellazzini, M. Mintchev. Quantum fields on star graphs, *J. Phys. A*, 2006, **39**, P. 11101.
- [18] B. Bellazzini, M. Mintchev, P. Sorba. Quantum fields on star graphs with bound states at the vertex, *J. Math. Phys.*, 2010, **51**, P. 032302.
- [19] S. A. Fulling, L. Kaplan, J. H. Wilson. Vacuum energy and repulsive Casimir forces in quantum star graphs. *Physical review A*, 2007, **76**, P. 012118.
- [20] G. Plunien, B. Muller, W. Greiner, The Casimir Effect, *Phys.Rep.*, 1986, **134**, P. 87.

Quantum dynamics of hydrogen-like atom in one-dimensional box with oscillating walls

S. Rakhmanov¹, O. Karpova^{1,2,*}, D. R. Rakhimboeva³, F. Khashimova⁴, D. Babajanov²

¹National University of Uzbekistan, 100174, Tashkent, Uzbekistan

²Turin Polytechnic University in Tashkent, 17. Niyazov Str., 100095, Tashkent, Uzbekistan

³Tashkent Transport College, 100148, Tashkent, Uzbekistan

⁴Navoiy State Mining Institute, 27 Janubiy str., Navoiy, Uzbekistan

*ola_july@mail.ru

PACS 03.65.-w, 05.45.Ac

DOI 10.17586/2220-8054-2015-6-6-767-772

The quantum dynamics of a hydrogen-like atom confined in one-dimensional box with oscillating walls is studied. The description of the system is reduced to a one-dimensional Schrödinger equation for Coulomb potential with time-dependent boundary conditions, which is solved numerically. Using the obtained solution, the average kinetic energy and binding energies are calculated as a function of time. It is found that both the average kinetic energy and the binding energies are periodic in time with the period depending on the wall's oscillation parameters. The probability density is also analyzed as a function of time and coordinate.

Keywords: confined atom, time-dependent box, average kinetic energy, atom-optic billiards.

Received: 1 November 2015

1. Introduction

The behavior of matter under the spatial confinement is of importance for many topics in contemporary nanoscale physics. Macroscopic properties of confined matter are considerably different than those of bulk matter. Such a difference is caused by underlying microscopic phenomena implying the difference between the quantum mechanical properties of atoms and molecules in confined and bulk spaces. The latter means that quantum mechanical wave equations describing atoms and molecules in bulk and confined spaces have different solutions which depend on the boundary conditions for such spaces. As the macroscopic characteristics (e.g., heat capacity, dielectric constant, thermal conductance, etc.) are obtained by statistical averaging of the microscopic quantities (to be calculated using the solution for the quantum mechanical wave functions) the results for confined and bulk matters should be different. Therefore, study of the behavior of atoms and molecules under confinement at the quantum mechanical level is of importance for understanding macroscopic features of confined matter. In this work, we address the problem of atom confined in a hard wall box by considering a one dimensional system. Such hard wall confinement can be realized by putting the atom in a strong constant electric field or in a so-called atom-optic billiards [1-3]. Here, we focus on the time-dependent boundaries, i.e. when the wall of a box is harmonically oscillating. Earlier, the box with oscillating walls has been the subject for extensive research(see e.g., [4-14]). By solving the time-dependent Schrödinger equation with time-dependent boundary conditions for Coulomb potential, we compute the time-dependence of the average energy, and the evolution of the probability density . Before proceeding to the treatment of the time-dependent system, in the next section, we briefly recall the description of the static system.

2. The one-dimensional Coulomb atom

Consider electron motion in a one-dimensional singular Coulomb field (atomic system of units is used $\hbar = m = e = 1$):

$$V(x) = -\frac{Z}{|x|}. \quad (1)$$

Such system is described by one-dimensional Schrödinger equation given as [15-17]:

$$-\frac{1}{2} \frac{d^2\psi}{dx^2} - \frac{Z}{|x|} \psi = E\psi. \quad (2)$$

The general solution of this equation can be written as:

$$\psi(x) = N(Z, E) \exp\left\{-\alpha|x|\right\} {}_1F_1\left(1 - \sqrt{-2E}, 2, \frac{2|x|}{\sqrt{-2E}}\right). \quad (3)$$

For an atom in bulk space, i.e. in the absence of confinement, one can require exponential decay of the wave function at $|x| \rightarrow \infty$ which leads to quantization condition of the form:

$$E_n = -\frac{Z^2}{2n^2}.$$

Then, the wave functions can be written as:

$$\psi(x) = \sqrt{\frac{2}{n^3}} |x| (\text{sgn}(n))^\sigma \exp\left\{-\frac{|x|}{n}\right\} {}_1F_1\left(1 - n, 2, \frac{2|x|}{n}\right), \quad (4)$$

where $n = 1, 2, \dots, \infty$ and ${}_1F_1$ is the confluent hypergeometric function.

For an atom confined in a one-dimensional box, the problem can be solved by imposing boundary conditions given as:

$$\psi(x = L) = 0,$$

where L is the size (length) of the box. Then, from Eq.(3), we have quantization condition in the form:

$${}_1F_1\left(1 - \sqrt{-2E}, 2, \frac{2|L|}{\sqrt{-2E}}\right) = 0, \quad (5)$$

which allows us to find eigenvalues (energy levels) for the confined atom. In Fig. 1, the first 7 eigenvalues of the hydrogen-like atom with charge $Z = 1$ in one dimensional box of size $L = 50$ are presented together with the Coulomb potential of the atomic nucleus.

3. Hydrogen-like atom confined in one-dimensional box with oscillating walls

Our purpose is to evaluate the quantum dynamics of the one-electron atom confined in a box with time-dependent walls. Such a system is described by the one-dimensional time-dependent Schrödinger equation for Coulomb potential. The time-dependence is caused by time-dependent boundary conditions imposed for the Schrödinger equation. Thus the Schrödinger equation we are going to treat can be written as:

$$i \frac{\partial \Psi(x, t)}{\partial t} = -\frac{1}{2} \frac{\partial^2 \Psi(x, t)}{\partial x^2} - \frac{Z}{x} \Psi(x, t), \quad (6)$$

where the boundary condition is given as:

$$\Psi(L(t), t) = 0,$$

where $L = L(t)$.

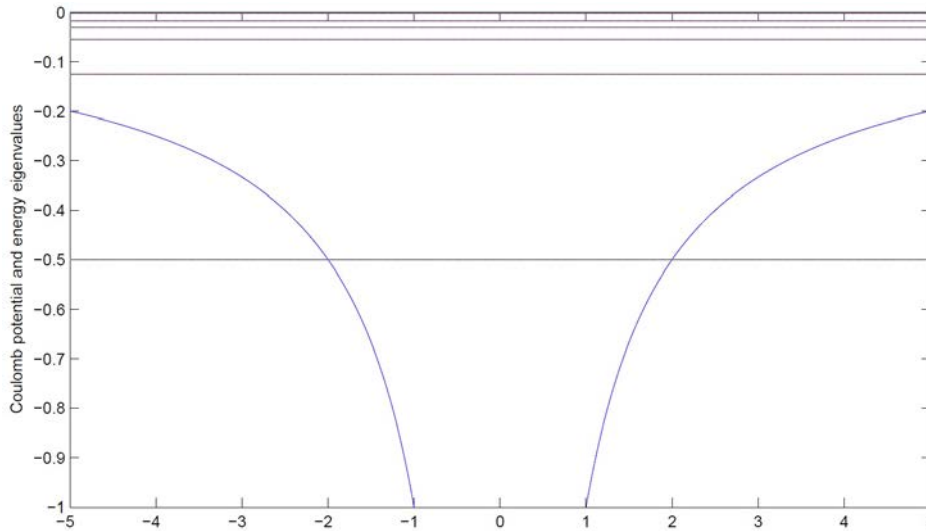


FIG. 1. Energy eigenvalues of the one-dimensional hydrogen-like atom confined in a box compared with Coulomb potential acting on an atomic electron

Using the coordinate transformations given by:

$$y = \frac{x}{L(t)}, \tag{7}$$

one can reduce these boundary conditions into time-independent form which can be written as:

$$\Psi|_{y=1} = 0.$$

Then Eq.(6) can be written as

$$i \frac{\partial \Psi(y, t)}{\partial t} = -\frac{1}{2L^2} \frac{\partial^2 \Psi(y, t)}{\partial y^2} + i \frac{\dot{L}}{L} y \frac{\partial \Psi(y, t)}{\partial y} - \frac{Z}{Ly} \Psi(y, t). \tag{8}$$

This equation contains an imaginary term that breaks self-adjointness of the problem. To restore the self-adjointness we use the following transformation for the wave function:

$$\Psi(y, t) = \sqrt{\frac{1}{L}} e^{i \frac{\dot{L}}{2} Ly^2} \Phi(y, t). \tag{9}$$

Then, inserting this into Eq.(8), we have:

$$i \frac{\partial \Phi}{\partial t} = -\frac{1}{2L^2} \frac{\partial^2 \Phi}{\partial y^2} + \frac{1}{2} L \ddot{L} y^2 \Phi - \frac{Z}{Ly} \Phi. \tag{10}$$

To solve Eq.(10), we expand $\Phi(y, t)$ in terms of a complete set of the eigenfunctions of the static one-dimensional box: $\varphi_n(y)$:

$$\Phi(y, t) = \sum_n C_n(t) \varphi_n(y), \tag{11}$$

where $\varphi_n(y)$ are the eigenfunctions of the stationary Schrödinger equation for one-dimensional box of size $L = 1$:

$$-\frac{1}{2L^2} \frac{d^2 \varphi_n(y)}{dy^2} = E_n \varphi_n(y), \tag{12}$$

obeying the following normalization conditions:

$$\int_0^1 \varphi_n(y) \varphi_m^*(y) dy = \delta_{nm}.$$

Inserting expansion (11) into Eq.(10), we obtain a system of first order differential equations with respect to the expansion coefficients, $C_n(t)$:

$$i\dot{C}_n(t) = E_n C_n(t) + \sum_m V_{nm} C_m(t), \quad (13)$$

where:

$$V_{nm} = \frac{1}{2} L \ddot{L} \int_0^1 y^2 \varphi_n(y) \varphi_m^*(y) dy - \frac{Z}{L} \int_0^1 \frac{1}{y} \varphi_n(y) \varphi_m^*(y) dy.$$

Solving Eqs.(13), one can find the wave function for the hydrogen-like atom confined in a one-dimensional box with oscillating walls. Having found the wave function, we can calculate physically observable quantities, such as time-dependent average kinetic energy, $\langle E(t) \rangle$ and the binding energy $\langle \varepsilon(t) \rangle$. The average kinetic energy can be calculated as:

$$E(t) = \int_0^{L(t)} \Psi^*(x, t) \left(-\frac{1}{2} \frac{\partial^2}{\partial x^2} \right) \Psi(x, t) dx = \frac{1}{2} \int_0^{L(t)} \left| \frac{\partial \Psi}{\partial x} \right|^2 dx \quad (14)$$

or as:

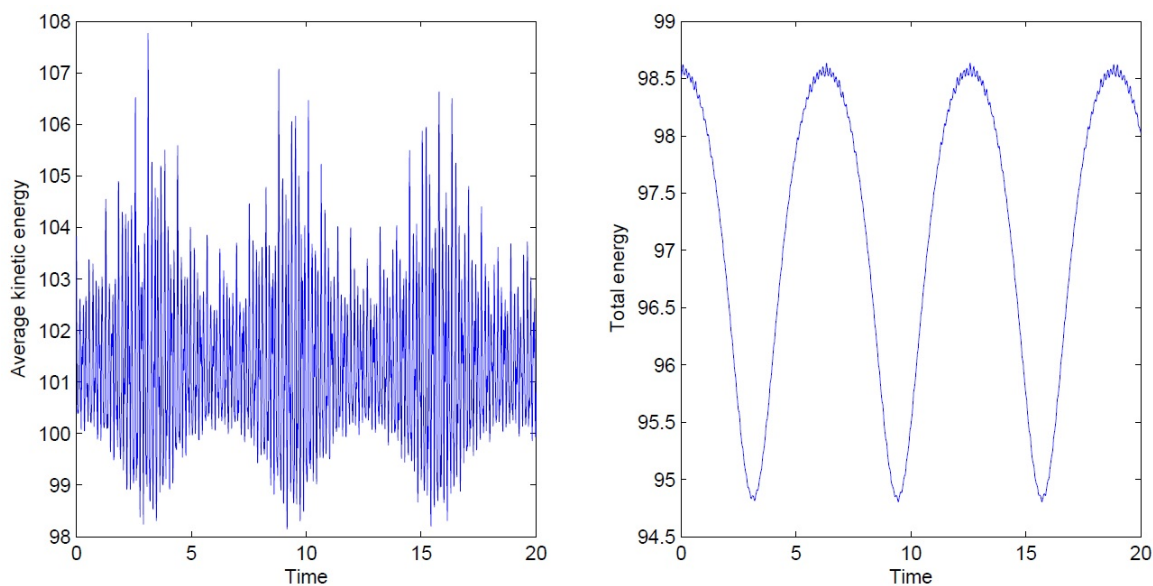
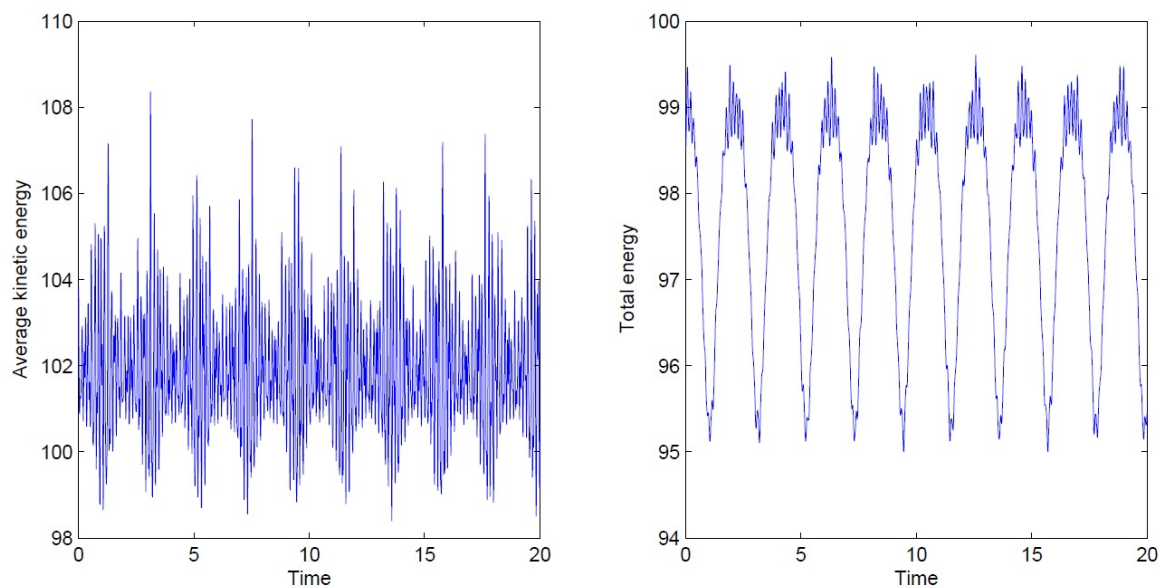
$$E(t) = \sum_n |C_n(t)|^2 E_n + \frac{1}{2} \dot{L}^2 \sum_n \sum_m C_n^*(t) C_m(t) \int_0^1 y^2 \varphi_n^*(y) \varphi_m(y) dy + \frac{\dot{L}}{4L} \text{Im} \left(\sum_m C_n^*(t) C_m(t) \int_0^1 y \frac{\partial \varphi_n(y)}{\partial y} \varphi_m(y) dy \right). \quad (15)$$

In Fig. 2, the average kinetic energy, $\langle E(t) \rangle$ and the binding energy, $\langle \varepsilon(t) \rangle$ are plotted as a function of time for the wall's oscillation frequency $\omega = 1$ and amplitude $a = 0.4$ for the box size $L = 1$. Fig. 3 presents similar plots for the wall's oscillation parameter values $\omega = 3$ and amplitude $a = 0.4$ ($L = 1$). As it can be seen from these plots, both the average kinetic and average binding energies show a certain periodicity in time and the period depends on that of wall's oscillation; that is, the longer the wall's oscillation frequency, the shorter the period for its average kinetic energy. Such a correlation between the behavior of the average kinetic energy and wall's oscillation parameters allows one to tune the atomic electron's acceleration, the pressure on the atom and electronic state transitions.

An important quantity which can be measured in experimentally by realizing the above model in atom-optic billiards, is the probability density. Fig. 4 presents plots of the probability density corresponding to Figs. 2 and 3. Periodicity in the temporospatial localization of an atomic electron can be observed from these plots. This explains the periodicity of the average kinetic energy as a function of time.

4. Conclusions

In this work, we studied the quantum dynamics of the one-electron atom confined in a one-dimensional box with oscillating wall. Time-evolutions of the average kinetic and binding energies are analyzed by solving the time-dependent Schrödinger equation for Coulomb potential with time-dependent boundary conditions. The latter is solved numerically by expanding the wave function in terms of static system eigenfunctions. Both the average kinetic and the binding energies were found to be periodic in time. Additionally, the temporospatial evolution of the probability density was computed. The probability density clearly exhibits

FIG. 2. Time dependence of the average kinetic and total energy ($\omega = 1, A = 0.4$)FIG. 3. Time dependence of the average kinetic and total energy ($\omega = 3, A = 0.4$)

periodicity in both space and time. The model studied in this paper can be realized for so-called atom-optic billiards which provide spatial confinement with the required boundary geometry. The obtained results are importance for the study of atomic behavior under high pressure confinement. That information is necessary for the engineering of mechanical and electric nanoscale devices with tunable properties.

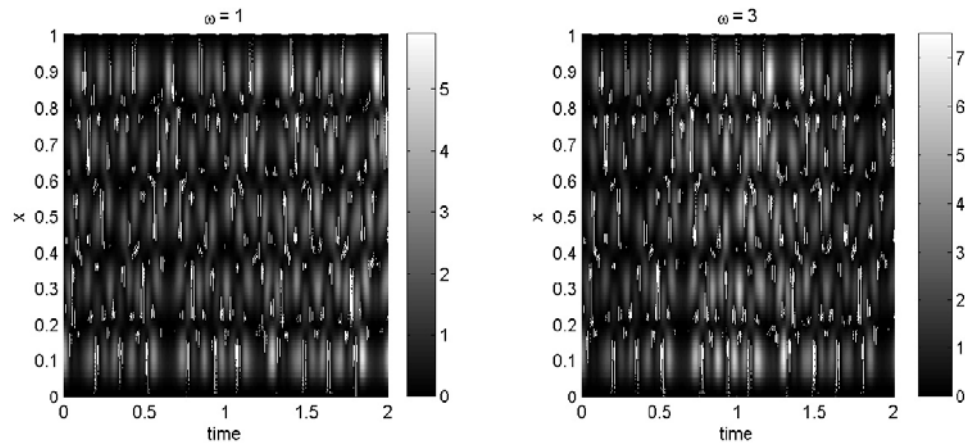


FIG. 4. Time and coordinate dependence of the probability density ($\omega = 1$ and $\omega = 3$, $A = 0.4$)

References

- [1] M.F. Andersen, A. Kaplan, N. Friedman, N. Davidson. Stable islands in chaotic atom-optics billiards, caused by curved trajectories. *J. Phys. B: At. Mol. Opt. Phys.*, 2002, **35**, P. 2183-2190.
- [2] A. Kaplan, N. Friedman, M. Andersen, N. Davidson. Observation of Islands of Stability in Soft Wall Atom-Optics Billiards. *Physics Letters V.*, 2001, **87** Nu. **27**.
- [3] B. Rohwedder. Quantum billiard atom optics. *Europhys. Lett.*, 2002, **60**(4), P. 505-511.
- [4] S.W. Doeschel, M.H. Rice. Infinite Square-Well Potential with a Moving Wall., 1969, *Am. J. Phys.*, **37**, P. 1246.
- [5] A. Munier, J.R. Burgan, M. Feix, E. Fijalkow. Schrödinger equation with time-dependent boundary conditions. *J. Math. Phys.*, 1981, **22**, P. 1219.
- [6] J.V. Jose, R. Gordery. Study of a quantum fermi-acceleration model. *Phys. Rev. Lett.*, 1986, **56**, P. 290.
- [7] P. Seba. Quantum chaos in the Fermi-accelerator model. *Phys. Rev. A*, 1990, **41**, P. 2306.
- [8] Pinder D.N. The contracting square quantum well. *Am. J. Phys.*, 1990, **58**, P. 54.
- [9] M. Razavy. Time-dependent harmonic oscillator confined in a box. *Phys. Rev. A*, 1991, **44**, P. 2384.
- [10] P. Pereshogin, P. Pronin. Effective Hamiltonian and Berry phase in a quantum mechanical system with time dependent boundary conditions. *Phys. Lett. A*, 1991, **156**, P. 12-16.
- [11] C. Scheininger, M. Kleber. Quantum to classical correspondence for the Fermi-acceleration model. *Physica D*, 1991, **50**, P. 391-404.
- [12] A.J. Makowski, S.T. Dembinski. Exactly solvable models with time-dependent boundary conditions. *Phys. Lett. A*, 1991, **154**, P. 217-220.
- [13] A.J. Makowski. Two classes of exactly solvable quantum models with moving boundaries. *J. Phys. A: Math. Gen.*, 1992, **25**, P. 3419.
- [14] B. Jaramillo, R.P. Martínez-y-Romero, H.N. Núñez-Yépez, A.L. Salas-Brito. On the one-dimensional Coulomb problem. *Physics Letters A*, 2009, **374**, P. 150-153.
- [15] F. Domínguez-Adame, A. Rodríguez. A one-dimensional relativistic screened Coulomb potential. *Physics Letters A*, 1995, **198**, P. 275-278.
- [16] K.D. Schotte, T.T. Truong. Phase transition of a one-dimensional Coulomb system. *Phys. Rev. A*, 1980, **22** Nu. **5**.
- [17] F. Gesztesy. On the one-dimensional Coulomb Hamiltonian. *J. Phys. A: Math. Gen.*, 1980, **13**, P. 867-875.

Kicked particle dynamics in quantum graphs

J. Yusupov¹, V. Eshniyozov², O. Karpova^{1,2}, D. Sh. Saidov³

¹Turin Polytechnic University in Tashkent, 17. Niyazov Str., 100095, Tashkent, Uzbekistan

²National University of Uzbekistan, 100174, Tashkent, Uzbekistan

³Urganch Branch of Tashkent University of Information Technologies, Urganch, Uzbekistan
j.yusupov@polito.uz

PACS 03.65.Aa, 03.65.Ge

DOI 10.17586/2220-8054-2015-6-6-773-778

The quantum dynamics of a delta-kicked driven particle in a star-shaped network is studied by obtaining an exact solution for the time-dependent Schrödinger equation within a single kicking period. The time-dependence of the average kinetic energy and the Gaussian wave packet evolution are analyzed.

Keywords: quantum graph, periodically kicked system, wave packet dynamics.

Received: 1 November 2015

1. Introduction

Particle dynamics in branched systems, such as networks and lattices are of importance in many topics of physics such as optics, acoustics, condensed matter and polymer physics. Particle and wave transport in such systems can be effectively modeled using the evolution equation on so-called metric graphs. Earlier, the Schrödinger equation on a metric graph was subject of extensive research (see review papers [1-8] and references therein). The nonlinear wave equation on metric graphs has also attracted much attention recently [9-16]. Graphs are the systems consisting of bonds which are connected at the vertices. The bonds are connected according to a rule, which is called the topology of a graph. The topology of a graph is given in terms of the adjacency matrix [1, 2]:

$$C_{ij} = C_{ji} = \begin{cases} 1, & \text{if } i \text{ and } j \text{ are connected;} \\ 0, & \text{otherwise.} \end{cases} \quad i, j = 1, 2, \dots, V. \quad (1)$$

A graph is called a metric graph when each of its bonds is associated with an interval $[0, L_{ij}]$.

Earlier, quantum graphs were extensively studied in the context of quantum chaos theory [17-21]. Strict mathematical formulation of the boundary conditions was given by Kostykin and Schrader [4]. Inverse problems on quantum graphs have been studied in Refs. [5]- [7]. An experimental realization of quantum graphs on (optical) microwave waveguide networks is discussed in the Ref. [8].

Despite the fact that different issues of quantum graphs and their applications have been discussed in the literature, the problem of graphs driven by external fields has not yet been treated.

In this paper, we address the problem of particle dynamics in periodically driven graphs by considering, as a perturbation, delta-kicking potential. The quantum dynamics of delta-kicked systems were extensively discussed in the context of quantum chaos and related issues [17] - [21]. A remarkable feature of the kicked quantum system is so-called quantum localization, which implies suppression of diffusive growth of the average kinetic

energy as a function of time [18]. For classical kicked systems, energy grows linearly as a function of time [17, 18]. Such a phenomenon can be considered as an analog of the Anderson localization [18]. We consider delta-kicked particle dynamics in the simplest graph topology, the so-called star graph. In particular, we study wave-packet evolution in such a system and the time-dependence of the average kinetic energy.

2. Schrödinger equation on graphs

Quantum particle dynamics on a graph is described by the one-dimensional Schrödinger equation [1, 2] (in the units $\hbar = 2m = 1$):

$$\frac{d^2 \Psi_b(x)}{dx^2} = k^2 \Psi_b(x), \quad b = (i, j), \quad (2)$$

where b denotes a bond connecting i th and j th vertices, and for each bond b , the component Ψ_b of the total wave function Ψ_b is a solution of the Eq.2. This equation is a multi-component equation where the components are related through boundary conditions, providing continuity and current conservation [1]:

$$\left\{ \begin{array}{l} \bullet \text{ Continuity,} \\ \Psi_{i,j}|_{x=0} = \varphi_i, \quad \Psi_{i,j}|_{x=L_{i,j}} = \varphi_j \text{ for all } i < j \text{ and } C_{i,j} \neq 0 \\ \bullet \text{ Current conservation,} \\ \sum_{j < i} C_{i,j} \frac{d}{dx} \Psi_{j,i}(x) \Big|_{x=L_{i,j}} + \sum_{j > i} C_{i,j} \frac{d}{dx} \Psi_{i,j}(x) \Big|_{x=0} = -\lambda_i \varphi_i. \end{array} \right. \quad (3)$$

Here, the parameters λ_i are free parameters which determine the type of boundary conditions. In particular, the special case of zero λ_i 's corresponds to the Neumann boundary conditions. The Dirichlet boundary conditions correspond to the case when all the $\lambda_i = \infty$.

The eigenfunctions obeying continuity conditions can be written as:

$$\Psi_{i,j} = \frac{C_{i,j}}{\sin kL_{i,j}} (\varphi_i \sin k(L_{i,j} - x) + \varphi_j \sin kx), \quad (4)$$

while current conservation gives:

$$\sum_{j \neq i} \frac{kC_{i,j}}{\sin kL_{i,j}} (-\varphi_i \cos kL_{i,j} + \varphi_j) = \lambda_i \varphi_i. \quad (5)$$

Corresponding eigenfunctions can be found from the following quantization condition:

$$\det(h_{i,j}(k)) = 0, \quad (6)$$

where

$$h_{i,j}(k) = \begin{cases} -\sum_{m \neq i} C_{i,m} \cot kL_{i,m} - \frac{\lambda_i}{k}, & i = j \\ C_{i,j} \sin^{-1} kL_{i,j}, & i \neq j \end{cases} \quad (7)$$

For the star graph, the boundary conditions can be written as [22]:

$$\left\{ \begin{array}{l} \Psi_1|_{y=0} = \Psi_2|_{y=0} = \dots = \Psi_N|_{y=0}, \\ \Psi_1|_{y=L_1} = \Psi_2|_{y=L_2} = \dots = \Psi_N|_{y=L_N} = 0, \\ \sum_{j=1}^N \frac{d}{dy} \Psi_j|_{y=0} = 0. \end{array} \right. \quad (8)$$

where N is the number of bonds emanating from the central vertex.

In the case of the star graph, the energy spectrum can be found from the following spectral equation [22]:

$$\sum_{j=1}^N \tan^{-1}(k_n L_j) = 0, \tag{9}$$

while the corresponding eigenfunctions are written as [22]:

$$\Psi_j^{(n)} = \frac{B_n}{\sin(k_n L_j)} \sin(k_n(L_j - y)) \tag{10}$$

where the normalization coefficients are given by:

$$B_n = \left[\sum_j (L_j + \sin(2k_n L_j)) \sin^{-2}(k_n L_j) / 2 \right]^{-1/2}. \tag{11}$$

3. Kicked star graph

Consider a quantum particle on a primary star graph, i.e. on a graph with three bonds, in the presence of an external time-periodic potential. Such system is described by the following time-dependent Schrödinger equation:

$$i \frac{\partial \Psi_b(x, t)}{\partial t} = \left[-\frac{\partial^2}{\partial x^2} - \varepsilon \cos x \delta_T(t) \right] \Psi_b(x, t), \quad b = 1, 2, 3. \tag{12}$$

where:

$$\delta_T(t) = \sum_{l=-\infty}^{\infty} \delta(t - lT), \tag{13}$$

with T being the kicking period.

Eq.12 can be analytically integrated over a single kicking period. To do this, we note that the solution of Eq. 12 can be expanded in terms of complete set $\{\phi_b^{(n)}\}$ ($b = 1, 2, 3$), of solutions of Eq. 2 as:

$$\Psi_b(x, t) = \sum_n A_n(t) \phi_b^{(n)}(x) \tag{14}$$

Integrating Eq.12 over a single period T , using the same prescription as in the case of the kicked rotor [17, 18] for the time evolution of $A_n(t)$, during one kicking, period we have:

$$A_m(t + T) = \sum_n A_n(t) V_{mn} e^{-iE_n T}, \tag{15}$$

where E_n represents the eigenvalues of unperturbed star graph:

$$V_{mn} = \sum_{b=1}^3 \int_0^{L_b} \phi_b^{(m)*}(x) e^{i\varepsilon \cos x} \phi_b^{(n)}(x) dx. \tag{16}$$

Using Eq.15, we can compute wave function for an arbitrary number of kicks and average kinetic energy as:

$$\langle E(t) \rangle = -\frac{1}{2} \sum_{b=1}^3 \int_0^{L_b} \Psi_b^*(x, t) \frac{\partial^2 \Psi_b(x, t)}{\partial x^2} dx. \tag{17}$$

In Fig. 1, $\langle E(t) \rangle$ is plotted as a function of time for different kicking strength values.

As is seen from these plots, the average energy is a periodic function of time with a period much longer than that of the kicking period. This behavior is completely different than

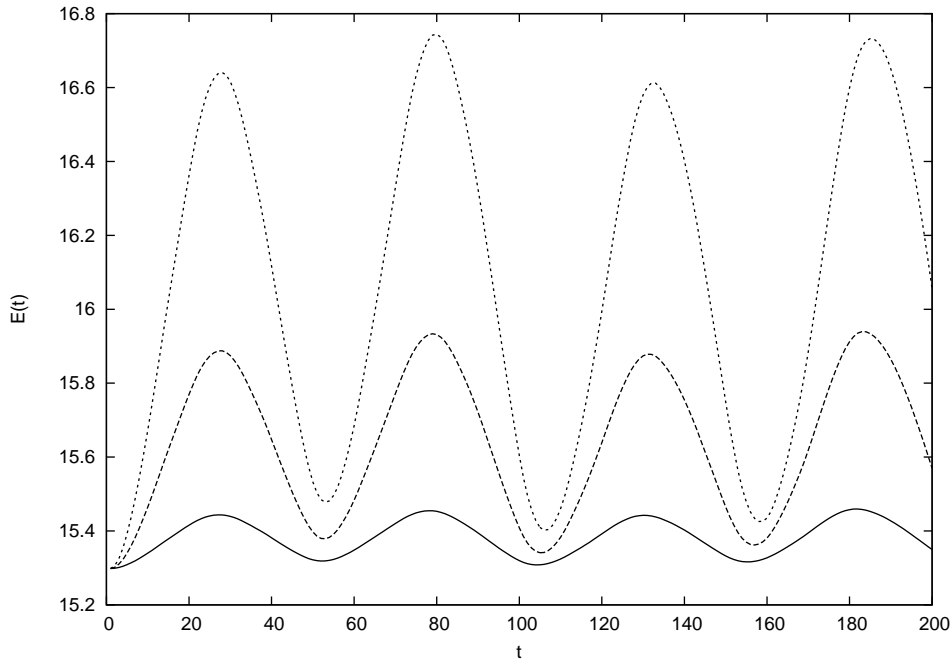


FIG. 1. Average kinetic energy as a function of time for different kicking strength values: $\varepsilon = 0.3$ (dotted), $\varepsilon = 0.2$ (dashed) and $\varepsilon = 0.1$ (solid) at the kicking period, $T = 0.001$

that of the kicked rotor case [18] and the kicked one dimensional box [20]. Such a periodicity may be caused by a more complicated structure for the graph, which implies different (than those for kicked rotor or box) boundary conditions in the Schrödinger equation.

Furthermore, we consider wave packet evolution in kicked star graph by taking the wave function at $t = 0$ (for the first bond) as the following Gaussian wave packet:

$$\Psi_1(x, 0) = \Phi(x) = \left(\sqrt{2\pi}\sigma\right)^{-1/2} e^{-(x-\mu)^2/4\sigma}, \quad (18)$$

with μ and σ being the initial position and the width of the packet. For other bonds, initial wave function is assumed to be zero, i.e. $\Psi_2(x, 0) = \Psi_3(x, 0) = 0$. Then for the initial values of the wave functions $\Psi_b(x, t)$, the expansion coefficients at $t = 0$ can be written as:

$$A_n(0) = \int_0^{L_1} \Phi(x)\phi_1^{(n)*}(x)dx. \quad (19)$$

Fig. 2 presents the time evolution of the Gaussian wave packet on kicked star graph for kicking parameters $\varepsilon = 0.1$ and $T = 0.01$ at time moments $t = 100T$, $300T$ and $500T$. As these plots show, complete dispersion of the wave packet is not possible, even for a high number of kicks, due to the confined nature of the system. Also, wave packet revival can be observed in such systems.

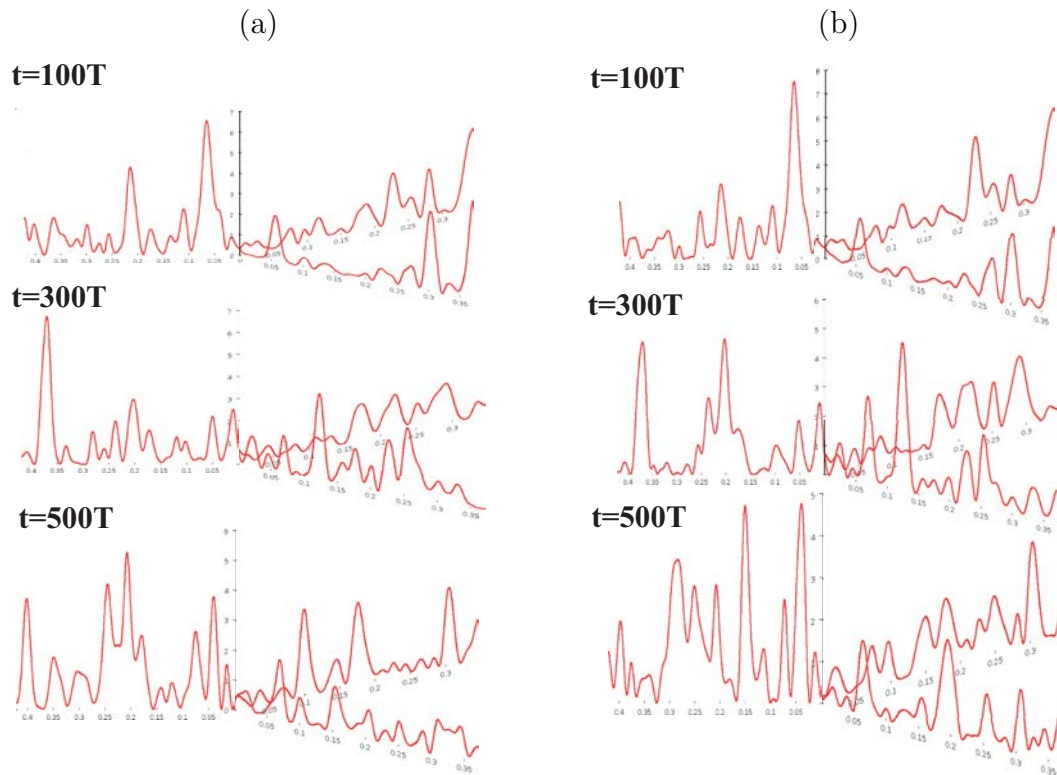


FIG. 2. Time evolution of the Gaussian wave packet in kicked quantum star graph for kicking parameters $\varepsilon = 0.1$, $T = 0.001$

4. Conclusion

In this work, we have studied the quantum dynamics of a delta kicked particle in a star graph driven by external periodic delta-kicking field by considering the time-dependence of the average kinetic energy and wave packet evolution. It was shown that the average kinetic energy of a kicked particle in a star graph is a periodic function of time. The amplitude and period of the average kinetic energy depend on the kicking parameters (kicking strength and period). By tuning the kicking parameters, it is possible to find a regime when the average kinetic energy grows monotonically over time. The absence of complete wave packet dispersion was also shown for this system. The results can be used for the realization of quantum Fermi acceleration in nanoscale networks and achieving tunable electronic transport in nanoscale devices.

References

- [1] T. Kottos, U. Smilansky. Periodic Orbit Theory and Spectral Statistics for Quantum Graphs. *Ann.Phys.*, 1999, **274**(1), P. 76–124.
- [2] S. Gnutzmann, U. Smilansky. Quantum graphs: Applications to quantum chaos and universal spectral statistics. *Adv.Phys.*, 2006, **55**(5-6) P. 527–625.
- [3] S. Gnutzmann, J.P. Keating, F. Pietet. Eigenfunction statistics on quantum graphs. *Ann.Phys.*, 2010, **325**(12) P. 2595–2640.
- [4] R. Kostyrykin, R. Schrader. Kirchhoff’s rule for quantum wires. *J. Phys. A: Math. Gen.*, 1999, **32**, P. 595.
- [5] B. Gutkin, U. Smilansky. Can one hear the shape of a graph? *J. Phys A.*, 2001, **31**, P. 6061.
- [6] J. Boman, P. Kurasov. Symmetries of quantum graphs and the inverse scattering problem. *Adv. Appl. Math.*, 2005, **35**(1), P. 58–70.

- [7] T. Cheon, P. Exner, O. Turek. Approximation of a general singular vertex coupling in quantum graphs. *Ann.Phys.*, 2010, **325** P. 548–578.
- [8] O. Hul, S. Bauch, P. Pakonski, N. Savytsky, K. Zyczkowski, L. Sirko. Experimental simulation of quantum graphs by microwave networks. *Phys. Rev. E*, 2004, **69**, P. 056205.
- [9] Z. Sobirov, D. Matrasulov, K. Sabirov, S. Sawada, K. Nakamura. Integrable nonlinear Schrödinger equation on simple networks: Connection formula at vertices. *Phys.Rev.E*, 2010, **81**, P. 066602.
- [10] R. Adami, C. Cacciapuoti, D. Finco, D. Noja. Fast solitons on star graphs. *Rev. Math. Phys.*, 2011, **23**(04), P. 409–451.
- [11] R. Adami, C. Cacciapuoti, D. Finco, D. Noja. Stationary states of NLS on star graphs. *Europhys. Lett.*, 2012, **100**, P. 10003.
- [12] R. Adami, C. Cacciapuoti, D. Finco, D. Noja. On the structure of critical energy levels for the cubic focusing NLS on star graphs. *J. Phys. A: Math. Theor.*, 2012, **45**, P. 192001.
- [13] R. Adami, D. Noja, and C. Ortoleva. Orbital and asymptotic stability for standing waves of a nonlinear Schrödinger equation with concentrated nonlinearity in dimension three. *J. Math. Phys.*, 2013, **54**, P. 013501.
- [14] K. Sabirov, Z. Sobirov, D. Babajanov, D. Matrasulov. Stationary Nonlinear Schrödinger Equation on Simplest Graphs. *Phys.Lett. A*, 2013, **377**, P. 860.
- [15] D. Noja. Nonlinear Schrödinger equation on graphs: recent results and open problems. *Philos. Trans. R. Soc. A*, 2013, **372**, P. 20130002.
- [16] C. Cacciapuoti, D. Finco, D. Noja. Topology-induced bifurcations for the nonlinear Schrödinger equation on the tadpole graph. *Phys. Rev. E*, 2015, **91**, P. 013206.
- [17] G. Casati, B.V. Chirikov, J. Ford, F.M. Izrailev. *Lecture Notes in Physics*, Vol. 93, P. 334 (Springer, Berlin, 1979).
- [18] G.M. Izrailev. Simple models of quantum chaos: spectrum and eigenfunctions. *Phys. Rep.*, 1990, **196**, P. 299–392.
- [19] A. Buchleitner, D. Delande, J. Zakrzewski. Non-dispersive wave packets in periodically driven quantum systems. *Phys. Rep.*, 2002, **368**(5), P. 409–547.
- [20] R. Sankaranarayanan, V. Sheorey. Accelerator modes of square well system. *Phys. Lett. A*, 2005, **338**, P. 288–296.
- [21] F. Haug, M. Bienert, W.P. Schleich, T.H. Seligman, M.G. Raizen. Motional stability of the quantum kicked rotor: A fidelity approach. *Phys. Rev. A*, 2005, **71**, P. 043803.
- [22] J.P. Keating. Fluctuation statistics for quantum star graphs. *Quantum graphs and their applications. Contemp. Math.*, 2006, **415**, P. 191–200.

On theory of second harmonic generation in 2D nonlinear photonic crystals with arbitrary structures

V. E. Eshniyazov¹, B. Kh. Eshchanov¹, D. B. Yusupov², Q. Ya. Ergashev², U. K. Sapaev^{1,*}

¹Department of Physics, National University of Uzbekistan, named after Mirzo Ulugbek, 100095, Tashkent, Uzbekistan

²Tashkent State Technical University, named after Abu Raikhan Beruni, Universitetskaya ul. 2, 100095, Tashkent

^{1*}usapaev@gmail.com

PACS 42.65.Ky

DOI 10.17586/2220-8054-2015-6-6-779-785

Second harmonic generation in 2D nonlinear photonic crystals based on rectangular symmetry with rectangular motifs has been analyzed theoretically. An approximate solution of the spectral response for the second harmonic generation in any designed 2D nonlinear photonic crystal is obtained within the un-depleted pump approximation. Rapid calculation of the temporal profile of multidirectional second harmonic pulse in such nonlinear lattices has been also shown.

Keywords: 2D nonlinear photonic crystals, second harmonic generation, frequency conversion, quasi-phase matching, arbitrary domain structures, linearly chirped domain structures, randomly sized domain structures.

Received: 1 November 2015

1. Introduction

One of the fundamental problems of nonlinear optics and laser physics is the creation of laser radiation in specific regions of a spectrum, where direct laser emission is either inefficient or impossible. In this regard, frequency converters, based on nonlinear photonic crystals (NPC) are of great interest in practice. The technique of significant importance is quasi-phase matching, based on NPC, where real phase matching does not occur, but high conversion efficiencies are nevertheless obtained in a crystal where the sign (or strength) of the nonlinearity varies periodically. This type of periodic nonlinearity variation can be achieved by e.g. periodic poling. For the first time, this technique was developed by N. Bloembergen [1]. Since the first report in 1961, quasi-phase matched interactions in NPC have developed into widely used tools for the generation of coherent radiation. While more than five decades old, this field is still rapidly developing today.

In the last few years, 2D NPC, proposed by V. Berger [2] have given new possibilities for frequency converters, since such lattices have several advantages in comparison with their 1D counterparts. For instance, they can be used to convert multiple frequencies with different directions from a single wave-length [3,4] or get high conversion efficiency [5], for simultaneous wavelength interchange [6], for all optical deflection and splitting realization [7], for realizing parametric solitons with purely nonlinear origin [8] and so on [9]. Relatively recently, an analytical solution was proposed to calculate the second harmonic intensity in rectangular 2D lattices for the nonlinear Raman–Nath diffraction process in the un-depleted pump approximation [10].

2. Statement of the problem

It is well known that 1D NPC with randomly sized domains have been the subject of intense studies due to possibilities of controlling spectral [11] or temporal profiles of generated harmonic, in particular, second harmonic generation (SHG) in the un-depleted [12] and depleted pump regimes [13-15]. It has been shown that harmonic generation with desired (e.g., amplitude and phase) parameters can be obtained by "exactly" designing 1D NPC. Pulse shaping technique via NPC with extremely short domains was also studied previously [16] for backward SHG energy conversion in the non-stationary regime. For this purpose and other tasks of frequency conversion problems, it is necessary to develop mathematical methods for analyzing spectral and temporal responses of 2D NPC at given three-wave interactions.

For the first time, the design of a SHG spectral response with any required profile in 1D NPC was developed in [11], where authors demonstrated this using a simulated annealing algorithm. Any amplitude and phase profile of second harmonic (SH) pulse in the un-depleted pump approximation was theoretically showed in [12]. It is necessary to note that this problem was also solved for the case of the depleted pump approximation using an effective numerical method using simulated annealing algorithm [13].

Most previous works have only focused on the 1 D NPC, not on the 2 D NPC with destroyed domain structures. We believe that for a solution to this kind of problem, it is necessary to develop a rapid numerical or analytical method for analyzing 2D NPC with any arbitrary domain structures.

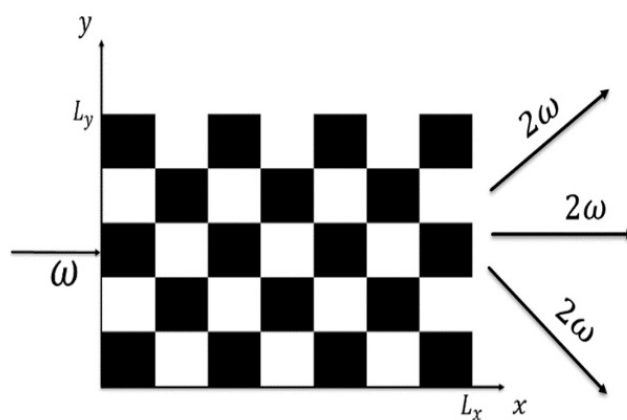


FIG. 1. Schematic picture of a 2D $\chi^{(2)}$ crystal. NPC has rectangular symmetry with rectangular motifs, where $\chi^{(2)}$ has positive sign in black motifs, while in white- negative

3. The concept of problem decision

Every nonlinear crystal with second order nonlinearity has spectral bandwidth for chosen three-wave interaction, which is an important parameter during the generation of short laser pulses. This parameter is dependent on crystal length and/or temperature in "normal" quadratic nonlinear optical crystals and is very difficult to increase it for the generation of short laser pulses. For one's turn, NPC's spectral bandwidth is flexible and can be increased by changing domain sizes on various configurations. In our opinion, previous

works on NPC with no “standard” (i.e., arbitrary sized) domain structures have been limited for only 1D NPC [11-15].

In the present work, we developed a rapid method for exactly calculating spectral and temporal response of SHG in 2D NPC with arbitrary structures. We focus on 2D NPC of rectangular symmetry with a rectangular motif.

4. Realization of the concept

The SHG process in 2D NPC is described by the following integral equation in the undepleted pump approximation [2,9,17](see Fig.1):

$$E^{2\omega}(\Delta k) = -i\alpha (E^\omega)^2 \int_0^{L_y} \int_0^{L_x} dy dx \exp(-i\Delta \mathbf{k} \times \mathbf{r}) d(\mathbf{r}), \tag{1}$$

where, $\Delta \mathbf{k} = \mathbf{k}^{2\omega} - 2\mathbf{k}^\omega$ is the phase mismatch of the interacting fields, $\alpha = \frac{2\omega^2 d_{33}}{k^{2\omega} c^2 L_y}$, d_{33} – the effective coefficient of nonlinear susceptibility NPC, E^ω , ω – respectively, the complex amplitude and frequency of the fundamental wave, $d(\mathbf{r})$ is a sign of second order nonlinearity which could be 1 or -1 depending on motif positions; L_x and L_y are length and width(see Fig. 1).

Taking into account the sign change of the $d(\mathbf{r})$ function, the integral part of the equation (1) can be rewritten by the following way:

$$E^{2\omega}(\Delta k) = -i\alpha (E^\omega)^2 \sum_{m=1}^M \sum_{n=1}^N (-1)^{m-n} \int_{B_{m-1}}^{B_m} dy \int_{A_{n-1}}^{A_n} dx \exp(-i \cdot (\Delta k_x x + \Delta k_y y)). \tag{2}$$

Furthermore, one can get the following solution (see also in [10, 11]):

$$E^{2\omega}(\Delta k) = -i\alpha (E^\omega)^2 \sum_{m=1}^M \sum_{n=1}^N (-1)^{m-n} \cdot \frac{e^{-i\Delta k_x A_n} - e^{-i\Delta k_x A_{n-1}}}{\Delta k_x} \cdot \frac{e^{-i\Delta k_y B_m} - e^{-i\Delta k_y B_{m-1}}}{\Delta k_y}. \tag{3}$$

$$A = [a_1; a_1 + a_2; a_1 + a_2 + a_3; \dots; a_1 + a_2 + \dots + a_N]$$

$$B = [b_1; b_1 + b_2; b_1 + b_2 + b_3; \dots; b_1 + b_2 + \dots + b_M]$$

Another crucial feature of SHG in 2D NPC is multidirectional generation and their symmetry. The phase mismatch of the interacting fundamental frequency and SH can be calculated by using the following formula (see Fig. 2) [2,16]:

$$\Delta k = -2k^\omega \cdot \cos \phi + k^{2\omega} \cdot \sqrt{1 - \left(\frac{2k^\omega}{k^{2\omega}}\right)^2 \cdot \sin^2 \phi} \tag{4}$$

Using (4) and (3), spectral response of SHG can be calculated.

Figure 3 shows the results of numerical (dashed) and analytical (solid) calculations of SH’s spectral response in 2D NPC of rectangular symmetry with rectangular motif depending on the angle of rotation. To demonstrate it, we looked at a realistic case: 2D NPC with $N = 100$ and $M = 100$ based on lithium niobate by 1550 nm fundamental frequency emission. For this case, we calculated:

$$a_1 = a_2 = \dots = a_N = b_1 = b_2 = \dots = b_M \approx 9.4\mu\text{m}$$

for $\mathbf{G}(1, 0)$ lattices wave-vector [2,16]. As is seen from the figure, numerical and analytical results correspond to each other with high accuracy for any configuration of NPC. Analytical

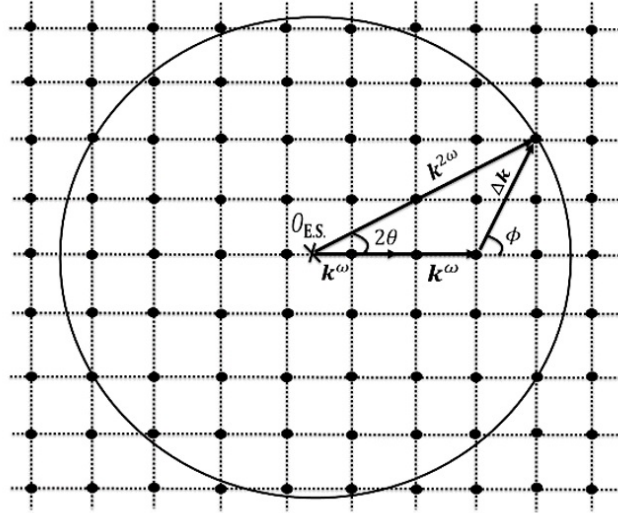


FIG. 2. Phase mismatch schema for SHG in 2D NPC

calculation took much less time than numerical one during calculation. (In our case it was 25 times less, due to each motif being divided by 5 steps on x -axis and y -axis coordinates for numerical calculation). Figure 3 (1) shows the uniform NPC, where all domains have the same height and width (i.e., $\sim 9.4 \mu\text{m}$). As it is seen here $\mathbf{G}(1,1)$, the quasi-phase matching order is higher than $\mathbf{G}(1,0)$, although the opposite would be expected. From the above equation (3), it is easily seen that the maximum value of $|E^{2\omega}(\Delta k)|$ is achieved when $|e^{-i\Delta k_x A_n} - e^{-i\Delta k_x A_{n-1}}|$ and $|e^{-i\Delta k_y B_m} - e^{-i\Delta k_y B_{m-1}}|$ takes their highest values, i.e. ± 2 . Therefore, the phase mismatch vector $\Delta k (\frac{\pi u}{a}; \frac{\pi v}{b})$ is considered as the best frequency conversion condition where u and v are odd integers, whereas they are even integers SHG will be shut down. So SHG occurs more intensely at $\phi = 45^\circ$ ($u = 1, v = 1$) than at $\phi = 0^\circ$ ($u = 1, v = 0$).

Figure 3 (2) shows results, when 2D NPC has linear chirp on the x -axis coordinate only such as from the first motif $(9.4 - 9.4 \cdot 0.05)\mu\text{m}$ the last motif $(9.4 + 9.4 \cdot 0.05)\mu\text{m}$ on both coordinates. As we expected, there we can see the spectral broadening of the SH wave in both directions at an angle $\phi = 45^\circ$. This is a well-known effect in 1D NPC. Figure 3 (3) shows results when 2D NPC has randomly-sized motifs in both the x - and y -axis directions. In this case, it appears (1,0) quasi-phase matching order due to decreasing phase mismatch between the fundamental frequency and SH waves. To calculate the last case, we randomly changed sizes of every motif on both directions by 5 % of their original sizes. By increasing the factor of random sizes, we were able to get overlapping all three peaks. In a realistic case, this can allow one to obtain broader broadband bandwidth of spectrum of 2D NPC in all directions spatially.

The main advantage of the analytical method is its quickness and its utility if we concentrate 2D NPC with very large numbers of motifs. This is especially important, as the design of this type of nonlinear optical medium could require a large number of calculations (e.g. around 1000 or more motifs).

Finally, we studied the possibility of calculating the temporal profile of a SH pulse at different angles. For this, we used the previously-developed convolution method [18]. Within this method, equation (3) can be used as a spectral response of the nonlinear medium, i.e. in our case 2D NPC and by multiplying it to the spectral profile of the square of the fundamental

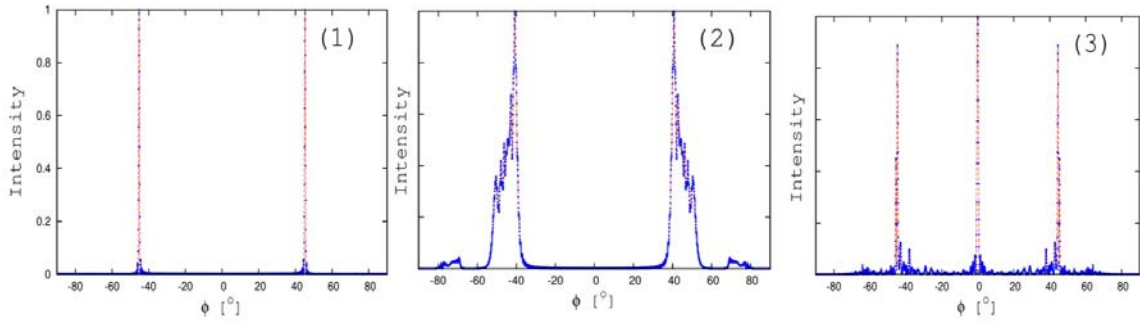


FIG. 3. Comparison of results of analytical results, based on equation (3) with numerical method for different realistic cases of SHG: (1) uniform 2D NPC; (2) linearly chirped 2D NPC; (3) randomly sized 2D NPC

pulse. The convolution method can be written by this formula:

$$A_{sh}(t) = BFT(E_{sh}(\Omega) * FFT(A^2(t))), \tag{5}$$

here BFT and FFT are the backward and forward Fourier transform, respectively; $A(t)$ is the temporal profile of input pulse. Equation (5) takes into account the dispersion of the nonlinear medium.

Figure 4 show results of the calculation, based on equation (5), where the input pulse was taken to be a 50 femtosecond at FWHM and the spectral response of 2D NPC was taken approximately at an angle of $\sim 45^\circ$. The spectral response of the nonlinear lattices was divided by the same number of the steps for the temporal profile of the fundamental pulse from 42° to 48° . One can see from the figure that the temporal profile of the SH pulse is increased due to a group velocity mismatch between the fundamental and SH pulses. (By increasing numbers of motifs on both coordinates, we were able to receive broader SH pulse relatively to the fundamental one, because of influence of the group velocity mismatch. This data is not presented here).

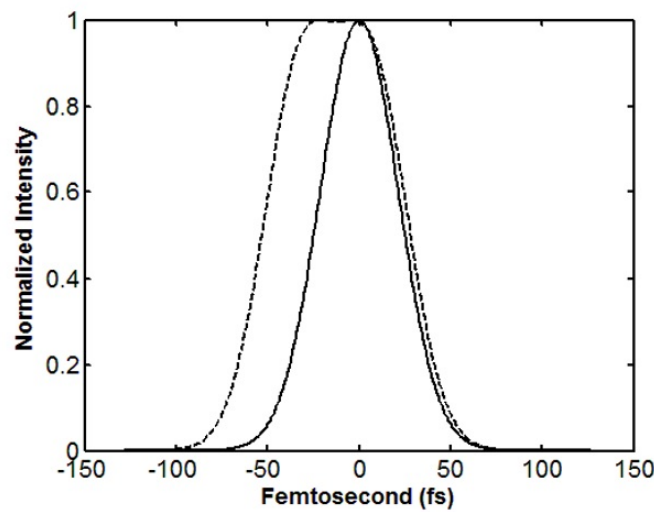


FIG. 4. Results of rapid calculation (5): temporal profiles of input (solid) and second harmonic (dashed) pulses at around angle $\sim 45^\circ$

5. Conclusion

In conclusion, we have theoretically studied SHG in 2D nonlinear photonic crystals, based on rectangular symmetry with rectangular motif. We obtained an approximation solution for the spectral response of SHG in any designed 2D nonlinear photonic crystals within the un-depleted pump approximation. We also showed a calculation of the temporal profile of SH pulse in such nonlinear lattices. We focused on a realistic case of the frequency doubling in 2D NPC of lithium niobate by a femtosecond fundamental pulse with fundamental wavelength of 1550 nm. Theoretical methods of this work can be used for other frequency conversion processes and another type and motifs of 2D NPC. This method can also be applied to multiple harmonic generation in 2D NPC, simultaneously. The latter is possible, if there is no pump depletion of the fundamental frequency. Finally, the presented mathematical method, due to its quickness, can be used to design 2D NPC with arbitrarily sized structures using various optimization algorithms.

Acknowledgments

D. B. Yusupov and U. K. Sapaev thank A. S. Chirkin and A. M. Vyunishev for enlightening discussions. This work was supported by the Basic Research Foundation of the Ministry of Higher and Secondary Special Education of the Republic of Uzbekistan Under contract N F2-49.

References

- [1] J.A. Armstrong, N. Bloembergen, D. Ducuing, P.S. Pershan. Interaction between light waves in a nonlinear dielectric. *Phys. Rev.*, 1962, **127**, P. 1918.
- [2] V. Berger. Nonlinear photonic crystals. *Phys. Rev. Lett.*, 1998, **81**, P. 4136.
- [3] N. G. R. Broderick, R. T. Brafalean, T. M. Monro, D. J. Richardson, C. M. de Sterke. Temperature and wavelength tuning of second-, third-, and fourth-harmonic generation in a two-dimensional hexagonally poled nonlinear crystal. *J. Opt. Soc. Am. B*, 2002, **19**, P. 2263.
- [4] S. Saltiel, Y. S. Kivshar. Phase matching in nonlinear photonic crystals, *Opt. Lett.*, 2000, **25**, P. 1204.
- [5] N.G.R. Broderick, G.W. Ross, H.L. Offerhaus, D.J. Richardson, D.C. Hanna: Hexagonally poled lithium niobate: a two-dimensional nonlinear photonic crystal. *Phys. Rev. Lett.*, 2000, **84**, P. 4345.
- [6] A. Chowdhury, C. Staus, B.F. Boland, T.F. Kuech, L. McCaughan, Experimental demonstration of 1535–1555 nm simultaneous optical wavelength interchange with a nonlinear photonic crystal. *Opt. Lett.*, 2001, **26**, P. 1353.
- [7] S.M. Saltiel, Y.S. Kivshar: All – optical deflection and splitting by second – order cascading. *Opt. Lett.*, 2002, **27**, P. 921.
- [8] K.Gallo, A.Pasquazi, S.Stivala, G.Assanto. Parametric Solitons in Two-Dimensional Lattices of Purely Nonlinear Origin. *Phys. Rev. Lett.*, 2008, **100**, P. 053901.
- [9] A.Arie, N.Voloch. Periodic, quasi-periodic, and random quadratic nonlinear photonic crystals. *Laser & Photon. Rev.*, 2010, **4**, P. 355.
- [10] A.M.Vyunishev, A.S.Chirkin. Multiple quasi-phase-matching in nonlinear Raman-Nath diffraction. *Opt. Lett.*, 2015, **40**, P. 1314.
- [11] D. T. Reid. Engineered quasi – phase – matching for second – harmonic generation. *Journal of optics A - pure and applied optics*, 2003, **5**(4), P. 97.
- [12] U. K. Sapaev, D. T. Reid. General second – harmonic pulse shaping in grating – engineered quasi – phase – matched nonlinear crystals. *Optics Express*, 2005, **13**, P. 3264.
- [13] U. K. Sapaev, G. Assanto. Femtosecond pulse synthesis by efficient second – harmonic generation in engineered quasi phase matching gratings. *Optics Express*, 2007, **15**, P. 7448.
- [14] U. K. Sapaev. Optimum Formation of the Response of Aperiodic Nonlinear Crystals in the Process of Second Harmonic Generation. *Opt. and Spect.*, 2007, **102**, P. 939.
- [15] D.B.Yusupov, U. K. Sapaev. *Nonlinear Optics in Photonic Crystals*. Tashkent, FAN, 2012, p. 128.

- [16] U.K.Sapaev, D.B. Yusupov, A.A. Sherniyzov, A.A. Uzakov. Theory of backward second-harmonic generation of short laser pulses in periodically and a periodically poled nonlinear crystals. *Journal of Russian Laser Research*, 2012, **33**, P. 103.
- [17] S.M. Russel, P.E. Powers, M.J. Missey, K.L. Schepler. Broadband mid – infrared generation with two dimensional quasi-phase-matched structures. *IEEE J. Quant. Electron*, 2001, **37**, P. 877.
- [18] M.A. Arbore, O. Marco, M.M. Fejer. Pulse compression during second – harmonic generation in a periodic quasi-phase – matching gratings. *Opt. Lett.*, 1997, **22**, P. 438.

A topological formulation for exotic quantum holonomy

A. Tanaka¹, T.Cheon²

¹Department of Physics, Tokyo Metropolitan University,
Hachioji, Tokyo 192-0397, Japan

² Laboratory of Physics, Kochi University of Technology,
Tosa Yamada, Kochi 782-8502, Japan

tanaka-atushi@tmu.ac.jp

PACS 03.65.-w,03.65.Vf,02.40.Pc **DOI** 10.17586/2220-8054-2015-6-6-786-792

An adiabatic change of parameters along a closed path may interchange the (quasi-)eigenenergies and eigenspaces of a closed quantum system. Such discrepancies, induced by adiabatic cycles are referred to as the exotic quantum holonomy, which is an extension of the geometric phase. “Small” adiabatic cycles induce no change on eigenspaces, whereas some “large” adiabatic cycles interchange eigenspaces. We explain the topological formulation for the eigenspace anholonomy, where the homotopy equivalence precisely distinguishes the larger cycles from smaller ones. An application to two level systems is explained. We also examine the cycles that involve the adiabatic evolution across an exact crossing, and the diabatic evolution across an avoided crossing. The latter is a nonadiabatic example of the exotic quantum holonomy.

Keywords: exotic quantum holonomy, homotopy, disclination.

Received: 1 November 2015

1. Introduction

An adiabatic quasi-static cycle may induce a nontrivial change on a closed quantum system. A well-known example is the geometric phase factor [1, 2], which is also called as the quantum holonomy because of its geometrical interpretation [3, 4].

Recently, it has been recognized that the geometric phase has exotic relatives, where (quasi-)eigenenergies and eigenspaces of stationary states exhibit nontrivial change as a result of an adiabatic cycle. Namely, eigenenergies and eigenspaces may be interchanged by adiabatic cycles.

The exotic quantum holonomy has been found in various physical systems: a particle confined in a one-dimensional box with a generalized pointlike potential [5], a quantum map under a rank-1 perturbation [6], the Lieb-Liniger model [7], and a quantum graph [8]. Other examples are reported in the references cited in Ref. [9].

In the following, we will briefly explain the topological formulation for the exotic quantum holonomy [9], which may be considered as a counterpart to the geometrical formulation for the geometric phase factor [3, 10]. Using the homotopic classification, we discuss “large” cycles that exhibit exotic quantum holonomy in Hamiltonian systems that involve the exact level crossing and avoided crossing.

2. Topological formulation

The quantum holonomies including both the geometric phase and the eigenspace anholonomy, are discrepancies induced by an adiabatic cycle, i.e., a closed path in an adiabatic parameter space \mathcal{M} . A lifting of the adiabatic cycle is helpful to characterize the quantum holonomies.

As for the geometric phase, we define a lift of the adiabatic path as the trajectory of the state vector, which satisfies the adiabatic time-dependent Schrödinger equation with an adiabatic initial state. We assume that the dynamical phase is excluded from the lift.

The lift of an adiabatic cycle C induces a mapping, which is denoted by ϕ_C , from the initial adiabatic state to the final adiabatic state. ϕ_C puts a geometric phase factor to the initial state vector. In terms of differential geometry, ϕ_C is an element of the holonomy group. This fact allows us to thoroughly investigate the geometric phase with the help of differential geometry [3].

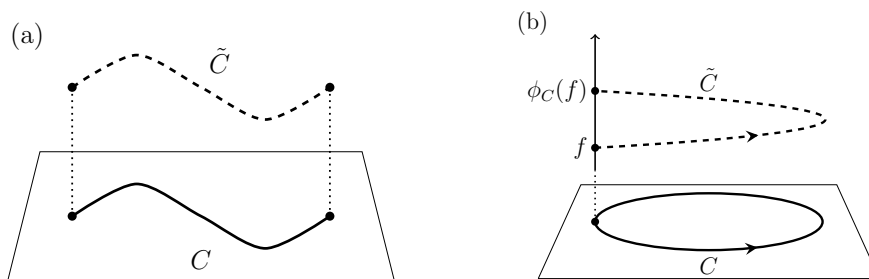


FIG. 1. Lifting structure behind quantum holonomies. (a) Lift \tilde{C} (dashed line) of a path C (bold line) in the adiabatic parameter space \mathcal{M} . A lift is the trajectory of an eigenobject under the adiabatic time evolution with an adiabatic initial condition. The dotted lines represent the projection π from the lifted space to \mathcal{M} . As for the case of the geometric phase, the lift is the trajectory of the state vector excluding the dynamical phase. On the other hand, the lift for the exotic quantum holonomy is the trajectory of p (Eq. (1)). (b) Lift of the closed path (i.e., adiabatic cycle) for a given initial eigenobject f . We denote the final point of the lift by $\phi_C(f)$. The mapping ϕ_C describes the discrepancy of the eigenobject induced by the cycle C

We carry over the concept of lifting to the exotic quantum holonomy. Instead of the adiabatic state vector for the geometric phase, we employ an ordered set of eigenprojectors

$$p \equiv (\hat{P}_1, \hat{P}_2, \dots) \tag{1}$$

where \hat{P}_j is j -th eigenprojector under a given value of the adiabatic parameter. We denote p -space by \mathcal{P} .

We explain two kinds of adiabatic parameter space \mathcal{M} , which is located at the bottom of the lifting structure. One is a c -number parameter space. Alternatively, it is useful to introduce a canonical “adiabatic parameter space”, whose point is a set of projectors:

$$b \equiv \{\hat{P}_1, \hat{P}_2, \dots\}, \tag{2}$$

where the order of the projectors are disregarded. b -space is a counterpart of the projective Hilbert space in the Aharonov-Anandan theory of the geometric phase [10].

We explain the lifting of an adiabatic cycle C in \mathcal{M} to \mathcal{P} , and the corresponding ϕ_C . For a given adiabatic path, the adiabatic Schrödinger equation induces the adiabatic

time evolution of p . The lifted path is the trajectory of p , and naturally induces ϕ_C . The mapping of ϕ_C between the initial and final p is essentially a permutation of \hat{P}_j 's. For example, if C does not induce the exotic quantum holonomy, ϕ_C is equivalent with the identical permutation. On the other hand, ϕ_C may be a non-identical permutation, which describes the interchange of the eigenspaces, induced by C .

Here, our task is to characterize ϕ_C completely. We utilize the fact that there is a covering map $\pi : \mathcal{P} \rightarrow \mathcal{M}$, where π is the projection that satisfies the axiom of the covering projection (not shown here). We remark that the covering space is a fiber bundle with a discrete structure group due to the discreteness of p for a given value of the adiabatic parameter.

The covering map structure allows us to investigate the exotic quantum holonomy with the help of topology. First, ϕ_C and $\phi_{C'}$ are the same if C and C' are homotopic, where we say that a cycle C is homotopic to another cycle C' if C can be smoothly deformed to C' with the initial and final points remaining unchanged. Hence, we may denote the mapping ϕ_C as $\phi_{[C]}$, where $[C]$ is the class of paths that are homotopic to C .

Next, we need to enumerate all possible $[C]$'s in the adiabatic parameter space \mathcal{M} . This is equivalent to finding $\pi_1(\mathcal{M}) = \{[C] \mid C \text{ is a closed path in } \mathcal{M}\}$, which is called the first fundamental group of \mathcal{M} .

Hence, it suffices to enumerate $\phi_{[C]}$ for all $[C] \in \pi_1(\mathcal{M})$. When \mathcal{P} is contractible to a point (i.e., there is no "hole"), there is a one-to-one correspondence between $\pi_1(\mathcal{M})$ and $\phi_{[C]}$, i.e.:

$$\{\phi_{[C]}\}_{[C] \in \pi_1(\mathcal{M})} \simeq \pi_1(\mathcal{M}). \quad (3)$$

In other words, if C is not homotopic to C' , two permutations $\phi_{[C]}$ and $\phi_{[C']}$ are different. The extension of Eq. (3) to an arbitrary \mathcal{P} is shown in Ref. [9].

3. Analysis of two level systems

We examine the exotic quantum holonomy in two level systems. For a while, we suppose the system has no spectral degeneracy. Hence, the Hamiltonian \hat{H} has the following spectral decomposition:

$$\hat{H} = E_1 \hat{P}_1 + E_2 \hat{P}_2. \quad (4)$$

where E_1 and E_2 are eigenvalues of H . In two level systems, the eigenprojections \hat{P}_1 and \hat{P}_2 may be specified by a normalized 3-vector \mathbf{a} , which is called as the Bloch vector, as

$$\hat{P}_1 = \frac{1}{2}(1 + \mathbf{a} \cdot \hat{\boldsymbol{\sigma}}), \quad \hat{P}_2 = \frac{1}{2}(1 - \mathbf{a} \cdot \hat{\boldsymbol{\sigma}}). \quad (5)$$

Non-degenerate periodically driven systems can be examined in the same manner once we replace \hat{H} with a Floquet operator.

We explain that p and b have a simple geometrical interpretation in two level systems (see, Fig. 2 (a)). First, p is equivalent to \mathbf{a} , a point in a sphere S^2 , as is seen from Eq. (5). Second, b is equivalent to the director (headless vector) \mathbf{n} [11], which correspond to a point in the real projective plane $\mathbb{R}P^2$. This is because both \mathbf{a} and $-\mathbf{a}$ correspond to the same value of b , and the identification of antipodal point on the sphere leads to $\mathbb{R}P^2$.

Once we employ \mathbf{n} as the adiabatic parameter space, the topological formulation provides an intuitive interpretation of the exotic quantum holonomy. The lifts of a "small" cycle in \mathbf{n} -space are closed in \mathbf{a} -space, i.e., the sphere (Fig. 2 (b)). Conversely, the lifts of a "large" cycle in \mathbf{n} -space can be open in \mathbf{a} -space. The exotic quantum holonomy reflects such a discrepancy between the trajectories of \mathbf{n} and \mathbf{a} .

A complete way to distinguish the smaller and larger cycles is provided by the homotopy equivalence. In \mathbf{n} -space, i.e., $\mathbb{R}P^2$, there are only two classes of cycles, i.e., $\pi_1(\mathbb{R}P^2) = \{[e], [\gamma]\}$, where e is a “small” cycle that is homotopic to a point (i.e., the zero-length closed path), and a “large” cycle γ is not homotopic to e (Fig. 2 (b)).

Now Eq. (3) is applicable to classify $\phi_{[C]}$ completely, since \mathbf{a} -space, i.e. S^2 , has no hole. Namely, $\phi_{[e]}$ and $\phi_{[\gamma]}$ correspond to different permutations, the identical and the cyclic permutations of two items, respectively (see, Fig. 2 (b)).

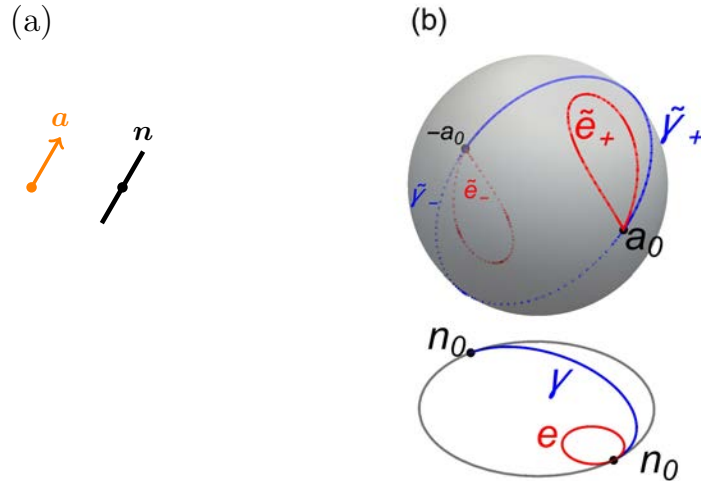


FIG. 2. (a) Bloch vector \mathbf{a} and director \mathbf{n} (schematic). (b) Two homotopically inequivalent cycles e and γ in $\mathbb{R}P^2$ (bottom), and their lifts to S^2 (upper). The initial point of the cycles is denoted as \mathbf{n}_0 . The lifts of the cycles with initial point $\pm\mathbf{a}_0$ are \tilde{e}_\pm and $\tilde{\gamma}_\pm$. Since the former are closed in S^2 , $\phi_{[e]}$ correspond to the identical permutation of eigenspaces. On the other hand, the latter are open so that $\phi_{[\gamma]}$ corresponds to the cyclic permutation of the two eigenspaces, i.e., γ induces the exotic quantum holonomy

4. Examples of nontrivial cycle γ

We explain how we realize the adiabatic cycles γ , which induces the cyclic permutation of eigenspaces as well as (quasi-)eigenenergies in non-degenerate two level systems.

The first example is a family of a quantum map under a rank-1 perturbation, which is described by a periodically-kicked Hamiltonian $\hat{H}(\lambda, t) = \hat{H}_0 + \lambda|v\rangle\langle v| \sum_{n=-\infty}^{\infty} \delta(t - n)$, where $|v\rangle$ is a normalized vector. We introduce a Floquet operator, which describes the time evolution during a unit time interval,

$$\hat{U}(\lambda) = e^{-i\hat{H}_0} e^{-i\lambda|v\rangle\langle v|}. \tag{6}$$

The stationary state of this system for a given value of λ is described by an eigenvector of $\hat{U}(\lambda)$, and the time evolution induced by an adiabatic variation of λ is essentially governed by the parametric evolution of eigenvectors of $\hat{U}(\lambda)$ [12]. Since $\hat{U}(\lambda)$ has a period 2π as a function of λ , the trajectory of \mathbf{n} induced by $\hat{U}(\lambda)$ for $0 \leq \lambda \leq 2\pi$ makes a closed path in $\mathbb{R}P^2$. Nevertheless, the lift of the closed path to S^2 is generically open to exhibit the non-identical permutation of eigenprojectors, as these closed paths are homotopic to γ (Fig. 3). See, Refs. [6, 9] for details.

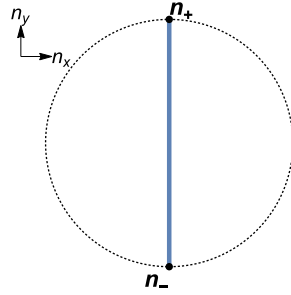


FIG. 3. Trajectories of the director \mathbf{n} . We depict the trajectories in n_x - n_y plane. The first example is the quantum map (6) with $\hat{H}_0 = \frac{\pi}{2}\hat{\sigma}_y$ and $|v\rangle\langle v| = (1 + \hat{\sigma}_x)/2$, which implies $\mathbf{a} = \mathbf{e}_y \cos(\lambda/2) - \mathbf{e}_z \sin(\lambda/2)$, whose director moves along n_y -axis. Note that the initial and end points \mathbf{n}_{\pm} are same in $\mathbb{R}P^2$. Hence the trajectory is closed, and homotopic to γ . The Bloch vector of the second example (7) is shown in Eq. (8). The trajectory of the director coincides with the one of the first example, and agrees with the one for the third nonadiabatic example

Second, we examine the adiabatic cycles that involve a level crossing [13] using the following Hamiltonian

$$\hat{H}(\lambda) \equiv \frac{1}{4} [(1 + \cos \lambda)\hat{\sigma}_y + (\sin \lambda)\hat{\sigma}_z]. \quad (7)$$

which is periodic in λ with a period 2π , and degenerates at $\lambda = \pi$. We introduce a Bloch vector

$$\mathbf{a} \equiv \cos(\lambda/2)\mathbf{e}_y + \sin(\lambda/2)\mathbf{e}_z, \quad (8)$$

for Eq. (7), which leads to the spectrum decomposition (4) with the eigenprojectors (5), $E_1 = \frac{1}{2}\cos(\lambda/2)$ and $E_2 = -\frac{1}{2}\cos(\lambda/2)$ (Fig. 4). We note that the Bloch vector \mathbf{a} smoothly depends on λ even in the vicinity of the crossing point $\lambda = \pi$. Hence, the adiabatic time evolution follows the corresponding parametric evolution of eigenprojectors (5) [14]. Although $\hat{H}(\lambda)$ is periodic in λ with the period 2π , the eigenenergies, as well as the eigenprojectors, are not, which implies the presence of the exotic quantum holonomy. Hence, the trajectory of the director for $0 \leq \lambda \leq 2\pi$ is closed, and is homotopic to γ (see, Fig. 3).

Third, we examine the second case under a generic small perturbation, which generically breaks the spectral degeneracy. For example, we consider:

$$\hat{H}_\epsilon(\lambda) \equiv \hat{H}(\lambda) + \frac{1}{2}\epsilon\sigma_x. \quad (9)$$

The level crossing point becomes an avoided crossing point due to the perturbation (Fig. 4). Hence, the exotic quantum holonomy do not occur in the adiabatic limit. However, the use of the diabatic process across the avoided crossing recovers the exotic quantum holonomy [13]. Along the closed path $0 \leq \lambda \leq 2\pi$ involving the diabatic process, the trajectory induced by the time evolution of the state projector, which is initially an eigenprojector of $\hat{H}(0)$, mimics the parametric evolution of the corresponding eigenprojector of the unperturbed system $\hat{H}(\lambda)$. In this sense, the diabatic cycle plays the role of nontrivial cycle γ . We remark that this is a nonadiabatic example of the exotic quantum holonomy.

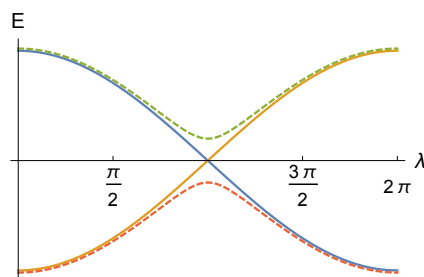


FIG. 4. Eigenenergies of the level crossing Hamiltonian $\hat{H}(\lambda)$ (Eq. (7)) (thick lines) and the perturbed Hamiltonian $\hat{H}_\epsilon(\lambda)$ (Eq. (9)) (dashed lines). Since the eigenenergies of $\hat{H}(\lambda)$ crosses at $\lambda = \pi$, the adiabatic cycle $0 \leq \lambda \leq 2\pi$ interchanges the eigenspaces at $\lambda = 0$. The adiabatic cycle for $\hat{H}_\epsilon(\lambda)$ do not induce the exotic quantum holonomy, due to the presence of the avoided crossing around $\lambda = \pi$. However, if λ is moved quickly around $\lambda = \pi$, the system follows the diabatic evolution. Such a diabatic cycle induces the exotic quantum holonomy along the nonadiabatic time evolution [13]

5. Summary

We briefly explained the topological formulation of the exotic quantum holonomy with an emphasis to its geometrical character in two level systems. An application to Hamiltonian systems with an exact or avoided crossing is explained.

Acknowledgements

This research was supported by the Japan Ministry of Education, Culture, Sports, Science and Technology under the Grant number 15K05216.

References

- [1] M. V. Berry. Quantal phase factors accompanying adiabatic changes. *Proc. R. Soc. London A*, 1984, **392** P. 45.
- [2] A. Shapere, F. Wilczek (Eds.). *Geometric phases in physics*. World Scientific, Singapore, 1989.
- [3] B. Simon, Holonomy, the Quantum Adiabatic Theorem, and Berry's Phase. *Phys. Rev. Lett.*, 1983, **51**, P. 2167.
- [4] A. Bohm, A. Mostafazadeh, H. Koizumi, Q. Niu, Z. Zwanziger. *The Geometric Phase in Quantum Systems*, Springer, Berlin, 2003; D. Chruściński, A. Jamiolkowski. *Geometric Phases in Classical and Quantum Mechanics*. Birkhäuser, Boston, 2004.
- [5] T. Cheon. Double spiral energy surface in one-dimensional quantum mechanics of generalized pointlike potentials. *Phys. Lett. A*, 1998, **248**, P. 285.
- [6] A. Tanaka, M. Miyamoto. Quasienergy anholonomy and its application to adiabatic quantum state manipulation. *Phys. Rev. Lett.*, 2007, **98**, P. 160407.
- [7] N. Yonezawa, A. Tanaka, T. Cheon. Quantum holonomy in the Lieb-Liniger model. *Phys. Rev. A*, 2013, **87**, P. 062113.
- [8] T. Cheon, A. Tanaka, O. Turek. Examples of quantum holonomy with topology changes. *Acta Polytechnica*, 2013, **53**, P. 410.
- [9] A. Tanaka, T. Cheon. Bloch vector, disclination and exotic quantum holonomy. *Phys. Lett. A*, 2015, **379**, P. 1693.
- [10] Y. Aharonov, J. Anandan. Phase change during a cyclic quantum evolution. *Phys. Rev. Lett.*, 1987, **58**, P. 1593.
- [11] P. G. de Gennes, J. Prost. *The Physics of Liquid Crystals*, 2-nd Edition, Oxford University Press, Oxford, 1993, Ch. 1; N. D. Mermin. The topological theory of defects in ordered media. *Rev. Mod. Phys.*, 1979, **51**, P. 591.

- [12] A. Dranov, J. Kellendonk, R. Seiler. Discrete time adiabatic theorems for quantum mechanical systems. *J. Math. Phys.*, 1998, **39**, P. 1340. A. Tanaka. Adiabatic theorem for discrete time evolution. *J. Phys. Soc. Japan*, 2011, **80**, P. 125002.
- [13] T. Cheon, A. Tanaka, S. W. Kim. Exotic quantum holonomy in Hamiltonian systems. *Phys. Lett. A*, 2009, **374**, P. 144.
- [14] T. Kato. On the Adiabatic Theorem of Qunatum Mechanics. *J. Phys. Soc. Japan*, 1950, **5**, P. 435.

An asymptotic analysis of a self-similar solution for the double nonlinear reaction-diffusion system

M. Aripov¹, Sh. Sadullaeva²

¹National University of Uzbekistan named after M. Ulugbek, Tashkent, Uzbekistan

²Tashkent University of information technology, Tashkent, Uzbekistan

mirsaidaripov@mail.ru, orif_sh@list.ru

PACS 02.30.Ik, 05.45.Yv

DOI 10.17586/2220-8054-2015-6-6-793-802

We study the solution for a system of reaction-diffusion equations with double nonlinearity in the presence of a source. A self-similar approach is used for the treatment of qualitative properties of a nonlinear reaction-diffusion system. It is shown that there exist some parameter values for which the effect of finite velocity of perturbation of distribution (FSPD), localization of solution, onside localization can occur. The problem for choosing the appropriate initial approximation for the iteration process used in numerical analysis is solved.

Keywords: reaction-diffusion system, double nonlinearity, qualitative properties.

Received: 1 November 2015

1. Introduction

Let us consider the Cauchy problem for the double nonlinear degenerate parabolic equation in the domain $Q = \{(t, x) : t > 0, x \in R^N\}$:

$$Au \equiv -\frac{\partial u}{\partial t} + \nabla(u^{m-1} |\nabla u^k|^{p-2} \nabla u^l) - \operatorname{div}(v(t)u) + \gamma(t)u^\beta = 0 \quad (1.1)$$

$$u|_{t=0} = u_0(x) \geq 0, \quad x \in R^N, \quad (1.2)$$

where β, p, m, l, k are the numerical parameters, $\nabla(\cdot) = \operatorname{grad}_x(\cdot)$, $0 < \gamma(t) \in C(0, \infty)$.

Equation (1.1) is used for the modeling of various physical processes [1-7, 9-14], such as reaction-diffusion phenomena, heat conductivity, polytrophic filtration of gases and liquids in nonlinear media with source power of the form $\gamma(t)u^\beta$.

A specific property of this equation is its degeneration. In the domain where $u = 0$ or $\nabla u = 0$ Eq. (1.1) degenerates to a first order equation. Therefore, one needs to investigate the weak solution, since in this case, solutions of (1.1) may not exist in the classical sense [1].

The solution of Eq. (1.1) may exhibit interesting features, such as phenomenon of a *finite speed of a propagation of distribution* (FSPD), blow up [1] and localization of solution [1, 4, 7, 9, 10, 12-14, 16, 17]. The FSPD was established first by Zeldovich-Kompaneets [1, 7], who constructed an exact self-similar solution for the following problem:

$$\begin{aligned} \frac{\partial u}{\partial t} &= \operatorname{div}(u^{m-1} |\nabla u|^{p-2} \nabla u), \\ u(0, x) &= P\delta(x) \geq 0, \quad x \in R^N \end{aligned} \quad (1.3)$$

where $\delta(x)$ is Dirac's delta function with the property of FSPD:

$$u(t, x) \equiv 0, \quad |x| \geq l(t), \quad 0 < l(t) \in C(0, \infty), \quad (1.4)$$

and the constant $P > 0$ is defined from condition $\int_{-\infty}^{\infty} u(t, x) dx = P$.

Barenblatt (1952) and Pattle (1958) constructed solution (1.2) ($p = 2$) considering problem (1.3), (1.4) as the problem of a nonlinear diffusion and a problem of gas filtration. For the case $p = 2$, and later for the case $p > 2$ Martinson and Pavlov (see [4] and references) established the localization of solution for problem (1.3), (1.4) by constructing its exact solution.

The qualitative properties of these solutions for different classes and initial data, in the case $p = 2$ or $m = 1$ were investigated by many authors [4-23]. Global and blow up properties of the solution, as well as the numerical aspects for solving of the initial and boundary value problems for the equation (1.1) have also been studied by many authors [1-23].

In the context of applications in physics, it is reasonable to consider the weak solution obeying the condition:

$$0 \leq u(t, x), \quad u^{m-1} |\nabla u|^{p-2} \nabla u^l \in C(Q).$$

Definition 1. We shall call the solution with properties if there exists the continuous function $L(t)$ for $t > 0$ such that $u(t, x) \equiv 0$ and for $|x| \geq L(t)$ the solution with a finite speed of propagation of disturbances.

The surface $|x| = L(t)$ is called a front of disturbance or a free boundary.

Definition 2. The solution of the Eq. (1.1) with properties $u(x, t) \equiv 0$ for $|x| \geq L(t) < \infty$, $t > 0$ is called the localized solution.

Definition 3. The solution, $u(x, t)$ is called a weak solution of the problem (1.1), (1.2) in Q , if $u(x, t) \geq 0$ almost everywhere for $(x, t) \in Q$, $0 \leq u$, $u^{m-1} |\nabla u^k|^{p-2} \nabla u^l \in C(Q)$.

Then, the function $u(x, t)$ satisfies the integral identity:

$$\int_0^t \int_{\Omega} [-u\eta_t + u^{m-1} |\nabla u^k|^{p-2} \nabla u^l \nabla \eta] dxdt - \gamma(t) u^\beta \eta dxdt + \int_{\Omega} u_0(x) \eta dx = 0, \quad \Omega \in R^N, \quad (1.5)$$

for any finite function $\eta(x, t) \in C_0^1(Q)$.

We note that the self-similar solution plays an important role in the study of qualitative properties for the solutions of the problem (1.1), (1.2). The self-similar analysis of the solution allows one to explore novel nonlinear effects in physics. In this work, we develop a method for constructing self-similar and approximately self-similar nonlinear reaction-diffusion equations and the method of nonlinear splitting (decomposition) and the method of standard equation [7] for their numerical solutions. Using these approaches, the numerical computations, visualization of solutions in animation form for one and two dimensional cases can be done. The numerical analysis of the solution presented is based on the use of Newton's linearization and Picard methods.

2. Method of nonlinear splitting

Our task is to solve the problem given by Eqs. (1.1), (1.2) using nonlinear splitting method.

We search for the solution of the equation (1.1) in the form:

$$u(t, x) = \bar{u}(t)w(\tau, \xi), \quad \xi = x - \int_0^t v(y)dy, \quad (2.1)$$

where the function $\bar{u}(t)$ is the solution of the equation:

$$\frac{d\bar{u}}{dt} = -\gamma(t)\bar{u}^\beta \quad ,$$

and $w(\tau, x)$ is the solution of the equation (1.1) without lower member.

Substituting Eq. (2.1) into (1.1), we obtain:

$$\frac{\partial w}{\partial \tau} = \nabla \left(w^{m-1} |\nabla w^k|^{p-2} \nabla w^l \right) + \gamma(t)\bar{u}^{\beta-(k(p-2)+m+l-1)}(w + w^\beta) \quad , \quad (2.2)$$

where $\tau(t) = \int [\bar{u}(t)]^{k(p-2)+m+l-2} dt$.

The main term in Eq. (2.2) has the self-similar solution of the kind:

$$w(\tau, x) = f(\eta), \quad \eta = |\xi| / [\tau(t)]^{\frac{1}{p}} \quad . \quad (2.3)$$

Substituting Eq.(2.3) into (2.2), we have the following approximately self-similar equation:

$$\eta^{1-N} \frac{d}{d\eta} \left(\eta^{N-1} f^{m-1} \left| \frac{df^k}{d\eta} \right|^{p-2} \frac{df^l}{d\eta} \right) + \frac{\eta}{p} \frac{df}{d\eta} + \gamma(t)\tau(t)\bar{u}^{\beta-(p+m+l-3)} (f + f^\beta) = 0. \quad (2.4)$$

Let $\gamma(t) = (T + t)^\sigma$ where σ is constant. Then,

$$\tau(t) = \frac{1}{p_1} (T + t)^{p_1}, \text{ if } p_1 > 0,$$

$$\tau(t) = \ln(T + t), \text{ if } p_1 = 0,$$

$$\text{with } p_1 = 1 - (\sigma + 1)(k(p - 2) + m + l - 2)/(\beta - 1).$$

Therefore, Eq. (2.4) becomes self-similar:

$$\eta^{1-N} \frac{d}{d\eta} \left(\eta^{N-1} f^{m-1} \left| \frac{df^k}{d\eta} \right|^{p-2} \frac{df^l}{d\eta} \right) + \frac{\eta}{p} \frac{df}{d\eta} + \frac{\sigma + 1}{\beta - 1 - (\sigma + 1)(k(p - 2) + m + l - 2)} (f + f^\beta) = 0. \quad (2.5)$$

Different properties of solutions of Eq.(2.6) in particular cases, when $\sigma = 0, p=2, m=k=l=1, \sigma = 0, m=k=l=1$ and for other particular numerical parameter values, have been studied by many authors (see, e.g. [1, 6-17]).

The case below,

$$\beta = \beta_c = 1 + (\sigma + 1)(k(p - 2) + m + l - 2)$$

is a singular case. For the case $\sigma = 0, k = l = 1$, the properties of the positive solutions of the problem (1.1), (1.2) were studied by I. Combi [26].

3. Global solvability and non-solvability of the Fujita-Samarskii type

Let

$$z_+(t, x) = \bar{u}(t)\bar{f}(\eta), \quad \bar{f}(\eta) = \left(a - b\eta^{p/(p-1)} \right)_+^{\frac{p-1}{q}},$$

where

$$q = k(p - 2) + m + l - 2, \quad b = [k(p - 2) + m + l - 2] \left(\frac{1}{p} \right)^{p/(p-1)}.$$

Theorem 1. Let us consider the following conditions: $u_0(x) \leq z_+(0, x), x \in R^N, \beta > k(p - 2) + m + l - 1 + N/p$. Then, there exists a global solution $u(t, x)$ for the Cauchy problem (1.1), (1.2) for a small initial data with the following estimate:

$$u(t, x) \leq z_+(t, x)$$

in Q and for the free boundary the estimate:

$$\sum_{i=1}^N (x_i - \int_0^t v_i(t) dt)^2 \leq (a/b)^{(p-1)/p} \tau^{1/p},$$

holds.

Corollary (generalization of the Fujita- Samarskii theorem).

Let

$$u_0(x) \leq z_+(0, x), \quad x \in R^N, \quad \beta > (1 + \sigma)(k(p - 2) + m + l - 2) + \frac{p}{N},$$

$$a^{\frac{(p-1)(\beta-1)}{k(p-2)+m+l-2}} < \frac{N}{p} - \frac{1}{\beta - (1 + \sigma)(k(p - 2) + m + l - 2)}.$$

Then for solution of the problem (1.1), (1.2) in Q the estimate:

$$u(t, x) \leq z_+(t, x)$$

holds true.

These results, with $l=m=1, p=2$ in Eq.(1) have been proven in the Refs.[2, 3], and the case $\sigma = 0, p = 2, l = m = k = 1$ has been treated by Samarskii A.A., Kurduomov S.P., Galaktionov V. A., Mikhaylov A. P., while the case $\sigma = 0, l = m = k = 1$ was studied by Galaktionov V.A. [1].

Proofs of these theorems and other propositions of the solution of problem (1.1), (1.2) are based on both the decomposition and comparison theorem method [1] as well as the use of function $\bar{f}(\eta)$ defined as the classical solution of equation:

$$\eta^{1-N} \frac{d}{d\eta} \left(\eta^{N-1} f^{m-1} \left| \frac{df^k}{d\eta} \right|^{p-2} \frac{df^l}{d\eta} \right) + \frac{\eta}{p} \frac{df}{d\eta} + \frac{N}{p} f = 0,$$

on the domain $|\eta| < \left(\frac{a}{b}\right)^{\frac{p-1}{p}}$.

4. Critical case

The method of nonlinear splitting gives the explanation of the meaning of so-called "critical case":

$$\gamma(t)\tau(t)[\bar{u}(t)]^{\beta-(p+m-2)} = N/p, \quad t > 0.$$

For example, if $\gamma(t) = (T + t)^\sigma, \sigma > -1$, then the critical value of β is given as:

$$\beta = \beta_* = 1 + (\sigma + 1)(k(p - 2) + m + l - 2) + p/N$$

and the doubly critical case is

$$\beta = \beta_* = 1 + (\sigma + 1)(p/N).$$

This result for $m = k = l = 1$ earlier was proved by Galaktionov V. A., Vazquez J.L [1, 8, 10].

5. Mutual reaction-diffusion case

We use self-similar analysis by constructing the exact solution the FSPD property and localization of weak solution from the class $0 \leq u, v, v^{m_1-1} |\nabla u^k|^{p-2} \nabla u^l \in C(Q), u^{m_2-1} |\nabla v^k|^{p-2} \nabla v^l \in C(Q)$ solution of double nonlinear system in Q

$$\begin{aligned} \frac{\partial u}{\partial t} &= \operatorname{div} \left(v^{m_1-1} |\nabla u^k|^{p-2} \nabla u^l \right) - \operatorname{div}(c(t)u) - \gamma_1(t)u, \\ \frac{\partial v}{\partial t} &= \operatorname{div} \left(u^{m_2-1} |\nabla v^k|^{p-2} \nabla v^l \right) - \operatorname{div}(c(t)v) - \gamma_2(t)v \end{aligned} \tag{5.1}$$

$$u(0, x) = u_0(x) \geq 0, \quad v(0, x) = v_0(x) \geq 0, \quad x \in R^N, \tag{5.2}$$

where $\beta_1, \beta_2, p, m_i, k, l, (i = 1, 2)$ are given numerical parameters, $\nabla(\cdot) = \operatorname{grad}_x(\cdot)$. System is degenerating. Therefore we study a weak solution in above mentioned class. Using the transformation:

$$\begin{aligned} u(x, t) &= (T + \tau(t))^{-\alpha_1} f(\xi), \quad v(x, t) = (T + \tau(t))^{-\alpha_2} \psi(\xi), \\ \xi &= |\eta| / [\tau(t)]^{1/p}, \quad \eta = \int_0^t c(y) dy - x \end{aligned}$$

where

$$\tau(t) = \int_0^t \exp\left(-n_1 \int_0^z \gamma_2(y) dy\right) dz = \int_0^t \exp\left(-n_2 \int_0^z \gamma_2(y) dy\right) dz$$

for the functions $f(\xi), \psi(\xi)$ we have the degenerating self-similar system:

$$\begin{aligned} \xi^{1-N} \frac{d}{d\xi} \left(\xi^{N-1} \psi^{m_1-1} \left| \frac{df^k}{d\xi} \right|^{p-2} \frac{df^l}{d\xi} \right) + \frac{\xi}{p} \frac{df}{d\xi} + b_1 f &= 0 \\ \xi^{1-N} \frac{d}{d\xi} \left(\xi^{N-1} f^{m_2-1} \left| \frac{d\psi^k}{d\xi} \right|^{p-2} \frac{d\psi^l}{d\xi} \right) + \frac{\xi}{p} \frac{d\psi}{d\xi} + b_2 \psi &= 0 \end{aligned} \tag{5.3}$$

with

$$\begin{aligned} b_1 &= \alpha_1 / [1 - \alpha_2(m_1 - 1) - k(p - 2) + l - 1] \alpha_1, \\ b_2 &= \alpha_2 / [1 - (m_2 - 1) \alpha_1 - (k(p - 2) + l - 1) \alpha_2]. \end{aligned}$$

By constructing the following solution of Zeldovich-Barenblatt [1] type:

$$\begin{aligned} u(x, t) &= (T + \tau(t))^{-\alpha_1} \bar{f}(\xi), \\ v(x, t) &= (T + \tau(t))^{-\alpha_2} \bar{\psi}(\xi), \quad \xi = |\eta| / [\tau(t)]^{1/p}, \end{aligned} \tag{5.4}$$

where

$$\begin{aligned} \bar{f}(\xi) &= (a - \xi^\gamma)_+^{\gamma_1}, \quad \bar{\psi}(\xi) = (a - \xi^\gamma)_+^{\gamma_2}, \\ \gamma_1 &= \frac{(p-1)(k(p-2) + l - m_1)}{q}, \quad \gamma_2 = \frac{(p-1)(k(p-2) + l - m_2)}{q}, \\ \gamma &= p/(p-1), \quad q = k(p-2) + l - 1 - (m_1 - 1)(m_2 - 1), \quad \alpha_1 = \frac{n_2}{n_1} \alpha_2, \\ \alpha_2 &= \frac{n_2}{n_2(p + n_2 N) + (p - (n_1(m_1 - 1))) N}. \end{aligned}$$

And using the self-similar analysis and comparison principle the following condition of a localization of a weak solution has proved the following:

$$\int_0^t (\exp(-n_1 \int_0^\eta \gamma(y)dy)d\eta < \infty, \forall t > 0, n_1 = k(p-2) + l + m_1 - 2 > 0, \int_0^t c(y)dy < \infty$$

$$\int_0^t (\exp(-n_2 \int_0^\eta \gamma(y)dy)d\eta < \infty, \forall t > 0, n_2 = k(p-2) + l + m_2 - 2 > 0$$

$$\tau(t) = \int_0^t (\exp(-n_1 \int_0^\eta \gamma(y)dy)d\eta = \int_0^t (\exp(-n_2 \int_0^\eta \gamma(y)dy)d\eta.$$

Thus, the following weak solution with a localization property is found:

Theorem 2. We assume $\gamma_1 > 0, \gamma_2 > 0$. Then, the system (5.3) at $y \rightarrow \infty$ ($y = -\ln(a - \xi^{p/(p-1)})$) has an asymptotic:

$$f(\xi) = A_1 \bar{f}(\xi)(1 + o(1)), \psi(\xi) = A_2 \bar{\psi}(\xi)(1 + o(1)),$$

where the coefficients $A_i > 0, i = 1, 2$ are the solutions to the system of nonlinear algebraic equation:

$$A_1^{k(p-2)+m+l-2} A_2^{m_1-1} = c_1, c_1 = \frac{1}{p(\gamma\gamma_1)^{p-1}},$$

$$A_1^{m_2-1} A_2^{k(p-2)+m+l-2} = c_2, c_2 = \frac{1}{p(\gamma\gamma_2)^{p-1}}.$$

We also established the asymptotics of self-similar system in the fast diffusion case $\gamma_1 < 0, \gamma_2 < 0$, and in the special case $q = 0$. An asymptotic analysis of a self-similar system (5.3) also considered.

6. Connection with a problem of the Kolmogorov-Fisher type biological population problem

Fisher, Kolmogorov, Piskunov and Petrovski studied [27, 30, 33] wave type solutions of the problem of the biological population described by the following mathematical model:

$$Au \equiv -\frac{\partial u}{\partial t} + \nabla(Du^{m-1} |\nabla u^k|^{p-2} \nabla u^l) + k_1 u(1 - u^\beta) = 0 \tag{6.1}$$

$$u|_{t=0} = u_0(x) \geq 0, \quad x \in R^N. \tag{6.2}$$

In the case when in (6.1) $k=m=l=1, p=2$. The numerical parameters $k, m, l \geq 1, p \geq 2$ for the velocity of wave type solution the estimate $c \geq 2(kD)^{1/2}$ was proved.

We notice that the following holds after the transformation:

$$u(t, x) = e^{k_1 t} w(\tau(t), x), \quad \tau(t) = \int_0^t e^{k_1(p-2)+m+l-2)y} dy.$$

Then, Eq. (6.1) can be rewritten as:

$$\frac{\partial w}{\partial \tau} = \nabla(Dw^{m-1} |\nabla w^k|^{p-2} \nabla w^l) - \gamma(\tau)w^\beta.$$

Thus, we reduced Eq.(6.1) into a form where, instead of the source, we have an absorption. Therefore, applying above method, one can use the self-similar analysis of the solutions to establish the novel nonlinear physical effects too [7].

One can show that for the problem (6.1)-(6.2) in the critical case $k(p-2)+l+m-2 = 0$ the speed c of the wave distribution has the following estimate $\frac{d(|x|)}{dt} = c \geq 2(Dk_1)^{1/p}t^{(2/p)-1}$ with depth of wave distribution for $t \sim \infty$.

$$(|x(t)| \sim p(k_1 D)^{1/p} t^{2/p} (1 + o(1)))$$

Since $u(x, t) = (T + t)^{-N/p} e^{k_1 t - (\xi/p)^p}$, $\xi = |x(t)|/(T + t)^{1/p}$ is a solution of a main part of the equation (6.2).

7. Results of the numerical experiments and visualization of the solutions

In the numerical solution for the above problem, the equation was approximated on a grid under the implicit circuit of variable directions (for a multidimensional case) in combination with the balance method. Iterative processes were constructed using Picard and Newton methods.

The results of numerical experiments show that the listed iterative methods are effective for the solution of nonlinear problems and leads to nonlinear effects if we will use as an initial approximation the solutions for self-similar equations constructed by nonlinear splitting and standard equation methods [7, 22, 23]. As was expected, for achievement of identical accuracy, the Newton method requires a smaller number of iterations than that of Picard's method or the special method, primarily due to the successful choice of an initial approximation. We observe that in each considered case, Newton's method has the best convergence due to good initial approximation.

The results of numerical experiments for the problem (1.1), (1.2) in the two-dimensional case are presented in the below table. For numerical solution of the problem, the method of the variable directions were applied.

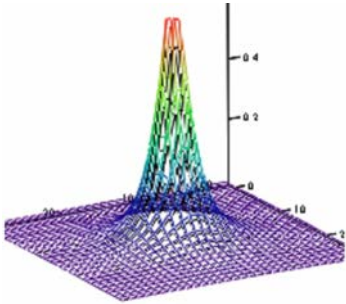
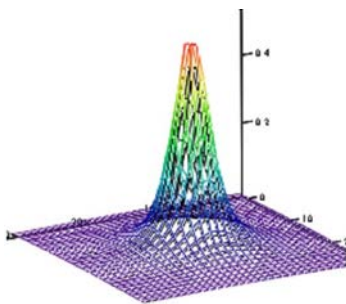
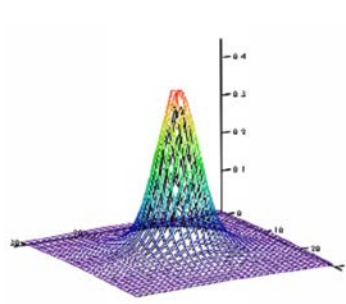
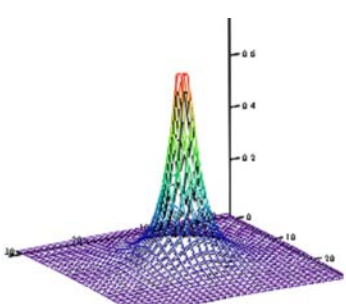
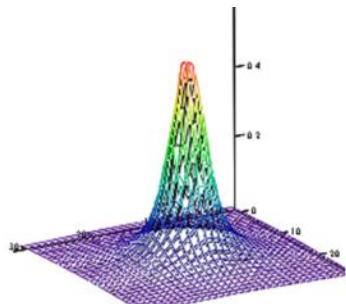
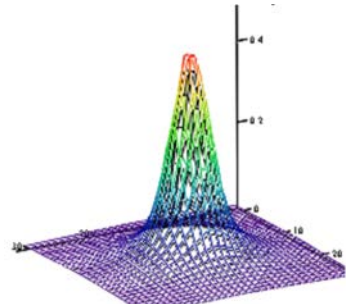
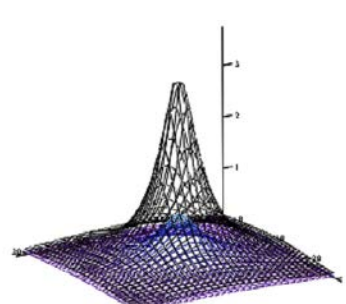
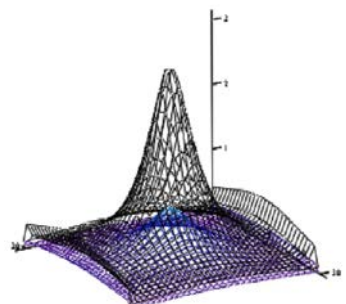
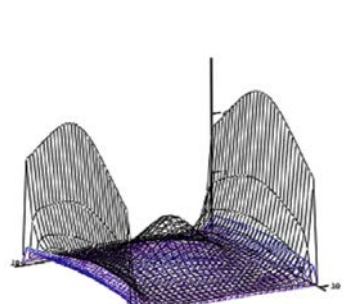
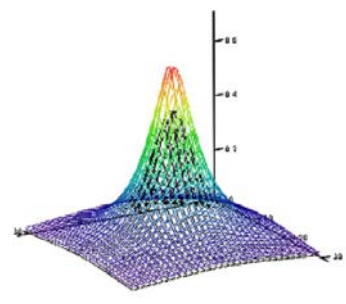
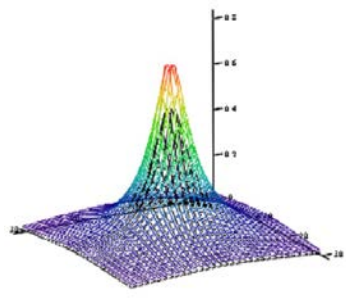
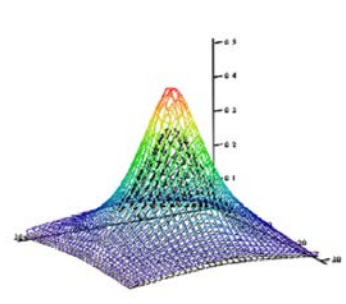
The figures show that results of the numerical experiment gives the effect of a finite speed of a perturbation of solution, and localization of solution depending on the value of numerical parameters. The computational experiment were carried out for a slowly and a quick diffusion cases.

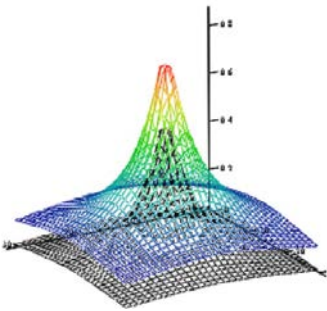
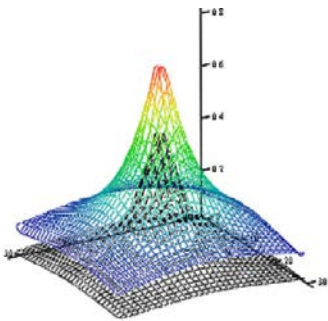
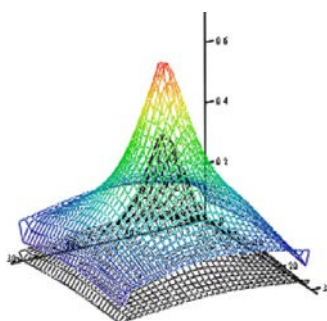
8. Conclusion

Using the self-similar approach, the localization of a solution for the equation with double nonlinearity was established. The influence of convective transfer to the process under consideration was studied. The significant role of the critical exponent was shown for the existing global and blow up solutions to the Cauchy problem for one equation with double nonlinearity with a convective transfer and a mutual (cross) system of parabolic equations. The appropriate initial approximation for the iteration process was suggested. The numerical computations, visualization of solutions in animation form were also discussed.

Acknowledgments

This work is supported by the grant of (Ref. Nr. A-5-44, 2015) of the Ministry of Higher Education of the Republic of Uzbekistan.

$t = 1$	$t = 10$	$t = 40$
		
$m_1 = 0.7, m_2 = 0.7, p = 3.3, k = l = 1, eps = 10^{-3}, \gamma_1 = 2.3 > 0, \gamma_2 = 2.3 > 0.$		
		
$m_1 = 0.2, m_2 = 0.2, p = 3.8, k = l = 1, eps = 10^{-3}, \gamma_1 = 2.8 > 0, \gamma_2 = 2.8 > 0.$		
		
$m_1 = 0.2, m_2 = 0.7, p = 2.1, k = l = 1, eps = 10^{-3}, \gamma_1 = -4.304 < 0, \gamma_2 = -1.913 < 0.$		
		
$m_1 = 1.4, m_2 = 1.4, p = 2.5, k = l = 1, eps = 10^{-3}, \gamma_1 = 1.667 > 0, \gamma_2 = 1.667 > 0.$		

$t = 1$	$t = 10$	$t = 40$
		
$m_1 = 0.2$, $m_2 = 0.7$, $p = 3$, $k = l = 1$, $eps = 10^{-3}$, $\gamma_1 = 4,737 > 0$, $\gamma_2 = 3,421 > 0$.		

References

- [1] Samarskii A.A., Galaktionov V.A., Kurduomov S.P., Mikhajlov A.P. *Blow-up in quasilinear parabolic equations*. Berlin, 4, Walter de Grueter, 1995, p.535.
- [2] Fujita H. On the blowing up of solutions to the Cauchy problem for $u_t = \Delta u + u^{1+\alpha}$, *J. Fac. Sci. Univ. Tokyo Sect. I* **13**, 1966, P. 109–124.
- [3] Hayakawa K. On nonexistence of global sol bal solutions of some semi linear parabolic differential equations, *Proc. Japan Acad. Ser. A Math. Sci.*, 1973, **49**, P. 503–505.
- [4] Granik I.C. To localization of a temperature perturbation in a nonlinear medium with absorption. *Journal of Comp. Math. Math. Phys.* 1978, **18**(3), P. 770–774.
- [5] Deng K. and Levine H.A. The role of critical exponents in blow-up theorems: The sequel, *J.Math. Anal. Appl.* 2000, **243**, P. 85–126.
- [6] Levine H.A. The role of critical exponents in blow-up theorems, *SIAM Rev.*, 1990, **32**, P. 262–288.
- [7] Aripov M. *Standard Equation's Methods for Solutions to Nonlinear problems* (Monograph), Tashkent, FAN, 1988, 137 p.
- [8] Victor A. Galaktionov and J. L. Vazquez. The problem of blow-up in nonlinear parabolic equations. *Discrete and continuous dynamical systems*, April 2002, **8**(2), P. 399–433.
- [9] Tedeyev A.F. Conditions for the existence and nonexistence of a compact support in time of solutions of the Cauchy problem for quasilinear degenerate parabolic equations. *Siberian Math. Jour.*, 2004, **45**(1), P. 189–200.
- [10] Vázquez J.L. *The porous medium equation. Mathematical theory*. Oxford Mathematical Monographs. The Clarendon Press, Oxford University Press, Oxford, 2007, 430 p.
- [11] Chien-Hong Cho. On the computation of the numerical blow-up time. *Japan Journal of Industrial and Applied Mathematics*, 2013, **30**(2), P. 331–349.
- [12] Pan Zheng, Chunlai Mu. A complete upper estimate on the localization for the degenerate parabolic equation with nonlinear source. *Mathematical methods in the Applied Sciences*. Online publication date: 1-Jan-2014.
- [13] M. Aripov, S. A. Sadullaeva. To properties of solutions to reaction-diffusion equation with double nonlinearity with distributed parameters. *J. Siberian Federal University. Math. Phys.*, 2013, **6**(2), P. 157–167.
- [14] Aripov M. Asymptotes of the Solutions of the Non-Newton Polytrophic Filtration equation. *ZAMM*, 2000, **80**(3), P. 767–768.
- [15] Martynenko A.V. and A.F. Tedeev. The Cauchy problem for a quasilinear parabolic equation with a source and inhomogeneous density, *Comput. Math. Math. Phys.*, 2007, **47**(2), P. 238–248.
- [16] Martynenko A.V. and A. F. Tedeev, On the behavior of solutions to the Cauchy problem for a degenerate parabolic equation with inhomogeneous density and a source, *Comput. Math. Math. Phys.* 2008, **48**(7), P. 1145–1160.
- [17] Afanas'eva N.V. and Tedeev A.F. Fujita type theorems for quasilinear parabolic equations with initial data slowly decaying to zero. *Sbornik: Math.*, 2004, **195**(1), P. 3–22.

- [18] Escobedo M., Levine H. A. Explosion et existence global pour un system habilitment couple deration direction diffusion. *C. R. Acad. Sci. Ser.1*, 1992, **314**(10), P. 735–739.
- [19] Chien-Hong Cho. On the computation of the numerical blow-up time. *Japan Journal of Industrial and Applied Mathematics*, 2013, **30**(2), P. 331–349.
- [20] Pan Zheng, Chunlai Mu, Iftikhar Ahmed. Cauchy problem for the non-Newtonian polytrophic filtration equation with a localized reaction. *Applicable Analysis* 1–16. Online publication date: 20-Feb-2014.
- [21] Pan Zheng, Chunlai Mu. A complete upper estimate on the localization for the degenerate parabolic equation with nonlinear source. *Mathematical methods in the Applied Sciences*. Online publication date: 1-Jan-2014.
- [22] Aripov M. Approximate Self-similar Approach for Solving of the Quasilinear Parabolic Equation. *Experimentation, Modeling and Computation in Flow Turbulence and Combustion*. Willey&Sons, 1997, **2**, P.9–26.
- [23] Aripov M., Sadullaeva Sh. A. Properties of the solutions of one parabolic equation of non-divergent type. *Proceedings of CAIM*, 2003, **2**, P. 130–136.
- [24] Gilding B. H., Pelletier L. A. On a class of similarity of the porous media equation 2. *J. Math. Anal. And Appl.*, 1977, **57**, P. 522–538.
- [25] Knerr B. F. The behavior of the support of solutions of the equation of nonlinear heat conduction with absorption in one dimension. *Trans. of Amer. Math. Soc.*, 1979, **249**, P. 409–424.
- [26] Kombe I. Double nonlinear parabolic equations with singular lower order term, *Nonlinear Analysis*, 2004, **56**, P. 185–199.
- [27] Kolmogorov A.N., Petrovskii I.G., Piskunov N..S. Investigation of the equation of the diffusion connected to increase of quantity of substance and its application to one biological problem. *Acta the Moscow State University, ser. Mathematics and mechanics*, 1937, **1**, P. 1–25.
- [28] Kurduomov S.P., Kurkina E.S., Telkovskii. Blow up in two componential media. *Mathematical Modeling*, 1989, **5**.
- [29] Aripov M. Self-Similar and Approximately Self-Similar Method to Solving of Problems of Nonlinear Unsteady a Filtration. Proceedings of the 1-st Turkish world mathematics symposium. *Elazig/Turkey*, 1999, P. 239–248.
- [30] Marri Dj. *Nonlinear diffusion equations in biology*. M., Mir, 1983, 397 p.
- [31] Dimova S.N., Kastchiev M.S., Koleva M.G., Vasileva D.P., Numerical analysis of the blow-up regimes of combustion of two-component nonlinear heat-conducting medium. *JVM and MF*, 1995, **35**(3), P. 303–319.
- [32] Aripov M., Muhammadiev J. Asymptotic behavior of automodel solutions for one system of quasilinear equations of parabolic type. Buletin Stiintific-Universitatea din Pitesti, *Seria Matematica si Informatica*, 1999, **3**.
- [33] Holodnyok M., Klich A., Kubichek M., Marec M. *Methods of analysis of dynamical models*. Moscow, Mir, 1991, 365 p.

Intra pseudogap- and superconductivity-pair spin and charge fluctuations and underdome metal-insulator (fermion-boson)-crossover phenomena as keystones of cuprate physics

B. Abdullaev¹, D. B. Abdullaev¹, C.-H. Park², M. M. Musakhanov³

¹Institute of Applied Physics, National University of Uzbekistan, Tashkent 100174, Uzbekistan

²Research Center for Dielectric and Advanced Matter Physics, Department of Physics, Pusan National University, 30 Jangjeon-dong, Geumjeong-gu, Busan 609-735, Korea

³National University of Uzbekistan, Tashkent 100174, Uzbekistan
bakhodir.abdullaev@yandex.ru, cpark@pusan.ac.kr, yousufmm@list.ru

PACS 74.72.-h, 74.20.Mn, 74.25.Fy, 74.25.Bt, 74.25.Jb, 74.25.Ha

DOI 10.17586/2220-8054-2015-6-6-803-824

The most intriguing observation of cuprate experiments is most likely the metal-insulator-crossover (MIC), seen in the underdome region of the temperature-doping phase diagram for copper-oxides under a strong magnetic field, when superconductivity is suppressed. This MIC, which results in such phenomena as heat conductivity downturn, anomalous Lorentz ratio, nonlinear entropy, insulating ground state, nematicity- and stripe-phases and Fermi pockets, reveals the nonconventional dielectric property of the pseudogap-normal phase. Since conventional superconductivity appears from a conducting normal phase, the understanding of how superconductivity arises from an insulating state becomes a fundamental problem and thus the keystone for all of cuprate physics. Recently, in interpreting the physics of visualization in scanning tunneling microscopy (STM) real space nanoregions (NRs), which exhibit an energy gap, we have succeeded in understanding that the minimum size for these NRs provides pseudogap and superconductivity pairs, which are single bosons. In this work, we discuss the intra-particle magnetic spin and charge fluctuations of these bosons, observed recently in hidden magnetic order and STM experiments. We find that all the mentioned MIC phenomena can be obtained in the Coulomb single boson and single fermion two liquid model, which we recently developed, and the MIC is a crossover of sample percolating NRs of single fermions into those of single bosons.

Keywords: high critical temperature superconductivity, cuprate, metal-insulator-crossover, temperature-doping phase diagram, heat conductivity downturn, anomalous Lorentz ratio, nonlinear entropy, insulating ground state, stripe phase, Fermi pocket.

Received: 1 November 2015

1. Introduction

The origin of pseudogap (PG) and high-temperature superconductivity (HTS) phases in copper oxides (cuprates) is one of the most puzzling and challenging problem in condensed matter physics. Despite being almost three decades since their discovery, intensive experimental and theoretical studies have yielded little clear understanding of these phases so far. The experimental studies of HTS and PG in cuprates have provided physicists with numerous interesting and fascinating materials with unconventional properties. Among the

most puzzling and thus far most intriguing is the observation of the metal-insulator-crossover (MIC), seen in the underdome region of a temperature-doping phase diagram in the presence or absence of a strong external magnetic field [1,2]. The MIC, detected after suppression of the HTS by a strong magnetic field, results in a number of different phenomena: heat conductivity downturn and anomalous Lorentz ratio [3,4], nonlinear entropy [5,6], insulating ground state [1,2], dynamic nematicity [7] and static stripe phases [8] and Fermi pockets [8,9]. This reveals the highly unconventional dielectric property of the PG-normal phase of these superconductors. Since superconductivity appears in conventional superconductors from the conducting normal state only, the understanding of how HTS arises from an insulating state becomes a fundamental problem, and thus, the keystone for cuprate physics. This MIC also separates previously applied mechanisms and models for conventional superconductors from the consideration. However, the answer to the question “What quasiparticles do provide the PG and HTS phases?” still remains elusive.

In Ref. [10], we demonstrated that these quasiparticles are PG and HTS pairs. We came to this conclusion when trying to interpret the physics visualized in STM real space PG and HTS nanoregions [11,12], which exhibited an energy gap. In [10], we showed that the minimal size of these nanoregions are real space pairs and furthermore, these pairs are single bosons. We also have a good qualitative understanding of all elements for the temperature-doping phase diagram for copper-oxides. We have shown that the precursor mechanism for HTS is valid, when bulk superconductivity at the critical temperature T_c or at the first critical doping x_{c1} appears as a percolation phase transition for the spatial overlapping of separated PG pairs.

In this work, we discuss the intra particle spin and charge fluctuations of PG and HTS pairs - single bosons, observed recently in hidden magnetic order [13] and STM [14] experiments. We find that all the above-mentioned MIC phenomena might be obtained in the framework of the Coulomb single boson and single fermion two liquid model [10], which naturally emerges from the analysis of the STM experimental data [11,12] and thus draw a conclusion about the single boson nature of the visualized in the STM experimental pairs.

Currently, we realize that the non-Fermi liquid property of these phenomena and thus of copper oxides is related to the mutual single boson and MIC physics. The insulating ground state of cuprates is a result of a gas composed of single bosons. According to the Bogoliubov approach for gas of charged bosons [15], at high gas density, where this approach is valid, the ground state energy consists of components for the Bose-Einstein condensate and a gas of quasi-particles. At high magnetic fields or at lower levels with doping, to the first critical level, for which all MIC phenomena are measured, the Bose-Einstein condensate vanishes and there, only a gas of quasi-particles exists, i.e., a gas of 2D plasmons of singly-charged bosons. However, the latter is insulating, therefore, the insulator is the whole ground state of copper oxides for underdome dopings from the first critical level (x_{c1}) up to the second critical level (x_{c2}). It is worth noting here that typically, the experiment detects the MIC up to the critical value of doping x_c , which, for some cuprates, coincides with the optimal doping, at which the T_c is maximum in the temperature-doping phase diagrams, and for others, with the second critical doping level x_{c2} . For the sake of simplicity, we assume that x_c coincides with x_{c2} .

According to the phenomenological Coulomb single boson and single fermion two liquid model, fermions, which are responsible for the electrical conductivity, emerge in the system at the first critical doping level x_{c1} . They are not active in the sense of contributing to the bulk electrical conductivity in the range between x_{c1} and x_{c2} . Only from the second critical doping level x_{c2} , beyond which the spatial percolation of NRs for fermions occurs,

do these fermions contribute to penetration of charges in entire volume of a sample. From this analysis, we realize that the MIC is the fermion - boson crossover of sample percolating NRs of single fermions into that of single bosons. As it was shown below (see also Ref. [10]), NRs of single fermions start to percolate from x_{c2} while those of single bosons do so from x_{c1} .

The insulating behavior of fermions in the normal phase underdome region of doping results in the insulating property of Fermi pockets, which is a generalization of the insulating Fermi pockets, seen in angle resolved photoemission spectroscopy (ARPES) experiment [9] (for details see Sec. 9). The observed underdome doping evolution of these pockets qualitatively coincides with that of a gas of fermions in the Coulomb two liquid model. These insulating fermions also result in an insulating stripe phase (the smectic phase), seen in the PG phase of some copper oxides [8], when fermion charges, with their collective static electric field, deform the parent compound lattice, consisting of electrically polar atoms.

It is interesting that the spatially intra rare charge density of each single boson (see the size of last one in the table of Sec. 6) allows one to understand the nature of the intra-unit cell nematic order (the dynamic charge fluctuations) for the sample hole density and its evolution with doping, which was recently observed in the STM experiment [14]. This is also the result of the strong ferrielectric crystal field of the parent compound and the decrease of single bosons with doping.

The interesting hidden magnetic order experiment [13] has revealed the existence of objects in the PG phase with zero total spin but with its fluctuations inside. Despite the authors' (Ref. [13]) interpretation of the physical meaning of both spins, by suggesting either a pair of oppositely flowing intra-structural cell loop-currents or staggered spins in the same cell, the role of these objects in cuprate physics was not understood. One could assume that these objects are the PG and HTS pairs (for justification of this assumption see Sec. 7 below), however, the two mentioned mechanisms for explaining the object's spins were unable to provide the large experimental value for the pair energy gap which was observed for cuprates. This shortcoming was improved upon in our research [16, 17], which appeared in publication in the same year as the experiment described in [13] and reproduced the experimental values of the T_c . In these papers, we have succeeded in understanding not only the nature of both object spins, but also predict their evolution with doping. This evolution was successfully observed in further experiments on the hidden magnetic order.

In Sec. 2, we demonstrate the rigorous proof that $2D$ fermions can bosonize. Then, in Sec. 3, the results for the ground-state energy calculations of a charged anyon gas will be given. We apply the difference between the ground state energies of fermions and bosons to derive the single boson doping-temperature phase diagram for cuprates in Sec. 4. In Sec. 5, it will be demonstrated that this difference in the ground state energies yields the microscopic origin of the phenomenological Uemura relation. Sec. 6 will be devoted to the charge and percolation analysis of NRs on the basis of experimental data given in Refs. [11] and [12]. This analysis provides the interpretation for some elements of the phase diagram doping-temperature for $Bi_2Sr_2CaCu_2O_{8+\delta}$. In Sec. 7, we will demonstrate that intra-structural cells, for which the hidden magnetic order has been observed, are NR's, as displayed by the STM experiment [11] and thus single bosons. We also show in this section that intra cell spin fluctuations and an electronic nematicity [14] can naturally be understood within the single boson model. The MIC and insulating ground state, observed in a set of copper oxides, and their possible understanding within the framework of the Coulomb two liquid model is subject of Sec. 8. The origin of Fermi pockets and stripe phases, seen experimentally in some cuprates, is discussed in Sec. 9 for our model. The answer for the interesting question:

“Why is the ground state of YBCO copper oxides in a strong magnetic field an oscillating Fermi Liquid, while for $Bi_2Sr_2CaCu_2O_{8+\delta}$ cuprate, it is insulating?” can be found in the Sec. 10. Sec. 11 will describe the origin of the non-Fermi liquid heat conductivity and the entropy of copper-oxides. We summarize and conclude our paper in Sec. 12.

2. Real Bosonization of 2D Fermions

The 2D topology allows fractional statistics [18], characterized by a continuous parameter ν , having values between 0 (for bosons) and 1 (for fermions). The particles with $0 < \nu < 1$ are generically called anyons [19]. One can apply the last criterion to investigate the properties of the $a - b$ planes of CuO_2 atoms, which play a dominant role in the determination of cuprate physics.

In a manner similar to Ref. [10], we briefly outline the rigorous derivation of the real bosonization of 2D fermions in this section. This can be achieved by exact cancellation of terms in the Hamiltonian arising from fermion (anyon) statistics and a Zeeman interaction of spins $\hbar/2$ of particles with statistical magnetic field [20] produced by vector potential of anyons.

Let us consider the Hamiltonian

$$\hat{H} = \frac{1}{2M} \sum_{k=1}^N \left[\left(\vec{p}_k + \vec{A}_\nu(\vec{r}_k) \right)^2 + M^2 \omega_0^2 |\vec{r}_k|^2 \right] + \frac{1}{2} \sum_{k=1}^N \left[V(\vec{r}_k) + \sum_{j \neq k}^N \frac{e^2}{|\vec{r}_{kj}|} \right] \quad (1)$$

of the gas of N anyons with mass M and charge e , confined in a 2D parabolic well, interacting through Coulomb repulsion potential in the presence of a uniform positive background [21] $V(\vec{r}_k)$. Here, \vec{r}_k and \vec{p}_k represent the position and momentum operators of the k th anyon in 2D space dimension,

$$\vec{A}_\nu(\vec{r}_k) = \hbar\nu \sum_{j \neq k}^N \frac{\vec{e}_z \times \vec{r}_{kj}}{|\vec{r}_{kj}|^2} \quad (2)$$

is the anyon gauge vector potential [22], $\vec{r}_{kj} = \vec{r}_k - \vec{r}_j$, and \vec{e}_z is the unit vector normal to the 2D plane. In the expression for $\vec{A}_\nu(\vec{r}_k)$ and hereafter, we assume that $0 \leq \nu \leq 1$.

In the bosonic representation of anyons we take the system wave function in the form [23]:

$$\Psi(\vec{R}) = \prod_{i \neq j} r_{ij}^\nu \Psi_T(\vec{R}). \quad (3)$$

Here, $\vec{R} = \{\vec{r}_1, \dots, \vec{r}_N\}$ is the configuration space of the N anyons. The product in the right hand side of this equation is the Jastrow-type wave function. It describes the short distance correlations between two particles due to anyonic (fermionic) statistical interaction.

Let us consider first the term in the Hamiltonian \hat{H} , Eq. (1), containing the anyon vector potential $\vec{A}_\nu(\vec{r}_k)$. Substituting $\Psi(\vec{R})$, Eq. (3), into the Schrödinger equation with this Hamiltonian, we obtain an equation $\hat{H}\Psi_T(\vec{R}) = E\Psi_T(\vec{R})$ with the novel Hamiltonian $\tilde{H} = \tilde{H}_1 + \tilde{H}_2$, where:

$$\tilde{H}_1 = \sum_{k=1}^N \left(\frac{-\hbar^2 \Delta_k}{2M} - \frac{\hbar^2 \nu}{M} \sum_{j \neq k} \frac{\vec{r}_{kj} \cdot \vec{\nabla}_k}{|\vec{r}_{kj}|^2} \right) \quad (4)$$

and

$$\tilde{H}_2 = -i \frac{\hbar}{M} \sum_{k=1}^N \left(\vec{A}_\nu(\vec{r}_k) \cdot \vec{\nabla}_k + \nu \sum_{j \neq k} \frac{\vec{A}_\nu(\vec{r}_k) \cdot \vec{r}_{kj}}{|\vec{r}_{kj}|^2} \right). \quad (5)$$

As shown in Ref. [23], the ν interaction Hamiltonian in \tilde{H}_1 , i.e., the second its term, is equivalent to the sum of the two-body potentials (accuracy of this term discussed in [10])

$$\frac{\pi \hbar^2 \nu}{M} \sum_{j \neq k} \delta^{(2)}(\vec{r}_k - \vec{r}_j). \quad (6)$$

Therefore, the Hamiltonian \tilde{H}_1 now reads

$$\tilde{H}_1 = \sum_{k=1}^N \left(\frac{-\hbar^2 \Delta_k}{2M} + \frac{\pi \hbar^2 \nu}{M} \sum_{j \neq k} \delta^{(2)}(\vec{r}_k - \vec{r}_j) \right). \quad (7)$$

Now, we demonstrate the real bosonization of $2D$ fermions for the example of anyons in a parabolic well. To do this, we consider the Zeeman interaction term:

$$\frac{\hbar}{M} \sum_{k=1}^N \hat{s} \cdot \vec{b}_k \quad (8)$$

of spins with the statistical magnetic field [20]

$$\vec{b}_k = -2\pi \hbar \nu \vec{e}_z \sum_{j \neq k} \delta^{(2)}(\vec{r}_k - \vec{r}_j), \quad (9)$$

which can be derived if one calculates $\vec{b}_k = \vec{\nabla} \times \vec{A}_\nu(\vec{r}_k)$ by using Eq. (2).

For $s_z = \hbar/2$, and using the expression, Eq. (9), one obtains the following for the Zeeman term:

$$\frac{\hbar}{M} \sum_{k=1}^N \hat{s} \cdot \vec{b}_k = -\pi \nu \frac{\hbar^2}{M} \sum_{k(j \neq k)} \delta^{(2)}(\vec{r}_k - \vec{r}_j). \quad (10)$$

It is easy to see that the contribution to the energy from the Hamiltonian \tilde{H}_2 is zero. On the other hand, this expression for the Zeeman term, added to Eq. (7), exactly cancels the second term of \tilde{H}_1 , which is responsible for fermion (for $\nu = 1$) and anyon statistics. Since the energy for bosons is lower than that of fermions and anyons, there appears a coupling of spin with statistical magnetic field for every particle or bosonization of $2D$ fermions and anyons. From this, one can conclude that if anyon concept is correct for the description of any $2D$ quantum system, its ground state should be bosonic with $\nu = 0$, while its excited state should be fermionic ($\nu = 1$) or anyonic ($0 < \nu < 1$), depending upon the fixed value for ν .

3. The ground-state energy of charged anyon gas

In Ref. [15], we derived an approximate analytic formula for the ground-state energy of a charged anyon gas. Our approach was based on the harmonically confined two-dimensional ($2D$) Coulomb anyon gas and a regularization procedure for vanishing confinement. To take into account the fractional statistics and Coulomb interaction, we introduced a function, which depends on both the statistical and density parameters (ν and r_s , respectively). We determined this function by fitting our energy to the ground state energies of the classical electron crystal at very large r_s (the $2D$ Wigner crystal), and to the Hartree-Fock (HF)

energy of the spin-polarized 2D electron gas, and the dense 2D Coulomb-Bose gas for very small r_s . The latter was calculated by use of the Bogoliubov approximation. When applied to the boson system, ($\nu = 0$), our results were very close to those obtained recently from Monte Carlo (MC) calculations. For spin-polarized electron systems ($\nu = 1$), our comparison led to a critical judgment concerning the density range, to which the HF approximation and MC simulations apply.

We have found in Ref. [15] the expression for the ground-state energy per particle (in Ry units) in the form

$$\mathcal{E}_0(\nu, r_s) \approx \frac{2f(\nu, r_s)}{r_s^2} \left[\frac{\nu}{2K_X^2} + \frac{K_X^2}{2} - \frac{K}{K_X} \right]. \quad (11)$$

Here,

$$K_X = (K_A + K_B)^{1/2} + [-(K_A + K_B) + 2(K_A^2 - K_A K_B + K_B^2)^{1/2}]^{1/2}, \quad (12)$$

and

$$\begin{aligned} K_A &= \left[K^2/128 + ((\nu/12)^3 + (K^2/128)^2)^{1/2} \right]^{1/3}, \\ K_B &= \left[K^2/128 - ((\nu/12)^3 + (K^2/128)^2)^{1/2} \right]^{1/3}, \end{aligned} \quad (13)$$

with $K = c_{WC} r_s / f^{1/2}(\nu, r_s)$.

For the Bose gas ($\nu = 0$), we obtained from Eq. (11):

$$\mathcal{E}_0(0, r_s) = -\frac{c_{WC}^{2/3} f^{2/3}(0, r_s)}{r_s^{4/3}}. \quad (14)$$

We found for small r_s that $f(0, r_s) \approx c_{BG}^{3/2} r_s / c_{WC}$, which matched the ground-state energy of Coulomb Bose gas calculated in Ref. [15] using the Bogoliubov approximation with $c_{BG} = 1.29355$. For large r_s , the ground-state energy does not depend on statistics and equals the energy of the classical 2D Wigner crystal [24], $E_{WC} = -2.2122/r_s$. This matches with Eq. (14) if at low densities $f(0, r_s) \approx r_s^{1/2}$ with $c_{WC}^{2/3} = 2.2122$. For large r_s , we obtained:

$$\mathcal{E}_0(\nu, r_s \rightarrow \infty) = \frac{c_{WC}^{2/3} f^{2/3}(\nu, r_s)}{r_s^{4/3}} \left(-1 + \frac{7\nu f^{2/3}(\nu, r_s)}{3c_{WC}^{4/3} r_s^{4/3}} \right). \quad (15)$$

For an arbitrary r_s , the interpolating functional form is:

$$\begin{aligned} f(\nu, r_s) &\approx \nu^{1/2} c_0(r_s) e^{-5r_s} \\ &+ \frac{c_{BG}^{3/2} r_s / c_{WC}}{1 + c_1(r_s) c_{BG}^{3/2} r_s^{1/2} / c_{WC}} + \frac{0.2c_1(r_s) r_s^2 \text{Ln}(r_s)}{1 + r_s^2} \end{aligned} \quad (16)$$

with $c_0(r_s) = 1 + 6.9943r_s + 22.4717r_s^2$ and $c_1(r_s) = 1 - e^{-r_s}$ satisfying all constraints for the $f(\nu, r_s)$ function (see Ref. [15]) and, in addition, yields in the fermion case ($\nu = 1$) for the ground-state energy per particle the following HF result [25]:

$$E_{HF} = \frac{2}{r_s^2} - \frac{16}{3\pi r_s}. \quad (17)$$

In Fig. 1, we show the results for the ground-state energy per particle on the large scale $1.0 \leq r_s \leq 15.0$. The upper four curves refer in descending order to the following fermion cases ($\nu = 1$): HF energies for spin-polarized electrons from Ref. [25] (open triangles); interpolation by Padè approximant MC data from Ref. [26] for spin-polarized electrons (crosses); our results from Eq. (11) (on the given scale identical with those of Eq. (15))(plus

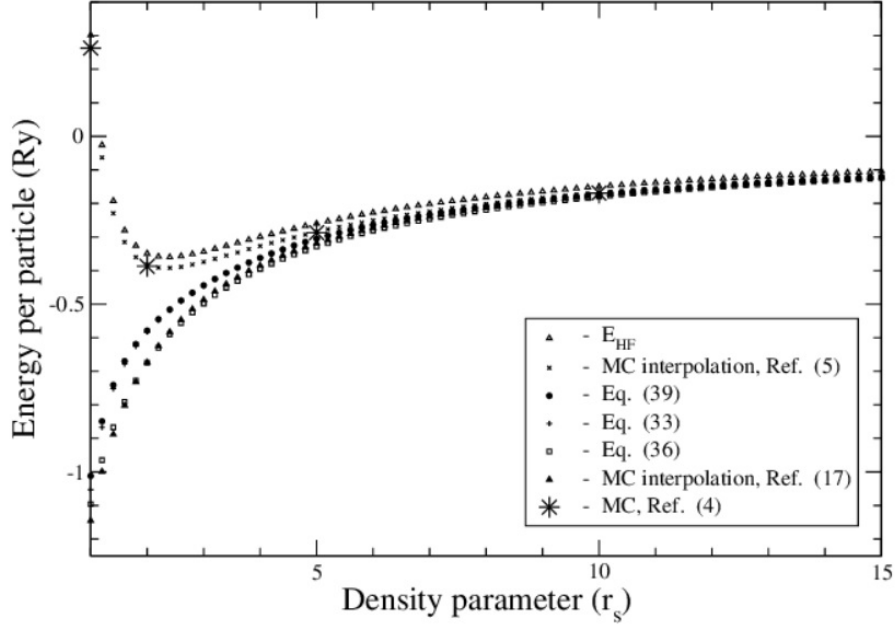


FIG. 1. Ground-state energies per particle vs density parameter r_s values ranging from $1.0 \leq r_s \leq 15.0$ from top to bottom: for fermions ($\nu = 1$) HF approximation (Eq. (17) and Ref. [25], open triangles), MC interpolation data (from Ref. [26] (Ref.[5] in [15])), (crosses), and present results from Eq. (15) (Eq.(39) in [15]) (closed circles) and Eq. (11) (Eq.(33) in [15]) (plus signs), and for bosons ($\nu = 0$) present results from Eq. (14) (Eq.(36) in [15]) (open squares) and MC data from Ref. [27] (Ref.[17] in [15]) (closed triangles). MC data of Ref. [28] (Ref.[4] in [15]) for some particular values of r_s are indicated by star symbols

signs); and our results from Eq. (15) for spin-polarized electrons (closed circles). The lower two curves are for charged bosons ($\nu = 0$) and result from MC calculations of Ref. [27] (closed triangles) and from our Eq. (14) (open squares). By star symbols, we indicated the MC data [28] (without interpolation) obtained for some particular r_s values.

4. Single Boson doping-temperature phase diagram

Following Refs. [16,17], one can assume that coupled to anyon magnetic field spins of fermions are fluctuating. Therefore, bosons with effective spins might appear as Fermi particles. However, fermions with different spins are independent [29]. Thus, the spins of bosons interact with each other and do not interact with spins of another fermions if they exist in the system. We introduce a correlation length, inside of which, spins of bosons interact with each other. For temperature $T = 0$ we denote it by ξ_0 . The increase of fluctuations destroys the coupling, and bosons become the anyons or fermions. This occurs when the gain in the energy due to fluctuations of spins of bosons is equal to energy difference between the anyon (or Fermi) and Bose ground states.

For the interaction of boson spins, we introduce the following form:

$$e^{-r_0/\xi_0} \sum_{k=1}^N \hat{s}_{k+\delta} \cdot \hat{s}_k . \quad (18)$$

Here, a factor e^{-r_0/ξ_0} was introduced with r_0 being the mean distance between particles. For screening by magnetic field spins, ξ_0 is assumed to be phenomenological and taken from the experiment.

We establish the explicit form of Eq. (18). The growth of boson spin fluctuations should cancel term, Eq. (8), in the Hamiltonian. Therefore, for a dense Bose gas ($r_0 < \xi_0$), the following should hold: $\hat{s}_{k+\delta} = -\hbar\vec{b}_k/M$.

The Hamiltonian of a bosonized infinite anyon Coulomb gas with spin interaction has the form:

$$\hat{H} = \frac{1}{2M} \sum_{k=1}^N \left[\left(\vec{p}_k + \vec{A}_\nu(\vec{r}_k) \right)^2 + MV(\vec{r}_k) \right] + \frac{1}{2} \sum_{k,j \neq k}^N \frac{e^2}{|\vec{r}_{kj}|} + \frac{\hbar(1 - e^{-r_0/\xi_0})}{M} \sum_{k=1}^N \hat{s}_k \cdot \vec{b}_k. \quad (19)$$

For an anyon Coulomb gas with density parameter $r_s > 2$, where r_s is r_0 in Bohr radius a_B units, the approximate ground state energy per particle is expressed by Eq. (15). In our treatment we consider the bosonized fermions with $\nu = 1$. To become fermions, bosons should overcome the energy difference:

$$\Delta_0^B = \frac{7(1 - e^{-r_s/\xi_0})f^{4/3}(0, r_s)}{3c_{WC}^{2/3}r_s^{8/3}}, \quad (20)$$

i.e., the superconductivity gap. Our approach in [15] corresponds to spinless or fully spin-polarized fermions. Our system is a normal, i.e., non-spin-polarized electron liquid. However, for intermediate values of r_s , in which we have interest, according to Ceperley MC data [26], there is a tiny difference of ground state energies for spin-polarized and non-spin-polarized electrons. Therefore, we can use ground-state energy for spin-polarized fermions.

The Fig. 2 displays the PG boundary energy E_g (Fig. 11 from paper [30]), superconductivity gap energy $\Delta_0 = 4K_B T_c$, which was evaluated using the empirical formula $T_c = T_{c,max}[1 - 82.6(p - 0.16)^2]$ with $T_{c,max} = 95 K$ for $Bi_{2-x}Sr_2CaCu_2O_{8+\delta}$ compound, and energy gap calculated from Eq. (20) as function of doping p . As seen from this figure, our Δ_0^B has the same magnitude as the experimental gap, but is qualitatively different from the generally accepted ‘‘dome’’ like doping-temperature phase diagram. However, it is in accordance with Fig. 10 of paper [30] of Tallon and Loram and their conclusion that PG energy E_g up to $p_c \approx 0.19$ separates the Bose-Einstein condensate into regions, where the densities of Cooper pairs are small and large (weak and strong superconductivity).

For the phase diagram data of electron-doped cuprates, we use Ref. [31] for NCCO ($Nd_{2-x}Ce_xCuO_4$) and Ref. [32] for PCCO ($Pr_{2-x}Ce_xCuO_4$). It was shown there that $E_g/(k_B T^*) \approx 10$ for NCCO and $E_g/(k_B T^*) \approx 11$ for PCCO, therefore, we assume $E_g/(k_B T^*) \approx 10$ for both materials. For the experimental superconductivity gap, we also assume $\Delta_0/(k_B T_c) \approx 10$. Fig. 3 shows the doping p dependence of experimental E_g , $\Delta_0 = 10k_B T_c$ and Δ_0^B calculated from Eq. (20) by using the above spacing constants of a and b for an elementary structural cell. Comparing with Fig. 2, we see similar qualitative and quantitative results. More obvious is the extension of our Δ_0^B to small values of p , while experimental Δ_0 starts with $p = 0.13$. However, the absolute values for both superconductivity gaps of hole- and electron-doped materials are nearly equal.

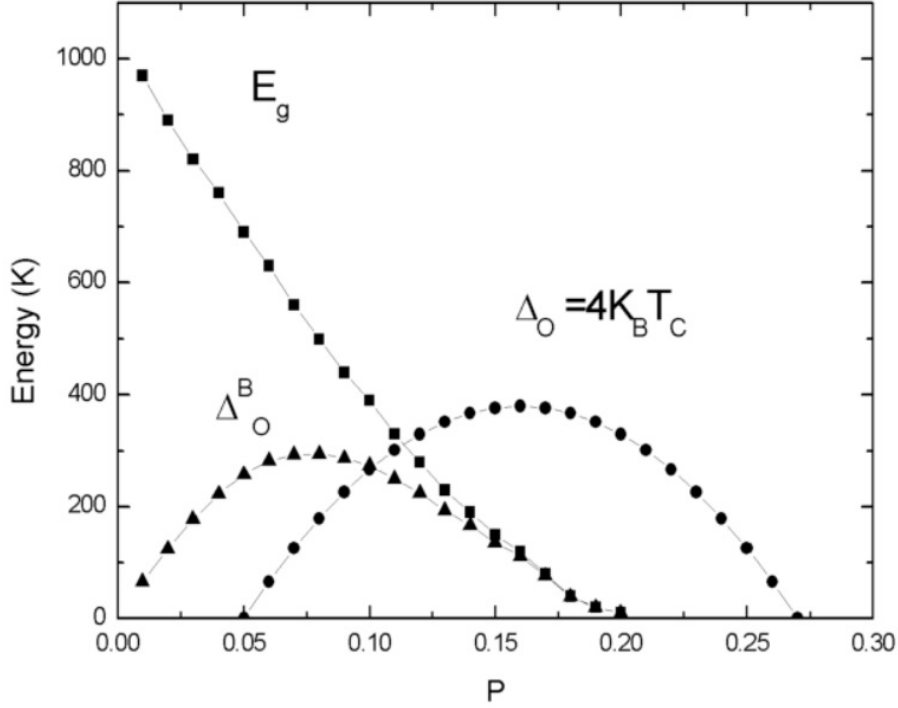


FIG. 2. The experimental PG E_g , superconductivity gap $\Delta_0 = 4K_B T_c$ (experiment for hole-doped *Bi* - 2212 compound), and calculated from formula Eq. (20) one for bosons Δ_0^B energies in Kelvin temperature (K) units as function of concentration of holes p

5. Origin of Uemura Relation

In this section, following Ref. [10], we describe the single boson origin of the phenomenological Uemura relation for $2D$ superconductors.

Currently, it is widely accepted (see Ref. [33]) that the Uemura relation (UR), i.e. the linear dependence of T_c on the concentration of the charge carriers, originally observed in Refs. [34] and [35] for under-doped cuprate, bismuthate, organic, Chevrel-phase and heavy-fermion superconductors, also survives for the extended class of other superconductors and has a fundamentally universal character. An experiment clearly relates the UR with $2D$ geometry of samples. Motivated by this observation, in Ref. [10], we investigated the possible role of the fermion bosonization, which is a result of the topology of $2D$, to the origin of UR.

The experimental doping dependence of r_0 mean distance between two holes, can be approximated by the relationship $r_0 \approx a/x^{1/2}$ (see Fig. 34 in Ref. [36]), where a is the lattice constant in an elementary structural plaquette for the CuO_2 $a-b$ plane of a copper oxide. Since, in [10], the doping value is denoted by the variable x , we keep this notation in this and another section below, which are written on the basis of Ref. [10]. This relationship is derived in Ref. [36] for $La_{2-x}Sr_xCuO_4$ with $a \approx 3.8\text{\AA}$. This lattice constant a is the nearly identical to the other copper oxide compounds, thus it is also valid for investigating $Bi_2Sr_2CaCu_2O_{8+\delta}$. It is worth noting that $b \approx a$ for the lattice constant b for the same structural plaquette.

Applying the relationship $r_0 \approx a/x^{1/2}$, where $a \approx 3.8\text{\AA}$, we estimate the values of r_0 , expressed in Bohr radius a_B unit ($r_s = r_0/a_B$), corresponding to the doping interval

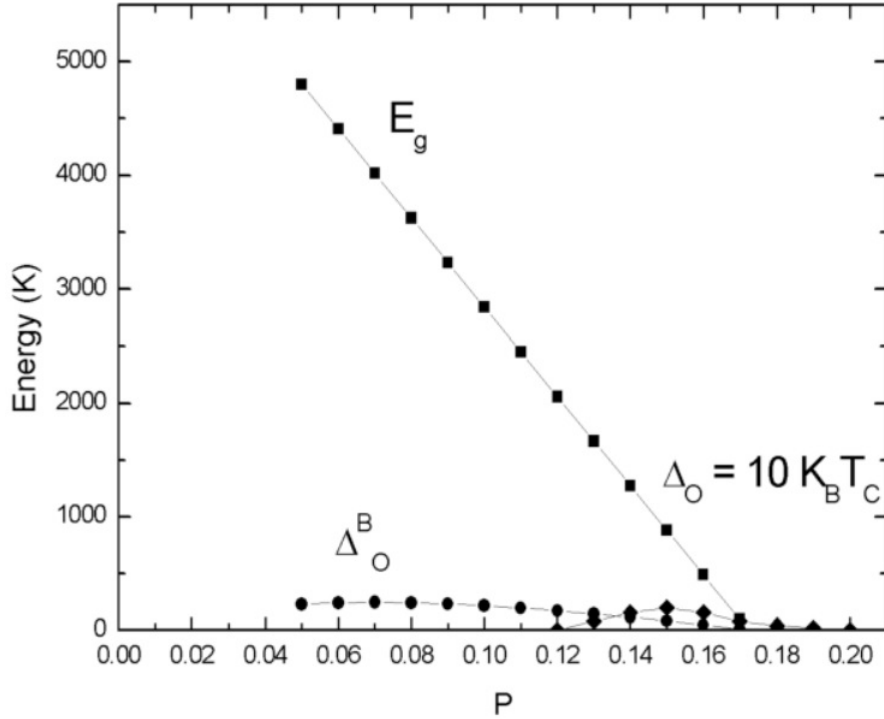


FIG. 3. The experimental PG E_g , superconductivity gap $\Delta_0 = 10K_B T_c$ (experiments for electron-doped NCCO and PCCO compounds), and value calculated from formula Eq. (20) for bosons energies Δ_0^B in Kelvin temperature (K) units as a function of electron concentration, p

$x_{c1} \leq x \leq x_{c2}$, where x_{c1} and x_{c2} are the first and second critical dopings in the doping-temperature phase diagram. When doing so, one sees that $13.12 \leq r_s \leq 32.14$. For this interval of r_s , we obtained the expression, Eq. (15), for the ground state energy per particle of the Coulomb-interacting anyon gas. It is expressed in Ry (Rydberg) energy units, and for large r_s , equals the energy of the classical 2D Wigner crystal [24], $E_{WC} = -c_{WC}^{2/3}/r_s$ with $c_{WC}^{2/3} = 2.2122$.

Taking into account from the previous section that the excited state of the 2D system is fermionic and the ground state is bosonic, one can write the explicit expression for an energy gap between these two states in the following manner:

$$\Delta(r_s) = \mathcal{E}(\nu = 1, r_s) - \mathcal{E}(\nu = 0, r_s) = \frac{7E_{WC}^2}{3c_{WC}^2}. \quad (21)$$

The meaning of this expression is that to become a fermion, the boson should gain the energy $\Delta(r_s)$. Substituting in Eq. (21) the expression for E_{WC} , and introducing the 2D density, $n = 1/(\pi r_0^2)$, one derives:

$$\Delta(n) = \frac{7\pi n a_B^2}{3c_{WC}^{2/3}}. \quad (22)$$

Since the critical temperature T_c is proportional to $\Delta(n)$, one can conclude that the 2D topology driven bosonization of fermions may explain the UR for a variety superconductors, whose physics is quasi - two dimensional.

6. Experiment implied single boson elements of the doping-temperature phase diagram

Recently, Gomes *et al.* [11] have visualized the gap formation in NRs above the critical temperature T_c in the HTS $Bi_2Sr_2CaCu_2O_{8+\delta}$ cuprate. It has been found that, as the temperature lowers, the NRs expanded in the bulk superconducting state consisted of inhomogeneities. The fact that the size of the inhomogeneity [12] is close to the minimum size of the NR [11] leads to a conclusion that the HTS phase is a result of these overlapped NRs. In the present section, we reproduce the main results of Ref. [10], where the charge and percolation regime analysis of NRs was performed and shown that at the first critical doping x_{c1} , when the superconductivity initiates, each NR carries a positive electric charge of one (in units of electron charge), thus we attributed the NR to a single hole boson, and the percolation lines connecting these bosons emerged. At the second critical doping x_{c2} , when superconductivity disappears, our analysis demonstrated that the charge of each NR equals two. The origin of x_{c2} can be understood by introducing additional normal phase hole fermions in NRs, whose concentration appearing above x_{c1} increases smoothly with doping and breaks the boson percolation lines at x_{c2} . The latter resulted in the disappearance of the bulk bosonic properties of the PG region, which explained the upper bound for the existence of vortices in the Nernst effect [37]. Since [11] demonstrated the absence of NRs at the PG boundary, one can conclude that along this boundary, as well as in x_{c2} , all bosons disappear.

The authors of Ref. [11] have visualized the NRs in the PG region of $Bi_2Sr_2CaCu_2O_{8+\delta}$ at fixed hole dopings of $x = 0.12, 0.14, 0.16, 0.19, 0.22$. It has been determined that for $x = 0.16$ and $x = 0.22$, the minimum size of the NRs is $\xi_{coh} \approx 1 - 3$ nm. The estimated minimum size of NRs, ξ_{coh} , is 1.3 nm in the superconducting phase [12] ($T_c = 84K$). Another notable result obtained in Ref. [12] was the observation of spatial localization for the doped charges. The charges were localized in the same area as NRs [12] with the same coherence length ξ_{coh} .

The principal part of our analysis in Ref. [10] has been the doping x dependence of the NR charge $(\xi_{coh}/r_0)^2$. We started with the case of zero temperature. The parameter ξ_{coh}/r_0 contained essential information for our consideration. The factor $(\xi_{coh}/r_0)^2$ reduces to the expression $x(\xi_{coh}/a)^2$, which has a simple physical meaning: it is the total electric charge of $(\xi_{coh}/a)^2$ number of plaquettes, each having a charge x . Conversely, the parameter ξ_{coh}/r_0 describes the average spatial overlapping degree of two or more holes by one NR. If $\xi_{coh}/r_0 > 1$ then all NRs will be in close contact with each other, thus providing bulk superconductivity in the percolation regime.

In Table I, we outline the doping x dependencies for the function $(\xi_{coh}/r_0)^2$ for fixed experimental values $\xi_{coh} = 10\text{\AA}$ (the minimal size of the NR) and $\xi_{coh} \approx 13\text{\AA}$ taken from Ref. [11] and Ref. [12], respectively, and for the function ξ_{coh} , which fits $(\xi_{coh}/r_0)^2$ to $(10\text{\AA}/r_0)^2$ at $x = 0.28$ and for $x = 0.05$ provides $(\xi_{coh}/r_0)^2 \approx 1.0$. Numerical values for the ξ_{coh}/r_0 ratio are also shown in the table.

As is seen in Table I, the charges $(10\text{\AA}/r_0)^2$, $(13\text{\AA}/r_0)^2$, and $(\xi_{coh}/r_0)^2$ vary continuously with the doping x . This is not surprising because they are functions of $r_0(x)$ and $\xi_{coh}(x)$. From the analysis at the first critical doping, $x_{c1} = 0.05$, it follows that the charge $(\xi_{coh}/r_0)^2$ of the visualized NR in Ref. [11] equals +1. Thus, it corresponds to the charge of a single hole. We note that at the critical doping $x_{c1} = 0.05$, the percolation parameter is given by $\xi_{coh}/r_0 = 1.0$. This means the whole sample is entirely covered with mini areas $\xi_{coh}^2 = r_0^2$ contacting each other. It is unexpected that at the second critical doping, $x_{c2} = 0.28$, the charge of the visualized NR takes the value +2. This implies that at $\xi_{coh}^2 = 2r_0^2$, one has a

x	$(10\text{\AA}/r_0)^2$	$(13\text{\AA}/r_0)^2$	$\xi_{coh}(\text{\AA})$	$(\xi_{coh}/r_0)^2$	ξ_{coh}/r_0	N_{ob}
0.28	1.939	3.277	10	1.939	1.393	~ 1
0.22	1.524	2.575	10	1.524	1.235	~ 2
0.16	1.108	1.873	11	1.341	1.158	~ 3
0.14	0.969	1.638	12	1.396	1.182	~ 3
0.10	0.693	1.170	13	1.170	1.082	~ 6
0.05	0.346	0.585	17	1.000	1.000	
0.04	0.277	0.468	18	0.897	0.947	
0.02	0.139	0.234	20	0.554	0.744	

TABLE 1. The doping x dependencies of NR charges. The doping x dependencies for $(10\text{\AA}/r_0)^2$, $(13\text{\AA}/r_0)^2$ at fixed $\xi_{coh} = 10\text{\AA}$ and $\xi_{coh} = 13\text{\AA}$, respectively, for the coherent length ξ_{coh} , the charge $(\xi_{coh}/r_0)^2$ and the percolation parameter ξ_{coh}/r_0 at this ξ_{coh} are presented. The values for the number N_{ob} of bosons surrounding every fermion are shown in the last column.

pair of holes inside the NR and, as a result, the superconductivity disappears completely. For $x_{c2} = 0.28$, we have $\xi_{coh}/r_0 > 1.0$, so that the charge conductivity of the fermions still remains. As we presently understand, the normal state charge conductivity is provided only by percolated fermions-holes and at temperature $T = 0$ from x_{c2} doping, while at $T \neq 0$ by these fermions above the PG temperature boundary, for temperatures between T_c and PG boundary there exists (fermion-boson) MIC.

Notice, that there are no particles in the nature with a fractional charge, except quasi-particles, which can be produced by many-body correlations like in the fractional quantum Hall effect [21]. Hence, the problem having an extra fractional charge present inside the NR has yet to be solved. We are reminded in [11, 12] that the PG-visualized NRs constitute the bulk HTS phase below the critical temperature T_c , and therefore, they are a precursor for that phase. This undoubtedly implies that the NRs represent bosons at least. At $x_{c1} = 0.05$ one has the charge $(\xi_{coh}/r_0)^2 = 1$, so that one may surmise that the NR simply represents a boson localized in a square box ξ_{coh}^2 .

For $x > 0.05$, the charge $(\xi_{coh}/r_0)^2$ has fractional part in addition to that of the +1 (boson) part. We assign the former as the fractional part of a fermion charge. Thus, the total charge $(\xi_{coh}/r_0)^2$ of the NR includes a charge +1 for the boson and the fractional charge for the fermion. However, as mentioned above, the fractional charge cannot exist. Therefore, we take the number N_{ob} of NRs to be equal to the inverse value of the fractional part to form a charge of +1 for the fermion. As a result, we obtain one fermion surrounded by N_{ob} bosons. The values of N_{ob} are outlined in the last column of the Table 1.

The NRs introduced in such a manner allow one to understand clearly the fermion evolution over the following range $0.05 \leq x \leq 0.28$ of doping and to explain the origin of the second critical doping level, $x_{c2} = 0.28$. It is clear, that as x increases, the number of fermions increases inside the HTS phase. This means, that at x_{c2} , when the number of fermions becomes equal to the number of bosons, one has a breaking of the boson percolation lines, and, thus the HTS disappears.

The schematic single hole bosonic phase diagram for $Bi_2Sr_2CaCu_2O_{8+\delta}$ is depicted in the Fig. 4. The colored zones indicate the percentage of the sample that is gapped at a given temperature and doping. The solid lines correspond to the following observed

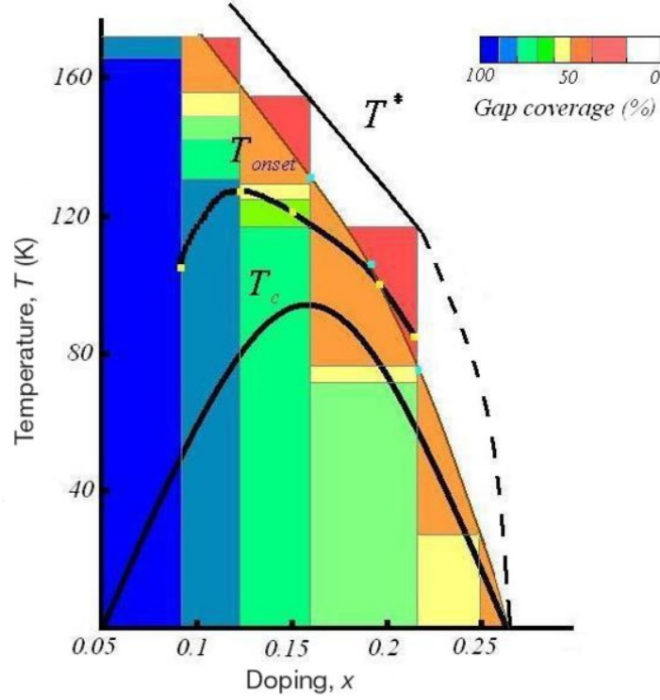


FIG. 4. Schematic single hole bosonic phase diagram for $Bi_2Sr_2CaCu_2O_{8+\delta}$

temperatures: PG boundary T^* and onset temperature T_{onset} for the Nernst effect signals taken from Ref. [37], and the critical temperature T_c from Ref. [11]. The extrapolation for the connection of T^* with the second critical doping, x_{c2} , is depicted by the dashed line. The yellow points correspond to fixed T_{onset} values from Ref. [37], and the blue points represent the temperature data for 50% of the gapped area in the sample from Ref. [11] measured at fixed dopings. The thin brown solid line fits the blue points. The percentage for the gapped doping is calculated using the equation $(1 - 1/(N_{ob} + 1)) \cdot 100\%$ under the assumption that the NRs overlap each other. It is remarkable that the T_{onset} line is substantially located in the brown zones, which means there is no bulk bosonic property above these zones.

The important qualitative issue, which is a result of the experiment performed in [11], will now be discussed. The random positions in real space for the observed pairs totally exclude any mechanism for pair formation. Since they are occasionally positioned in this space, coherent excitations (phonons, magnons or other quasi-particles), which create pairs, are problematic if the system is homogenous. The last observation deduced from the Gomes *et al.* paper, is the fundamental argument for the justification of the single hole nature of the cuprate physics.

Summarizing the physics of the above sections, we are at the stage to formulate the main positions of our Coulomb single boson and single fermion two liquid model. 1. The doping charges, in the form of individual NRs, are embedded in the insulating parent compound of HTS copper oxides. 2. Before the first critical doping level x_{c1} with NR size $\xi_{coh} = 17\text{\AA}$, they are not percolated single bosons. 3. The origin of single bosons is in the anyon bosonization of 2D fermions. 4. At the first critical doping level x_{c1} , percolation of single boson NRs and thus HTS appears; there also appears from x_{c1} doping single fermions, but up to second critical doping x_{c2} their NRs do not percolate, thus, single fermions between x_{c1} and x_{c2} are insulating. 5. The value $x_{c1} = 0.05$ is universal for all copper oxide HTSs, since percolating single boson NRs cover 50% of a 2D sample area (like connecting squares

in a chessboard); the same situation takes place with NRs for fermions at x_{c2} . 6. The normal phase charge conductivity appears from x_{c2} at $T = 0$ or above the PG temperature boundary $T = T^*$, where the percolation of single fermions appears, while for temperatures between T_c and T^* , there exists (fermion-boson) MIC. 7. The spatially rare charge density object, single boson, with NR size between $\xi_{coh} = 17\text{\AA}$ and $\xi_{coh} = 10\text{\AA}$, which correspond to x_{c1} and x_{c2} dopings, has zero total but fluctuating spin inside the NR (this rareness also leads to a fluctuating charge inside the NR). 8. Increasing the bosons' spin fluctuations with doping or temperature results in a transition of bosons into fermions, which occurs at PG T^* or at x_{c2} . 9. At zero external magnetic field, the HTS is result of the Bose-Einstein condensate for single bosons. 10. At high external magnetic fields, the PG insulating ground state is a result of the plasmon gas of these bosons.

7. Hidden magnetic order and electronic nematicity experiments

First observed in $YBa_2Cu_3O_{6+x}$ (Y123), using polarized elastic neutron diffraction [13], the hidden magnetic order has subsequently been found in three other copper oxide families: $HgBa_2CuO_{4+\delta}$ (Hg1201) [38,39], $La_{2-x}Sr_xCuO_4$ (La214) [40] and $Bi_2Sr_2CaCu_2O_{8+\delta}$ (Bi2212) [41] (see for references also [42]). Since the size of detection was a few structural cells, it was called the intra-unit-cell (IUC) hidden magnetic order.

This interesting experiment has revealed the existence of IUC objects in the PG phase with fluctuating spin components inside, which exactly cancel each other, so that the total spin of the every object was zero. Despite the authors of Ref. [13] having interpreted the physics of both, total and intra, spins either by invoking of a pair of oppositely flowing intra structural cell charge loop-currents or of staggered spins in the same cell, the role of these objects in the physics of copper oxides was not understood [43].

This role becomes unambiguously clear, if we connect these objects with the visualization of NR's which exhibit an energy gap in the STM experiment [11]. Since, as NR's, they exist in the PG region and disappear at the PG temperature boundary T^* [13]. There is no doubt that their evolution with temperature will be the same as for NRs. While their evolution with doping (see Refs. [13, 38, 39]) qualitatively coincides with that of NR's, described in [10]. However, minimal size NR's are single bosons, therefore, the IUC hidden magnetic order objects are also single bosons and PG and HTS pairs.

On the other hand, the spatially intra rare charge density of each single boson allows one to understand the nature of the intra unit cell electronic nematicity (the dynamic charge fluctuations) which were recently observed in the STM experiment [14]. The strong ferrielectric crystal field of the parent compound forms an atomic scale charge distribution within an individual NR. It is interesting that this distribution consists of fractional charges, since the charge of NR is one, attached to each atom of parent cuprate, which can be seen in the experiment.

The evolution of the dynamic charge fluctuations with doping resembles that of the IUC hidden magnetic order [7] (Ref. [7] contains a very thorough up-to-date list of references on the subject of IUC spin and charge fluctuations).

8. MIC and insulating ground state

The experimental investigation of lightly underdoped copper oxides, $La_{2-x}Sr_xCuO_4$, La_2CuO_4 , $YBa_2Cu_3O_x$, has revealed the MIC behavior in the $a - b$ plane resistivity at zero magnetic field [1], when the resistivity decreased with lowering temperature and then began to increase from its minimum value.

A similar MIC behavior for this resistivity has been observed for higher (up to critical) doping levels in several classes of HTS cuprates [2]: $La_{2-x}Sr_xCuO_4$, electron doped $Pr_{2-x}Ce_xCuO_4$, $Bi_2Sr_{2-x}La_xCuO_{6+\delta}$, under strong magnetic fields (up to 60 T), when the HTS was suppressed. The temperature-MIC boundary in the temperature-doping phase diagram resembles the temperature-PG boundary dependence.

The insulating ground state is intrinsic and robust, and therefore, belongs to the class which is fundamental for understanding the whole of HTS cuprates-based physics. As we pointed out in the introduction, it may be a result of a gas of single bosons, or more precisely, of a gas of 2D plasmons from singly-charged bosons, which is insulating, when the Bose-Einstein condensate of these bosons vanishes under a strong magnetic field or at lowering and tending of doping to the first critical value.

9. Fermi pockets and stripe phases

Fermi pockets and stripe phases belong to a very relevant and highly controversial subject of the PG cuprate physics. The experimental situation is that Fermi pockets, except for quantum oscillation experiments performed in a strong magnetic field [9], have been detected in an ARPES experiment once in an underdoped PG region with doping $x = 0.1$ and zero magnetic field above T_c in $YBa_2Cu_3O_{6+x}$ (see Fig.2 of Ref. [43]). However, stripe phases (density waves) are not observed in all copper oxides [8]. Nevertheless, Fermi pockets and stripe phases are well established in cuprate-based physics and, probably, the comprehensive description of their state-of-art and critical analysis is made in the second review of Ref. [8].

There is a widely accepted belief that there is a relationship between these two objects and furthermore, through Fermi surface reconstruction, stripe phases induce the formation of Fermi pockets (see reviews [8,43] and references therein). We consider both these objects as experimentally independent ones and try to understand their appearance within our Coulomb two liquid model.

Fermi pockets, as constituents of a Fermi surface, are a signature of fermion statistics. A manifestation of fermions in a parent compound's Brillouin zone starts at low dopings in the form of Fermi arcs [7]. Then, upon evolution with doping, it acquires Fermi pockets, and, finally, after optimal doping, it becomes circle-like, as for a homogenous Fermi gas.

The authors of quantum oscillation experiments, through the measurement of magnetoresistance oscillations at high magnetic fields in the underdome region of the temperature-doping phase diagram, have observed the Fermi liquid-like behavior of conducting quasi-particles and that measured Fermi surface had a form of Fermi pockets. This effect was found for dopings up to the optimal level for the YBCO family of cuprates (see second review of Ref. [8] for references, where there is an indication that the quantum oscillations have also been found in an electron doped cuprate). Unfortunately, this observation, under the mentioned conditions, has not been reproduced by the ARPES experiment.

However, as we pointed out in Sec. 8, for $x = 0.1$ doping and temperatures between T_c and the PG boundary T^* the system is close to the insulating state. Therefore, the Fermi pockets, found by the ARPES experiment, belong to fermions in the insulating state. This finding confirms position 4 of our Coulomb two liquid model (see end of Sec. 6), i.e. that holes-fermions between two critical dopings x_{c1} and x_{c2} are insulating, because of absence of percolation between their NRs. In our description, two limiting values for the Fermi pocket wave vector are approximately determined as $k_{F1} \approx 2\pi/\xi_{coh}(x_{c2})$ and $k_{F2} \approx 2\pi/\xi_{coh}(x)$, where x is a current doping.

As it was shown in Fig. 8 of Ref. [44], in which the schematic evolution of the nematic and stripe charge order phases with doping in underdoped cuprates is displayed, a nematic

charge order, with violation of the system rotational symmetry and small spatial size of this order, dominates at initial dopings of the HTS dome phase diagram. As we discussed in Sec. 7, the size of the nematic order coincides with the NR of single bosons. Therefore, the origin of this order is in the dynamical charge fluctuations inside the mentioned NR.

As is also seen from Fig. 8 of Ref. [44], the stripe phase appears for dopings close to the optimal (critical) one, where NRs for single fermions dominate the NRs for single bosons. This argument allows us to propose that the static charge order (stripe), which violates the parent lattice translational symmetry, is the result of insulating single fermions.

10. Why ground state of YBCO is Fermi liquid oscillating and of Bi-2212 is insulating?

As was mentioned in the previous section, the quantum oscillation experiment clearly indicates that the ground state of copper oxides from the YBCO family, in a strong magnetic field, is Fermi liquid-like, as is the case for conventional superconductors. Conversely, these copper oxides are absent in the list of materials (see section 8 or Ref. [2]), whose ground state is insulating in the same magnetic field. Does this mean that these quantum oscillating and insulating phenomena are the outcome of a single description for cuprates?

It seems, the answer to this question is “no” and it is in the following. The strong magnetic field “excites” a single boson from its ground state, so it occupies the first excited level of the system’s fermion state. Physically, a NR with a single boson occupation transits into a NR with a single fermion one. Therefore, all new formed single fermion NRs may provide percolation paths for the manifestation of the bulk Fermi liquid property, if the value for a critical doping x_c is low, as, for instance, the $x_c = 0.19$ for YBCO HTS compounds. This is the reason why holes-fermions in the quantum oscillation experiment are conducting. However, originally, without a strong magnetic field, they existed in an insulating state.

However, if the value for a critical doping x_c is large, as the $x_c = x_{c2}$ for *Bi-2212*, i.e., $Bi_2Sr_2CaCu_2O_{8+\delta}$ HTS compound, then single fermion NRs may not provide percolation paths for a bulk Fermi liquid conductor and the ground state of *Bi-2212* material in a strong magnetic field is insulating (see Ref. [45]).

11. Non-Fermi liquid heat conductivity and entropy

The puzzling side of the PG normal phase is that in this region some experimental data clearly demonstrate a failure of the Landau Fermi liquid theory (LFLT), which is the basis of the theory for normal metals. Hill et al. [3] reported that the heat conductivity of the electron doped copper-oxide $Pr_{2-x}Ce_xCuO_4$ measured at low temperature (low-T) deviated from the value predicted by the LFLT, i.e., as the temperature decreases, the temperature dependence of the heat conductivity (κ) changes from a normal linear $\kappa \sim T$ behavior into an anomalous $T^{3.6}$ one, which was described by the “downturn” behavior of the heat conductivity. They also reported another important non-Fermi liquid behavior: the Lorentz ratio of the Wiedemann – Franz law (WFL) in the region of the linear T-dependence of κ was significantly larger (1.7 times) than Sommerfeld’s value. These violations were also observed in the $Bi_{2+x}Sr_{2-x}CuO_{6+\delta}$ copper-oxide in the vicinity of the metal-insulator-crossover by Proust *et al.* [4].

The normal state electronic specific heat, c , for superconductors $YBa_2Cu_3O_{6+x}$ and $La_{2-x}Sr_xCuO_4$ above the high- T_c transition temperature T_c was experimentally investigated in [5] and [6], respectively. Due to existence of high- T_c superconductivity, it is impossible to extract information on the low- T dependence of the normal state c . On the other hand, Loram *et al.* [5] showed the T -dependence of the entropy (\mathcal{S}) $\mathcal{S} \sim T^i$ with $i > 1$ for the

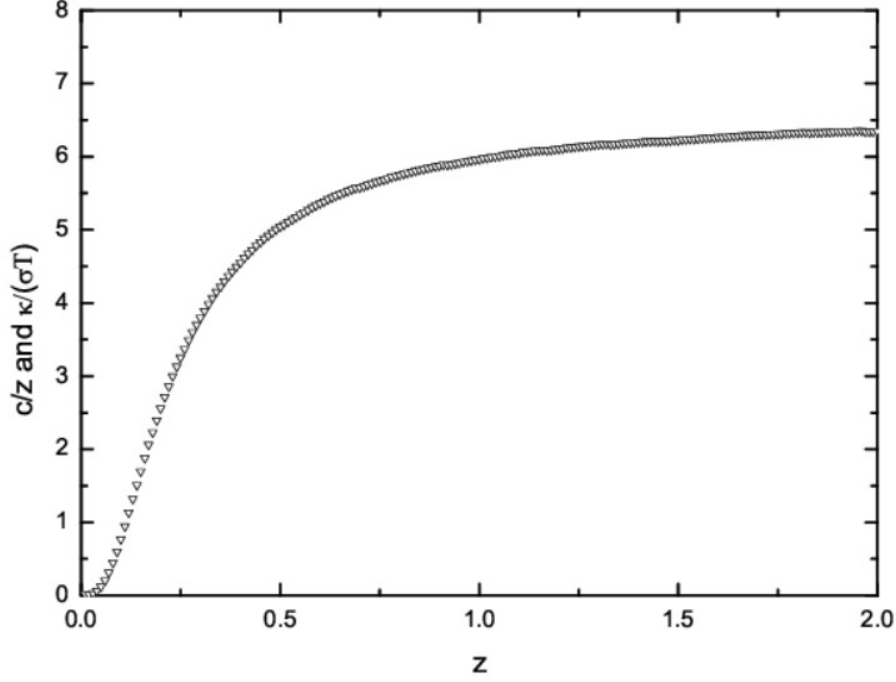


FIG. 5. The specific heat c/z and WFL $\kappa/(\sigma T)$ as function of z , where z is linearly proportional to temperature.

underdoped (insulating) material, which was driven from the measured electronic specific heat, ignoring the superconducting effects, while for the optimal doping compound, $\mathcal{S} \sim T$ was measured.

In Ref. [46], we tried to understand these non-Fermi liquid properties of the low- T heat conductivity, the specific heat and entropy of copper-oxides within a Coulomb two-liquid model, consisting of single boson and fermion holes.

In Fig. 5 we have plotted WFL and specific heat as a function of temperature for compounds investigated experimentally in Refs. [3] and [5,6]. Experiment [3] shows $\kappa \sim T^{3.6}$ for normal state quasiparticles, while our dependence is $\kappa \sim T^4$ and connected with the specific heat dependence $c_1 \sim T^4$ for the Coulomb Bose gas (single bosons).

For the Lorentz ratio of the WFL we have derived in Ref. [46] the formula:

$$L = L_0 \left[\frac{3.106}{t^{1/3}} \left(1 - \frac{t}{t_c} \right) + \frac{t}{t_c} \right], \quad (23)$$

where t and $t_c \approx 0.19$ (see [30]) are dopings, $L_0 = (\pi^2/3)(k_B/e)^2$ is the Fermi liquid Sommerfeld's value of the Lorentz ratio and the first term in square brackets originated from the single boson WFL $\kappa/(\sigma T) = 3.106 \cdot L_0/t^{1/3}$. In Fig. 6, we displayed L/L_0 as function of t in comparison with its values measured for different cuprates. The good agreement for L/L_0 with experimental data is obvious.

In Ref. [46], we also obtained the expression of the normal state entropy \mathcal{S} :

$$\mathcal{S} = \frac{c_1}{4} \left(1 - \frac{T}{T^*} \right) + c_F \frac{T}{T^*}, \quad (24)$$

where, c_F is the heat capacity for a gas of fermions and T^* is the PG boundary temperature. The entropy, as function of temperature at various dopings t , is depicted in Fig. 7. Comparing the calculated dependencies for \mathcal{S} with the experimental ones from Ref. [5], we

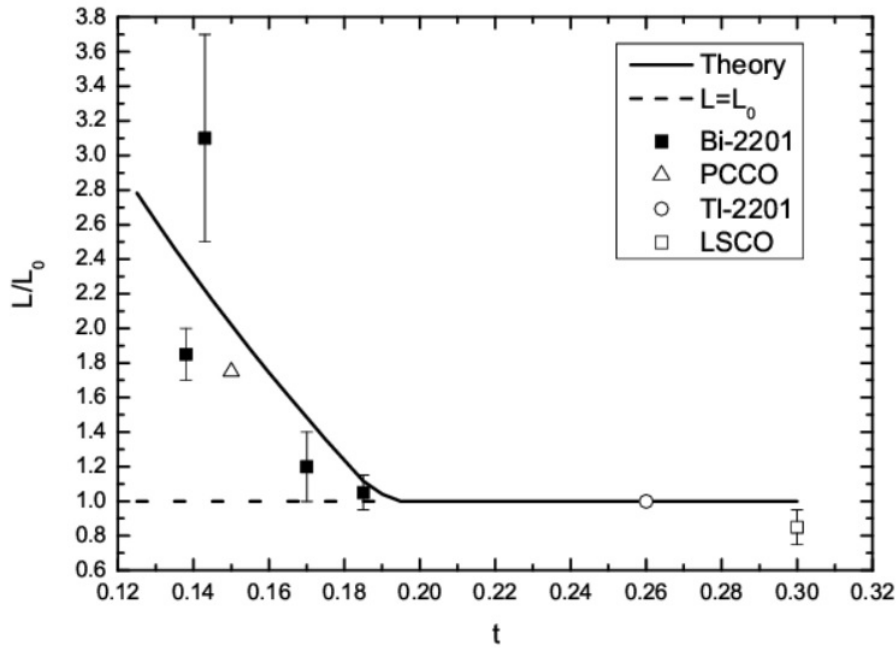


FIG. 6. The Lorentz ratio L/L_0 (Eq. (23)) vs. t (values for $t \geq 1$ are added artificially). Observed dots are from Ref. [4]

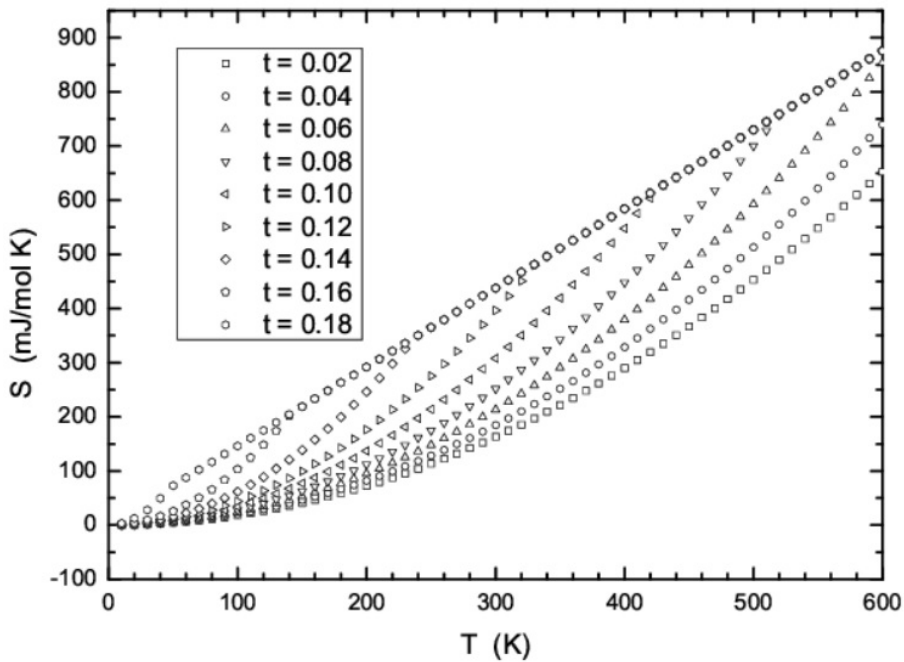


FIG. 7. The entropy \mathcal{S} (Eq. (24)) vs. T at various t (values of \mathcal{S} behind the crossing of linear and nonlinear parts of \mathcal{S} are added artificially)

see again the good agreement. As shown in [46], the nonlinear T dependence of the entropy \mathcal{S} at small temperatures is related to the insulating ground state.

12. Conclusion

In summary, we have formulated the Coulomb single boson single fermion two liquid model positions for HTS copper oxides: 1. The doping charges, in the form of individual NRs, are embedded in the insulating parent compound of HTS copper oxides. 2. Before the first critical doping x_{c1} with NR size $\xi_{coh} = 17\text{\AA}$, they are not percolated single bosons. 3. The origin of single bosons is in the anyon bosonization of 2D fermions. 4. At the first critical doping level, x_{c1} , the percolation of single boson NRs and thus HTS appears; there appear also from x_{c1} doping single fermions, but up to second critical doping level, x_{c2} , their NRs do not percolate, thus single fermions between x_{c1} and x_{c2} are insulating. 5. The value $x_{c1} = 0.05$ is universal for all copper oxide HTSs, since percolating single boson NRs cover 50% of the 2D sample area (like connecting squares in a chessboard); the same situation takes place with NRs for fermions at x_{c2} . 6. The normal phase charge conductivity appears from x_{c2} at $T = 0$ or above PG temperature boundary $T = T^*$, where the percolation of single fermions appears, while for temperatures between T_c and T^* , there exists (fermion-boson) MIC. 7. The spatially rare charge density object, single boson, with NR size between $\xi_{coh} = 17\text{\AA}$ and $\xi_{coh} = 10\text{\AA}$, which correspond to x_{c1} and x_{c2} dopings, has zero total but fluctuating inside of NR spin (this rareness leads also to fluctuating charge inside the NR). 8. The increase of boson spin fluctuations with doping or temperature results in a transition of bosons into fermions, which occurs at PG T^* or at x_{c2} . 9. At zero external magnetic field, the HTS is a result of the Bose-Einstein condensate of single bosons. 10. At high external magnetic field, the PG insulating ground state is the result of a plasmon gas consisting of these bosons.

Within these positions, we have succeeded in understanding the following constituents of the doping-temperature phase diagram for hole-doped copper oxides: (i) the first and second critical doping levels are a result of the emergence and disappearance of the single hole boson percolation lines, respectively; (ii) the disappearance of the percolation lines leads to the end of PG bulk bosonic property or to the end of Nernst effect signals; (iii) the fact that the PG boundary was bound, where the single hole bosons disappear, was confirmed by Ref. [11]. Our findings are consistent with the recent observation [47] of the superconducting phase which consisted of an array of nanoclusters embedded in an insulating matrix and of the percolative transition to this phase from the normal phase in $YBa_2Cu_3O_{6+\delta}$. A recent experiment [48] also displayed the percolative superconductor-insulator quantum phase transition in electron-doped $Pr_{2-x}Ce_xCuO_4$. Superconducting islands, introduced in insulating background, have been used to interpret the superconductor-insulator transition in $Bi_2Sr_{2-x}La_xCaCu_2O_{8+\delta}$ compound [49].

We are reminded of the possible scenario for the origin of PG phase in the copper-oxides. In Ref. [16], we pointed out that the PG boundary exactly coincides in the experiment with the structural phase transition line, where the symmetry of the sample structure changes. However, the structural phase transition induces a mechanical strain in the system. This mechanical strain changes the magnetic phase transition, existing in a system, from a second order into a first order one. However, this first order phase transition is close to the second order one. This effect is referred to in the literature as a striction. The phase transition of single bosons into fermions, discussed in Sec. 4, is possibly governed by a striction. Therefore, transition peaks in the specific heat increment are washed out in the cuprate underdoping regime [5]. On the other hand, the first order phase transition accepts the existence of a meta-stable phase. We believe that the PG phase of cuprates is a meta-stable phase of single bosons, whose effective spins are fluctuating and interacting with each

other. At the PG boundary, this interaction entirely destroys bosons, transforming them into fermions.

We predict the existence of non-percolated single bosons at low- T before the first critical doping x_{c1} in the doping-temperature phase diagram of copper-oxides, which is already seen in the experiment (see below). For these dopings, a scanning tunneling microscopy measurement may probe the same picture for minimal size NRs as for PG region, close to PG boundary. The Bose statistics of these particles may be experimentally detected by some methods described in Ref. [50]. These methods might also be applied to detect the insulating fermions inside the HTS dome, which is the main hypotheses of the present treatment.

We predict the existence of quantum oscillations in the ground state for copper oxides in a strong magnetic field with low critical doping values x_c and an insulating phase for HTS compounds having large x_c values.

Our Coulomb two liquid model also predicts there to be no Josephson and Andreev effects between the two $a - b$ planes of the underdoped HTS, belonging to two cuprates and separated by an insulating layer. It would be interesting to probe the atomic scale fractional charges in the STM experiment for electronic nematicity.

Recently, authors of Ref. [51] have reported on the emergent transition for superconducting fluctuations in the deep antiferromagnetic phase at a remarkably low critical doping level, $x_c = 0.0084$, for ruthenocuprates, $RuSr_2(R, Ce)_2Cu_2O_{10-\delta}$ with $R = Gd, Sm, Nd$. In this paper, it was claimed that those fluctuations have an intrinsic electronically-inhomogenous nature and provide new support for bosonic models of the superconducting mechanism.

In conclusion, we point out that the present paper is a substantially extended and critically revised version of our previous Ref. [52], in which we added the alternative physical insight into the background of HTS physics.

Acknowledgements

Authors B. Abdullaev and C.-H. Park acknowledge the support of the research by the National Research Foundation (NRF) Grant (NRF-2013R1A1A2065742) of the Basic Science Research Program of Korea.

References

- [1] Takagi H. et al. Systematic evolution of temperature-dependent resistivity in $La_{2-x}Sr_xCuO_4$. *Phys. Rev. Lett.*, 1992, **69**, P. 2975–2979; Keimer B. et al. Magnetic excitations in pure, lightly doped, and weakly metallic La_2CuO_4 . *Phys. Rev. B*, 1992, **46**, P. 14034; Wuyts B., Moshchalkov V. V., Bruynseraede Y. Resistivity and Hall effect of metallic oxygen-deficient $YBa_2Cu_3O_x$ films in the normal state. *Phys. Rev. B*, 1996, **53**, P. 9418; Abe Y. et al. Normal-state magnetotransport in $La_{1.905}Ba_{0.095}CuO_4$ single crystals. *Phys. Rev. B*, 1999, **59**, P. 14753.
- [2] Ando Y. et al. Logarithmic Divergence of both In-Plane and Out-of-Plane Normal-State Resistivities of Superconducting $La_{2-x}Sr_xCuO_4$ in the Zero-Temperature Limit. *Phys. Rev. Lett.*, 1995, **75**, P. 4662–4665; Boebinger G. S. et al. Insulator-to-Metal Crossover in the Normal State of $La_{2-x}Sr_xCuO_4$ Near Optimum Doping. *Phys. Rev. Lett.*, 1996, **77**, P. 5417–5420; Fournier P. et al. Insulator-Metal Crossover near Optimal Doping in $Pr_{2-x}Ce_xCuO_4$: Anomalous Normal-State Low Temperature Resistivity. *Phys. Rev. Lett.*, 1998, **81**, P. 4720–4723; S Ono S. et al. Metal-to-Insulator Crossover in the Low-Temperature Normal State of $Bi_2Sr_{2-x}La_xCuO_{6+\delta}$. *Phys. Rev. Lett.*, 2000, **85**, P. 638–641; Ando Y. et al. Supporting evidence of the unusual insulating behavior in the low-temperature normal-state resistivity of underdoped $La_{2-x}Sr_xCuO_4$. *J. Low Temp. Phys.*, 1996, **105**, P. 867–875.
- [3] Hill R. W. et al. Breakdown of Fermi-liquid theory in a copper-oxide superconductor. *Nature*, 2001, **414**, P. 711–715.
- [4] Proust C. et al. Heat transport in $Bi_{2+x}Sr_{2-x}CuO_{6+\delta}$: Departure from the Wiedemann-Franz law in the vicinity of the metal-insulator transition. *Phys. Rev. B*, 2005, **72**, P. 214511.

- [5] Loram J. W. et al. Electronic specific heat of $YBa_2Cu_3O_{6+x}$ from 1.8 to 300 K. *Phys. Rev. Lett.*, 1993, **71**, P. 1740–1743.
- [6] Loram J. W. et al. Evidence on the pseudogap and condensate from the electronic specific heat. *J. Phys. Chem. Solids*, 2001, **62**, P. 59–64.
- [7] Fujita K. et al. Simultaneous Transitions in Cuprate Momentum-Space Topology and Electronic Symmetry Breaking. *Science*, 2014, **344**, P. 612–616.
- [8] Vojta M. Lattice symmetry breaking in cuprate superconductors: stripes, nematics, and superconductivity. *Adv. Phys.*, 2009, **58**, P. 699–820; Vojta M. Stripes and electronic quasiparticles in the pseudogap state of cuprate superconductors. *Physica C*, 2012, **481**, P. 178.
- [9] Sebastian S. E., Harrison N., Lonzarich G. G. Towards resolution of the Fermi surface in underdoped high- T_c superconductors. *Rep. Prog. Phys.*, 2012, **75**, P. 102501.
- [10] Abdullaev B., Park C.-H., Musakhanov M. M. Anyon bosonization of 2D fermions and single boson phase diagram implied from experiment on visualizing pair formation in superconductor $Bi_2Sr_2CaCu_2O_{8+\delta}$. *Physica C*, 2011, **471**, P. 486–491.
- [11] Gomes K. K. et al. Visualizing pair formation on the atomic scale in the high- T_c superconductor $Bi_2Sr_2CaCu_2O_{8+\delta}$. *Nature*, 2007, **447**, P. 569–572.
- [12] Pan S. H. et al. Microscopic electronic inhomogeneity in the high- T_c superconductor $Bi_2Sr_2CaCu_2O_{8+x}$. *Nature*, 2001, **413**, P. 282–285.
- [13] Fauque B. et al. Magnetic order in the pseudogap phase of high- T_C superconductors. *Phys. Rev. Lett.*, 2006, **96**, P. 197001.
- [14] Lawler M. J. et al. Intra-unit-cell electronic nematicity of the high- T_c copper-oxide pseudogap states. *Nature*, 2010, **466**, P. 347–351.
- [15] Abdullaev B., Roessler U., Musakhanov M. An analytic approach to the ground state energy of charged anyon gases. *Phys. Rev. B.*, 2007, **76**, P. 075403(1-7).
- [16] Abdullaev B. *Implicit Anyon or Single Particle Boson Mechanism of HTCS and Pseudogap Regime*. In Trends in Boson Research, edit. by A. V. Ling. N. Y.: Nova Science Publisher Inc., 2006, p. 139–161.
- [17] B. Abdullaev B., Park C.-H. Bosonization of 2D Fermions due to Spin and Statistical Magnetic Field Coupling and Possible Nature of Superconductivity and Pseudogap Phases Below E_g . *J. Korean Phys. Soc.*, 2006, **49**, P. S642–S646; arxiv:cond-mat/0404668.
- [18] Leinaas J. M., Myrheim J. On the Theory of Identical Particles. *Nuovo Cimento Soc. Ital. Fis. B*, 1977, **37**, P. 1–23.
- [19] Wilczek F. Magnetic Flux, Angular Momentum, and Statistics. *Phys. Rev. Lett.*, 1982, **48**, P. 1144–1147.
- [20] Dunne G. et al. Exact multi-anyon wave functions in a magnetic field. *Nucl. Phys. B*, 1992, **370**, P. 601–635.
- [21] Laughlin R. B. in The Quantum Hall Effect, Edited by R. E. Prange and S. M. Girvin. New York, Springer-Verlag, 1987.
- [22] Wu Y. -S. Multiparticle Quantum Mechanics Obeying Fractional Statistics. *Phys. Rev. Lett.*, 1984, **53**, P. 111–115. Erratum *ibid*, 1984, **53**, P. 1028.
- [23] Comtet A., McCabe J., Ouvry S. Perturbative equation of state for a gas of anyons. *Phys. Lett. B*, 1991, **260**, P. 372–376.
- [24] Bonsal L., Maradudin A. A. Some static and dynamical properties of a two-dimensional Wigner crystal. *Phys. Rev. B*, 1977, **15**, P. 1959.
- [25] Rajagopal A. K., Kimball J. C., Correlations in a two-dimensional electron system. *Phys. Rev. B*, 1977, **15**, P. 2819.
- [26] Tanatar B., Ceperley D. M. Ground state of the two-dimensional electron gas. *Phys. Rev. B*, 1989, **39**, P. 5005.
- [27] De Palo S., Conti S., Moroni S. Monte Carlo simulations of two-dimensional charged bosons. *Phys. Rev. B*, 2004, **69**, P. 035109.
- [28] Attacalite C. et al. Correlation Energy and Spin Polarization in the 2D Electron Gas. *Phys. Rev. Lett.*, 2002, **88**, P. 256601; Erratum *ibid*, 2003, **91**, P. 109902.
- [29] Landau L. D., Lifshitz E. M. *Quantum Mechanics, Non-relativistic Theory*. Oxford, Pergamon Press, 1977, § 65.
- [30] Tallon J. L., Loram J. W. The doping dependence of T^* what is the real high- T_c phase diagram? *Physica C*, 2001, **349**, P. 53–68.
- [31] Onose Y. et al. Charge dynamics in underdoped $Nd_{2-x}Ce_xCuO_4$: Pseudogap and related phenomena. *Phys. Rev. B*, 2004, **69**, P. 024504.

- [32] A. Zimmers et al. Infrared properties of electron-doped cuprates: Tracking normal-state gaps and quantum critical behavior in $Pr_{2-x}Ce_xCuO_4$. *Europhys. Lett.*, 2005, **70**, P. 225.
- [33] Zaanen J. Superconductivity: Why the temperature is high. *Nature*, 2004, **430**, P. 512–513.
- [34] Uemura Y. J. et al. Universal Correlations between T_c and n/m (Carrier Density over Effective Mass) in High- T_c Cuprate Superconductors. *Phys. Rev. Lett.*, 1989, **62**, P. 2317–2320.
- [35] Uemura Y. J. et al. Basic similarities among cuprate, bismuthate, organic, Chevrel-phase, and heavy-fermion superconductors shown by penetration-depth measurements. *Phys. Rev. Lett.*, 1991, **66**, P. 2665–2669.
- [36] Kastner M. A., Birgeneau R. J., Shirane G., Endoh Y. Magnetic, transport, and optical properties of monolayer copper oxides. *Rev. Mod. Phys.*, 1998, **70**, P. 897–928.
- [37] Wang Y., Li L., Ong N. P., Nernst effect in high- T_c superconductors. *Phys. Rev. B*, 2006, **73**, 024510.
- [38] Li Y et al. Unusual magnetic order in the pseudogap region of the superconductor $HgBa_2CuO_{4+\delta}$. *Nature*, 2008, **455**, P. 372.
- [39] Li Y et al. Magnetic order in the pseudogap phase of $HgBa_2CuO_{4+\delta}$ studied by spin-polarized neutron diffraction. *Phys. Rev. B*, 2011, **84**, P. 224508.
- [40] V. Baledent V. et al. Two-Dimensional Orbital-Like Magnetic Order in the High-Temperature $La_{2x}Sr_xCuO_4$ Superconductor. *Phys. Rev. Lett.*, 2010, **105**, P. 027004.
- [41] De Almeida-Didry S. et al. Evidence for intra-unit-cell magnetic order in $Bi_2Sr_2CaCu_2O_{8+\delta}$. *Phys. Rev. B*, 2012, **86**, P. 020504.
- [42] Mangin-Thro L. et al. Characterization of the intra-unit-cell magnetic order in $Bi_2Sr_2CaCu_2O_{8+\delta}$. *Phys. Rev. B*, 2014, **89**, P. 094523.
- [43] Norman M. Fermi-surface reconstruction and the origin of high-temperature superconductivity. *Physics*, 2010, **3**, P. 86 (6 pages).
- [44] Caprara S. et al. Signatures of nematic quantum critical fluctuations in the Raman spectra of lightly doped cuprates. *Phys. Rev. B*, 2015, **91**, P. 205115.
- [45] Zavaritsky V. N. et al. Giant normal state magnetoresistances of $Bi_2Sr_2CaCu_2O_{8+\delta}$. *EPJ B*, 2004, **42**, P. 367–371.
- [46] Abdullaev B., Park C.-H., Park K.-S., Observed Non-Fermi Liquid Heat Transport and Entropy of Pseudogap Quasi-Particles as Possible Manifestations of Single Particle Bosons. // arxiv: cond-mat/0703290, 2007, 5 pages.
- [47] Gavrilkin S. Yu. et al. Percolative nature of the transition from 60 to 90 K-phase in $YBa_2Cu_3O_{6+\delta}$. *Physica C*, 2010, **470**, P. S996–S997.
- [48] Zeng S. W. et al. Two-dimensional superconductor-insulator quantum phase transitions in an electron-doped cuprate. *Phys. Rev. B*, 2015, **92**, P. 020503(R).
- [49] Oh S. et al. Doping Controlled Superconductor-Insulator Transition in $Bi_2Sr_{2-x}La_xCaCu_2O_{8+\delta}$. *Phys. Rev. Lett.*, 2006, **96**, P. 107003.
- [50] Stern A. Anyons and the quantum Hall effect – A pedagogical review. *Ann. Phys.*, 2008, **323**, P. 204.
- [51] Mclaughlin A. C., Attfield J. P. Emergent Transition for Superconducting Fluctuations in Antiferromagnetic Ruthenocuprates. *Phys. Rev. B*, 2014, **90**, P. R220509.
- [52] Abdullaev B. Anyon Bosonized 2D Fermions or a Single Boson Physics of Cuprates: Experimental Evidences. In Low Dimensional Functional Materials, NATO Science for Peace and Security Series B: Physics and Biophysics 2013. Netherlands, Springer, 2013, P. 251-268.

Degradation of perovskites and Dexter-Varley paradox

B. L. Oksengendler^{1,2}, S. E. Maksimov², M. B. Marasulov¹

¹Scientific Center of Chemistry and Physics of Polymers at National University of Uzbekistan, Tashkent, Uzbekistan

²Institute of Ion-Plasma and Laser Technologies, Uzbek Academy of Sciences, Tashkent, Uzbekistan

oksengendlerbl@yandex.ru, maksimov_s@yahoo.com

PACS 75.50.Tt, 81.16.Hc, 87.85.Rs DOI 10.17586/2220-8054-2015-6-6-825-832

This work presents a model for the degradation mechanism of organic–inorganic hybrid photovoltaic solar cells based on perovskites. The cross section for formation of Frenkel pairs in the sublattice of iodine is obtained. The channels for its annealing are found. Special attention is paid to the polaron states. It is shown that the stationary number of defects non-monotonically depends on the intensity of solar radiation. This allows one to analyze the properties of the radiation resistance of a device to ionizing radiation.

Keywords: perovskites, degradation, ionizing irradiation, Varley mechanism, polaronic states, organic solar cells.

Received: 1 November 2015

1. Introduction

Perovskite based solar-cells have attracted much attention due to their ever-increasing conversion efficiency. In the most general case, typical perovskite materials have a structure which is $\text{CH}_3\text{NH}_3\text{PbJ}_3$ or close variants [1]. The start of the “perovskite era” (see [2–5]) occurred in 2009; then, over 2012–2013 the conversion rate of solar energy into electrical energy increased from 10% to 15%. To date, the characteristic physical and mechanical structure of a perovskite solar cell (Figs. 1a, 1b, 1c, 1d) has been formed, which is characterized by the corresponding electronic band structure of the device (Fig. 1b). Along with excellent features of perovskite cells (inexpensive and relatively simple low-temperature technology and an understandable physical chemistry of the components), some difficulties have been identified, whose solution could lead, according to some experts [2], to a “new era of photovoltaics”: these are the very small sizes of the solar cells ($<1\text{ cm}^2$), environmental issues (dominant concentration of Pb), and issues of the stability of solar cells. The latter aspect, which consists of the interaction with the humidity in the environment (more precisely, with hydroxyl ions, OH^-), redox reactions involving oxygen, and the radiation stability of the working solar element, is particularly important and actually has not been studied (except for one experimental work [6]). The present work aims to examine this problem, namely, a theoretical analysis of the impacts of ultraviolet radiation on perovskite solar cells.

2. Generation of Defects

It follows from the most common considerations of radiation physics for solids (see [7, 8]), that the most sensitive element to ultraviolet radiation is perovskite, which belongs to a class of semiconductors. The band structure of this element is shown in the central part of Fig.1. The entire set of radiative processes affecting the electronic spectrum is reduced to the generation of radiation defects, their radiation-enhanced diffusion, quasi-chemical reactions,

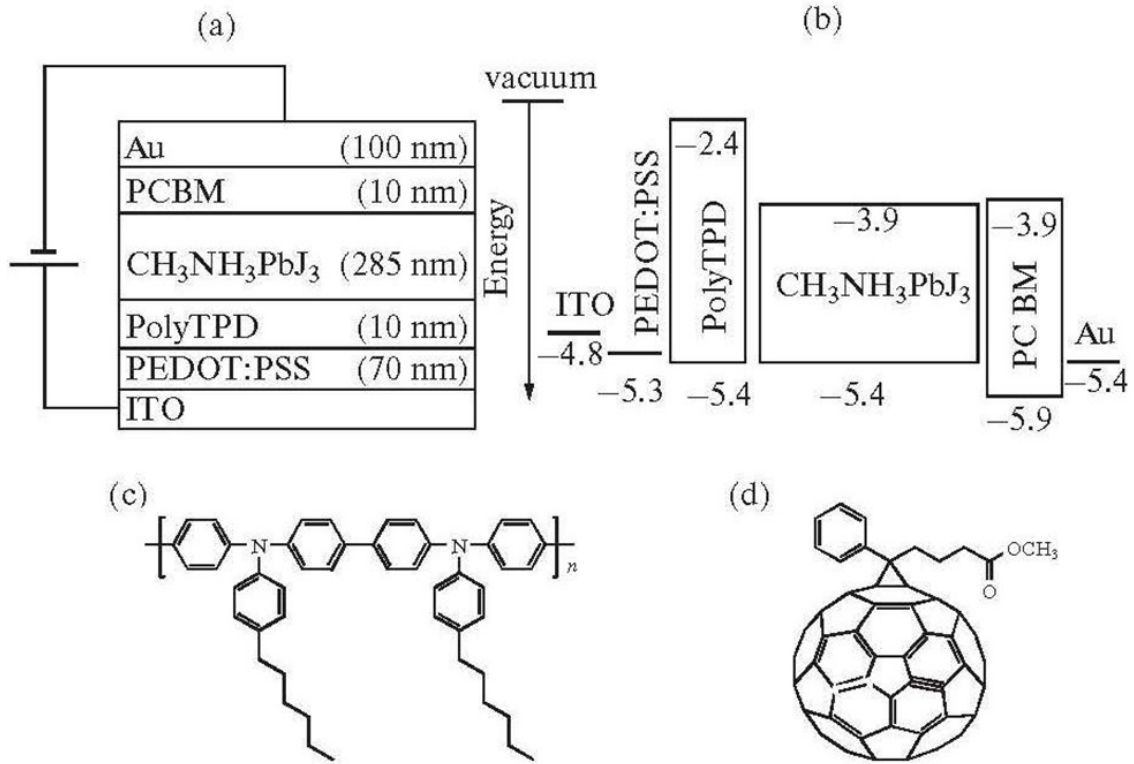


FIG. 1. The scheme of a solar cell based on perovskite: (a) the geometric structure of layers; (b) the electronic structure of layers; (c) the chemical structure of polerelomin (polyTPD); (d) the chemical structure of PCBM (see [1–3])

and the charge transfer (especially at the interface) of emerging local level modifications. Thus, the basic radiation phenomena producing the electronic spectrum of perovskite are reduced to the emergence of defects and their annealing.

3. The case of UV-irradiation

Varley-type mechanisms are the most important pathway for defect formation in perovskite-type materials [9, 10], since the elastic displacements are prevented due to the large difference between the masses of I and Pb atoms with the masses of bombarding particles. The scheme of the Varley mechanism applied to perovskite, $\text{CH}_3\text{NH}_3\text{PbI}_3$, is as follows. In the first stage ionization of the subvalent shell of the I atom, ultraviolet radiation occurs (see Fig. 2). In the second stage, the Auger process, which consists of a hole in the J subvalent shell and two electrons of the valence band constructed of 5p-functions of the I^- ion (see [11]) occurs. As a result of this process, a singly charged ion is formed at the position of iodine (the probability of such a process is defined as α_{Auger}) (Fig. 3).

In the third stage, the resulting positive I^+ ion, which is surrounded by positive Pb^{n+} ions that constitute perovskite, is on the precipice of the positive potential of the lattice of the inversion effect of the Madelung potential instead of being in the potential well; this state is unstable and is attributed, according to the classification of radiation physics, to dynamic instability [7, 8] (Fig.4).

The fourth stage implies dynamically unstable configurations of I_S^+ relax due to two competing processes: either by the offset of I_S to the nearest interstitial configuration (that

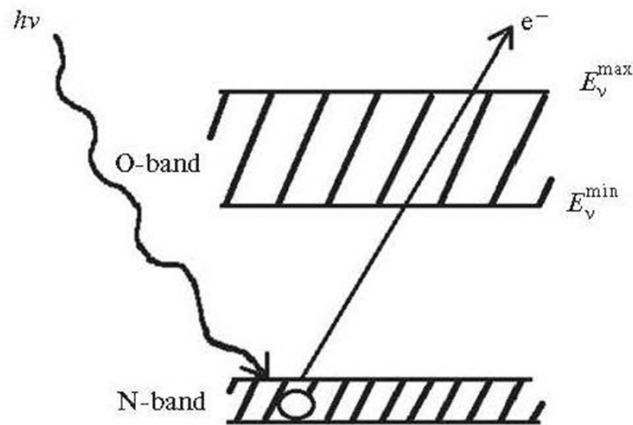


FIG. 2. The formation of a hole in the N-band of perovskite during the absorption of a photon

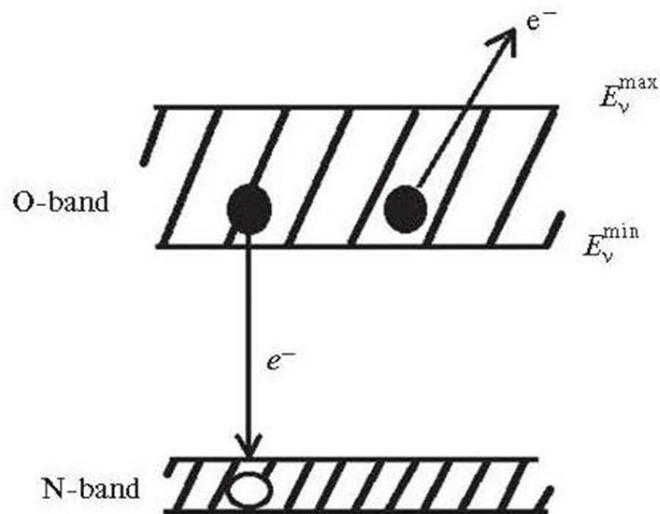


FIG. 3. The formation of two holes in the O-band of perovskite as a result of the Auger-process

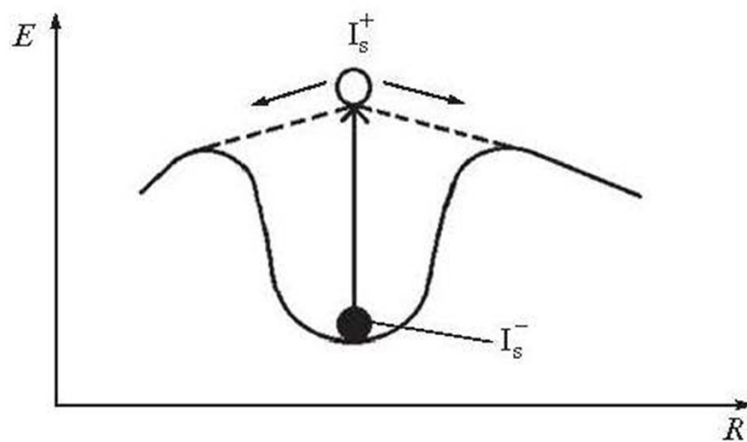


FIG. 4. The formation of dynamic Coulomb instability in the I-sublattice of perovskite

is, a defect via the reaction $I_S^+ \rightarrow V_I + J_i^+$ is formed, where V_I is the iodine vacancy, I_s and I_i are nodular and interstitial positions), or iodine ion neutralization $I_S^+ + e \rightarrow I_S^0$ thus, a Frenkel pair is not formed. The last step has probabilistic nature and the likelihood of the offset of the atom into the interstice is determined by the expression (Fig. 5):

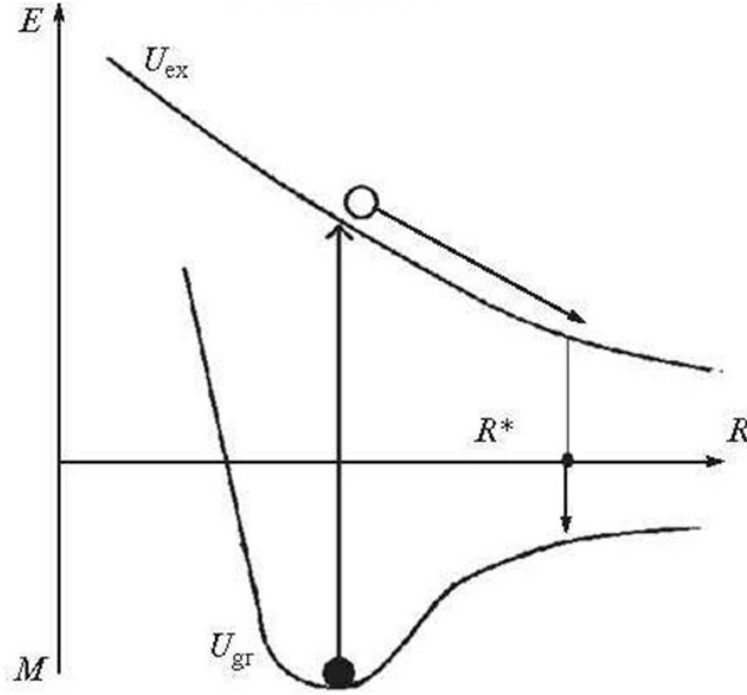


FIG. 5. The decay of an unstable local domain in the I-sublattice of perovskite

$$\eta = \exp(-\tau_+/\tau_e) \quad (1)$$

where $\tau_+ \approx 5 \times 10^{-14}$ s is the time of critical offset for the ion and $1/\tau_e$ is the probability of neutralizing the positive charge that fell into the valence band of perovskite as a result of the Auger process. Calculation of $1/\tau_e$ must consider two channels of neutralization: the expansion of two holes, which are localized on one node of iodine as a result of the Auger transition, over the valence band ($1/\tau_{e1}$) and capture by the excess charge on I_S^+ of the conduction band electrons that occur there due to the absorption of photons in the perovskite layer ($1/\tau_{e2}$). Calculations show [12-15] that $1/\tau_{e1} = \mu e/a^3$, where μ is the mobility of holes in the valence band that is formed by regular I^- iodine ions, e is the charge of the hole, and a is the distance between ions in the iodine sublattice. On the other hand, the second channel, where free electrons neutralize the conduction band, is a cavitation process [12] and the likelihood of the process is given by $1/\tau_{e2} = An^{5/12} = \tilde{A}n^{1/2}$, that is, it is symbatic to light pumping (here A and \tilde{A} are the parameters of the material and the values of the positive charge introduced into the band by the Auger transition).

Finally, the cross section for the generation of the Frenkel pairs during the exposure to ultraviolet radiation is given by:

$$\sigma_d = \sigma_i \alpha_{Auger} \exp(-\tau_+/\tau_e). \quad (2)$$

Assessment of this value at $\sigma_i \approx 10^{-17}$ cm², $\alpha_{Auger} \approx 0.5$, $\tau_e \approx 5 \times 10^{-15}$ s gives $\sigma_d \approx 5 \times 10^{-22}$ cm², that is, it is greater by four orders of magnitude than the similar value for the

Si crystal under X-ray irradiation [10,14]. In addition to this unexpected result, let us note an important fact: $\sigma_d \approx \exp(-\text{const} * n^{1/2})$, indicating an increase in the radiation resistance of the solar cell based on perovskite under intensive light fluxes (Fig. 6).

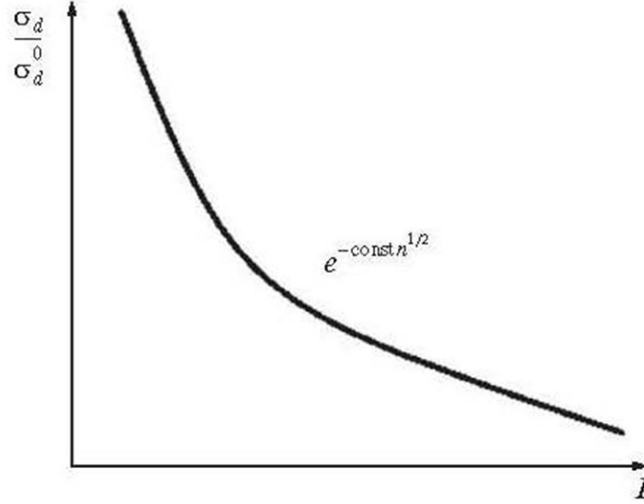


FIG. 6. The reduction of the normalized cross section of Frenkel defect formation in the I-sublattice on radiation intensity

4. The case of the light irradiation

The sequence of steps for defect formation is modified under the action of light (solar) irradiation. Indeed, the hole is formed at the first step directly in the valence band of perovskite (the cross-section of process is σ_i), so the Auger process with the involvement of the hole in subvalent shell falls off. Formally, this circumstance is reflected in the formula (2) as $\alpha_{Auger} = 1$, and σ_i corresponds to the photon disruption of the electron from the J_S^- ion. In addition, the relaxation channel for the single-site hole state into the delocalized state is a type of autoionization. So again, $\eta = \exp(-\tau_+/ \tau_e)$, however, for the $1/\tau_e$, another estimation $1/\tau_e = \Delta E_v / \hbar + \tilde{A} n^{1/2}$ will be valid, where ΔE_v is the width of the valence band. Finally, we obtain: $\sigma_d = \sigma_i \exp(-\tau_+/ \tau_e)$.

5. The possible role of the polaron effect in the degradation enhancement

Dependency of $1/\tau_e$ upon ΔE_v poses a very interesting question about the role of a strong polarization effect due to the presence of an organic dipole ($\text{CH}_3\text{-NH}_3^+$) in the perovskite. According to Prof. A.Zakhidov (Texas), electrons and holes in the perovskite turn into polarons. Without specifying what type of polarons are formed in the perovskite, it can be assumed that the effective mass of carriers will increase in this case (eg., by $m_{eff} = m_0 (1 + \tilde{\alpha}/6)$, where $\tilde{\alpha}$ is the parameter for the electron-ion interaction [15]). The latter condition reduces $1/\tau_e$ rapidly, which leads to an increase in the defect formation cross-section as $\sigma_d \sim \exp(-\text{const}/\tilde{\alpha})$. Moreover, it is interesting to note that the formation of biexciton states is also possible at a certain ratio of the material parameters (including the single-site ones in the so-called U-negative states [17]). Then, this can be expected to

increase the degradation under UV – irradiation action, since $1/\tau_e$ decreases sharply in this case.

6. Varley mechanism at the interfaces

The above-described mechanism for ionization defect formation in perovskites has a number of features at the interfaces. Primarily, it is due to the fact that ΔE_v is connected on the surface with the Tamm states band and is much smaller than ΔE_v in the bulk $E_v^S \ll \Delta E_v^b$ [18]. This leads to the following consequences: the scheme of the ordinary (non-radiation) degradation is effective, in which the surface is very important factor for photochemical reaction [19]. At the same time, however, it is necessary to take into account the reduction in these reactions' efficiencies according to the formula $\eta = \exp(-\tau_+/ \tau_e)$. In the problem of the ionization-stimulated desorption, which absolutely has not been studied yet for perovskites, the existence of highly polarizing $\text{CH}_3\text{-NH}_3^+$ components makes very interesting the appearance of bipolar hole U-states, occurring after the primary ionization of the subvalent shell of surface J^- ion; here, we can expect modifications of Knotek-Feibelman process (KF) [20] (for instance, the deepening of KF-state).

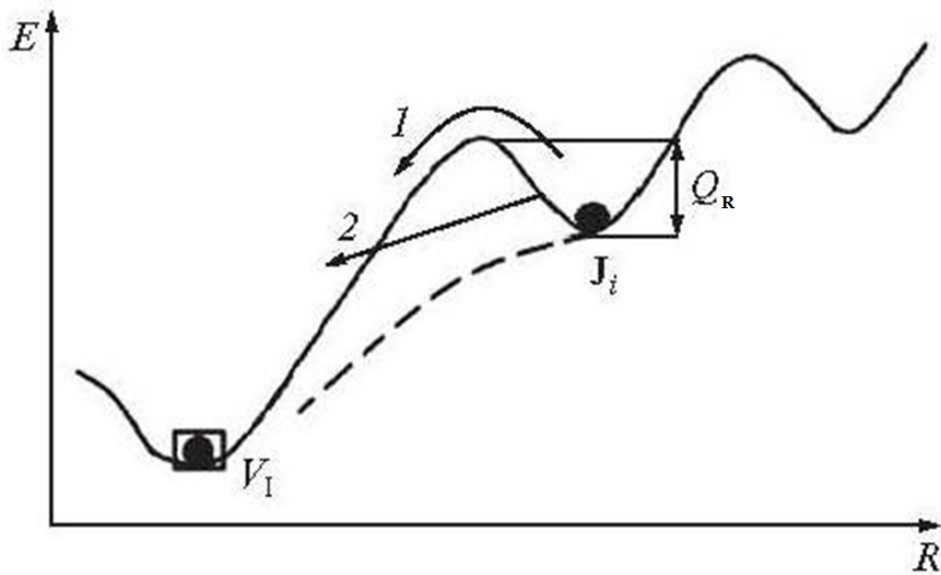


FIG. 7. The channels of the annealing of close Frenkel pair in the I-sublattice: (1) thermally activated channel; (2) recombination-stimulated channel

7. Annealing of defects

Under ionizing radiation, only the bound Frenkel pairs can be formed in the iodine sublattice (Fig.7). This results in a distinctiveness for the defect annealing process: a direct (single) jump of the iodine atom shifted into the interstice in the opened vacancy via the following reaction $I_i^- + V_I \rightarrow I_S^-$.

Defect recombination (J_i and V_J) can occur via two channels (Fig.7): (1) a thermofluctuation jump through a constant recombination barrier Q_R with probability $1/\tau_{R1} \approx \omega_D \exp(-Q_R/kT)$, ω_D -frequency of Debye) and (2) recombination-stimulated removal of the barrier when capturing the electron and the hole at the local level, which is introduced by a close Frenkel pair into the forbidden band, with probability $1/\tau_{R2} \approx [1/\sigma_n v_n \Delta_n +$

$1/\sigma_h v_h \Delta p]^{-1}$ (where v_n and v_h are the thermal velocities of electrons and holes; σ_n and σ_p are sections for the capture of electrons and holes generated by the light onto the local level; Δn and Δp are the excessive concentration of non-equilibrium carriers). The complete probability for annealing of the Frenkel pairs is defined as [14, 15] :

$$1/\tau_R = 1/\tau_{R1} + 1/\tau_{R2}. \quad (3)$$

In general, the value of $1/\tau_{R2}$ will depend on the light pumping intensity I : $1/\tau_{R2} = \text{const} * I^\alpha$ (where $\alpha \approx 1$ or $1/2$ depending on the excess carrier recombination mechanism [16]). Then, the kinetics of the accumulation of close Frenkel pairs [$J_i V_J$] is given by:

$$\frac{dN_d}{dt} = N_S^0 \sigma_d I - \frac{N_d}{\tau_R}, \quad (4)$$

which, at the initial condition of $t=0$, $N_d(0) = 0$, has the solution:

$$N_d = N_S^0 \sigma_d I \tau_R \left[1 - \exp\left(-t/\tau_R\right) \right]. \quad (5)$$

Accordingly, for the steady state, we have a constant concentration of defects:

$$N_d = N_S^0 \sigma_d I \tau_R, \quad (6)$$

here, N_S^0 is the concentration of iodine nodes in the regular perovskite lattice. From (7), (4), and (2) follows the completely non-trivial dependence of the steady-state concentration of close Frenkel pairs on the pumping light intensity $N_d(I)$, since, as it follows from the above-stated, $\frac{d\sigma_d}{dI} < 0$ and $\frac{d\tau_R}{dI} < 0$ (Fig. 8).

Thus, by selecting the actual mode of light irradiation ($I < I_{min}$ and $I > I_{max}$), one can reduce degradation to a minimum.

As for the comparison of the above theory with experimental data, then, due to the small number of experimental works (as noted, there is only one paper in which the degradation of perovskite solar cells has been detected [6]) one may as yet speak only of qualitative agreement between theory and experiment.

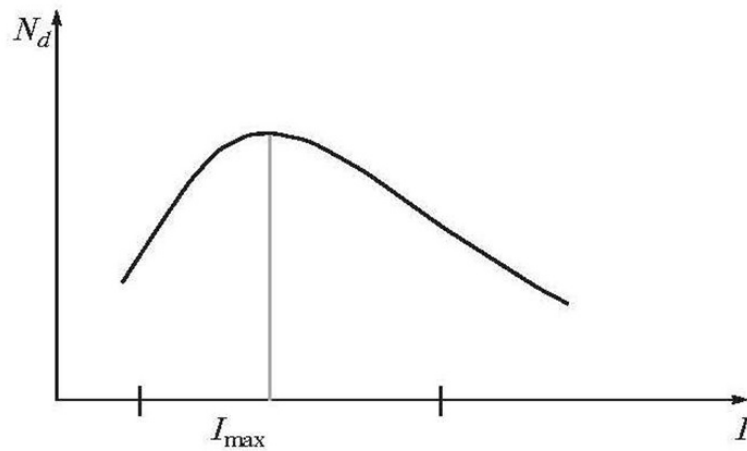


FIG. 8. The non-monotonic dependence of the concentration of Frenkel pairs in the I-sublattice on the intensity of radiation

8. Conclusions

In this work, we constructed a model for radiation-induced deep shell ionization of the iodine ion followed by an Auger process, recharging, and rolling of the latter ion into the neighboring interstice. The effect of competition between the ion and electron relaxation in dynamically unstable structure of the local region of the lattice was taken into account to obtain a semi-quantitative analysis. In addition, the role of both thermal and recombination-stimulated annealing of the Frenkel pairs is explored. This shows that the degradation process of perovskite solar cells is based on the modified mechanism of Varley. The above results can be applied to wide spectrum problems (rather than ultraviolet irradiation), viz., the problem of radiation resistance in relation to ionizing radiation (X-rays, electrons, and γ -quanta). The observed non-monotonic dependence of the number of stationary defects should allow one to optimize conditions for reducing the radiation-based degradation of devices.

References

- [1] Yin Wan-Jian, Yang J.-Hui, Kang J., et al. Halide perovskite materials for solar cell; a theoretical review. *J. Mat. Chem. A*. DOI: 10.10.39/c4ta05033a.
- [2] George G., Yamashita K. Organic-inorganic halide perovskites: an ambipolar class of materials with enhanced photovoltaic performances. *J. Mat. Chem. A*. DOI: 10.10.39/c4ta05046k.
- [3] Frost J., Butler K.T., Brivio F., et al. Atomistic origin of high-performance in hybrid halide perovskite solar cell. arXiv: 1402.4980v3 (Cond mat. mtrl-sci) apr. 2014.
- [4] Yin W.-J., Shi T., Yan Y. Unusual defect physics in $\text{CH}_3\text{NH}_3\text{PbJ}_3$ perovskite solar cell absorber. *Appl. Phys. Lett.*, 2014, **104**, P. 063903.
- [5] Oksengendler B.L., Ismailova O.B., Marasulov M.B., Urolov I.Z. On the degradation mechanism of functioning solar cells based on organic-inorganic perovskites. *Appl. Solar Energy*, 2014, **50**(4), P. 255–259.
- [6] Burschka J., Pelle, N., Soon-Jin Moon, et al. Sequential deposition as a route to high-performance perovskite-sensitized solar cells. *Nature*, 2013, **499**, P. 316–319.
- [7] Itoh N., Stoneham A.M. *Materials Modification by Electronic Excitation*, Cambridge, Univ. Press, 2001.
- [8] Oksengendler B.L., Turaeva, N.N. *Radiatsionnaya fizika kondensirovannykh sred* (Radiation Physics for Condensed Mediums), v. 1: Kontseptsii (Conceptions), Tashkent, Fan, 2006.
- [9] Varley J. Discussion on Some Mechanisms of F- centre Formation in Alkali Halides. *I Phys. Chem. Sol.*, 1962, **23**, P. 985–1005.
- [10] Yunusov M.C., Abdurakhmanova S.N., Oksengendler B.L., et al., Fizicheskie svoistva obluchennogo kremniya (Physical Properties of Irradiated Silicon). Tashkent, Fan, 1987.
- [11] Parilis E.E. *Effekt Ozhe* (Auger Effect). Tashkent, Fan, 1969.
- [12] Yunusov M.S., Zaykovskaya M.A., Oksengendler B.L. et al. Subthreshold defect production in Si. *Phys. Status Solidi A*, 1976, **35**, P. K145–149.
- [13] Dexter D. Varley Mechanism of Defect Formation in Alkali Halides. *Phys. Rev.*, 1960, **118**(4), P. 934–935
- [14] Yunusov M.S., Abdurakhmanova S.N., Oksengendler B.L. et al. *Podporogovye radiatsionnye efekty v poluprovodnikakh* (Subthreshold Radiation Effects in Semiconductors). Tashkent, Fan, 1989.
- [15] Yunusov M.S., Abdurakhmanova S.N., Oksengendler B.L. et al. The influence of minority carrier injection on subthreshold defects in Si. *Phys. Status Solidi A*, 1984, **81**, P. K145–149.
- [16] Davydov A.S. *Teoriya tverdogo tela* (Theory of solid state). Moscow, Nauka, 1976, 640 p.
- [17] Toyozawa Y. Self-Trapping and Defect Reaction. *Semicond and Insulators*, 1985, **5**, P. 175–200.
- [18] Davison S., Levine Y. *Surface (Tamm's) States*. Mosc. Mir, 1973, p. 232.
- [19] Schoonman. R. Organic – inorganic lead halide perovskite Solar cells materials. A possible stability problem. *Chem. Phys.Lett.*, 2015, **619**, P. 193–195.
- [20] Itoh N. Nakayama T. Desorption from compound Semiconductors and Oxides induced by Laser irradiation. *Semicond. and Insulators*, 1983, **5**, P. 383–400.

Influence of the radius of the quantum dot and the nonequilibrium degree on the conversion efficiency of light emitting diodes

Kh. B. Ashurov, M. M. Adilov, S. E. Maksimov, B. L. Oksengendler

Institute of Ion-Plasma and Laser Technologies, Uzbek Academy of Sciences,
Tashkent, Uzbekistan

oksengendlerbl@yandex.ru

PACS 75.50.Tt, 81.16.Hc, 87.85.Rs DOI 10.17586/2220-8054-2015-6-6-833-836

We describe the features of the conversion of electrical current into light in light diodes based on an organic matrix containing semiconductor quantum dots. It is shown that the relaxation channels of nonequilibrium electron-hole plasma injected into the quantum dot of the current density through the device. The conversion efficiency increases significantly with a decrease in the radius of the quantum dot.

Keywords: light diode, quantum dot, nonequilibrium e-h-plasma, internal efficiency.

Received: 1 November 2015

1. Introduction

The problem of converting electrical energy into light has remained an attractive topic for many years [1,2]. Due to the ongoing progress in modern nanotechnology, that problem has become crucially important. From a functional viewpoint, it is also caused by the fact that the electronic spectra of nanoparticles have spectral features both atomic and solid-state structures. On the other hand, the transition to highly non-equilibrium systems is of important for the generation of light from electricity. The possibility of such combination can be estimated for light-emitting diodes (LEDs), having the polymers as the matrix and the quantum dots as the light-converting objects.

2. Relaxation processes in quantum dot

The possibility of increasing of the conversion efficiency of the electric current into light can be analyzed on the structure presented in Fig. 1.

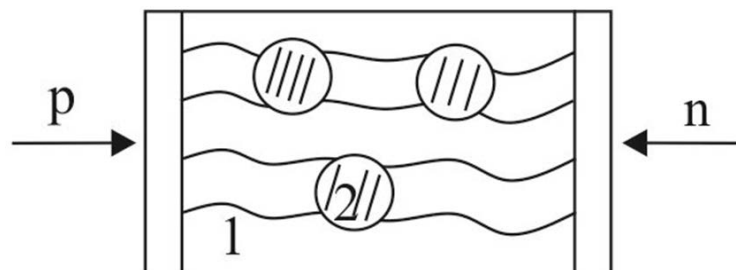


FIG. 1. Schematic diagram of the LEDs on the quantum dots embedded in a polymer matrix (1 is the polymer matrix, 2 is the quantum dot)

Let us assume that the electrons and holes are injected into a quantum dot using a double injection method. Such plasma of e-h pairs relaxes through the three processes: the recombination of electrons and holes by birth of phonons (the probability of relaxation is $1/\tau_1$), recombination by the Auger decay ($1/\tau_2$) and the recombination by emission of a photon ($1/\tau_3$) (Fig.2). Earlier analysis showed [3], that the first process is less effective than the other ones, so that the internal efficiency for conversion of the current into the light can be written as [4]:

$$\eta_{intern} = \frac{1/\tau_3}{1/\tau_3 + 1/\tau_2}. \quad (1)$$

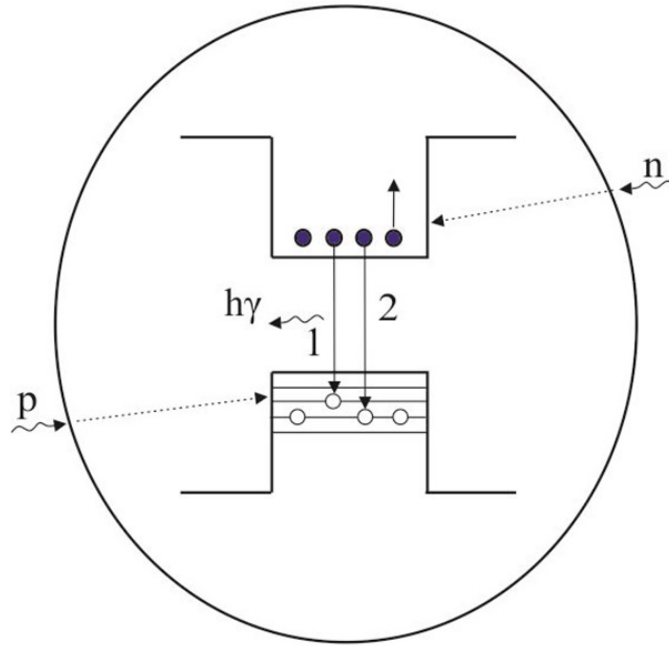


FIG. 2. Recombination processes in quantum dot after injection of electrons (n) into the conduction band and holes (p) into the valence band

It is important to note that the second and third processes, and hence the probabilities $1/\tau_2$ and $1/\tau_3$ have the special features in quantum dots, which are fundamentally different from their behaviors in atoms and in bulk materials. In the following, we will discuss them separately.

Auger recombination

Quantum dot-based Auger relaxation has been discussed in [5]. The matrix element M_{if} , whose squared value is proportional to the probability $1/\tau_2$ of the process, can be written as [6]:

$$M_{if} = \int \psi_f^*(1)\varphi_f^*(2)\frac{e^2}{r_{12}} \exp(-\lambda r_{12}) \chi_i(1)\phi(2)d^3r_1d^3r_2. \quad (2)$$

Here, “i” and “f” means the initial and final states of the wave function of two electrons, respectively, r_{12} is the distance between the electrons, $\lambda^2 = (4\pi e^2 \bar{n}/kT)$ is the square of the inverse radius of the Debye screening, \bar{n} is the plasma density.

Calculation of the probability by the method developed in [6,7] allows one to obtain an interesting result, which includes the approach of the atom and the approach of the volume semiconductor as the particular special cases:

$$1/\tau_3 = \frac{\gamma S \bar{n}^2 A}{(\lambda^2 + B)^4}. \tag{3}$$

Here, A and B are constants depending on the dielectric constant and the width of the electron band gap of quantum dot. We assume that $S = S_0 R^3$, $\bar{n} = Z_{\max}/R^3$, and $Z_{\max} = j\tau R^2$, where j is the current density through the device, τ is the lifetime of the e-h-plasma, S_0 is the constant (see. [5]), Z_{\max} is the maximum number of e-h-pairs injected into the quantum dot. Then, the probability of Auger recombination will depend on the specific density of the current through the device and on the radius R of the quantum dot:

$$1/\tau_3 = \gamma S_0 R^3 \frac{\bar{n}^2 \tilde{A}}{(\bar{n} + \tilde{B})^4} = \gamma S_0 R^3 \frac{\tilde{A} [j\tau/R]^2}{[\tilde{B} + j\tau/R]^4}. \tag{4}$$

Here, \tilde{A} and \tilde{B} are the renormalized parameters A and B . It is clear from (4) that at low current densities and large quantum dot radii of the (at $j\tau/R < \tilde{B}$) we have:

$$1/\tau_3 = \gamma S_0 \frac{\tilde{A}\tau}{\tilde{B}^4} j^2 R, \tag{5}$$

i.e. the probability of non-radiative Auger recombination increases rapidly with increased current density and weaker with increased quantum dot radii. At high current densities and small quantum dot radii, the situation is changing fundamentally:

$$1/\tau_3 = \gamma S_0 \tilde{A} \frac{R^5}{j^2 \tau^2}. \tag{6}$$

Thus, the probability of Auger recombination is reduced to smaller R and high densities.

Radiative recombination

The probability of radiative recombination (the spontaneous emission of a photon in the transition of the electron from a higher state to a lower one) is very different for the atom and for the bulk semiconductor. Namely, the first probability is many times larger than the second one. Taking into account that the quantum dot is an “intermediate object” between the atom and the bulk semiconductor, we consider the following situation. A system of quantum dots with the captured nonequilibrium $e - h$ -plasma is similar to that of the Thomson atom model, in which the electrons move in quasi-atomic orbits (see. [8]) on the spread background of positive charge Z_{\max} , with an average density Z_{\max}/R^3 . If the orbit of the excited $Z(1 \leq Z \leq Z_{\max})$, then the probability for spontaneous emission of a photon can be written as (in atomic units) [9]:

$$1/\tau_3 = \frac{Z^4}{c^3}, \tag{7}$$

where $c \approx 137$ is the speed of light in atomic units.

We note that the value of Z is concentrated to the center of the electron orbit of radius a_0 , with the random probability determined by the Poisson distribution:

$$\bar{Z}^Z e^{-\bar{Z}} / Z! \tag{8}$$

Here, $\bar{Z} = \bar{Z}_{\max} a_0^3 / R^3$ is the average charge run by the electron with the radius of orbit a_0 .

The internal conversion efficiency of current into light in a quantum dot

We determine the value of the boundary charge from the relation $1/\tau_2 = 1/\tau_3$. Obviously, at $Z > Z^* = \left[\tau_{at} \gamma s_0 c^3 \tilde{A} / \tau^2 (R^5/j^2) \right]^{1/4}$, the fluorescence probability is greater than that for Auger recombination, and the partial internal efficiency can be written as:

$$\eta_{intern}(Z) = 1 - \frac{(1/\tau_2)}{(1/\tau_3)} = 1 - \frac{D (R^5/j^2)}{Z^4}. \quad (9)$$

We imply here a strong non-equilibrium (large j values) and the small quantum dot radius size (R); $D = \gamma s_0 \tilde{A} c^3 \tau_{at}$, τ_{at} is the characteristic atomic time.

The value $\eta_{intern}(Z)$ must be averaged over all $Z \geq Z^*$; we do this using not the Poisson distribution, but with a normal Gaussian distribution:

$$\bar{\eta}_{intern} \geq \int_{Z^*}^{\infty} \frac{1}{\sqrt{2\pi}\sigma} \exp \left[-\frac{(Z - \bar{Z})}{2\sigma^2} \right] dZ - \int_{Z^*}^{\infty} \frac{D (R^5/j^2)}{Z^4} \frac{1}{\sqrt{2\pi}\sigma} \exp \left[-\frac{(Z - \bar{Z})}{2\sigma^2} \right] dZ, \quad (10)$$

where $\sigma = \sqrt{Z_{\max} (a_0/R)^3 (1 - a_0/R)^3}$,

$$\bar{Z} = Z_{\max} (a_0/R)^3, \quad Z^* = [D (R^5/j^2)]^{1/3}.$$

It is clear that the main contribution comes from the first term of Eq. (10). This shows that $\bar{\eta}_{intern}$ increases as Z^* decreases, i.e. the efficiency of conversion of current energy into light increases with decreased quantum dot size.

Acknowledgments

This work is supported by the Committee for Coordination of Science and Technology Development under Cabinet of Ministers of the Republic of Uzbekistan (contract F3-FA-F158).

References

- [1] Berg A., Dean P. *Light-emitting diodes*. Moscow, Mir, 1979, 686 p. (in Russian).
- [2] Pope M., Swenberg Ch. *Electronic Processes in Organic Crystals*. Clarendon Press, Oxford University Press, New York, 1982, V.1 (543 p.), V.2. (462 p.).
- [3] Ridley B. *Quantum Processes in Semiconductors*. University of Essex, Clarendon Press, Oxford, 1982, 304 p.
- [4] Vikulin I.M., Stafeev V.I. *Physics of Semiconductor Devices*. Moscow, Radio and communication, 1990, 264 p. (in Russian).
- [5] Klimov V.I. Nanocrystal Quantum Dots: From fundamental photophysics to multicolor lasing. *Los Alamos Science*, 2003, **28**, P. 214–220.
- [6] Parilis E.S., *Effekt Ozhe (Auger Effect)*, Tashkent, Fan, 1969, 211 p. (in Russian).
- [7] Landsberg P.T. *Recombination in Semiconductors*. Cambridge University Press, Cambridge, 1991, 595 p.
- [8] Shpolsky E.V. *Atomic physics*. V.1. Moscow, Science, 1984. (in Russian).
- [9] Migdal A.B. *Qualitative methods in quantum theory*. Moscow, Science, 1975. (in Russian).

The lateral capacitance of nanometer MNOSFET with a single charge trapped in oxide layer or at $\text{SiO}_2 - \text{Si}_3\text{N}_4$ interface

A. E. Atamuratov¹, U. A. Aminov², Z. A. Atamuratova²,
M. Halillaev², A. Abdikarimov², H. Matyakubov²

¹Urganch Branch of Tashkent University of Information Technologies, Tashkent, Uzbekistan

²Urganch State University, Tashkent, Uzbekistan

a.atamuratov@tuit.uz

PACS 85.30.Tv

DOI 10.17586/2220-8054-2015-6-6-837-842

In this work the dependence between the position of single charge trapped in an oxide layer or at $\text{SiO}_2 - \text{Si}_3\text{N}_4$ interface and the concentration distribution of charge carriers on a semiconductor substrate surface of the nanometer n-channel Metal-Nitride-Oxide-Semiconductor Field Effect Transistor (MNOSFET) and p-channel MNOSFET with n^+ drain area is studied. It is shown that the lateral capacitances of nanometer MNOSFET depend on the position of single charge in oxide or at interface. This dependence allows one to estimate the position of trapped charges along the channel of transistor.

Keywords: Defects, lateral capacitances, oxide trapped charge, interface trapped charge, nanometer MNOSFET.

Received: 1 November 2015

1. Introduction

The ultra thin oxide layers of MOSFETs exhibit unusual behavior, such as atomic-scale heterogeneity in thickness and in composition. Even a small number of atomic-scale defects are problematic, as they can trap a superfluous amount of electrons or holes which can be sources for instability and degradation of MOSFET. Therefore, it is very important to investigate such defects. Macroscopic C-V methods show only the average properties of the area under gate without specification of exact spatial distribution of the trapped charge. In [1-6], by applying a technique of scanning tunnel microscopy, the spatial distribution of the trapped charge was shown. However these methods are labor-intensive, have limited speed of scanning and require the application of mechanical parts.

In this work, we study the dependence between the position of a single charge trapped in an oxide layer or on a $\text{SiO}_2 - \text{Si}_3\text{N}_4$ interface and the concentration distribution of charge carriers on a semiconductor substrate surface of MNOSFET. In particular, the source-substrate and drain-substrate transitions depletion layer width dependence on position is considered for a trapped single charge in an oxide layer and at interface. In the flat capacitor approximation, through the determination of depletion layer width, it is possible to estimate the capacity of the above-specified transitions and this can be used for obtaining information about the position of a trapped charge in an oxide layer or at the interface.

Prior works [5, 6] have stated that it is possible in SiO_2 to provide the density of states $3 \cdot 10^{13} \text{ cm}^{-2}$. For this density of states, one can calculate volume of space, where the single carrier can be located in an area with a linear size 1.8 nm. For simulation of single trapped charge influence on the carrier concentration distribution, the MNOSFET with an oxide layer

of thickness 1.8 nm was created. Captured single charge in an oxide layer is simulated by introducing the homogeneously distributed fixed charge with the surface density recalculated to the volume density. The length of the channel of considered transistor is 55 nm.

2. Simulation results and discussion

It is considered the width of depletion layer of a source-substrate transition with the single charge trapped in an oxide layer of nMOSFET. For such a system, we calculated the depletion layer width d at various applied voltages and positions for the oxide layer-trapped charge. The source-substrate (drain-substrate) transition consists of two parallel parts: the source-channel and source-substrate parts. The trapped charge exerts its main influence on the source-channel part. Therefore, we consider the change of this part only. The depth of the channel from the Si-SiO₂ interface, where the changes of depletion layer width occur is appreciable, 10 nm. As an average, a depletion layer width of 5 nm depth from the surface of the substrate is considered. In Fig. 1, the charge carrier concentration distribution along the channel at various depths from surface of the semiconductor is shown for an applied voltage $V=1$. It can be seen that the width of transition at a depth 5 nm is equal to the total average.

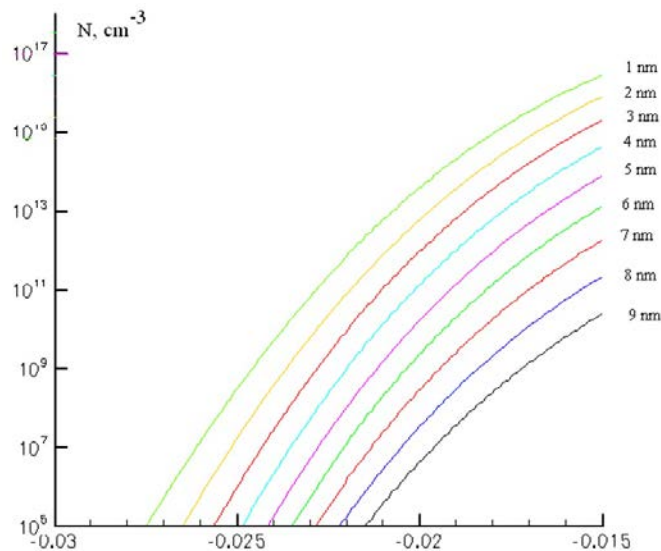


FIG. 1. Charge carrier concentration distribution along the channel at different depths from Si-SiO₂ interface

The transition capacitance can be found by the formula $C = \epsilon\epsilon_0 S/d$ in the flat capacitor approximation. As the metallurgical border of lateral transitions do not change in charge trapping, the area of transition S also does not change. Therefore, the quantity $C'=1/d$ is the main parameter which can be used for estimating the transition capacitance.

A negative voltage is applied to source substrate. In Fig. 2, the C' (V) dependence is shown for various positions of the trapped charge.

As it can be seen from this plot, the C' - V characteristics are non-monotonously displaced to area with high C' in all trapped charge positions. In Fig.3 the C' , the dependence on position of oxide trapped charge at applied voltage 0V is shown. C' is increased when the trapped charge is positioned near the source end. At longer distances from the source end, C' monotonically decreases to a value corresponding to the case of absence of trapped charge.

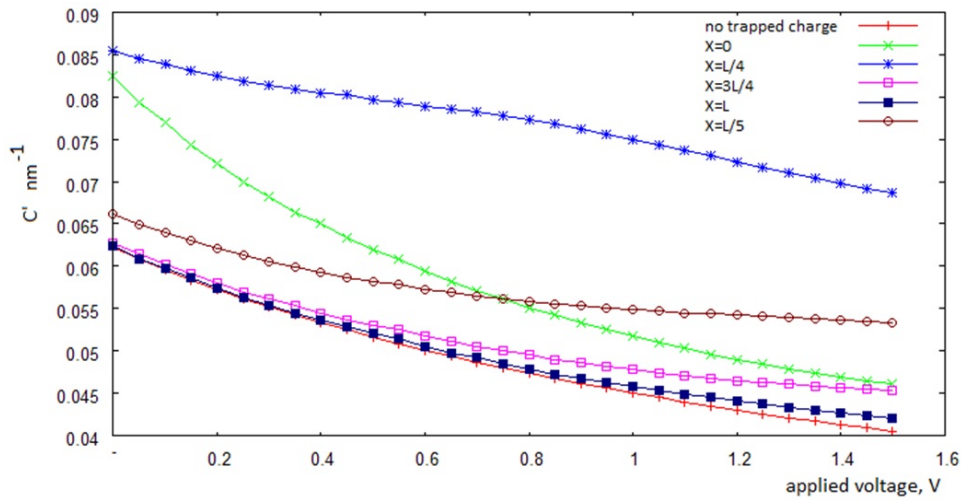


FIG. 2. $C'(V)$ dependence for various positions of oxide trapped charge. X is the distance between center of the trapped charge and source end of oxide, L is the oxide length

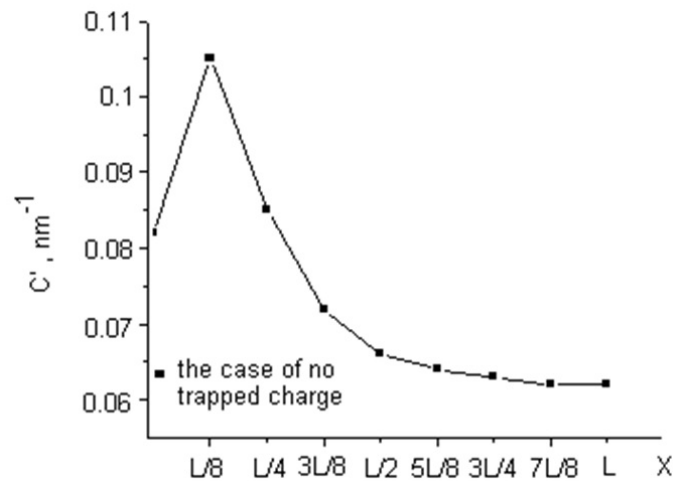


FIG. 3. C' dependence on position of oxide trapped charge at applied voltage 0V. X is the distance between the trapped charge center and source end of oxide, L is the oxide length

The charge trapped on a non-central area of oxide have different influences to the width of the depletion layer. One can obtain from this effect information about the position of the trapped charge. The dependences between the ratios of C' for source-substrate and drain-substrate transitions and position of the trapped charge is shown in Fig.4.

For ease of structure at lateral C-V measurement, it is reasonable to propose the p-channel MNOSFET with p^+ -source and n^+ -drain area. In case of such structure, one can consider the influence of single charge trapped at $\text{SiO}_2 - \text{Si}_3\text{N}_4$ interface to $C(V)$ dependence (Fig.5). In this case, $C'-V$ characteristics are also non-monotonically displaced to the area with high capacitance for all interface trapped charge positions (Fig. 6).

In order to study the possibility for detecting defect distribution by voltage scanning, we calculated derivative of C' over the voltage at different trapped charge positions. For

such the structure, the local minimum of dC'/dV can be observed for all trapped charge positions (Fig.7).

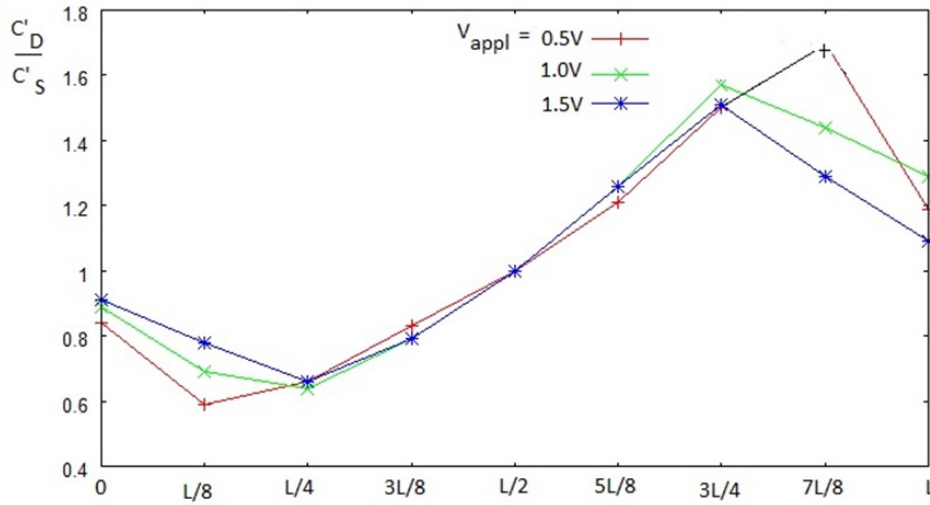


FIG. 4. Ratio of C' for source-substrate and drain-substrate transitions vs trapped charge position. C'_D is $1/d$ for drain-substrate transition and C'_S is $1/d$ for source-substrate transition. L is the length of oxide layer along channel

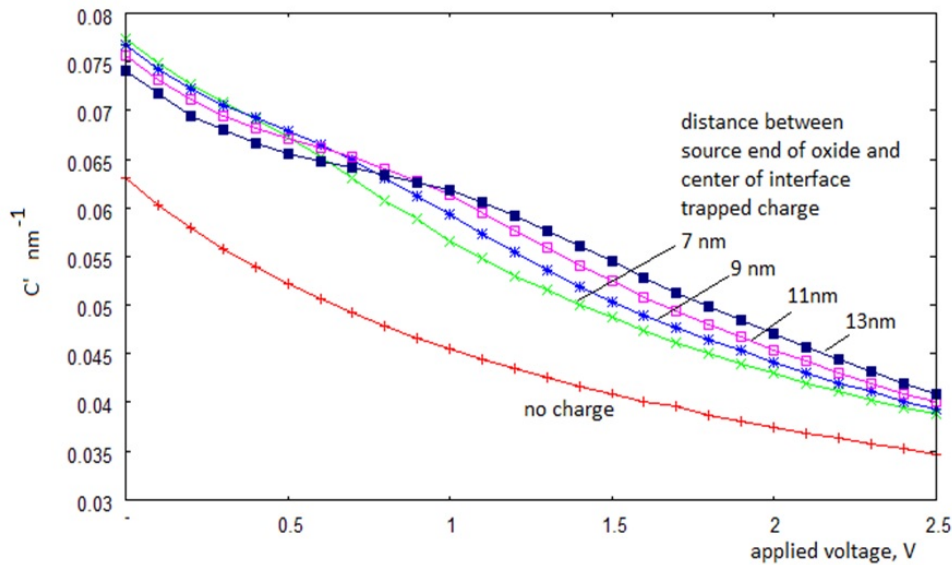


FIG. 5. $C'(V)$ dependence for various positions of charge trapped on $\text{SiO}_2\text{-Si}_3\text{N}_4$ interface

The above results show that the values for the applied voltage corresponding to a local minimum of dC'/dV depend on the position of the trapped charge. This value increases with removal of the trapped charge from source edge (Fig 8). This dependence has a monotonic character and allows one to identify the positions of defects along the channel of MNOSFET.

3. Conclusion

The nanometer n-channel MNOSFET with n^+ -source and drain area and p-channel MNOSFET with p^+ -source and n^+ - drain area is studied in this work. For the n-channel

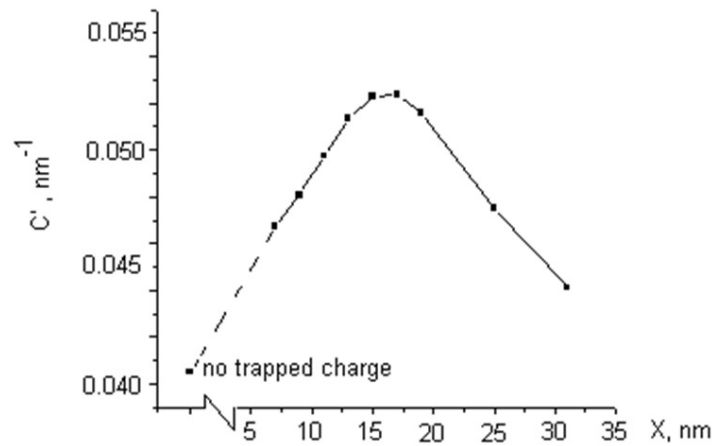


FIG. 6. C' dependence on positions of charge trapped on $\text{SiO}_2\text{-Si}_3\text{N}_4$ interface. X is the distance between source edge and center of trapped charge area. Applied source-substrate voltage is 1.5 V

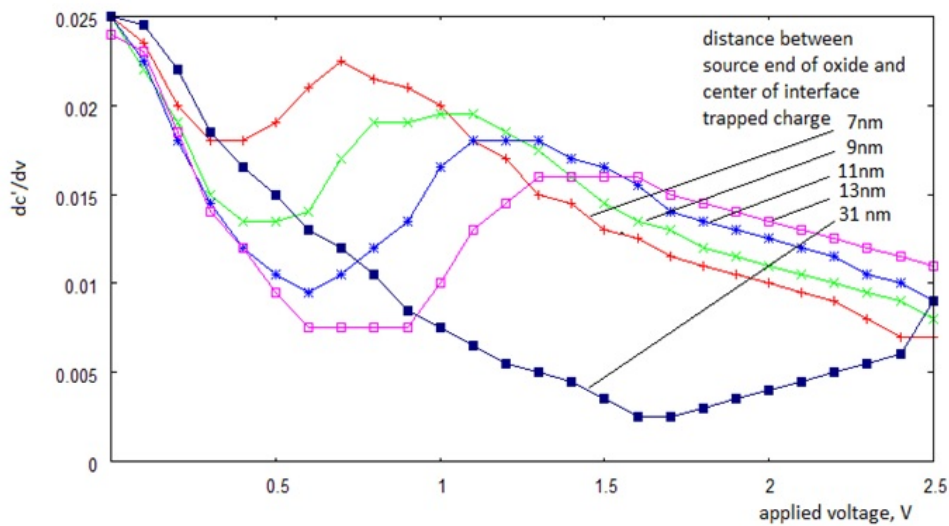


FIG. 7. dC'/dV vs source-drain voltage for different position of interface trapped charge

MNOSFET, C' increases when the position of trapped charge is close to the source and decreases at longer distances from the source. The dependence of the C'_d/C'_s ratio on the position of the trapped charge shows that positioning of the trapped charge on left half of oxide makes this ratio less than 1. Accordingly, localization on right (drain) half of the oxide makes this ratio greater than 1. Such relations allow one to estimate the positions of the charged defects relative to the center of channel.

For p-channel MNOSFET with n^+ - drain area, positioning of a trapped charge near the source edge of $\text{SiO}_2\text{-Si}_3\text{N}_4$ interface increases C' . With increased distance from the source edge, at a certain distance, C' monotonically decreases. Local minima in the dC'/dV dependence on voltage were also observed. The bias voltage values corresponding to these minima depend on the position of the trapped charge along the channel. Such dependence allows one to define the distribution of charge defects at the interface along the channel.

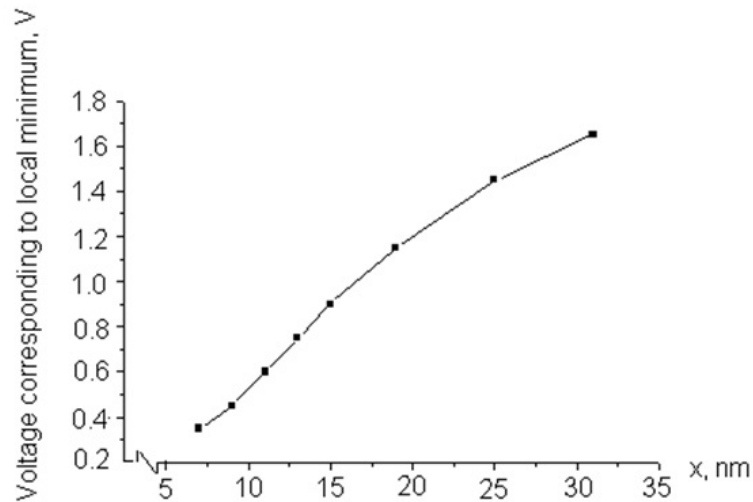


FIG. 8. Dependence between value of applied voltage corresponding to local minimum of dC'/dV and position of trapped charge along channel

References

- [1] Kasumov Yu.N., Kozlov S.N., Time Variation in the Electrical Parameters of the Si-SiO₂-Metal System under Injectional Degradation, *Mikroelektronika*, 1993, **22**(2), P. 20–26.
- [2] Di Maria D.J., Stasiak J.W. Trap Creation in Silicon Dioxide Produced by Hot Electrons, *J. Appl. Phys.*, 1989, **65**(6), P. 2342–2356.
- [3] Kaczer B., Im H.-J., Pelz J.P., Wallace R.M. Microscopic Characterization of Hot-Electron Spreading and Trapping in SiO₂ Films Using Ballistic Electron Emission Microscopy, *Appl. Phys. Lett.*, 1998, **73**(13), P. 1871–1873.
- [4] Groeseneken G., Bellen, R., Vander L.G., Bosch G., Maes H.E., Hot-Carrier Degradation in Submicrometre MOSFETs: From Uniform Injection towards the Real Operating Conditions, *Semicond. Sci. Technol.*, 1995, **10**(11), P. 1208–1220.
- [5] Verwey J.F., Amerasekera E.A., Bisschop J. The Physics of SiO₂ Layers, *Rep. Prog. Phys.*, 1990, **53**, P. 1297–1331.
- [6] Nicollian E.H., Brews J.R. *MOS (Metal Oxide Semiconductor) Physics and Technology*, New York: Wiley, 1982.

Red-ox reactions in aqueous solutions of $\text{Co}(\text{OAc})_2$ and $\text{K}_2\text{S}_2\text{O}_8$ and synthesis of CoOOH nanolayers by the SILD method

A. A. Lobinsky, V. P. Tolstoy

Institute of Chemistry, Saint Petersburg State University, Saint Petersburg, Russia
lobinsky.a@gmail.com, vptol@yandex.ru

PACS 81.07.Bc

DOI 10.17586/2220-8054-2015-6-6-843-849

CoOOH nanolayers were first prepared by the successive ionic layer deposition (SILD) method using aqueous $\text{Co}(\text{OAc})_2$ and $\text{K}_2\text{S}_2\text{O}_8$ solutions. The obtained nanolayers were investigated by SEM, EDX, XRD, FTIR spectroscopy and electrochemical techniques. SEM images showed that the layers formed by nanosheets of size approximately 80-100 nm which had a hexagonal crystal structure. Electrochemical study of nickel foam electrodes modified by CoOOH layer prepared by 50 SILD cycles demonstrates that specific capacitance of the film is 1520 F/g at current density 1 A/g. Repeated cycling for 1000 charge-discharge cycles demonstrates 2% capacitance fade, so such electrodes may be used as pseudocapacitor electrodes.

Keywords: cobalt oxyhydroxide, nanolayers, SILD, electrochemical properties.

Received: 1 November 2015

1. Introduction

Cobalt oxide is known to be a transition metal oxide with intriguing electrocatalytic, optical, magnetic, electronic and electrochemical properties. In recent years, cobalt oxyhydroxide and oxides have found wide applications as materials for electrochemical sensors [1], catalysts [2], drug delivery systems [3] and lithium-ion batteries [4]. In particular, cobalt oxyhydroxide attracts special attention as a material for pseudocapacitors because they showing large specific capacitance, low cost, natural abundance and environmental friendliness [5].

Previously, cobalt oxyhydroxide was obtained by electrodeposition [6], CBD [7], hydrothermal [8] and chemical precipitation [9] methods.

In this work, we describe a new simple route for synthesis of cobalt oxyhydroxide nanolayers by the successive ionic layer deposition (SILD) method from aqueous solutions of a cobalt (II) salt and potassium persulfate and investigate its electrochemical properties as electrode materials for pseudocapacitors. The SILD method is based on the sequential adsorption of anions and cations onto a substrate surface with the formation of a nanolayer of insoluble compounds [10].

The problem of achieving irreversible reactions at each stage of processing reagents is one of the main problems for this method of nanolayer synthesis. For the synthesis of metal oxide layers by this method, the obtained layer is most commonly formed by oxidation-reduction reactions, e.g. a layer of $\text{SnO}_2 \cdot n\text{H}_2\text{O}$ is formed by the interaction of the Sn (II) cations and a slightly alkaline solution of H_2O_2 [11], a layer of $\text{TiO}_2 \cdot n\text{H}_2\text{O}$ – solutions of $\text{Ti}_2(\text{SO}_4)_3$ and NaNO_2 [12], the layer of nanoparticles Ag - AgNO_3 solutions and $\text{N}_2\text{H}_5\text{OH}$ [13;14], etc.

The major advantage of this method is its simplicity and equipment, its suitability for coating of most surfaces, the application to substrates with irregular shapes and sizes

and precision control of the multilayer thickness. These advantages for the SILD method permit one to obtain nanolayers based on a wide range of substances which may be used in optics, microelectronics, energy storage devices. The SILD method provides a simple and effective means for creating metal oxide nanolayers for thin-film electrodes, which may result in significantly improved electronic conductivity and high electrochemical performance of pseudocapacitors. The possibility of creating electrode materials on the basis of thin-film nanolayers of layered double hydroxides, which showed a good electrochemical performance, has been shown in our previous work [15,16].

2. Experimental methods

As substrates for nanolayer synthesis, single-crystal silicon plates ($10 \times 30 \times 1$ mm with $\langle 100 \rangle$ orientation) and polycrystalline nickel foam (NF) plates (110 PPI, $10 \times 25 \times 0.35$ mm) were used. The layers, obtained on the silicon plates, were characterized by physical methods, while those formed on NF plates were characterized by electrochemical methods. Substrates of silicon were cleaned in an ultrasonic bath filled with acetone for 10 minutes. Then plates were sequentially treated for 10 minutes in concentrated HF, water, 70% HNO_3 , water, 1 M KOH and then flushed with water. NF plates were treated for 15 minutes in aq. 6 HCl, then rinsed several times with deionized water and dried aerobically at 120°C for 30 minutes.

For SILD synthesis, the following solutions were used: aqueous 0.01 M $\text{Co}(\text{OAc})_2$ with (stable pH) and aq. 0.01 M $\text{K}_2\text{S}_2\text{O}_8$ with pH 9.5, which was achieved by addition of a KOH solution. All the reagents used were of analytical grade. Deionized water with resistivity $18.2 \text{ M}\Omega\cdot\text{cm}$ (Mili-Q) was used for solution preparation.

CoOOH films were synthesized on silicon and NF substrates by SILD techniques. First, plates were sequentially immersed for 30 seconds into a solution of cobalt salt, then washed in distilled water. Next, plates were dipped for 30 seconds in a potassium persulfate solution and again washed in water. This sequence corresponds to one SILD cycle, which is repeated 50 times to obtain the desired film thickness. Finally, the sample was annealed in air at 150°C for 10 minutes at a rate of $5^\circ\text{C}/\text{min}$.

The morphology and composition of the CoOOH films were investigated by scanning electron microscope (SEM) at an accelerating voltage 20 kV on Zeiss EVO-40EP microscope and energy-dispersive X-ray spectroscopy (EDX) used detector Oxford INCA350. FTIR transmission spectra of synthesized films on silicon surface were registered by FSM 2201 spectrophotometer using a differential technique with respect to the spectra for the bare silicon plate. X-ray diffraction (XRD) was carried out on Rigaku Miniflex II diffractometer with $\text{Cu K}\alpha$ radiation, 30 kV voltage, and 10 mA current.

The electrochemical measurements of NF electrodes with the synthesized CoOOH layer were carried out in a three-electrode electrochemical cell in aq. 1M KOH as an electrolyte using Elins P-30I potentiostat. After 50 SILD cycles, the NF electrode was used as the working electrode. For the reference electrode, a Ag/AgCl (aq.KCl sat.) electrode was used, while a platinum plate served as the counter electrode. Electrochemical characterization of the films was made by cyclic voltammetry (CV) and galvanostatic charge-discharge (CD) techniques. The CVs were performed in a voltage window between -100 and 800 mV at different scan rates of 5, 10 and 20 mV/s. The CDs were carried out in a voltage window between 0 and 600 mV under different current density from 1 to 5 A/g. Specific capacitance (C) values were calculated using following equations:

$$C = I\Delta t/\Delta Vm,$$

where $I(\text{mA})$ is a galvanostatic current, $\Delta V(\text{mV})$ is the potential window, $\Delta t(\text{s})$ is the discharge time of a cycle and $m(\text{g})$ is the mass of the active material in the film electrode. The electroactive mass of CoOOH for the working electrode was measured using an OHAUS PioneerTM PA54C microbalance.

3. Result and discussion

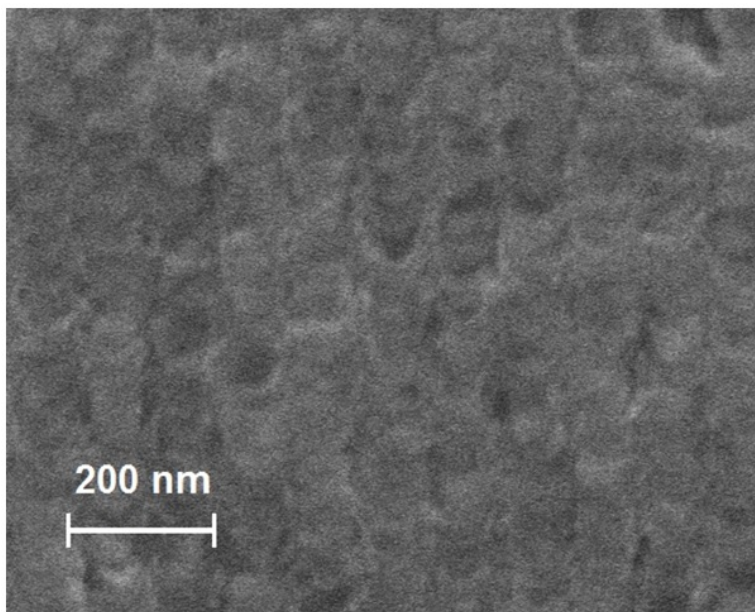


FIG. 1. SEM image of CoOOH layer on a silicon surface

SEM investigation of the synthesized sample shows that they formed by nanosheets of size approximately 80–100 nm (Fig. 1). The results of the dispersive X-ray spectroscopy showed significant energy signal intensity of the Co, O, and C elements in the sample. Average content of K and S in layer was no more than a few percent.

The XRD patterns of sample by XRD are shown in Fig. 2. Sample represents typical diffraction peaks (003), (101), (012), (015), (110), (113), which correspond to hexagonal crystal structure of $\beta\text{-CoOOH}$ (JCPDS 14-0673) [8].

Fig. 3 shows the FTIR absorption spectrum of the CoOOH nanolayer. The broad band at 3400 cm^{-1} is attributed to O-H valence vibrations of the hydroxyl groups. The band at 1640 cm^{-1} attributed to O-H deformation vibrations [17]. The bands with peaks at 1472 and 1364 cm^{-1} corresponds to the valence vibrations of carbonyl group of acetate contained in CoOOH [18]. In this spectrum, one can identify the absorption band with peak at 1107 cm^{-1} , corresponding to valence vibrations of S-O in impurity ions of $\text{S}_2\text{O}_8^{2-}$ and SO_4^{2-} , which is probably adsorbed onto the surface of CoOOH nanoparticles [19]. The band observed at 594 cm^{-1} was ascribed to Co-O vibrations in CoOOH [20].

In order to explain the obtained results, a scheme of chemical reactions, occurring on the surface, can be suggested. During the first step, after dipping in the cobalt acetate solution and wash for remove excess of salt on the surface, a layer of cobalt(II) hydroxide is formed:



Then, after treatment with excess $\text{K}_2\text{S}_2\text{O}_8$ solution, an atoms of cobalt (II) from adsorbed hydroxide is transferred in the oxidation state 3+ and form insoluble oxyhydroxide

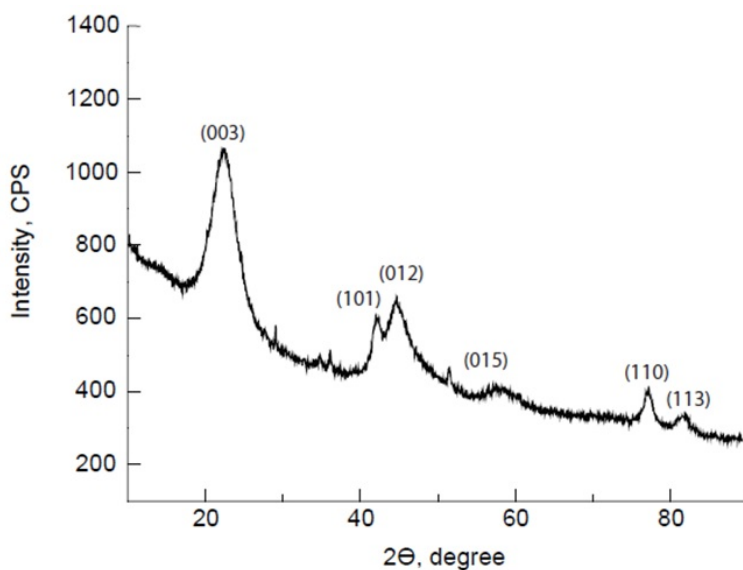


FIG. 2. XRD pattern of synthesized sample

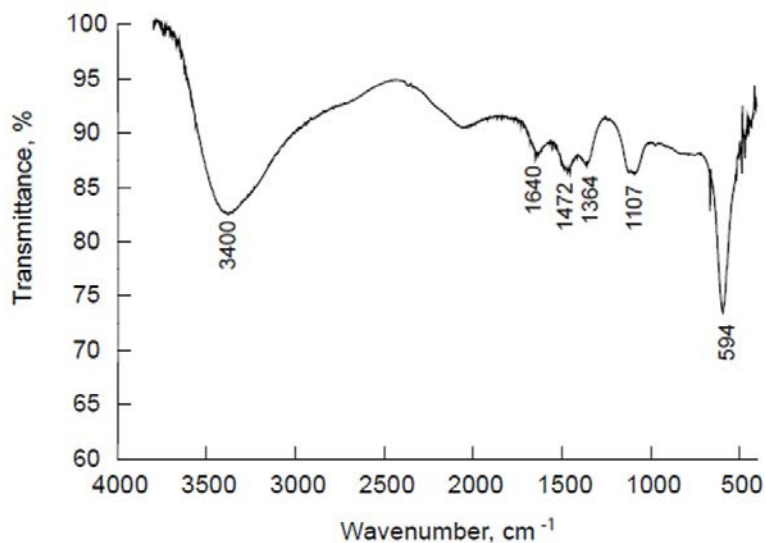


FIG. 3. FTIR transmission spectrum of CoOOH layer on silicon surface

CoOOH.



On the second SILD cycle, during the treatment with cobalt acetate solution, cobalt (II) cations are also adsorbed onto the surface of this layer, and then subsequently react with $\text{S}_2\text{O}_8^{2-}$ anions in the processing of the following solution, thus, the thickness of the synthesized layer increases. On the second and all subsequent cycles, when the layer is forming, the bonds of Co-O-Co form, and as result, the crystal lattice of CoOOH is generated.

Important results were obtained by electrochemical study of NF electrode with SILD synthesized CoOOH layer. As demonstrated in Fig. 4, at a scan rate 5 mV/s, two redox processes takes place in the layer, including the $\text{Co}^{3+} \rightarrow \text{Co}^{4+}$ transformation at 670 mV and the $\text{Co}^{4+} \rightarrow \text{Co}^{3+}$ at 170 mV [5]. The proportionality of currents to the square root of scan

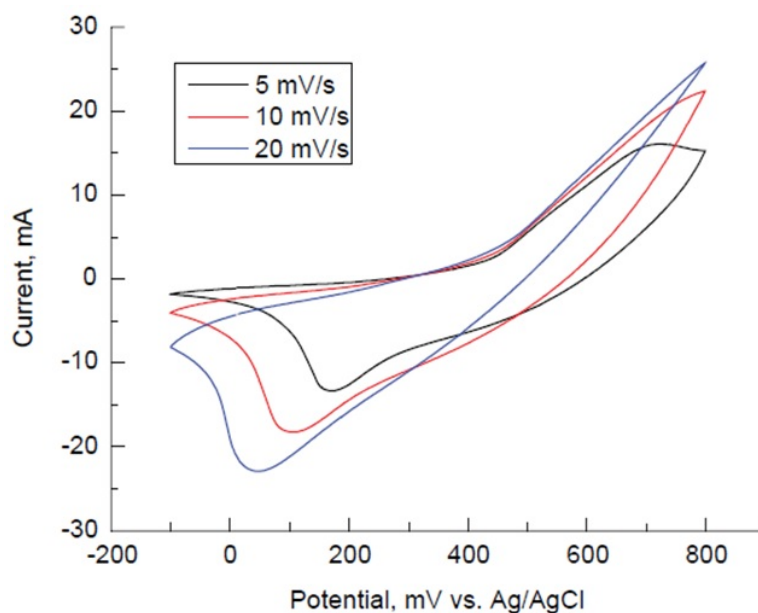


FIG. 4. Cyclic voltammograms of nickel foam electrode, covered by CoOOH layer, recorded at different scan rates

rate provides information that the film is thick enough, and charge transfer rate is limited by diffusion of charge carriers in the film.

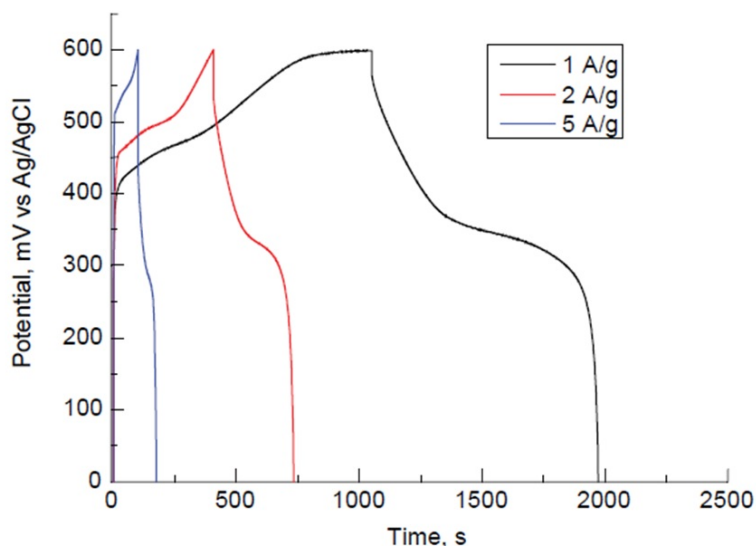


FIG. 5. Galvanostatic charge-discharge curves of nickel foam electrode, covered by CoOOH layer, recorded at different current densities

Charge-discharge curves of CoOOH-NF electrode at different currents (Fig. 5) allow one to determine its capacitance. For instance, specific capacitance of a sample, formed by 50 SILD cycles, is 1520 F/g at a current density of 1 A/g. The long-term cycle stability of the CoOOH-NF electrodes was evaluated by repeating the charge-discharge tests at 5 A/g for 1000 cycles. A capacitance retention ratio of 98% was obtained after 1000 charge-discharge cycles, illustrating the long-term electrochemical stability of the CoOOH-NF electrodes.

4. Conclusion

In this paper, we obtained CoOOH nanolayers with hexagonal crystal structure of β -CoOOH. The SILD method used $\text{Co}(\text{OAc})_2$ and $\text{K}_2\text{S}_2\text{O}_8$ aqueous solutions. The electrochemical study of CoOOH nanolayer-modified nickel foam electrodes, prepared by 50 SLID cycles, demonstrates that the specific capacitance of the film is 1520 F/g at a current density of 1 A/g. Repeated cycling for 1000 charge-discharge cycles demonstrate a relatively small 2% capacitance fade. The results illustrate the long-term electrochemical stability of the system, and thus its potential application as materials for electrode of pseudocapacitors.

Acknowledgments

This research was financial supported by grant of the RFBR 15-03-08253. The authors are grateful to the Centers for X-ray diffraction studies and Nanotechnology of Saint-Petersburg State University.

References

- [1] Muhammad Mehmood Shahid, Perumal Rameshkumar, Alagarsamy Pandikumar, et al. An electrochemical sensing platform based on a reduced graphene oxide-cobalt oxide nanocube@platinum nanocomposite for nitric oxide detection. *J. Mater. Chem. A*, 2015, **3**, P. 14458–14468.
- [2] Xiaohui Deng, Harun Tüysüz. Cobalt-Oxide-Based Materials as Water Oxidation Catalyst: Recent Progress and Challenges. *ACS Catal*, 2014, **4**, P. 3701–3714.
- [3] Karimi Z., Karimi L., Shokrollahi H. Nano-magnetic particles used in biomedicine: Core and coating materials. *Mater. Sci. Eng. C Mater*, 2013, **33**, P. 2465–2475.
- [4] Mengmeng Zhang, Rong Li, Xiaoxuan Chang, Chao Xue, Xinglong Gou. Hybrid of porous cobalt oxide nanospheres and nitrogen-doped graphene for applications in lithium-ion batteries and oxygen reduction reaction. *Journal of Power Sources*, 2015, **290**, P. 25–34.
- [5] Kian Keat Lee, Wee Shong Chin, Chornng Haur Sow. Cobalt-based compounds and composites as electrode materials for high-performance electrochemical capacitors. *J. Mater. Chem. A*, 2014, **2**, P. 17212–17248.
- [6] A.D. Jagadale, D.P. Dubal, C.D. Lokhande. Electrochemical behavior of potentiodynamically deposited cobalt oxyhydroxide (CoOOH) thin films for supercapacitor application. *Materials research bulletin*, 2012, **47**(3), P. 672–676.
- [7] Eiji Hosono, Shinobu Fujihara, Iraru Honma, Masaki Ichihara, Haoshen Zhou. Synthesis of the CoOOH fine nanoflake film with the high rate capacitance property. *Journal of Power Sources*, 2006, **158**, P. 779–783.
- [8] Jinhu Yang, Takehiko Sasaki. Synthesis of CoOOH hierarchically hollow spheres by nanorod self-assembly through bubble templating. *Chem. Mater.*, 2008, **20**, P. 2049–2056.
- [9] Zhaorong Chang, Huaqi Li, Hongwei Tang, Xiao Zi Yuan, Haijiang Wang. Synthesis of γ -CoOOH and its effects on the positive electrodes of nickel batteries. *International Journal of Hydrogen Energy*, 2009, **34**(5), P. 2435–2439.
- [10] V.P. Tolstoy. Successive ionic layer deposition. The use in nanotechnology. *Russ. Chem. Rev.*, 2006, **75**(2), P. 161.
- [11] Korotcenkov Ghenadii, Cho Beongki, Tolstoy Valeri. SnO₂-based thin film gas sensors with functionalized surface. *Advanced Materials Research*, 2010, **93-94**, P. 145–148.
- [12] Konstantin Semishchenko, Valeri Tolstoy, Artem Lobinsky. A novel oxidation-reduction route for layer-by-layer synthesis of TiO₂ nanolayers and investigation of its photocatalytical properties. *Journal of Nanomaterials*, Volume 2014, Article ID 632068, 7 pages.
- [13] L. B. Gulina, G. Korotcenkov, B. K. Cho, S. H. Han, V. P. Tolstoy. Ag nanoclusters synthesized by successive ionic layer deposition method and their characterization. *Journal of Materials Science*, 2011, **46**(13), P. 4555–4561.
- [14] G. Korotcenkov, B.K. Cho, L.B. Gulina, V.P. Tolstoy. Gas sensor application of Ag nanoclusters synthesized by SILD method. *Sensors and Actuators B: Chemical*, 2012, **166-167**, P. 402–410.

- [15] A.A. Lobinsky, V.P. Tolstoy, L.B. Gulina. Direct synthesis of $\text{Co}_2\text{Al}(\text{OH})_{7-2x}(\text{CO}_3)_x \cdot n\text{H}_2\text{O}$ layered double hydroxide nanolayers by successive ionic layer deposition and their capacitive performance. *Appl. Surf. Sci.*, 2014, **320**, P. 609–613.
- [16] V.P. Tolstoy, A.A. Lobinsky, O.V. Levin, L.I. Kuklo. Direct synthesis of $\text{Ni}_2\text{Al}(\text{OH})_{7-x}(\text{NO}_3)_x \cdot n\text{H}_2\text{O}$ layered double hydroxide nanolayers by SILD and their capacitive performance. *Materials letters*, 2015, **139**, P. 4–6.
- [17] J. Xie, H. Cao, H. Jiang, Y. Chen, W. Shi, H. Zheng, Y. Huang. Co_3O_4 -reduced graphene oxide nanocomposite as an effective peroxidase mimetic and its application in visual biosensing of glucose. *Anal. Chim. Acta*, 2013, **796**, P. 92.
- [18] Zhangpeng Li, Jinqing Wang, Lengyuan Niu, Jinfeng Sun, Peiwei Gong, Wei Hong, Limin Ma, Shengrong Yang Rapid. Synthesis of graphene/cobalt hydroxide composite with enhanced electrochemical performance for supercapacitors. *Journal of Power Sources*, 2014, **245**, P. 224–231.
- [19] Vanitha Duraikkan, Sultan Asath Bahadur, Shunmuganarayanan Athimoolam. Crystal growth and characterization of potassium manganese nickel sulphate hexahydrate— A new UV filter. *Journal of Minerals and Materials Characterization and Engineering*, 2012, **11**, P. 1121–1125.
- [20] Chih-Wei Tang, Chen-Bin Wang, Shu-Hua. Characterization of cobalt oxides studied by FT-IR, Raman, TPR and TG-MS. *Chien Thermochimica Acta*. 2008, **473**, P. 68–73.

Quasi free-standing one-dimensional nanocrystals of PbTe grown in 1.4 nm SWNTs

A. V. Lukashin^{1,2}, N. S. Falaleev¹, N. I. Verbitskiy^{1,3,4}, A. A. Volykhov²,
I. I. Verbitskiy², L. V. Yashna², A. S. Kumskov⁵, N. A. Kiselev⁵, A. A. Eliseev^{1,2}

¹Department of Materials Science, Moscow State University, 119992, Moscow, Russia

²Department of Chemistry, Moscow State University, 119992, Moscow, Russia

³Faculty of Physics, University of Vienna, A-1090 Vienna, Austria

⁴Institute of Physics 2, University of Cologne, 50937 Cologne, Germany

⁵Shubnikov Institute of Crystallography RAS, 119333, Moscow, Russia

fnm@fnm.msu.ru

PACS 81.05.U-

DOI 10.17586/2220-8054-2015-6-6-850-856

Here, we show successful filling of 1.4 nm single-walled carbon nanotubes (SWNT) with PbTe nanocrystals. The structure of one-dimensional PbTe in SWNT was determined using high-resolution transmission electron microscopy (HRTEM). The electronic structure of composites was studied by optical absorbance and Raman spectroscopies indicating no noticeable interaction of encapsulated PbTe with SWNT wall. Experimental data are supported by *ab-initio* calculations, showing non-zero density of states at the Fermi level of PbTe@SWNT(10,10) provided by both SWNT and PbTe states and thus metallic conductivity of the composite.

Keywords: Encapsulated SWNT, SWCNT, quasi free-standing nanocrystals, PbTe@SWCNT, doping, electronic properties, HRTEM, HAADF STEM.

Received: 20 October 2015

Revised: 29 October 2015

1. Introduction

Current progress in microelectronics has nearly attained the extensive miniaturization limit of silicon technology, which necessitates development of new paradigm for semiconductor engineering. One possible pathway to expand the boundaries of traditional silicon technology involves elaboration of nanowire- and nanotube-based integrated circuits. Most attention is paid to single-walled carbon nanotube (SWNT) based electronics [1, 2]. SWNTs are characterized by their outstanding electrical conductivity [3], extreme mechanical strength [4] and unique electronic structure. They may possess metallic conductivity, or act as wide or narrow gap semiconductor, depending on their chirality and doping level.

It is generally accepted that the electronic structure of SWNTs can be successfully altered by chemical modification of their internal channels. Encapsulation of nanotubes with electron-donor or electron-acceptor compounds allows one to increase or, accordingly, decrease an electron density on nanotube walls [5–7]. This makes it possible to control the electronic properties of SWNTs by intercalating an electron-acceptor or electron-donor substances and even form a p-n junction, for example, in the case of a partially-filled nanotube, which is essential for application in nanoelectronics. Moreover, encapsulation of perfect 1D crystals into nanotube channels enables one to take advantage of specific properties of nanocrystalline materials, including one-dimensional semiconductor, conductive or magnetic nanostructures. SWNTs are known as an atomically smooth and chemically inert template, which protects 1D

nanocrystal from the external influences, and enables one to take advantage of quasi-freestanding inorganic 1D crystals with atomically-designed electronic properties.

The properties of such one-dimensional crystals are known to differ drastically from that of the bulky phases [8]. For instance, band gap expansion has been observed for 1D crystals of SnSe, while a gapless energy spectrum was found for 1D crystals of SnTe [9, 10] or S [11]. It was even possible to detect 1D semiconductor crystal singularities in the electron DOS [9]. However, experimental works on the electronic structure of quasi-free standing nanocrystals are still very rare, which restricts the formulation of the general principles for the design of electronic properties for 1D nanocrystals on an atomic level.

The electronic structure of X@SWNT composite materials is known to be governed by the work function difference of SWNT and guest crystals [12]. To minimize crystal interaction with the SWNT, one needs to equalize the work functions of the guest compound to that of the SWNTs. Among others, PbTe with $\varphi = 4.52$ eV looks to be a promising candidate for growing quasi free-standing nanocrystals inside SWNTs. Therefore, in the present study we have focused on synthesis of PbTe@SWNT composites and determination of their atomic arrangement and electronic structure using HRTEM, optical absorption and Raman spectroscopies. Experimental data are supported by *ab-initio* calculation, showing metallic type of conductivity in the obtained nanostructures.

2. Experimental

SWNT were synthesized by the catalytic arc-discharge method using Y/Ni powder catalyst (atomic ratio 1:4) at 550 Torr helium pressure and electric current of 100 – 110 Å on 0.8 – 1.0 cm diameter graphite electrodes. The synthesized nanotubes were purified by a multistage purification process, which consisted of oxygen treatment at 350 – 400 °C and rinsing with HCl to remove the remaining catalyst. Then, SWNT were opened by aerobic treatment at 500 °C over 30 mins. Pre-opened nanotubes were filled using capillary technique. SWNTs were mixed with PbTe (Aldrich, 99.998 %) (mass ratio 1:10) and crushed in an agate mortar. The mixture was evacuated to a pressure of 10 – 5 mbar and sealed in a quartz ampule. The mixture in the ampule was treated at 1024 °C for 6 hours, which lead to filling of nanotubes with PbTe melt. Subsequent cooling at 0.1 °C/min to 944 °C, 0.02 °C/min to 904 °C and 0.1 °C/min to 824 °C resulted in formation of 1D PbTe crystals in the nanotube channels.

High-resolution transmission electron microscopy (HRTEM) was performed with FEI Titan 80 – 300 and Zeiss Libra 200 electron microscopes with a spherical/chromatic aberration correction. The samples were dispersed onto lacey carbon-coated grids. Optical absorption spectra were acquired using PerkinElmer Lambda 950 UV/Vis/NIR spectrophotometer with a spectral resolution of 1 nm. Raman spectroscopy was performed on a Renishaw InVia Raman spectroscope (based on a Leica DMLM microscope equipped with 100× lens) using a 20-mW 514-nm argon laser, a 17-mW 633-nm HeNe laser, and a 300-mW 785-nm NIR diode laser, variable power ND filters (power range 0.00005 – 100 %) and near-excitation tunable (NeXT) filters. A CCD camera with resolution 1024×532 pixels was used as a sensor. The resonance lines positions in the spectra were determined by least-squares fitting of experimental data by Voight function using WiRE 3.1 software. All Raman spectra were acquired at room temperature.

Ab-initio calculations were performed using Vienna *ab-initio* simulation package (VASP) software. The PAW-potential (Projector Augmented Wave potential) was used and the exchange-correlation energy was treated in a GGA (generalized gradient approximation). The first Brillouin zone integrations were made using Monkhorst and Pack approximation [13];

10 – 50 k-points were used for calculation. Plane-wave cut-off energies were chosen to be 400 eV.

3. Discussion

HRTEM is a powerful method to study structure of such systems, however, the high locality of this technique should be considered. For this reason, a large number of images were taken and analysis was performed for a total nanotube length of over 1000 nm. Fig. 1 shows the microphotograph of single SWNT filled with PbTe. The capillary technique resulted in successful encapsulation of PbTe and formation of a quasi-one-dimensional crystal inside the inner channel. According to statistical analysis, the composites are characterized by $\sim 80\%$ loading factor (i.e. the ratio between the filled internal space and the total internal volume), and over 70% crystallization factor (the fraction of filled nanotubes with a well-defined structure). These high numbers give evidence for the high efficiency of the chosen technique to produce PbTe quasi-one-dimensional crystals.

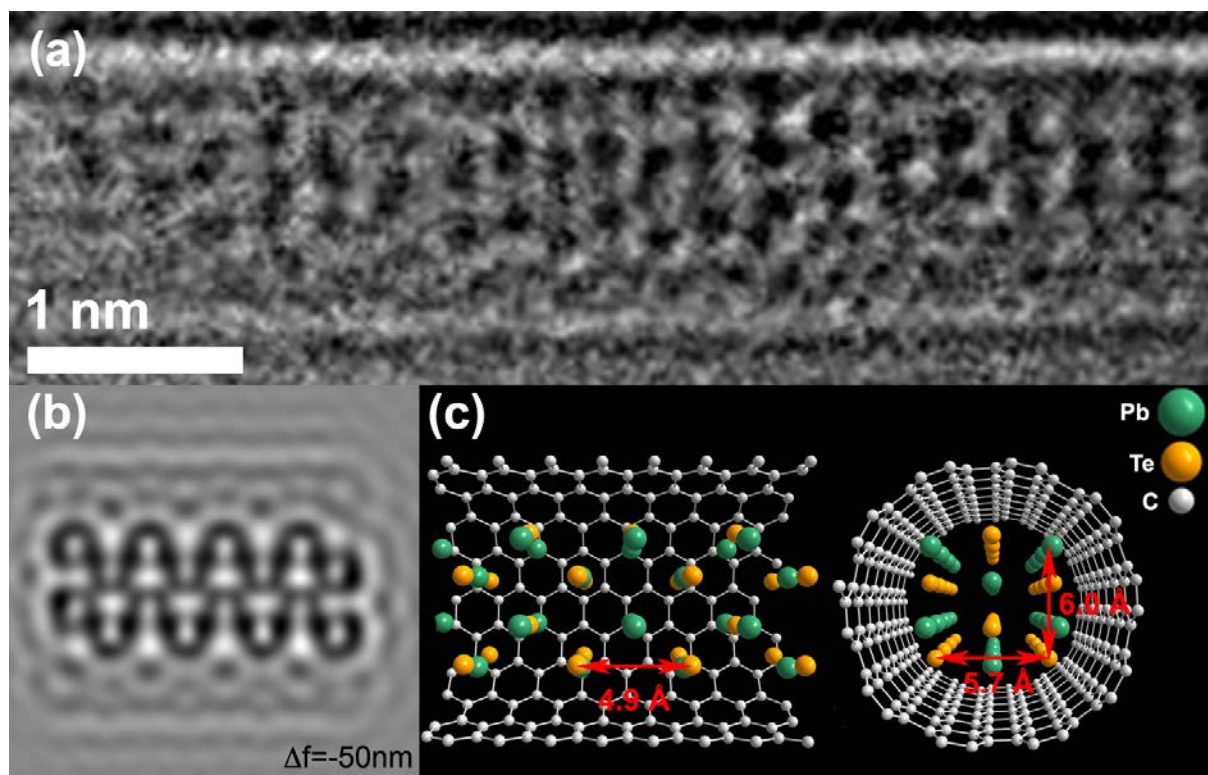


FIG. 1. HRTEM image of PbTe@SWNT (10,10) (a), simulated image (b) and calculated structure model (c)

Further analysis of HRTEM data allowed us to unveil atomic structure of encapsulated PbTe nanocrystals. The crystal periodicity along tube was found equal to be 5.0 \AA , and the distance between edging atomic columns equals 6.1 \AA . It is known that bulk PbTe crystallizes in a cubic rock salt structure. Taking this fact into account, and the diameter of SWNT of 1.4 nm the structure of the encapsulated crystal was suggested. This structure possesses 6 atoms in the cross-section and 12 atoms in the unit cell and can be derived by cutting the bulk structure along the $\langle 110 \rangle$ direction. The obtained structure was introduced into the inner channel of (10,10) SWNT and geometry of the whole system was optimized in VASP software package. The geometry of the resulting structure was verified by image simulation using SimulaTEM software.

The model fits well the experimental data. According to DFT modeling, encapsulation causes slight deformation of the crystal, which can be seen as slightly modified interatomic distances as compared to the bulk structure. The interatomic Pb-Te distance in bulk PbTe is 3.23 Å. Upon intercalation it changes to 2.97 Å along the nanotube axis, and 2.91 Å in the cross-section, as it is shown in Fig. 1. Such deformation can be caused by undercoordination of 1D crystal atoms. Notably, such compression will necessarily result in a change of the electronic structure of 1D nanocrystal compared to the bulk state.

An average diameter of the tubes obtained by HRTEM measurements (1.4 nm) is well supported by the optical absorption data, shown in Fig. 2. Peaks in the optical absorption spectrum correspond well with the allowed transitions between van Hove singularities of 1.4 – 1.6 nm semiconductor and metallic nanotubes [14]: 0.6 – 0.8 eV (E_{11}^S transition), 1.0 – 1.4 eV (E_{22}^S transition), 1.7 – 2.0 eV (E_{11}^M transition) and 2.3 – 2.5 eV (E_{33}^S transition). To analyze the structure of pristine SWNTs, Raman spectroscopy was employed (Fig. 3). According to optical spectroscopy, 785 nm (1.58 eV) irradiation resonantly excites E_{11}^M transition of metallic nanotubes with 1.5 – 1.6 nm diameter, 633 nm (1.96 eV) laser resonantly excites E_{11}^M transition of ~ 1.4 nm metallic nanotubes and ~ 1.6 nm semiconducting nanotubes, and exposure to 514 nm (2.41 eV) laser leads to resonant excitation of E_{33}^S transition of semiconducting tubes in the sample. The corresponding Raman spectra are shown in Fig. 3. Detailed analysis of obtained spectra, including SWNT chirality sets present the studied sample as derived from RBM- and G-modes positions is presented in Table 1.

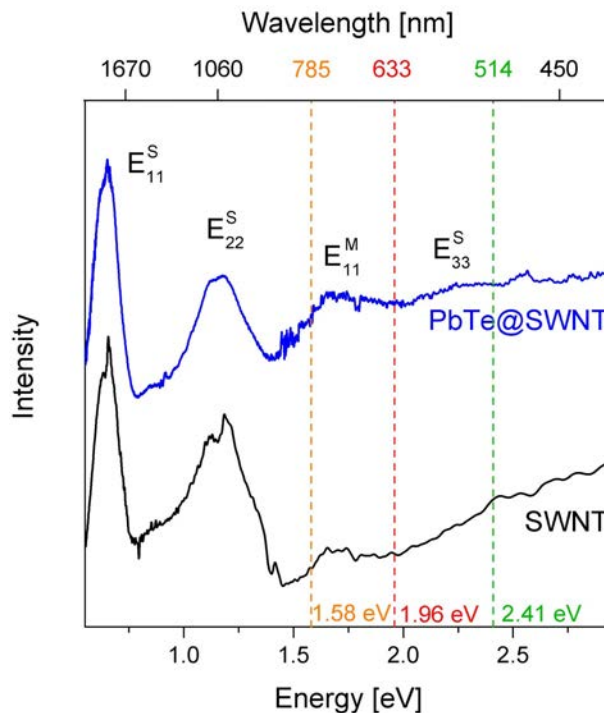


FIG. 2. Optical absorption spectra of pristine SWNT and PbTe@SWNT. Dashed lines indicate excitation laser energy used in Raman spectroscopy

Optical absorption data for PbTe@SWNT composites reveal no significant effect of PbTe intercalation on the electronic structure of SWNTs. No detectable energy shifts of the allowed transitions between van Hove singularities or intensity redistribution were observed, which points towards the possibility of electronic structure description in the framework of the rigid band structure model. Moreover, this also indicates that Fermi level shift does not exceed

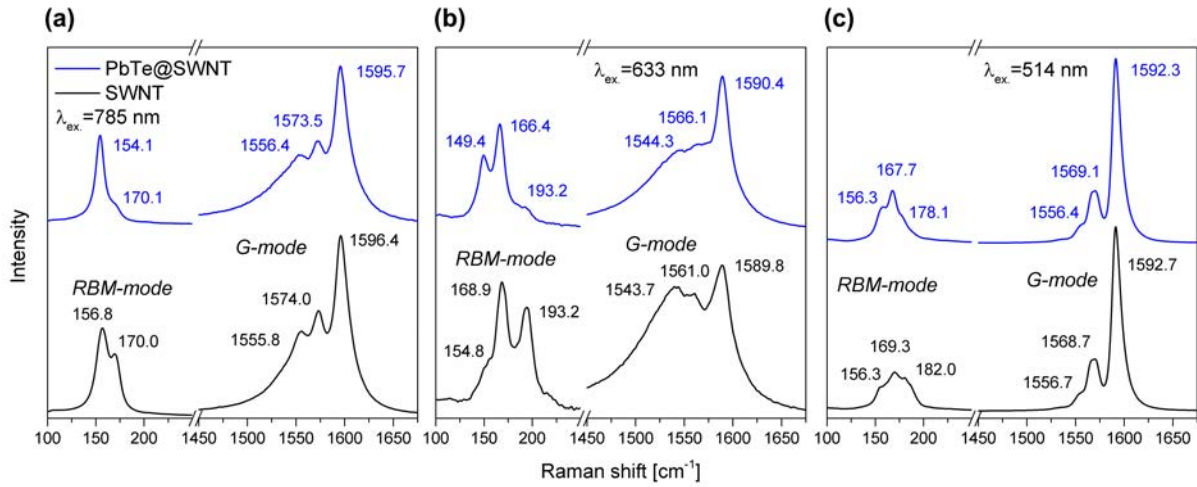


FIG. 3. Raman spectra of pristine SWNT and PbTe@SWNT obtained with 785 nm, 633 nm and 514 nm laser excitation

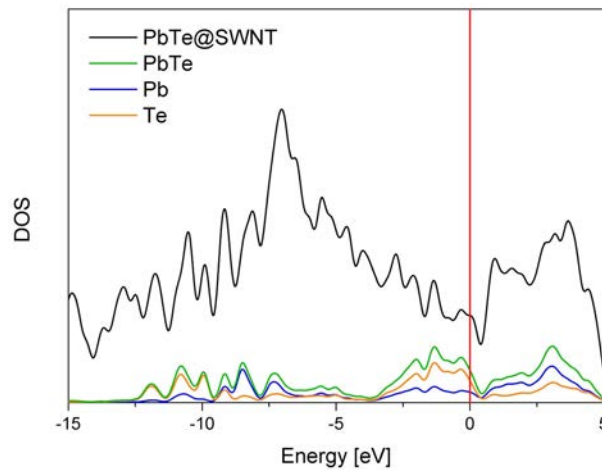


FIG. 4. Calculated density of states of PbTe 1D crystal inside (10,10) SWNT. Red line indicates Fermi level

0.3 eV (first van Hove singularity). Raman spectra acquired at 785 nm, 633 nm and 514 nm laser excitation wavelengths show only slight modification of RBM- and G-band frequencies (Table 2), illustrating no change of resonant excitation conditions and weak interaction between intercalated PbTe crystal and SWNT. It should be noted, that Raman spectra of resonantly excited metallic tubes (633 and 785 nm excitation, Fig. 3a, b) in PbTe@SWNT sample also shows typical ‘metallic’ G-band profile, while the effect on the metallic tubes is known to be most pronounced in the Raman spectra of doped SWNTs [15, 16]. This points towards the metallic conductivity of PbTe@m-SWNTs. The obtained data suggest the absence of chemical bonding between guest PbTe crystal and nanotube and formation of quasi-free-standing PbTe nanocrystal inside SWNT. Similar behavior was observed early for nanotubes filled with SnTe [9].

The obtained experimental data was supported by *ab-initio* calculations. No significant SWNT-PbTe interactions or localized states were obtained by modeling from C1s chemical shifts of carbon atoms. This is in line with earlier peculiarities of SWNT guest crystal interactions due to work function difference [12]. Density of the electronic states near Fermi level was derived for the optimized structure (Fig. 1b,c). Resulting DOS for PbTe@SWNT(10;10) composite

TABLE 1. Structural parameters of raw SWNT according to the Raman spectroscopy

Excitation energy [eV]	Dominant ω_{RBM} [cm^{-1}]	ω_{G+} [cm^{-1}]	Nanotube diameter [nm]	Nanotube type	Possible chiralities
1.58	156.8*	1555.8	1.45	<i>m</i> -SWNT	(14, 7)*, (16, 4), (15, 6)
	170.0	1574.0 1596.4	1.33	<i>s</i> -SWNT	(13, 6)*, (10, 9)*, (14, 4)
1.96	154.8	1543.7	1.47	<i>m</i> -SWNT	(15, 6)*, (16, 4)*, (12, 9)
	168.9*	1561.0 1589.8	1.34	<i>m</i> -SWNT	(15, 3)*, (16, 1)*, (11, 8)
2.41	156.3	1556.7	1.46	<i>s</i> -SWNT	(11, 10)*, (15, 5), (14, 6)
	169.3*	1568.6	1.34	<i>s</i> -SWNT	(13, 6)*, (12, 7)*, (10, 9)
	182.0	1592.2	1.24	<i>s</i> -SWNT	(15, 1)*, (12, 5), (11, 6)

* Predominantly excited SWNTs

TABLE 2. Positions of the RBM- and G-lines in the Raman spectra of pristine SWNTs and PbTe@SWNT composites acquired at different excitation laser wavelength. The shifts of the peak positions are given in parentheses

Sample	Excitation energy [eV]	Dominant ω_{RBM} [cm^{-1}]	Possible SWNT diameter and type	$\omega_{G+}(\Delta\omega_{G+})$ [cm^{-1}]		
SWNT	1.58	156.8	1.45 nm <i>m</i> -SWNT	1555.8	1574.0	1596.4
PbTe@SWNT		154.1 (-2.7)	1.48 nm <i>m</i> -SWNT	1551.7 (-4.1)	1572.0 (-2)	1596.4 (0)
SWNT	1.96	168.9	1.34 nm <i>m</i> -SWNT	1543.7	1561.0	1589.8
PbTe@SWNT		166.4 (-2.5)	1.36 nm <i>m</i> -SWNT	1544.3 (+0.6)	1566.1 (+5.1)	1590.4 (+0.5)
SWNT	2.41	169.3	1.33 nm <i>s</i> -SWNT	1556.7	1568.6	1592.2
PbTe@SWNT		167.7 (-1.6)	1.33 nm <i>s</i> -SWNT	1556.4 (-0.3)	1569.1 (+0.5)	1592.3 (+0.3)

illustrates a non-zero density of states at the Fermi level position (Fig. 4). It should be noted that not only *m*-SWNT states contribute total DOS at Fermi level but also 1D PbTe, which conforms one-dimensional nanocrystal metallic character.

4. Conclusion

Single-walled carbon nanotubes filled with PbTe were synthesized using capillary filling of pre-opened SWNTs from melt and subsequent slow cooling. HRTEM study showed high efficiency of chosen technique which results in high loading and crystallinity factors. Structure of intercalated PbTe 1D crystal was studied using HRTEM and was found to correspond bulk

PbTe crystal cut along $\langle 110 \rangle$ direction. Slight compression of Pb-Te distances was observed in 1D nanocrystal as compared to bulk structure due to undercoordination of 1D crystal atoms. Electronic structure of PbTe@SWNT composite studied by an optical absorption and Raman spectroscopies showed no notable interaction of guest PbTe crystal with SWNT walls, which points towards the formation of quasi-free-standing 1D PbTe crystal inside SWNT. Experimental data are supported by *ab-initio* calculations for PbTe@SWNT(10,10) structure which show non-zero density of states at the Fermi level with contribution from both PbTe and SWNT, revealing the metallic conductivity of PbTe@SWNT.

Acknowledgements

SWNTs were synthesized at the Institute of Problems of Chemical Physics, RAS, Chernogolovka, Russia by A. V. Krestinin. The VASP program package calculations were performed using the SKIF MSU ‘Chebyshev’ and ‘Lomonosov’ supercomputers. This work was supported by Russian Science Foundation (Grant No. 14-13-00747).

References

- [1] P.G. Collins, H. Bando, A. Zettl. Nanoscale electronic devices on carbon nanotubes. *Nanotechnology*, 1998, **9** (3), P. 153–157.
- [2] L. Chico, V.H. Crespi, et al. Pure Carbon Nanoscale Devices: Nanotube Heterojunctions. *Phys. Rev. Lett.*, 1996, **76** (6), P. 971–974.
- [3] T.W. Ebbesen, H.J. Lezec, et al. Electrical conductivity of individual carbon nanotubes. *Nature*, 1996, **382**, P. 54–56.
- [4] M.M.J. Treacy, T.W. Ebbesen, J.M. Gibson. Exceptionally high Young’s modulus observed for individual carbon nanotubes. *Nature*, 1996, **381** (6584), P. 678–680.
- [5] P. Chaturvedi, P. Verma, et al. Carbon Nanotube–Purification and Sorting Protocols. *Def. Sci. J.*, 2008, **58** (5), P. 591–599.
- [6] M. Weissmann, G. Garca, et al. Theoretical study of iron-filled carbon nanotubes. *Phys. Rev. B*, 2006, **73**, (12), P. 125435.
- [7] M. Mahmudur Rahman, M. Kisaku, et al. Electric and Magnetic Properties of Co-filled Carbon Nanotube. *J. Phys. Soc. Jpn.*, 2005, **74** (2), P. 742–745.
- [8] A.S. Kumskov, V.G. Zhigalina, et al. The structure of 1D and 3D CuI nanocrystals grown within 1.5 – 2.5 nm single wall carbon nanotubes obtained by catalyzed chemical vapor deposition. *Carbon*, 2012, **50** (12), P. 4696–4704.
- [9] L.V. Yashina, A.A. Eliseev, et al. Growth and Characterization of One-Dimensional SnTe Crystals within the Single-Walled Carbon Nanotube Channels. *J. Phys. Chem. C*, 2011, **115** (9), P. 3578–3586.
- [10] A.S. Kumskov, A.A. Eliseev, B. Freitag, N.A. Kiselev. HRTEM of 1DSnTe@SWNT nanocomposite located on thin layers of graphite. *J. Microsc.*, 2012, **248** (2), P. 117–119.
- [11] T. Fujimori, A. Morelos-Gmez, et al. Conducting linear chains of sulphur inside carbon nanotubes. *Nat. Commun.*, 2013, **4**, P. 2162.
- [12] A. Eliseev, L. Yashina, M. Kharlamova, N. Kiselev. One-Dimensional Crystals inside Single-Walled Carbon Nanotubes: Growth, Structure and Electronic Properties. In *Electronic Properties of Carbon Nanotubes*, ed. by J. M. Marulanda, InTech, 2011.
- [13] H.J. Monkhorst, J.D. Pack. Special points for Brillouin-zone integrations. *Phys. Rev. B*, 1976, **13** (12), P. 5188–5192.
- [14] H. Kataura, Y. Kumazawa, et al. Optical properties of single-wall carbon nanotubes. *Synthetic Metals*, 1999, **103** (1), P. 2555–2558.
- [15] S. Piscanec, M. Lazzeri, et al. Optical phonons in carbon nanotubes: Kohn anomalies, Peierls distortions, and dynamic effects. *Phys. Rev. B*, 2007, **75** (3), P. 035427.
- [16] A.A. Eliseev, L.V. Yashina, et al. Interaction between single walled carbon nanotube and 1D crystal in CuX@SWCNT (X = Cl, Br, I) nanostructures. *Carbon*, **50** (11), P. 4021–4039.

Parameterization of an interaction operator of optical modes in a single-mode optical fiber

G. P. Miroshnichenko

ITMO University, St. Petersburg, 197101, Russia

gpmirosh@gmail.com

PACS 03.67.-a 03.67.Dd 42.50.-p 42.50.Ex 42.81.Qb

DOI 10.17586/2220-8054-2015-6-6-857-865

The phenomenological parameters of the Hamiltonian for the photons produced in earlier studies [4] are associated with the parameters of the deformed optical fiber (OF). This Hamiltonian is necessary for the correct description of the propagation of photons through the quantum channel in a quantum communication protocols. Models of a compressing strain of the OF profile and a twisting deformation are considered. As a consequence, the phenomenological parameters of the Hamiltonian expressed in terms of such strains characteristics, as a relative compression of the profile, OF radius, the orientation angle of the deformed profile, rotation angle per unit length, elasto-optical tensor, and refraction coefficient.

Keywords: Hamiltonian of photons, deformed optical fiber, quantum channel, phenomenological parameters of the Hamiltonian.

Received: 30 October 2015

1. Introduction

For an electromagnetic wave, an optical fiber (OF) represents a non-uniform stochastic anisotropic environment. The principles of radiation quantization in the non-uniform anisotropic environment are stated, for example, in works [1–3]. The Hamiltonian for the photons in a single mode OF was obtained in [4], taking into account the small, isotropic, inhomogeneous, smoothly varying (along the OF) addition to the tensor of the dielectric permittivity. Photons are defined on the basis of the normal modes of an ideal single-mode OF. In [4], the problem of mode interactions in an OF was resolved using a properly chosen gauge. The transversality of the electric displacement vector is provided. The Hamiltonian conserves the number of photons. We used the approach of smooth perturbations (by analogy with the classical method of coupled waves). In this approach, researchers neglect the interaction of oppositely directed waves. The permittivity tensor was parameterized by three phenomenological parameters that determine the interaction of orthogonally polarized modes of the OF.

The classical theory of information transmission in an OF is well developed. Of particular interest is the single mode OF, in which two perpendicular polarized waves can propagate, phase front which is close to the plane (HE_{11} mode, [5, 6]). Currently, a single mode OF with low absorption (in windows of transparency) has been developed. They find broad application in optical communication systems over long distances with high speed information transfer [7]. The distortion features have been studied in detail for classical information in a single mode OF. In [8], the effect of optical activity in a twisted single mode OF was considered. The relationship of the single-mode OF curvature with the effect of the birefringence is discussed in [9]. The effect of tension on the occurrence of anisotropy in the one mode OF was studied in [10].

The new direction of modern informatics (the science of methods of communication, storage and processing of information) involve optical quantum information technologies. Quantum communication protocols – quantum cryptography, quantum teleportation, dense coding [11, 12] operate on the principles of quantum optics. The coding of information on a photon's polarization and degrees of freedom were used in [13]. A scheme using phase encoding was presented in [14], while in-phase light modulation was utilized in [15]. Additionally, a quantum key distribution protocol, using entangled photon polarization states, was proposed in [16]. In [17] the generation of entangled biphoton states with orbital-angular-momentum in triangular quadratic waveguide arrays with twisted geometry was considered.

In the following works, the phenomenological parameters of the photon Hamiltonian obtained in [4], are associated with parameters of the OF strain. The phenomenological parameters of the Hamiltonian were determined by the inverse permittivity tensor averaged over the volume of the OF segment. The dielectric permittivity of a deformed OF depends on the deformation parameters. Models for a compressing strain of the OF profile and a twisting deformation are considered. As a consequence, the phenomenological parameters of the Hamiltonian are expressed in terms of such characteristics, as a relative compression of the profile, OF radius, the orientation angle of the deformed profile, rotation angle per unit length, elasto-optical tensor, and refraction coefficient.

2. The Hamiltonian of photons in a single mode OF

The Hamiltonians of photons in a single mode OF, expressed in terms of the operators $\hat{b}_{\beta\mu}^\dagger$, $\hat{b}_{\beta\mu}$, according to [4], has the form:

$$\hat{H} = \sum_{\beta} \omega(\beta) \left(\sum_{\mu=H,V} \left(\hat{b}_{\beta\mu}^\dagger \hat{b}_{\beta\mu} + \frac{1}{2} \right) + \frac{1}{2} \sum_{\mu,\mu'=H,V} \hat{b}_{\beta\mu}^\dagger \cdot \Delta\Xi_{\mu,\mu'}^{(\beta)} \cdot \hat{b}_{\beta\mu'} \right). \quad (1)$$

The formula is written in the approximation of a smooth dependence of the tensor $\varepsilon(\mathbf{r}) = \varepsilon_0(\mathbf{r}) + \Delta\varepsilon(\mathbf{r})$ on the longitudinal coordinate z . In this approximation, the Hamiltonian \hat{H} becomes single-mode, modes with different wave vectors do not interact. The matrix $\Delta\Xi^{(\beta)}$ has the form:

$$\Delta\Xi_{\mu,\mu'}^{(\beta)} = - \int dz \iint dx dy (\Delta\varepsilon(\mathbf{r}) \boldsymbol{\alpha}_{\beta,\mu}(x,y), \boldsymbol{\alpha}_{\beta,\mu'}^*(x,y)), \quad (2)$$

where $\Delta\varepsilon(\mathbf{r})$ – a random correction to the dielectric permittivity $\varepsilon_0(\mathbf{r})$ of the ideal OF. The emission quantized on the basis of modes for an ideal OF satisfy the following equation, boundary conditions and transversality conditions:

$$\begin{cases} \omega(\beta)^2 \varepsilon_0(\mathbf{r}) \mathbf{A}_{\beta,\mu}(\mathbf{r}) - c^2 \nabla \times \nabla \times \mathbf{A}_{\beta,\mu}(\mathbf{r}) = 0, \\ \nabla \cdot (\varepsilon_0(\mathbf{r}) \mathbf{A}_{\beta,\mu}(\mathbf{r})) = 0, \end{cases} \quad (3)$$

where $\omega(\beta)$ – eigenvalues, β – longitudinal wave vector, $\nabla \cdot$ – the divergence operation, $\nabla \times$ – the rotor operation, $\mathbf{A}_{\beta,\mu}(\mathbf{r}) = \boldsymbol{\alpha}_{\beta,\mu}(x,y) \cdot \exp(-i\beta z)$ – basis of spatial modes, $\mu = H, V$ – polarization index. The property of the basis orthogonality is as follows:

$$\int \varepsilon_0(\mathbf{r}) (\mathbf{A}_{\beta,\mu}(\mathbf{r}), \mathbf{A}_{\beta,\mu'}^*(\mathbf{r})) dV = \delta_{\mu,\mu'}.$$

We use a phenomenological description and parameterized of Hermitian matrix $\Delta\Xi^{(\beta)}$ (2):

$$\Delta\Xi^{(\beta)} = \begin{pmatrix} \varepsilon & \Gamma \cdot \exp(-i\delta) \\ \Gamma \cdot \exp(i\delta) & -\varepsilon \end{pmatrix}, \tag{4}$$

by the real parameters $\varepsilon, \Gamma, \delta$. The anisotropy and gyrotropy of the OF which arises from the random correction $\Delta\varepsilon(\mathbf{r})$ are thought to be small. That is, the parameters ε, Γ satisfy the following relation:

$$\Omega = \sqrt{\varepsilon^2 + \Gamma^2} \ll 1. \tag{5}$$

In a typical OF, the parameter $\Omega \approx 10^{-5} \div 10^{-7}$. Parameter $\Gamma \sin \delta$ is typically referred to as the component optical activity vector (along the OF axis) [18]. If the axis of the laboratory coordinate system does not coincide with the axes of the OF, the photons in the laboratory frame of reference, determined by the operators $\hat{b}_{\beta\mu}^\dagger, \hat{b}_{\beta\mu}, \mu = H, V$ interact.

3. Guided modes of weakly guiding fiber

We consider the case of the so-called weakly guiding cylindrical OF. Fiber parameters satisfy the inequality:

$$\frac{n_c^2 - n_{cl}^2}{2n_c^2} \ll 1, \tag{6}$$

where n_c, n_{cl} – the refractive indices of the core and cladding of OF. We will choose the axis z of the laboratory coordinate system along the axis of the OF segment. In an ideal OF, the dielectric permittivity $\varepsilon_0(\mathbf{r})$ depends on the transverse coordinates – x, y . Analysis of the solutions for equation (3) shows [19] that there are OF waveguide (guided) modes with a discrete spectrum of frequencies and not guided modes having a continuous spectrum. Under the condition (6), often implemented in practice, the structure of the guided modes is simplified. Of special interest for this practice is the so-called single-mode OF, in which one doubly-degenerate mode HE_{11} can be propagated. The refraction coefficient of the OF has the form of a step depicted in Fig. 1. We obtain the solution (3) for the mode HE_{11} . The first vector \mathbf{A}_H is horizontal $q = H$:

$$\begin{aligned} \mathbf{A}_H &= \boldsymbol{\alpha}_H(x, y) \cdot \exp(-i\beta z), \\ \boldsymbol{\alpha}_H(x, y) &= \alpha_H(x, y)_y \mathbf{j} + \alpha_H(x, y)_z \mathbf{k}. \end{aligned}$$

The solution in the two regions (region 1: $r \leq a$, region 2: $r > a$) has the form:

$$\begin{cases} \begin{cases} \alpha_H^{(1)}(r, \phi)_x = 0, \\ \alpha_H^{(1)}(r, \phi)_y = A \cdot \frac{J_0(ur/a)}{J_0(u)}, \\ \alpha_H^{(1)}(r, \phi)_z = A \cdot \frac{i u J_1(ur/a)}{a\beta J_0(u)} \sin \phi, \end{cases} & r \leq a \\ \begin{cases} \alpha_H^{(2)}(r, \phi)_x = 0, \\ \alpha_H^{(2)}(r, \phi)_y = A \cdot \frac{K_0(wr/a)}{K_0(w)}, \\ \alpha_H^{(2)}(r, \phi)_z = A \cdot \frac{i w K_1(wr/a)}{a\beta K_0(w)} \sin \phi. \end{cases} & r > a \end{cases} \tag{7}$$

The second vector \mathbf{A}_V is vertical $q = V$:

$$\begin{aligned}\mathbf{A}_V &= \boldsymbol{\alpha}_V(x, y) \cdot \exp(-i\beta z), \\ \boldsymbol{\alpha}_V(x, y) &= \alpha_V(x, y)_x \mathbf{i} + \alpha_V(x, y)_z \mathbf{k}.\end{aligned}$$

The solution in the two regions (region 1: $r \leq a$, region 2: $r > a$) has the form:

$$\left\{ \begin{array}{l} \alpha_V^{(1)}(r, \phi)_x = A \cdot \frac{J_0(ur/a)}{J_0(u)}, \\ \alpha_V^{(1)}(r, \phi)_y = 0, \\ \alpha_V^{(1)}(r, \phi)_z = A \cdot \frac{iu}{a\beta} \frac{J_1(ur/a)}{J_0(u)} \cos \phi, \end{array} \right. \quad r \leq a \quad (8)$$

$$\left\{ \begin{array}{l} \alpha_V^{(2)}(r, \phi)_x = A \cdot \frac{K_0(wr/a)}{K_0(w)}, \\ \alpha_V^{(2)}(r, \phi)_y = 0, \\ \alpha_V^{(2)}(r, \phi)_z = A \cdot \frac{iw}{a\beta} \frac{K_1(wr/a)}{K_0(w)} \cos \phi. \end{array} \right. \quad r > a$$

The dispersion relation $\omega = \omega(\beta)$ for the mode HE_{11} , from the transversality conditions (3) has the form:

$$\begin{aligned}u \frac{J_1(u)}{J_0(u)} &= w \frac{K_1(w)}{K_0(w)}, \\ u &= a \cdot \chi, \quad w = a \cdot \gamma, \\ \chi^2 &= \left(\frac{\omega}{c} n_c\right)^2 - \beta^2, \\ \gamma^2 &= \beta^2 - \left(\frac{\omega}{c} n_{cl}\right)^2.\end{aligned}$$

Here A is the the normalization factor. The normalization A has the form:

$$A = \frac{w^2}{\sqrt{\pi L a} (n_c w^2 + n_{cl} u^2)} \left(\frac{J_0(u)}{J_1(u)} \right)^2.$$

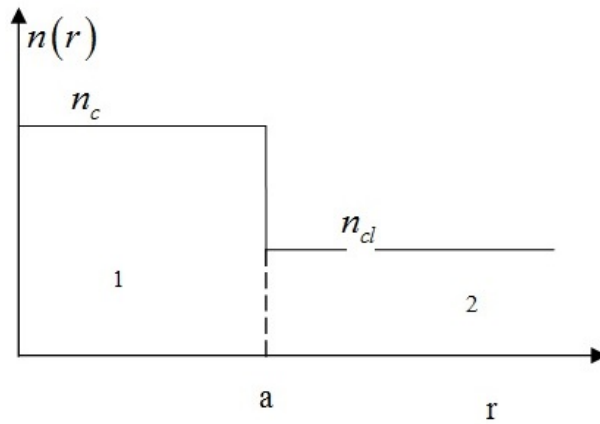


FIG. 1. The dependence of the refractive index $n(r)$ on the radial coordinate r in the cylindrical OF. n_c , n_{cl} – the refractive indices of the core and cladding of OF. 1, 2 – the core and cladding regions. a – the core radius

The dependence of frequency (for HE_{11} mode) on a dimensionless longitudinal wave vector $\beta \cdot a$ is shown in Fig. 2.

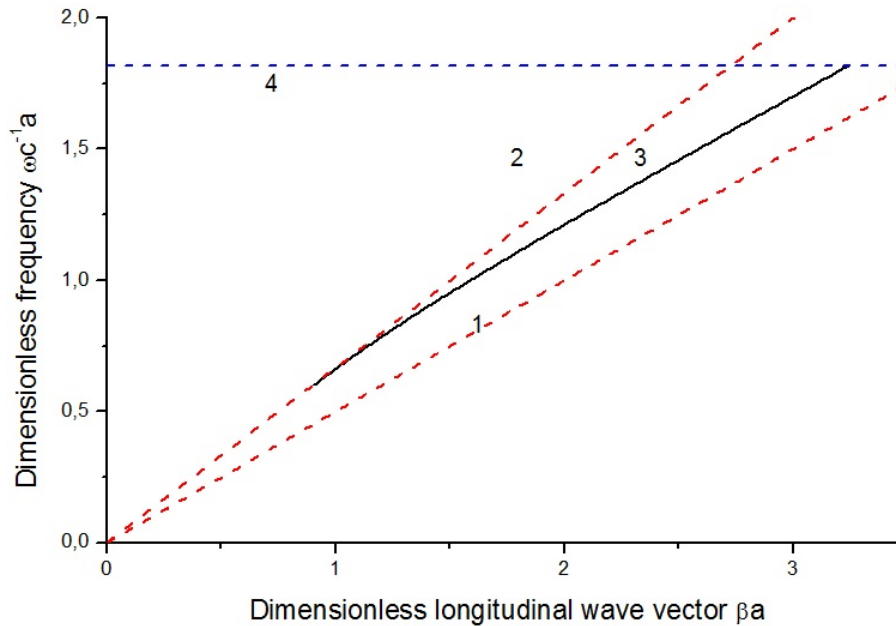


FIG. 2. The dispersion relation $\omega = \omega(\beta)$ for the mode HE_{11} , Plot 3. Plot 1 – the dispersion relation of the core $\omega = \beta a/n_c$. Plot 2 – the dispersion relation of the cladding $\omega = \beta a/n_{cl}$. Plot 4 – limit value of frequency $\omega a/c = 2.405/\sqrt{n_c^2 - n_{cl}^2}$. The wave vector multiplied by the radius of the core – βa – delayed along the horizontal axis. Value $\omega a/c$ is plotted along the vertical axis

4. Nonideal optical fiber

In the previous section, we obtained the basis of modes and dispersion relation for an ideal OF. In order to completely define a Hamiltonian for photons (1), it is necessary to connect phenomenological parameters ε , Γ , δ with the parameters of the OF. For this purpose we consider two models describing the dependence of the dielectric permittivity of the OF on a profile distortion and twisting of the OF [8–10]. The perturbation of the dielectric permittivity due to the deformation form of the OF is a scalar, and according to [8–10], has the form:

$$\Delta\varepsilon(r, \varphi) = -\eta \cdot r \cdot \varepsilon_0(r) \cos 2(\varphi - \varphi_B). \quad (9)$$

This perturbation connects z components (longitudinal components) of the two wave modes A_H and A_V . The graph of the OF cross section distorted by compression is submitted in Fig. 3. The oval cross section has the main axes turned in relation to laboratory system of coordinates on a angle φ_B . Calculation of a matrix $\Delta\Xi^{(\beta)}$ with use formulas (2), (7), (8), (9) yields the following result:

$$\Delta\Xi^{(\beta)} = \frac{\Delta(\beta) \eta a}{2} \begin{pmatrix} -\cos(2\varphi_B) & \sin(2\varphi_B) \\ \sin(2\varphi_B) & \cos(2\varphi_B) \end{pmatrix}.$$

Let's compare this matrix to matrix (4). We get a connection the phenomenological parameters ε , Γ , δ with the deformation parameters of the OF:

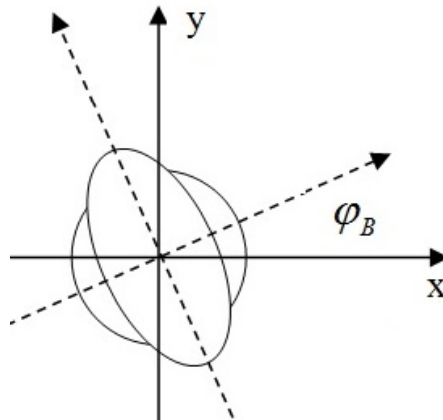


FIG. 3. Distortion of a OF core profile. η – relative compression of a profile $\varepsilon_0(r)$ at an angle φ_B

$$\begin{aligned} \delta &= 0, \\ \varepsilon &= -\frac{\Delta(\beta)\eta a}{2} \cos(2\varphi_B), \\ \Gamma &= \frac{\Delta(\beta)\eta a}{2} \sin(2\varphi_B). \end{aligned}$$

There, $\Delta(\beta)$ is the normalization function:

$$\Delta(\beta) = \frac{1}{4\pi a^2 \beta^2} \frac{n_c u^2 J_0^{-2}(u) \int_0^1 r^2 dr J_1^2(ur) + n_{cl} w^2 K_0^{-2}(w) \int_1^\infty r^2 dr K_1^2(wr)}{n_c J_0^{-2}(u) \int_0^1 r dr J_0^2(ur) + n_{cl} K_0^{-2}(w) \int_1^\infty r dr K_0^2(wr)}. \tag{10}$$

The graph of normalized function (10) is shown in Fig. 4. Distortion of the OF’s permeability tensor with twist deformation is described by formulas [8–10]:

$$\begin{aligned} \Delta\varepsilon(r, \varphi)_{yz} &= \Delta\varepsilon(r, \varphi)_{zy} = -p_{44} n_0^4 \tau \cdot x, \\ \Delta\varepsilon(r, \varphi)_{xz} &= \Delta\varepsilon(r, \varphi)_{zx} = p_{44} n_0^4 \tau \cdot y. \end{aligned} \tag{11}$$

where, x, y – transverse coordinates in the laboratory frame, τ – the angle of twist per unit length, n_0 – the average refractive index of the OF material, $p_{n,m}$ – elasto optical tensor. The scheme for twist deformation is shown in Fig. 5. Calculation of a matrix $\Delta\Xi^{(\beta)}$ with use formulas (2), (7), (8), (9) yields the following result:

$$\Delta\Xi^{(\beta)} = a\tau p_{44} n_0^4 S(\beta) \begin{pmatrix} 0 & -i \\ i & 0 \end{pmatrix}.$$

Let’s compare this matrix to matrix (4). We obtain a connection between the phenomenological parameters $\varepsilon, \Gamma, \delta$ with the deformation parameters of the OF:

$$\begin{aligned} \delta &= \frac{\pi}{2}, \\ \varepsilon &= 0, \\ \Gamma &= a\tau p_{44} n_0^4 S(\beta). \end{aligned}$$

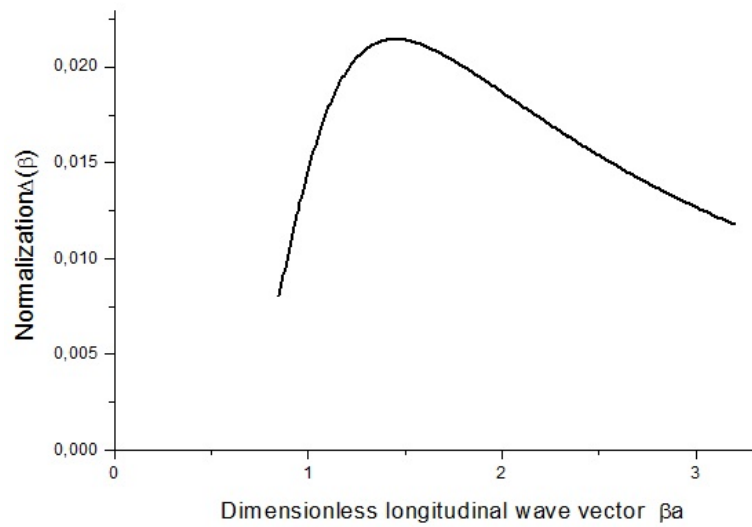


FIG. 4. The normalization function $\Delta(\beta)$, calculation by formula (10) for $n_c = 2, n_{cl} = 1.5$

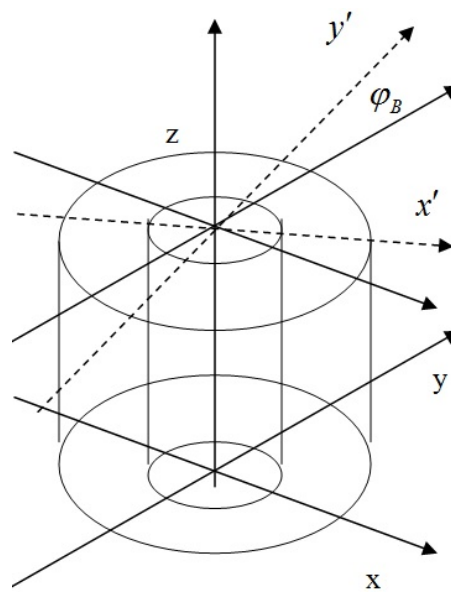


FIG. 5. The twist deformation of OF. There τ – angle of twist per unit length z . $n_0 = 1.46$ – the average refractive index of the OF material. $p_{44} = -0.075$ – elasto optical tensor, uniform along the fiber. The remaining coefficients of the permittivity tensor are zero. x, y – transverse coordinates of OF (laboratory frame), x', y' – transverse coordinates of OF (local frame), $\varphi_B = \tau z$

Here, the normalizing function $S(\beta)$ is defined in the following manner:

$$S(\beta) = \frac{1}{a\beta} \frac{n_c u J_0^{-2}(u) \int_0^1 r^2 dr J_1(ur) J_0(ur) + n_{cl} w K_0^{-2}(w) \int_1^\infty r^2 dr K_1(wr) K_0(wr)}{n_c J_0^{-2}(u) \int_0^1 r dr J_0^2(ur) + n_{cl} K_0^{-2}(w) \int_1^\infty r dr K_0^2(wr)}. \quad (12)$$

The graph of normalization function is shown in Fig. 6.

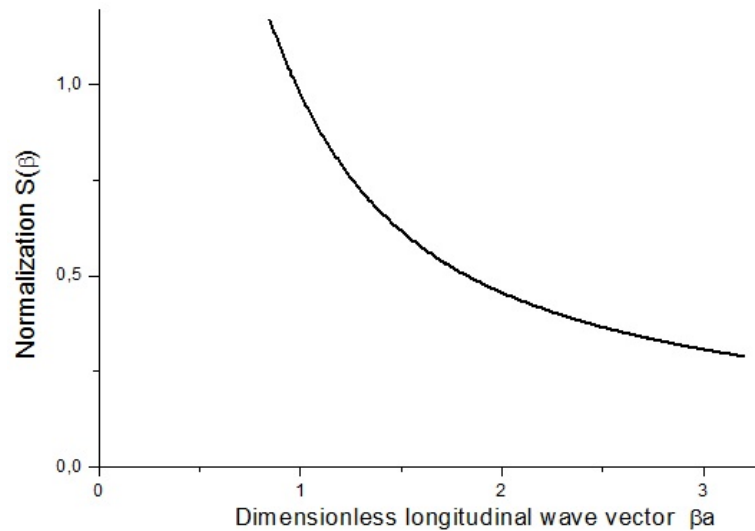


FIG. 6. The normalization function $S(\beta)$, calculation by formula (12) for $n_c = 2$, $n_{cl} = 1.5$

5. Conclusion

Quantum information, distributed by the OF, is encoded in the quantum states of photons. The transformation of information during the propagation of the photons through the OF is described by the Liouville equation for the density matrix of the photons. The Hamiltonian for the OF-based photons is required to write a quantum Liouville equation. The Hamiltonian of photons in the OF (1) contains phenomenological parameters ε , Γ , δ . These parameters depend on the longitudinal coordinate of the wave vector, β , and thus, determine the polarization mode for the dispersion of photons in the OF. To obtain the relationship between the phenomenological parameters ε , Γ , δ and β , we must use the distortion model for the optical and geometric characteristics of the OF against external influences. For this purpose, the model transverse compression and twist of the OF [8–10] were used in this work and the relationship between parameters ε , Γ , δ and β were determined in this work.

Acknowledgments

This work was partially financially supported by the Government of the Russian Federation (grant 074-U01), by Ministry of Education and Science of the Russian Federation (GOSZADANIE 2014/190, Project 14.Z50.31.0031 and ZADANIE No. 1.754.2014/K), by grant of Russian Foundation for Basic Researches and grant of the President of Russia (MK-2736.2015.2).

References

- [1] K. Nagy, T. Tel. Phenomenological quantum electrodynamics of anisotropic media. *Acta Phys. Acad. Sci. Hun.*, 1981, **51**, P. 125–137.
- [2] R.J. Glauber, M. Lewenstein. Quantum optics of dielectric media. *Phys. Rev. A*, 1991, **43**, P. 467–491.
- [3] L. Knoll, W. Vogel, D.G. Welsch. Action of passive, lossless optical systems in quantum optics. *Phys. Rev. A*, 1987, **36**, P. 3803–3818.
- [4] G.P. Miroshnichenko. Hamiltonian of Photons in a Single Mode Optical Fiber for Quantum Communications Protocols. *Optics and Spectroscopy*, 2012, **112** (5), P. 777–786.
- [5] S. Solimeno, B. Crosignani, P. Di Porto. *Guiding, diffraction, and confinement of optical radiation*. Academic Press Inc., 1986.

- [6] D. Gloge. Weakly Guiding Fibers. *Appl. Opt.*, 1971, **10**, P. 2252–2258.
- [7] D.J. Sterling Jr. *Technician's Guide to Fiber Optics*, Second Edition. Delmar Publishers Inc., 1993.
- [8] R. Ulrich, A. Simon. Polarization optics of twisted single-mode fibers. *Appl. Opt.*, 1979, **18**, P. 2241–2251.
- [9] R. Ulrich, S.C. Rashleigh, W. Eickhoff. Bending-induced birefringence in single-mode fibers. *Opt. Lett.*, 1980, **5**, P. 273–275.
- [10] S.C. Rashleigh, R. Ulrich. High birefringence in tension-coiled single-mode fibers. *Opt. Lett.*, 1980, **5**, P. 354–356.
- [11] M.A. Nielsen, I.L. Chuang. *Quantum Computation and Quantum Information*. Cambridge University Press, Cambridge, 2000.
- [12] D. Bouwmeester, A. Ekert, A. Zeilinger. *The Physics of Quantum Information*. Springer, Berlin, 2000.
- [13] A. Muller, H. Zbinden, N. Gisin. Quantum cryptography over 23 km in installed under-lake telecom fibre. *Europhys. Lett.*, 1996, **33**, P. 335–339.
- [14] G. Ribordy, J.-D. Gautier, et al. Fast and user-friendly quantum key distribution. *Mod. Opt.*, 2000, **47**, P. 517–531.
- [15] J.-M. M'erolla, Y. Mazurenko, J.-P. Goedgebuer, W.T. Rhodes. Single-Photon Interference in Sidebands of Phase-Modulated Light for Quantum Cryptography. *Phys. Rev. A*, 1999, **82**, P. 1656–1659.
- [16] A.K. Ekert. Quantum cryptography based on Bell's theorem. *Phys. Rev. Lett.*, 1991, **67**, P. 661–663.
- [17] D.N. Vavulin, A.A. Sukhorukov. Numerical solution of Schrodinger equation for biphoton wave function in twisted waveguide arrays. *Nanosystems: Phys., Chem., Math.*, 2015, **6** (5), P. 689–696.
- [18] L.D. Landau, E.M. Lifshitz, L.P. Pitaevskii. *Electrodynamics of continuous media*, 2nd ed., Elsevier, 2004.
- [19] D. Marcuse. *Theory of Dielectric Optical Waveguides*. Boston, MA:Academic, 1991.

Crystallization behavior and morphological features of YFeO_3 nanocrystallites obtained by glycine-nitrate combustion

V. I. Popkov^{1,3}, O. V. Almjashaeva^{2,3}, V. N. Nevedomskiy³, V. V. Sokolov³, V. V. Gusarov^{1,2,3}

¹ Saint Petersburg State Technological Institute (Technical University),
190013, St. Petersburg, Moskovsky prospect 26

² Saint Petersburg Electrotechnical University “LETI”,
197376, St. Petersburg, Professora Popova str. 5

³ Ioffe Physical Technical Institute,
194021, St. Petersburg, Politekhnikeskaya str. 26
vadim.i.popkov@gmail.com, almjashaeva@mail.ru

PACS 61.46.+w

DOI 10.17586/2220-8054-2015-6-6-866-874

Yttrium orthoferrite nanocrystallites with hexagonal and orthorhombic structures were obtained directly by the glycine-nitrate synthesis. The nanocrystallites have plate-like morphology and are strongly agglomerated in highly-porous structures, as was shown by the TEM investigation. The influences of the synthesis conditions on the yttrium orthoferrite crystallization, its nanocrystallite size and morphology are discussed.

Keywords: yttrium orthoferrite, YFeO_3 , glycine-nitrate combustion, nanoparticles.

Received: 30 October 2015

Revised: 2 November 2015

1. Introduction

Direct solution combustion synthesis of oxide nanoparticles is of great interest currently because of its rapidity, simplicity and cost effectiveness [1–13]. Nanoparticles obtained by this method, as a rule, possess comparatively narrow size distribution and high surface area [5–7], which provides the possibility for its industrial and technical use. In some cases, combustion products may take on the role of precursors for obtaining new nanostructures of another principal morphology, structure and surface state [14–16]. This and other factors have led to an increased number of research efforts having been dedicated to combustion synthesis in recent years.

Yttrium orthoferrite is the one of the most interesting representatives of the complex oxide multiferroics – materials that are both ferroelectric and magnetic. Previously, this compound had been obtained in a nanostructured state by a number of so-called ‘soft-chemical’ methods [17–23], including combustion methods [24–28]. Despite the successful synthesis of yttrium orthoferrite nanoparticles from different initial solutions, it should be noted that data about processes leading to YFeO_3 nanosized particle formation as well as about influence of synthetic conditions on its results are quite limited.

The present paper is an expansion of the investigations which were initiated previously [26–28] and aims to obtain detailed information about the interrelation between synthetic conditions, composition, structure, dispersity and properties of yttrium orthoferrite nanoparticles, obtained by glycine-nitrate combustion. This work will accomplish this by analyzing the phase composition, crystallinity and morphology features of yttrium orthoferrite nanocrystallites formed under combustion.

2. Experimental

2.1. Synthesis procedure

Yttrium orthoferrite nanocrystallites were obtained by combustion of a glycine-nitrate precursor with the glycine to total yttrium and iron nitrates ratio equal to 2.4, 3.0, 3.3, 3.6 and 4.2. This procedure was described in detail previously in work [26].

Glycine H_2NCH_2COOH (p.a.) was added in the required ratio to a solution of iron (III) nitrate $Fe(NO_3)_3$ (pur.) and yttrium nitrate $Y(NO_3)_3$ (puriss.), taken in equimolar amounts. The resulting solution changed the color to dark brown due to the formation of glycine complex with metal cations. Then, the solution was heated until complete water evaporation and then self-ignition occurred that resulted in formation of brown fluffy powder.

Then products of glycine-nitrate combustion were calcined at 800 °C for 15 minute to remove impurities associated with incomplete combustion products, predominantly consisting of carbon black.

2.2. Characterization of the prepared samples

The elemental composition of the specimens was analyzed by means of scanning electron microscopy (SEM) using a Hitachi S-570, coupled with Oxford Link Pentafet microprobe analyzer.

The phase composition of the specimens were controlled by powder X-ray diffraction (XRD) using a Shimadzu XRD-7000 with monochromatic $CuK\alpha$ radiation ($\lambda = 0.154051$ nm). Qualitative X-Ray analysis was carried out with powder base of the diffraction data PDF2-2012 using, quantitative X-Ray analysis was carried out with using of the Rietveld method [29]. Average crystallite size for spherical nanoparticles was calculated according to Scherer's formula [30]:

$$D = \frac{0.9 \cdot \lambda}{\beta \cdot \cos(\theta)},$$

where λ – X-ray wavelength, β – full width at half-maximum, θ – Bragg angle.

Specific surface areas were determined with Micromeritics ASAP 2020 by the BET method using nitrogen as the adsorbant. Pycnometric densities were measured with using Micromeritics AccuPyc 1330 helium pycnometer. Average wall thickness of the pores was estimated using the formula for an infinite plate of finite thickness, by which in the first approximation, we described the morphology of the system:

$$h = \frac{2}{S \cdot \rho},$$

where h – average wall thickness of the pores, S – specific surface area and ρ – density of the sample.

Transmission electron microscopy (TEM) image was taken on a JEOL TEM-100CX transmission electron microscope.

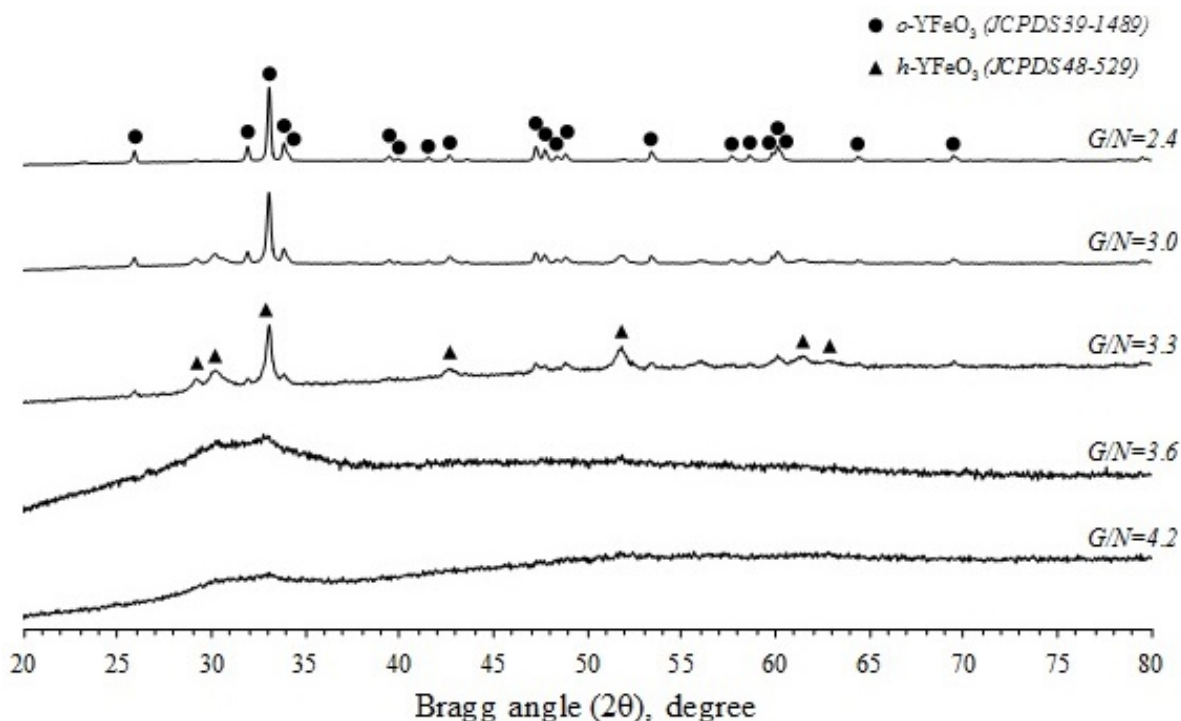
3. Results and discussion

Results of elemental analysis for compositions obtained after glycine-nitrate combustion showed that molar ratio Fe:Y equals to stoichiometric value for all the samples in the range of the method error [31] (Table 1).

According to the results of XRD analysis (Fig. 1), the phase composition of the combustion products strongly depends on the G/N ratio of the initial solution.

TABLE 1. X-ray microanalysis results of the glycine-nitrate combustion products

G/N	Fe:Y molar ratio, %	
	X-ray microanalysis	Synthesis
2.4	51.0:49.0	50:50
3.0	50.4:48.6	
3.3	51.3:48.7	
3.6	49.4:50.6	
4.2	50.8:49.2	

FIG. 1. XRD patterns of glycine-nitrate combustion products obtained at different G/N ratio

As one can observe, samples obtained at a glycine to nitrate ratio equal to 3.6 and 4.2 are X-ray amorphous. However with glycine molar fraction increasing, hexagonal (h - $YFeO_3$) and orthorhombic yttrium ferrite (o - $YFeO_3$) phase appearances are observed in XRD patterns samples. Finally at a G/N ratio of 2.4, the sample almost completely consists of stable o - $YFeO_3$ phase. The possible reasons for the considered system's behavior were discussed in earlier works [26,27] as well as the amorphous, hexagonal and orthorhombic phases' relations to their synthesis by glycine-nitrate combustion processes.

On the basis of XRD results, quantitative phase and disperse composition of the samples were obtained (Table 2). Additional data about pycnometric density and specific surface area are also shown.

TABLE 2. Phase and disperse compositions, pycnometric density and specific surface area of glycine-nitrate combustion products

G/N	Mole fraction, %			Average crystallite size, nm		Pycnometric density, g/cm^3	Specific surface area, m^2/g
	<i>o</i> - $YFeO_3$	<i>h</i> - $YFeO_3$	amorphous phase	<i>o</i> - $YFeO_3$	<i>h</i> - $YFeO_3$		
2.4	95.4	4.6	0	49 ± 5	< 7	5.3544	5.8
3.0	46.3	42.7	11.0	42 ± 4		5.0627	27.0
3.3	12.9	48.3	38.8	31 ± 3		4.2964	35.0
3.6	0	0	100	–	–	3.5366	24.8
4.2	0	0	100	–	–	2.9045	14.8

As it is shown in Table 2, the pycnometric density of the samples decreases with an increasing of amorphous phase mole fraction, which consist of amorphous $YFeO_3$ as well as of incomplete combustion products and absorbed water [28]. But even for a sample with G/N ratio of 2.4, its pycnometric density is quite far from X-ray densities for pure hexagonal and orthorhombic phases – 5.526 and 6.195 g/cm^3 respectively. This can be explained by the presence of closed porosity in the samples which can reach values of 30 % and higher.

The dependence of specific surface area upon the glycine/nitrates ratio is more complicated and has maximum (about 35 m^2/g) at G/N ratio equal to 3.3. This may be explained by decisive contribution of the hexagonal ultradisperse $YFeO_3$ phase in total surface area. Thus, in the G/N ratio range of 2.4 – 3.3 increasing of hexagonal $YFeO_3$ mole fraction causes an increase in the specific surface area of the sample. It should be noted that for the X-ray amorphous samples ($G/N = 3.6$ and 4.2) the observed total surface area decrease with higher G/N ratio may be due to the fouling of surface and porous structure by incomplete combustion products under conditions of excess glycine.

Compositions obtained by the glycine-nitrate combustion were then calcined at 800 °C for 15 minutes, which resulted in its significant weight loss and formation of monophasic samples of orthorhombic yttrium ferrite for all G/N ratios. Relative weight loss of the samples and average crystallite sizes of *o*- $YFeO_3$ depending on glycine to nitrates ratio in initial solution are shown in Fig. 2.

As one can see, the maximum weight loss after calcination is constant for the samples with high glycine excess toward its stoichiometric amount and reaches about 20 % for $G/N = 4.2$. Weight loss decreases monotonically with a decreasing glycine to nitrate ratio and for the sample with $G/N = 2.4$, it is comparable with accuracy of the used method. Thus, it can be concluded that in the case of a slight glycine deficiency toward reaction stoichiometry, it is possible to obtain nanocrystalline pure phase of orthorhombic yttrium orthoferrite by direct glycine-nitrate combustion without the necessity of additional thermal treatment.

Average crystallite size of orthorhombic $YFeO_3$ obtained after calcination of combustion products considerably changes from 30 to 50 nm with G/N ratio change from 4.2 to 2.4. Wherein this dependence upon G/N has two characteristic ranges – for G/N from 4.2 – 3.3, calcination of products leads to the formation of relatively smaller nanoparticles than in case of G/N equal to 3.3 – 2.4. This may be considered as result of presence a carbon skeleton

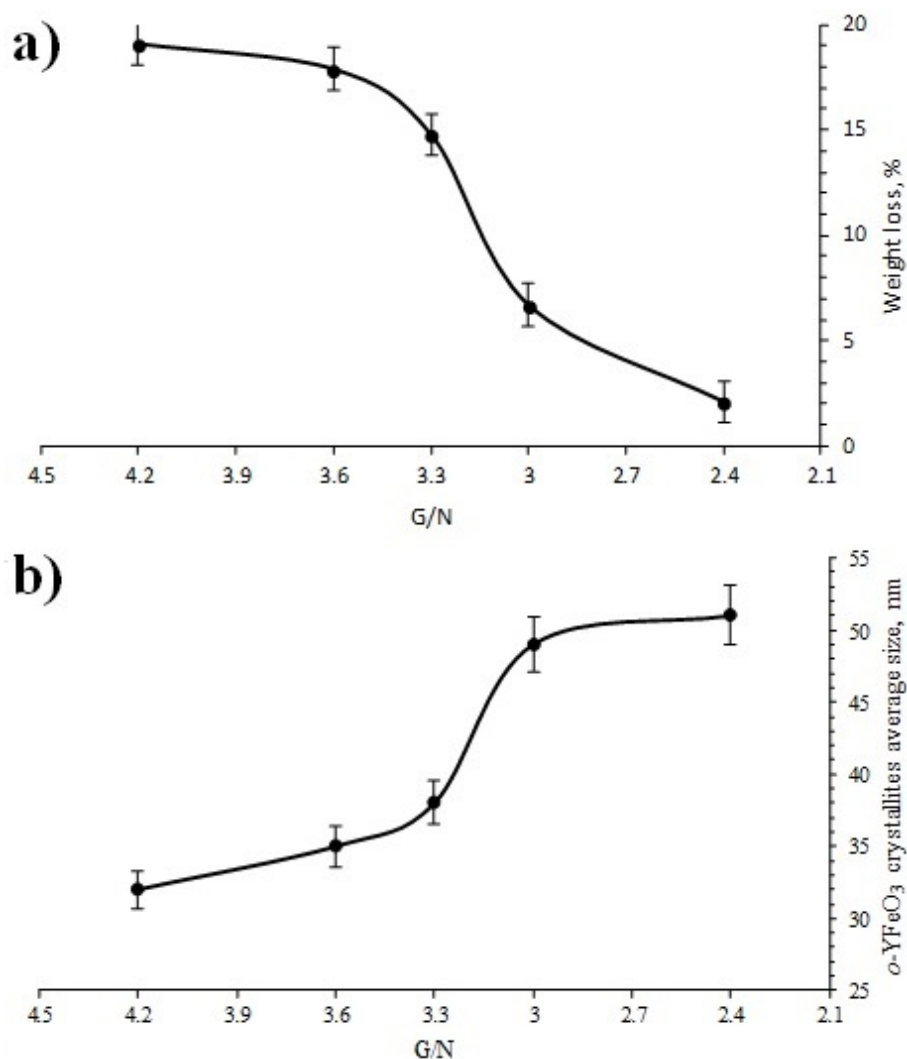


FIG. 2. Relative weight loss (a) and average *o*-YFeO₃ crystallites size (b) after calcination of glycine-nitrate combustion products at 800 °C for 15 minutes

in the samples obtained under conditions of glycine excess. This, in turn, leads to spatial separation of nanoparticles formed under thermal treatment of combustion products and restricts recrystallization processes. In the absence of a carbon skeleton, active mass transfer is possible thus leading to a significant increase in the average crystallite size.

To obtain comprehensive information about nanostructure morphology of the obtained YFeO₃, microstructure features and results of crystallization processes TEM analyses of as-prepared and calcined samples were carried out (Fig. 3).

A significant difference between the morphology and microstructure is observed for the samples obtained from initial solutions with G/N ratio 2.4, 3.3 and 4.2. With decreased glycine to nitrate ratio, the pore size and pore wall thickness, on the contrary, increase. Comparing this information with data about phase and disperse composition of the samples (Table 2) it can be assumed that spatial restrictions may also affect the result of the glycine-nitrate combustion in addition to the combustion reaction zone temperature factor [26]. In this case, the phase and disperse composition of glycine-nitrate combustion products are not only strongly dependent on reaction temperature, but also on the combustion reaction rate and the amount of evolved gases, so that all these factors govern final product microstructure. However, as it seen after

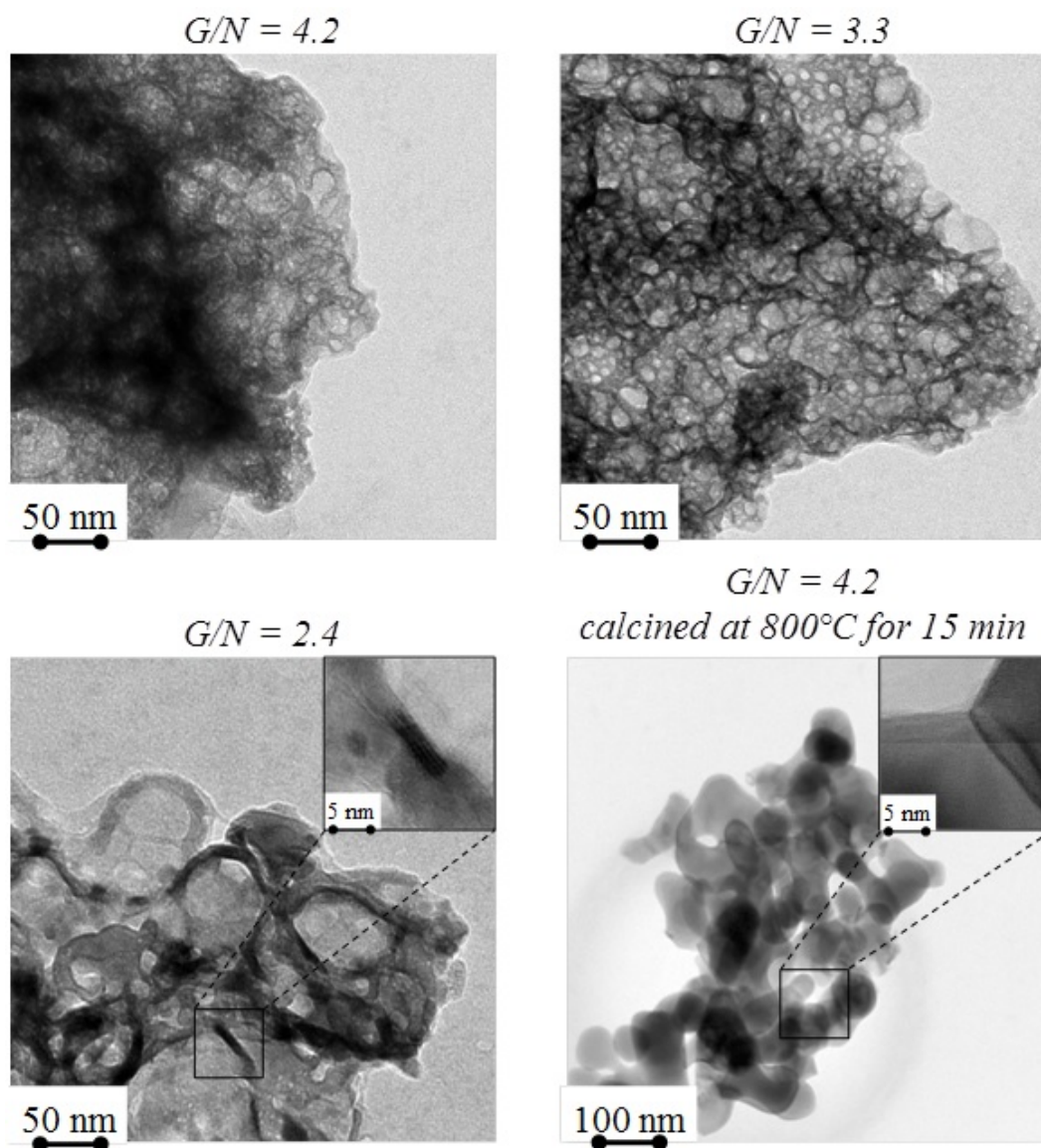


FIG. 3. TEM of glycine-nitrate combustion products as prepared ($G/N = 2.4, 3.3, 4.2$) and after heat treatment ($G/N = 4.2$, calcined 800°C , 15 min)

the heat treatment, the initial microstructure of the composite is disrupted and orthorhombic orthoferrite is present as weakly agglomerated nanoparticles with rounded shapes. Apparently, nanoparticles $o\text{-YFeO}_3$ are formed on the base of the previous pore walls in the areas with enhanced congestion of initial substance.

This assumption is also confirmed by matching results of both helium pycnometry analysis and analysis of nitrogen adsorption with using average wall thickness equation as described above. Results of these calculations and scheme of morphological and phase changes depending on the G/N ratio is shown in Fig. 4.

The products of glycine-nitrate combustion have a porous structure and can be characterized by the average wall thickness of pores, which depends on the G/N ratio. The minimum wall thickness was detected at a glycine/nitrate ratio of about 3.0 – 3.3. If G/N ratio is 4.2 and 2.4, the average wall thicknesses of pores are maximized, but the reasons for this increase in

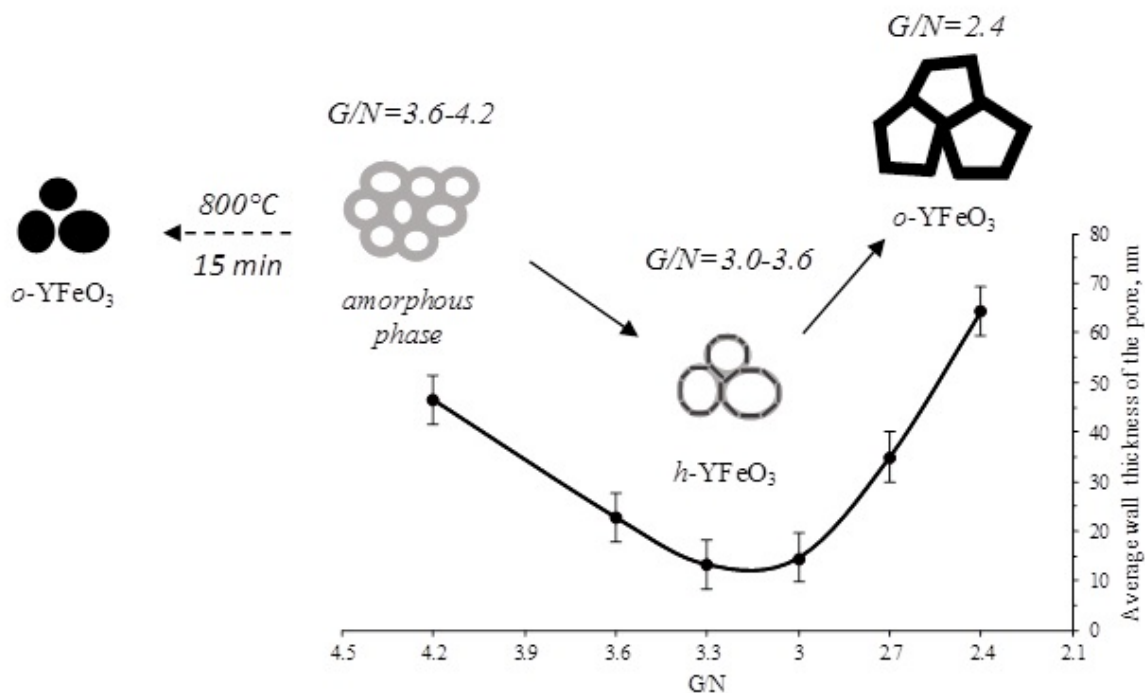


FIG. 4. Average wall thickness of the pores in glycine-nitrate combustion products at different G/N ratio and its phase and morphological transformation scheme

thicknesses are different. In the case of glycine excess ($G/N = 3.6 - 4.2$), the pore thickness is comparatively high mainly due to their structure formation from the abundance of unreacted substances. This leads to significant wall thickening, a reduction in the density of the sample, the formation of closed porosity and as a result, the foam morphology illustrated in Fig. 4. Otherwise, in the case of a decreased G/N ratio, in the range of 3.0 – 3.6, at the onset of crystallization processes, changes in the pore wall thickness and the morphology of the combustion products are observed, presumably due to the reduction of unreacted product amount. The sample obtained under minimal G/N ratio of 2.4 is characterized by maximal pore wall thickness due to its high crystallinity and high average crystallite size of YFeO₃. In this case, it is proper to consider nanostructure of the sample as fused plate-like structure, which is shown in Fig. 3. This assumption can be proved by comparing nanostructure average characteristic sizes estimated from XRD and TEM (Table 3). Average characteristic size of nanostructure refers to average wall thickness of the pores (TEM) or average crystallite size estimated from diffraction line broadening in different crystallographic directions (XRD).

Thus, it was shown a strong influence of unreacted combustion products on the morphology of obtained samples.

4. Conclusion

Nanostructured materials, based on the orthorhombic and hexagonal yttrium orthoferrite with different phase, disperse and morphological compositions, were obtained by direct glycine nitrate synthesis. It was shown that the composite morphology is strongly dependent upon the amount of evolved gases amounts and mass fraction of unreacted combustion products. Crystallization behavior of composites with different G/N ratio was shown mainly to depend on the reaction zone temperature as well as on spatial restrictions formed by the morphology

TABLE 3. Average characteristic sizes of nanostructures (from XRD and TEM) depending on synthesis conditions

G/N	Phase composition	Nanostructure average characteristic size, nm					TEM
		XRD					
		<i>o</i> - $YFeO_3$			<i>h</i> - $YFeO_3$		
		[200]	[002]	[040]	[010]	[004]	
4.2	Amorphous phase	–	–	–	–	–	> 40
3.3	<i>o</i> - $YFeO_3$ + <i>h</i> - $YFeO_3$	29±2	29±2	33±3	10±2	7±2	10 – 20
2.4	<i>o</i> - $YFeO_3$	46±4	46±4	51±5	–	–	15 – 50
4.2*	<i>o</i> - $YFeO_3$	50±5	49±5	51±5	–	–	> 50

* – the sample obtained by calcination of combustion products at 800 °C for 15 minutes

features and that leads to preferred formation of yttrium orthoferrite with amorphous, hexagonal or orthorhombic structures. As result of this work, a scheme for the morphological changes has been shown to be dependent upon the glycine to nitrate ratio.

Acknowledgments

This work was financially supported by the Russian Foundation for Basic Research (Project 13-03-12470).

References

- [1] Chick L.A., Pederson L.R., et al. Glycine-nitrate combustion synthesis of oxide ceramic powders. *Mater. Lett.*, 1990, **10** (1–2), P. 6–12.
- [2] Patil K.C., Aruna S.T., Mimani T. Combustion synthesis: an update. *Curr. Opin. Solid State Mater. Sci.*, 2002, **6**, P. 507–512.
- [3] Mukasyan A.S., Epstein P., Dinka P. Solution combustion synthesis of nanomaterials. *Proc. Combust. Inst.*, 2007, **31** (2), P. 1789–1795.
- [4] Aruna S.T., Mukasyan A.S. Combustion synthesis and nanomaterials. *Curr. Opin. Solid State Mater. Sci.*, 2008, **12** (3–4), P. 44–50.
- [5] Saket S., Rasouli S., et al. Solution Combustion Synthesis of Nano-Crystalline Alumina Powders. *J. Mater. Sci. Eng.*, 2010, **4** (8), P. 80–84.
- [6] Zhuravlev V.D., Vasil'ev V.G., et al. Glycine-nitrate combustion synthesis of finely dispersed alumina. *Glas. Phys. Chem.*, 2010, **36** (4), P. 506–512.
- [7] Zhuravlev V.D., Bamburov V.G., et al. Solution combustion synthesis of α - Al_2O_3 using urea. *Ceram. Int.*, 2013, **39** (2), P. 1379–1384.
- [8] Verma A., Dwivedi R., et al. Microwave-Assisted Synthesis of Mixed Metal-Oxide Nanoparticles. *J. Nanoparticles*, 2013, **2**, P. 1–11.
- [9] Nair S.R., Purohit R.D., et al. Role of glycine-to-nitrate ratio in influencing the powder characteristics of La(Ca)CrO₃. *Mater. Res. Bull.*, 2008, **43** (6), P. 1573–1582.
- [10] Chiu T.-W., Yu B.-S., et al. Synthesis of nanosized CuCrO₂ porous powders via a self-combustion glycine nitrate process. *J. Alloys Compd.*, 2011, **509** (6), P. 2933–2935.
- [11] Jiang L., Liu W., et al. Rapid synthesis of DyFeO₃ nanopowders by auto-combustion of carboxylate-based gels. *J. Sol-Gel Sci. Technol.*, 2011, **61** (3), P. 527–533.
- [12] Kondakindi R.R., Karan K., Peppley B.A. A simple and efficient preparation of LaFeO₃ nanopowders by glycine-nitrate process: Effect of glycine concentration. *Ceram. Int.*, 2012, **38** (1), P. 449–456.

- [13] Komlev A.A., Vilezhaninov E.F. Glycine-nitrate combustion synthesis of nanopowders based on nonstoichiometric magnesium-aluminum spinel. *Russ. J. Appl. Chem.*, 2013, **86** (9), P. 1344–1350.
- [14] Jose R., James J., John A.M., et al. A new combustion process for nanosized $\text{YBa}_2\text{ZrO}_{5.5}$ powders. *Nanostructured Mater.*, 1999, **11** (5), P. 623–629.
- [15] Reddy B.M., Reddy G.K., Rao K.N., et al. Characterization and photocatalytic activity of $\text{TiO}_2\text{-M}_x\text{O}_y$ ($\text{M}_x\text{O}_y = \text{SiO}_2, \text{Al}_2\text{O}_3, \text{and ZrO}_2$) mixed oxides synthesized by microwave-induced solution combustion technique. *J. Mater. Sci.*, 2009, **44** (18), P. 4874–4882.
- [16] Khetre S.M., Jadhav H.V., Jagadale P.N., et al. Studies on electrical and dielectric properties of LaFeO_3 . *Adv. Appl. Sci. Res.*, 2011, **2** (4), P. 503–511.
- [17] Tien N.A., Almjashaeva O.V., Mittova I.Ya., et al. Synthesis and magnetic properties of YFeO_3 nanocrystals. *Inorg. Mater.*, 2009, **45** (11), P. 1304–1308.
- [18] Gil D.M., Navarro M.C., Lagarrigue M.C., et al. Synthesis and structural characterization of perovskite YFeO_3 by thermal decomposition of a cyano complex precursor, $\text{Y}[\text{Fe}(\text{CN})_6]\cdot 4\text{H}_2\text{O}$. *J. Therm. Anal. Calorim.*, 2010, **103** (3), P. 889–896.
- [19] Tang P., Chen H., Cao F., et al. Magnetically recoverable and visible-light-driven nanocrystalline YFeO_3 photocatalysts. *Catal. Sci. Technol.*, 2011, **1** (7), P. 1145–1148.
- [20] Zhang R.L., Fang C., Yin W., et al. Dielectric behavior of hexagonal and orthorhombic YFeO_3 prepared by modified sol-gel method. *J. Electroceramics*, 2014, **32**, P. 187–191.
- [21] Popkov V.I., Almjashaeva O.V. Formation Mechanism of YFeO_3 Nanoparticles under the Hydrothermal Conditions. *Nanosyst.: Phys., Chem., Math.*, 2014, **5** (5), P. 703–708.
- [22] Tugova E.A., Karpov O.N. Nanocrystalline Perovskite-Like Oxides Formation in $\text{Ln}_2\text{O}_3\text{-Fe}_2\text{O}_3\text{-H}_2\text{O}$ ($\text{Ln} = \text{La, Gd}$) Systems. *Nanosyst.: Phys., Chem., Math.*, 2014, **5** (6), P. 854–860.
- [23] Popkov V.I., Almjashaeva O.V., Schmidt M.P., et al. Formation mechanism of nanocrystalline yttrium orthoferrite under heat treatment of the coprecipitated hydroxides. *Russ. J. Gen. Chem.*, 2015, **85** (6), P. 1370–1375.
- [24] Wu L., Yu J.C., Zhang L., et al. Selective self-propagating combustion synthesis of hexagonal and orthorhombic nanocrystalline yttrium iron oxide. *J. Solid State Chem.*, 2004, **177** (10), P. 3666–3674.
- [25] Zhang W., Fang C., Yin W., et al. One-step synthesis of yttrium orthoferrite nanocrystals via sol-gel auto-combustion and their structural and magnetic characteristics. *Mater. Chem. Phys.*, 2013, **137** (3), P. 877–883.
- [26] Popkov V.I., Almjashaeva O. V. Yttrium orthoferrite YFeO_3 nanopowders formation under glycine-nitrate combustion conditions. *Russ. J. Appl. Chem.*, 2014, **87** (2), P. 167–171.
- [27] Popkov V.I., Almjashaeva O.V., Gusarov V.V. The investigation of the structure control possibility of nanocrystalline yttrium orthoferrite in its synthesis from amorphous powders. *Russ. J. Appl. Chem.*, 2014, **87** (10), P. 1417–1421.
- [28] Popkov V.I., Almjashaeva O.V., Schmidt M.P., et al. Features of Nanosized YFeO_3 Formation under Heat Treatment of Glycine-Nitrate Combustion Products. *Russ. J. Inorg. Chem.*, 2015, **60** (10), P. 1193–1198.
- [29] Young R.A. *The Rietveld Method*. Oxford Univ. Press., Oxford, 1993, 312 p.
- [30] Patterson A. The Scherrer formula for X-ray particle size determination. *Phys. Rev.*, 1939, **56**, P. 978–982.
- [31] Goldstein J.I., Newbury D.E., Echlin P., et al. *Scanning Electron Microscopy and X-ray Microanalysis*. Springer, New York, 2003, 690 p.

Influence of the oxidation of GaAs on the work of light-emitting spintronic diodes with InGaAs/GaAs quantum wells

S. Saeid

Lobachevsky State University of Nizhni Novgorod, 23 Gagarin Avenue,
Nizhny Novgorod, 603950, Russia

s.saeed34@yahoo.com

PACS 72.25.-b, 72.25.Ba, 72.25.Hg, 75.47.-m DOI 10.17586/2220-8054-2015-6-6-875-881

A study of oxygen atoms' interactions on a GaAs (001) structure surface shows that these atoms are getting adsorbed onto the surface, form an oxide layer, and over time its thickness increases. This oxide layer hinders the injection of electrons and the holes from the metal layer to the semiconductor, thus affecting the photoelectroluminescence and the work of Metal-oxide-semiconductor diodes. These studies also examine the growth rate of oxide layers on the surface of the structure with different deposition degrees (400 °C, 630 °C) of cover layers and the extent of the oxygen atoms' penetration into the structure.

Keywords: tunnel effect, spin injector, metal-oxide-semiconductor diodes, oxides of GaAs, storage time, diffusion penetration.

Received: 13 October 2015

Revised: 30 October 2015

1. Introduction

Metal-oxide-semiconductor diodes and transistors are considered as essential components of an advanced electronic device. The formation of an oxide layer on the semiconductor structure's surface may cause some difficulties in the preparation of such elements since the thickness of the oxide layer is time dependent. So it is necessary to treat the semiconductor surface before the insulator and metal deposition.

In this work, the influence of storage time on the surface of gallium arsenide is explored. The storage time (1 year) creates a difference in the growth rates for oxide layers on stored wafer surfaces over those which were 'freshly-processed', both with two different deposition temperatures of 400 °C and 630 °C.

Also the comparison of the oxide layer formed on the surface of the structure and Al₂O₃ layer is performed, revealing the fact that although the oxide thickness slightly increases over time, the chemical bonding of the uppermost surface layers remains in an unstable condition [1]. It means that the steps used to prepare GaAs surfaces can have a profound effect on the diode manufacturing process.

The elimination of contaminants and oxide which are present on the GaAs surface can be simply accomplished by etching and degreasing. Degreasing is achieved with acetone and ethanol [2]. The etching process can be performed by several dry and wet methods. Various solutions, such as H₂O₂/NH₄OH/H₂O [3], H₂SO₄/H₂O₂/H₂O [4, 5], HCl/H₂O [6], or H₂SO₄/H₂O₂/HCl [7], are used for wet-etching.

The oxidation products of GaAs are the following oxides: Ga₂O₃ and As₂O₃ [8]. The As oxide is highly soluble in oxygenated water, so, that fact gives one an opportunity to remove

it from the GaAs surface photochemically [8]. The aqueous solutions of hydrofluoric acid are used to remove surface oxides [2], and to passivate GaAs surface either sulfide or gallium oxide can be applied to the oxidized GaAs surface [8].

2. Experimental

Semiconductor/metal structures with substrates of n-GaAs (001) were grown under atmospheric pressure of hydrogen using metallo-organic chemical vapor deposition (MOCVD) for the semiconductor part. For the tunnel barrier/ferromagnetic metal part, they were grown in vacuum [9] using electron-beam evaporation.

The structures contain three quantum wells (QWs) with different contents of In $x = 0.25$, 0.20 and 0.15 which are located at different depths 30, 70, and 110 nm from the surface respectively. The temperature during deposition of the cover layer with the thickness up to 30 nm was 400 °C for the first structure, and 630 °C – for the second structure. The data obtained in the investigation of the structure was confirmed on cross-sectional samples using transmission electron microscopy (JEM-2100F).

At this point, electro-photoluminescence is measured. Impurities and the distribution of components were analyzed at the cross-sectional structure with the help of Energy dispersive X-ray spectroscopy (EDS), integrated in the electron microscope. The PL was excited by He–Ne laser with power of 30 mW, and spectra were recorded at 77 K.

The Co layer was deposited directly on ‘freshly-processed’ wafer surfaces and on the wafer surfaces with 1 year of storage time with different deposition temperatures (400 °C, 630 °C) of cover layers.

3. Results and discussion

Figure 1 shows that the photoluminescence spectra of the structure with Co layer deposited on the structure’s surface right after sample preparation (curve 4) differ from the photoluminescence spectra of the structure with the Co layer deposited on the sample with 1 year of storage time (curve 3). The temperature during these depositions was 400 °C. The difference of the photoluminescence spectra comes from the formation of oxide layer on the structure’s surface.

Curve 4 reflects the complete quenching of photoluminescence in 1st, 2nd and 3d QWs. This quenching comes from Co atoms penetrating into 3 QWs (110 – 130 nm) and diffusing inside the structure. The diffusion of Co atoms leads to the formation of non-radiative recombination centers (defects) which hinder the process of radiation emission (electro-photoluminescence).

Curve 3 shows that, the oxide layer on the surface of the structure becomes a barrier which prevents the diffusion penetration of Co atoms into QWs (20 – 40 nm) in the structure. Thus the intensity of photoluminescence has not practically changed after deposition of the Co layer.

Curve 2 and 3 point out that PL peaks at 1.280, 1.332 and 1.385 eV, which correspond to the energies of the basic transitions in QWs with $x = 0.25$, 0.20 and 0.15, have shifted from their places to 1.283, 1.342 and 1.391 eV. This shift (i.e. change of the wavelengths) happens due to diffusion penetration of O atoms into QWs (120 – 140 nm) of the structure and due to formation of new energy levels within the QWs. The energy levels appear from the influence of indium atom concentration in QWs.

In Fig. 2, curve 4 shows that Co penetrates into 2 QWs on the depth of 80 – 100 nm and diffuses inside the structure. The temperature during this deposition was 630 °C. Curve 3 indicates that a decrease in intensity of radiation for the first PL peak is larger than a decrease

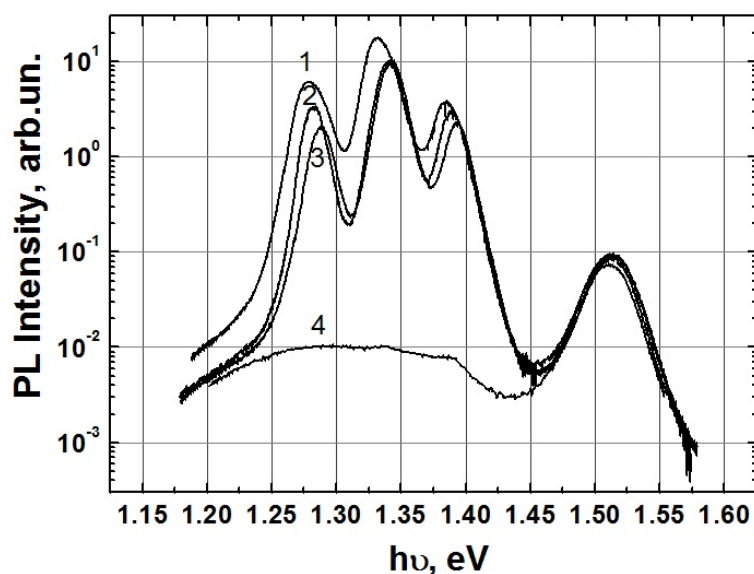


FIG. 1. The photoluminescence spectra of the structure with three quantum wells and with a low deposition degree (400 °C) of cover layer: 1 – initial sample; 2 – initial sample in a year; 3 – after deposition of Co in a year; 4 – after deposition of Co

shown in Fig. 1 curve 3. It means that the Co atoms penetrate deeper into the structure and that's why they form a larger number of defects across the diffusion barrier in the QW-1 (Fig. 1, curve 3), than a number of defects formed in the QW-1 (Fig. 2, curve 3). It is evident that the oxide layer formed on the surface of the sample becomes a diffusion barrier. The thickness of the oxide layer on the surface of the structure deposited at the low temperature (400 °C) is larger than the thickness of the oxide layer on the surface of the structure deposited at high temperature (630 °C), thus the oxidation speed is higher. It means that the temperature during the deposition of the cover layer plays a major role in reducing the oxidation rate.

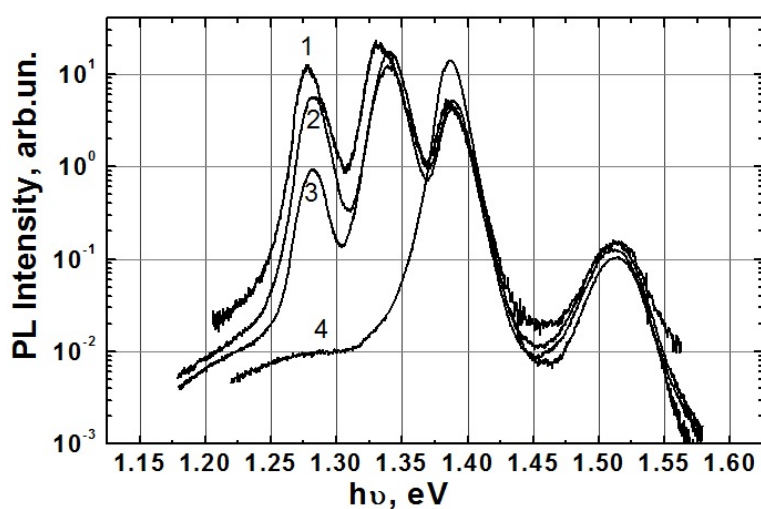


FIG. 2. The photoluminescence spectra of the structure with three quantum wells and with a high deposition degree (630 °C) of cover layer: 1 – initial sample; 2 – initial sample in a year; 3 – after deposition of Co in a year; 4 – after deposition of Co

Figure 3 reveals the fact that Al₂O₃ insulator layer (1.2 nm) deposited on the oxide layer (1.1 nm to 1.3 nm) prevents diffusion penetration of Co. Thus PL spectrum remains practically unchanged, but the tunnel effect disappears as the thickness of the insulator becomes about 2.5 nm. The crystal structures of both oxides are different from each other as shown in Fig. 4.

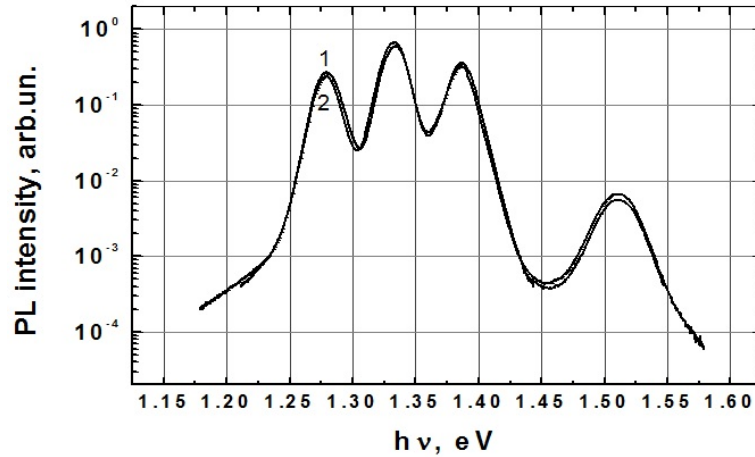


FIG. 3. The photoluminescence spectra of the structure with three quantum wells: 1 – initial sample; 2 – deposition of Al₂O₃ (1.2 nm)/Co on oxide layer (in a year)

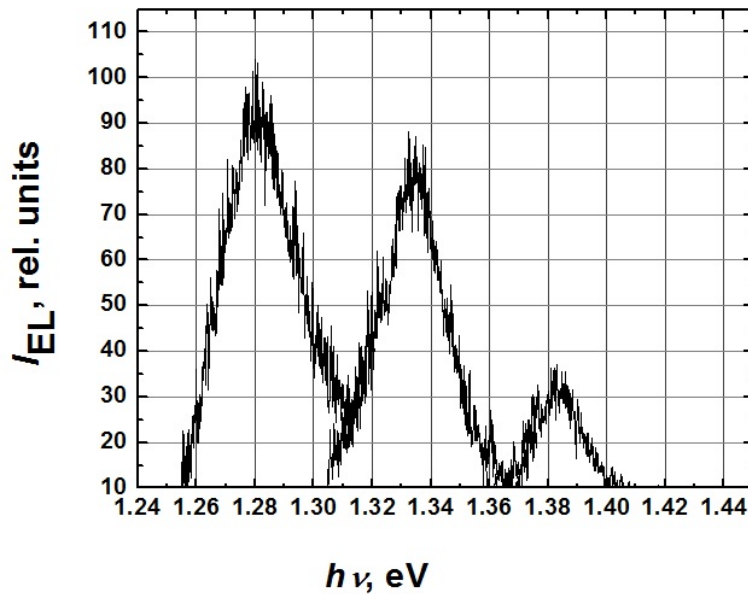


FIG. 4. The electroluminescence spectra of the structure with three quantum wells with oxide layer (in a year) and Al₂O₃ (1.2 nm)/Co layer

From Figs. 5 and 6, it is clear that the thickness of the oxide layer formed on the surface of the structure after a year is approximately 1.1 – 1.3 nm. Although, comparing to the quality of Al₂O₃, the quality of oxide insulator, is lower due to the large amount of defects formed in the interface.

Figures 5 and 6 show that the diode with cover layer deposited at low temperature of 400 °C and with 1 nm of Al₂O₃ begins emitting radiation by the current up to 2 mA while

the diode with oxide needs the current up to 30 mA just for the start. It leads to loss of extra amount of energy without any yield. This indicates that the oxide layer plays a less efficient role as a tunneling and diffusion barrier than Al_2O_3 .

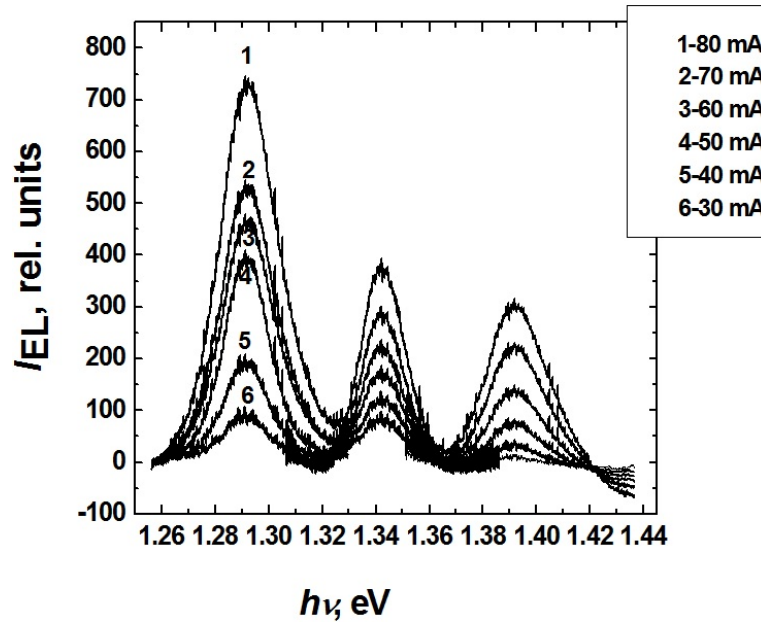


FIG. 5. The electroluminescence spectra of the structure with three quantum wells and a low deposition degree ($400\text{ }^\circ\text{C}$) of cover layer with oxide layer (in a year) and Co layer

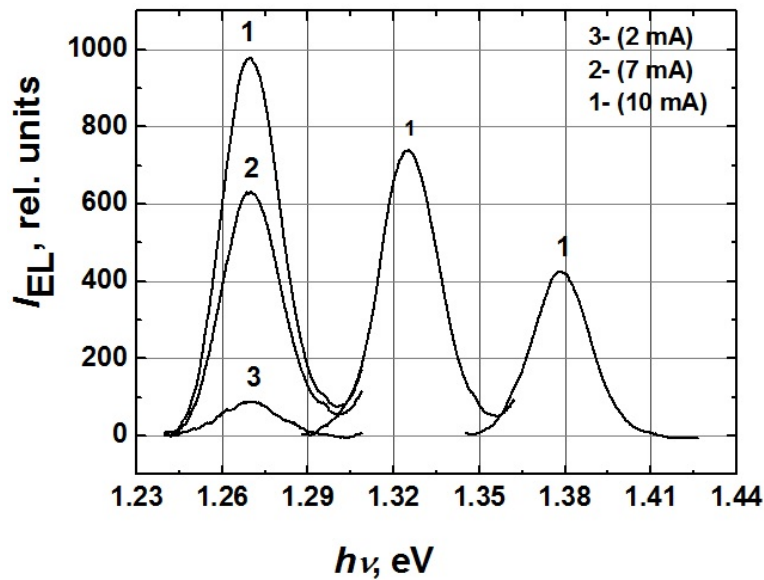


FIG. 6. The electroluminescence spectra of the structure with three quantum wells with Al_2O_3 (1 nm)/Co layers

Figure 7 confirms that O atoms penetrate into the structure but their concentration does not exceed 2 %. Also, Co atoms penetrate into Al_2O_3 and Au layers, and atoms of Al, O and Au penetrate into Co layer. Noticeably, the ratio of O atoms to Al atoms at the Al_2O_3 layer is 45/15 while in fact it should be 3/2. This is evidence for the oxide layer's presence.

Figure 8 shows that the resistance increases when an oxide layer is formed on the surface of the structure and this increase depends on the thickness of this oxide layer. The Schottky barrier height is 0.85 eV, however, after a year, it becomes 0.86 eV.

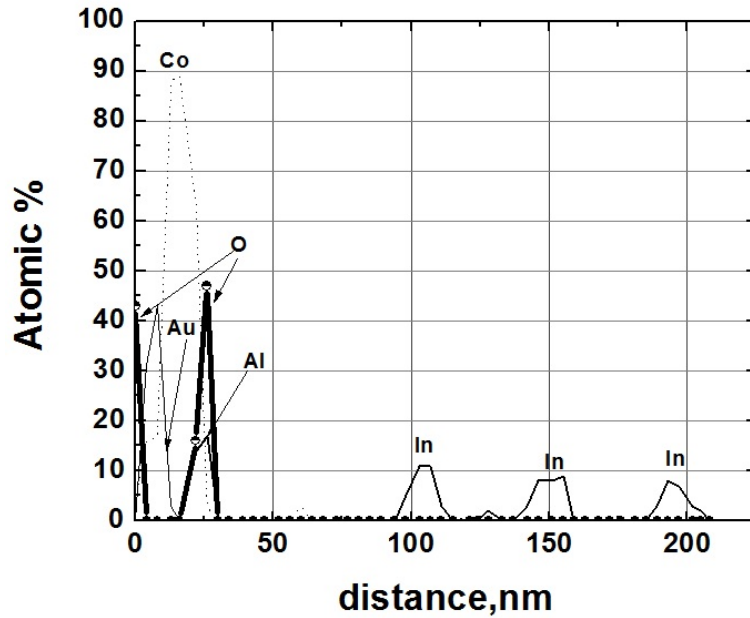


FIG. 7. Concentration profiles of the elements in the depth of the structure with three quantum wells and with deposition temperature of the cover layer at 400 °C and Al₂O₃/Co layers

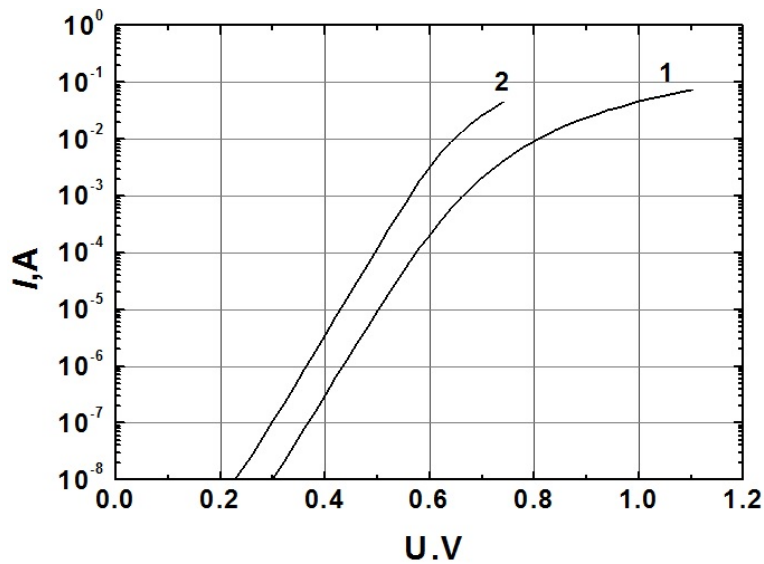


FIG. 8. The current-voltage characteristics of diode: 1 – with an oxide layer on the surface of the structure; 2 – without any oxide layer

4. Conclusions

In summary, the thickness of an oxide layer can have negative and positive impacts on the injection of a charged carrier. If the thickness of the oxide layer is more than 1 nm, the resistance in the structure and the amount of defects on its interface increase, which leads to reduction of radiation intensity emitted from the structures, and energy loss; if the thickness of the oxide layer is less than 0.7 nm, it prevents the penetration of metal atoms into the structures and increases possibility of electron transmission via a tunneling mechanism.

References

- [1] Th. Mirandi, D.J. Carlson. The Effects of Chemical Treatment and Storage Time on the Surface Chemistry of Semi-Insulating Gallium Arsenide. *Proceeding of 'CS MANTECH Conference'*, 2009, Tampa, Florida, USA, May 18th-21st.
- [2] Köhler M. *Etching in Microsystem Technology (1st edn.)* Wiley-VCH: Weinheim, 1999.
- [3] J.S. Song, Y.C. Choi, et al. Wet chemical cleaning process of GaAs substrate for ready-to-use. *J. Cryst. Growth*, 2004, **264** (98), P. 98–103.
- [4] H.C. Liu, S.H. Tsai, J.W. Hsu, H.C. Shih. The phase identification of the H₂SO₄-etched GaAs by X-ray diffraction. *Mat. Chem. Phys.*, 1999, **61** (2), P. 117–123.
- [5] A. Munoz-Yague, J. Piqueras, N.J. Fabre. Preparation of Carbon-Free GaAs Surfaces: AES and RHEED Analysis. *Electrochem. Soc.*, 1981, **128** (1), P. 149–153.
- [6] K. Matsushita, S. Miyazaki, S. Okuyama, Y. Kumagai. Observation of HCl- and HF-Treated GaAs Surfaces by Measuring Contact Angles of Water Droplets. *Jpn. J. Appl. Phys.*, 1994, **33** (8), P. 4576–4580.
- [7] Z.H. Lu, C. Lagarde, et al. A surface analytical study of GaAs (100) cleaning procedures. *J. Vac. Sci. Technol. A*, 1989, **7** (3), P. 646–650.
- [8] W. Wang, G. Lee, et al. First-principles study of GaA(001)-beta2(2X4) surface oxidation and passivation with H, Cl, S, F, and GaO. *J. Appl. Phys.*, 2010, **107**, P. 103720.
- [9] B.N. Zvonkov, O.V. Vikhrova, et al. Using laser sputtering to obtain semiconductor nanoheterostructure. *J. Opt. Tech.*, 2008, **75** (6), P. 389–393.

First observations of entropy vs free energy for lattice based Ising model for spin coarsening in conserved and non-conserved binary mixtures: a phenomenological study of phase transitions in 2D thin films

Satya Pal Singh

Department of Applied Sciences, Madan Mohan Malaviya University of Technology,
Gorakhpur, 273010, India
singh.satyalpal@hotmail.com

PACS 75.20.En, 75.70.Kw, 81.30.Bx, 75.10.-b, 75.10.Hk, 75.30.Kz, 64.60.De, 05.40.-a
DOI 10.17586/2220-8054-2015-6-6-882-895

This paper presents the results of Monte Carlo (MC) simulation for paramagnetic, ferromagnetic and anti-ferromagnetic transitions in 2D thin films. The spin coarsening which lowers energy brings order at the cost of lowering entropy in the presence of an external magnetic field, which in turn, may increase the free energy at relatively higher temperatures because of spin mixing. There is a competition between energy of the system and entropy in conserved and non-conserved binary mixtures in the presence of an external magnetic field. The simulation is done on a lattice of size 100×100 using Metropolis algorithm with periodic boundary conditions. All data are sampled for 20 K MC cycles after a regular interval of 100 MC cycles. The paramagnetic case with spin coupling coefficient and the ferromagnetic and anti-ferromagnetic cases with $|\varepsilon(AB)| = 0.0J_0, 0.25J_0, 0.50J_0, 0.75J_0$ & $1.0J_0$ (keeping $|\varepsilon(AA)| = |\varepsilon(BB)| = 1.0J_0$) (Here $J_0 = 1.0$ unit of energy) are studied at temperatures $kT = 0.25J_0, 0.50J_0, 0.75J_0, 1.0J_0, 1.25J_0, 1.5J_0, 1.75J_0, & 2.0J_0$ in presence of varying external magnetic field strengths in order to observe the organizational behavior of spins and the interplay between the free energy and entropy. The induced magnetization and the magnetic susceptibilities are found to be in qualitative agreement with the theory. The paramagnetic to ferromagnetic transition has been observed and explored at high T values. The spin correlation function plotted helps to reveal the spin transport properties of the systems. The spontaneous ferromagnetic transition temperatures for $\varepsilon(AB) = 1.0J_0, 0.75J_0$ & $0.50J_0$ are observed as $k_B T = 0.44J_0, 0.39J_0$ & $0.33J_0$ (i.e. nearly 96 % magnetizations are observed at these temperatures) respectively at $B = 0.0J_0/\mu$ (i.e. absence of any external magnetic field). This is in quantitative agreement with theory. The spin correlation function diverges at these transition temperatures, which can be understood as the theoretical evidence supporting the observation of spontaneous magnetization. The ferromagnetic to paramagnetic transitions are not very sharp but the range of the spin-spin interaction can be said to decay gradually. Even at higher temperature as $kT = 2.0J_0$, the opposite spin pair correlation function supports formation of tiny domains with spin transport from one domain to another, whereas for lower temperatures below $kT = 1.0J_0$, the presence of majority $+1/2$ spins diminish the effect. Tiny domain walls have lower energy surrounded by opposite spins and seem to be energetically preferred. This quasi nature of spin-spin interaction with temperature is also supported by the corresponding ensemble entropy averages.

Keywords: Ising model, spontaneous magnetization, thin films, spin conservation, super para-magnetism.

Received: 11 September 2015

Revised: 24 October 2015

1. Introduction

Magnetism is an old problem of study arising from the existence of naturally magnetic materials. Perhaps, the maritime use of a compass needle stands among the first few widely used applications of magnetic materials. Magnetic materials have drawn new attention in last few decades because of magnetic properties variability at nanoscale and their interplay with the electrical property because of charge of electronics. Thus, spintronics and magneto-electronics have emerged as new branch of science which can open doors for inventions having the potential for novel industrial applications [1–4].

Because of their extensive applications in diverse fields of electronics, optics, space science, aircrafts, defense and many other industries, thin films have led to a rise in phenomenal research. Molecular Simulation with thin films using lattice model and metropolis algorithm can give new insights into small scale problems with reduced dimensions. In order to understand the underlying physical process on the basis of fundamental principles of physics one can efficiently use computer models and obtain similar results similar to those determined experimentally. The simulation methods can also help to predict the molecular behavior at small scales which can be tested through well designed experiments. In studying phase transitions and sampling the data for physical observables, the concepts of advance statistical mechanics [5, 6] and thermodynamics [7] have been found to be very useful. Advanced generations of computers have made it possible to sample data with greater and greater accuracy. This paper deals with the thermodynamic and statistical study of coarse graining process of electron spins $\pm 1/2$ in two dimensional thin films with conserved ($A : B :: 50 : 50$) and non-conserved spins (i.e. spin flip-flop ensures minimization of free energy). The cases studied are paramagnetic, ferromagnetic & anti-ferromagnetic.

2. Methodology

Monte Carlo (MC) simulations have been used successfully to study a variety of problems ranging from wetting [8–11], dewetting and surface-directed phase separation [11, 12], magnetic properties of thin films etc. [13–16]. In this paper, the spin-spin interactions are calculated in the presence of external magnetic field to sample the ensemble average of internal energy and entropy. The configurational interaction energy is given by eq. (1) [17]:

$$H \{S_i\} = - \sum_{\langle ij \rangle} \epsilon_{ij} S_i S_j - B \sum_i S_i. \quad (1)$$

The initial configuration is generated by placing $\pm 1/2$ i.e. spin up & spin down on a 100×100 lattice in a random fashion so that the two types of spin populate in the ratio 1 : 1. The spin flip-flop move is accepted if $\exp(-\Delta E/k_B T) \geq p$ in case of non-conserved case. Here, p is a random number chosen between 0 – 1. The initial configuration is kept at high temperature $k_B T = 10.0 J_0$ for first 1 K MC Cycles and then is equilibrated at the given temperature for 10 K MC Cycles. The sampling for the thermodynamic observables as the internal energy and entropy, magnetization and spin correlation starts after 10 K MC Cycles. The sampling is done for next 10 K MC Cycles after a regular interval of 100 MC Cycles. For conserved binary mixture of spins the ratio of spin up and spin down is taken to be fixed throughout the run as 1 : 1 and in place of spin flip-flop spin interchange move is taken as the trial move. Again the move is accepted if $\exp(-\Delta E/k_B T) \geq p$ in case of conserved spin case otherwise the spins are restored to their original positions. In this case of conserved spins case only weak external magnetic field as $B = 0.50 J_0 / \mu_B$ is applied at $k_B T = 1.0 J_0$ in order to study the spin organization and restructuring of spins with a priori assumption that the weak field has

not sufficient strength to flip-flop the spins and hence forth the spins remain conserved for all practical purposes. This is likely to exist in the real world.

3. Results and discussion

Figures 1(a) & (b) show the magnetization vs applied external fields at different temperatures and spin-spin coupling constants respectively for the ferromagnetic case. Fig. 1(c) & (d) show the magnetization vs applied external fields at different temperatures and spin-spin coupling constants respectively for the anti-ferromagnetic case. These magnetization vs external magnetic field curves are plotted with $|\epsilon(AA)| = |\epsilon(BB)| = |\epsilon(AB)|$ following the standard Ising model. The curves are in qualitative agreement with theory [6, 7]. Fig. 2(a) shows avg.

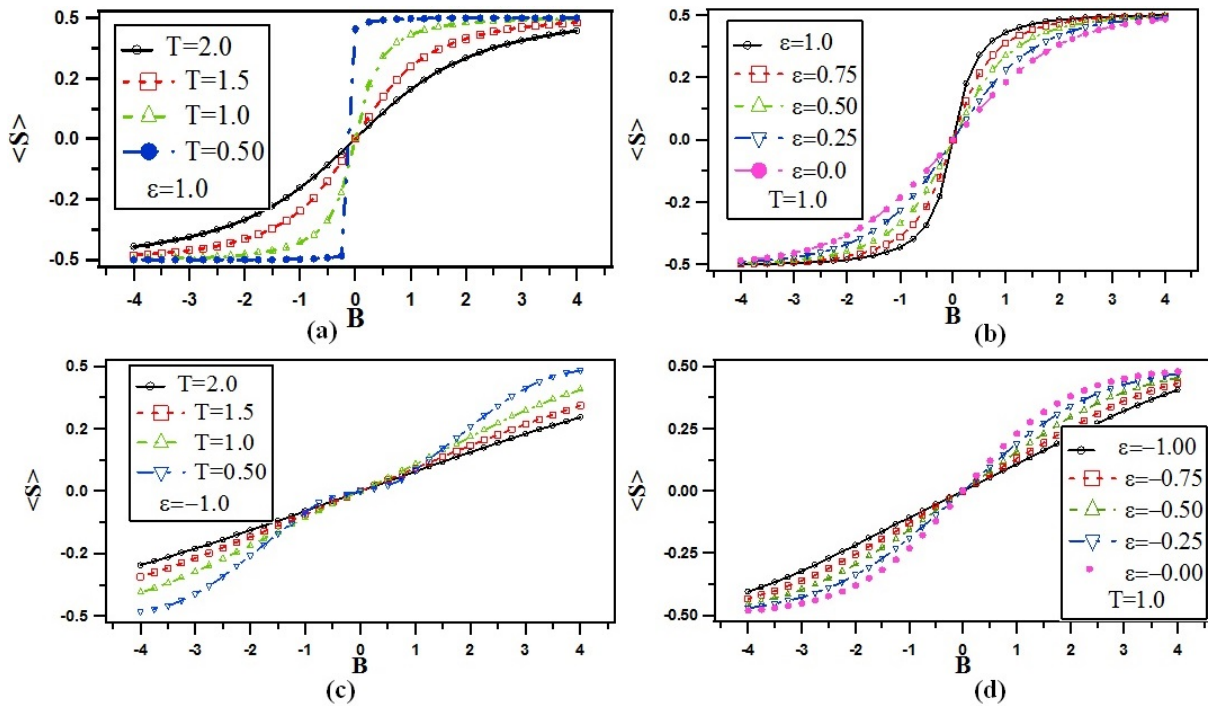


FIG. 1. shows the variation of external field vs magnetization a) for different temperatures as $kT = 0.50J_0, 1.0J_0, 1.5J_0$ & $2.0J_0$ for $\epsilon(AA) = \epsilon(BB) = \epsilon(AB) = \epsilon = 1.0J_0$ for ferromagnetic case; b) for different spin interactions as $\epsilon(AA) = \epsilon(BB) = \epsilon(AB) = \epsilon = 0.25J_0, 0.50J_0, 0.75J_0$ & $1.0J_0$ for ferromagnetic case; c) for different temperatures as $kT = 0.50J_0, 1.0J_0, 1.5J_0$ & $2.0J_0$ for $\epsilon(AA) = \epsilon(BB) = \epsilon(AB) = \epsilon = -1.0J_0$ for anti-ferromagnetic case; d) for different spin interactions as $\epsilon(AA) = \epsilon(BB) = \epsilon(AB) = \epsilon = -0.25J_0, -0.50J_0, -0.75J_0$ & $-1.0J_0$ for anti-ferromagnetic case. $J_0 = 1.0$ is taken to be unity in all cases of study. All the figures shown here for non-conserved spin cases using spin flip-flop method sampled after 20 K MC Cycles

energy vs MC Cycles run for the ferromagnetic case. Lowering the temperature results in better spin organization, which in turn, yield lower energies for the system. The effect of temperature on induced magnetization can be observed in Fig. 2(b). This also shows that variations in the repulsive interaction strength between two types of spins i.e. spin up (e.g. type A) and spin down (e.g. type B) also influence the magnetization. Reduced $\epsilon(AB)$ values enhances the mixing of types A and B spins. The ease of spin mixing lowers the induced magnetization. Fig. 2(c) plotted between entropy and MC Cycles looks to support the existence of a super-paramagnetic

type behavior for $\varepsilon(AB) = 1.0J_0$ at $kT = 2.0J_0$. This indicates rather a surprising trend be-

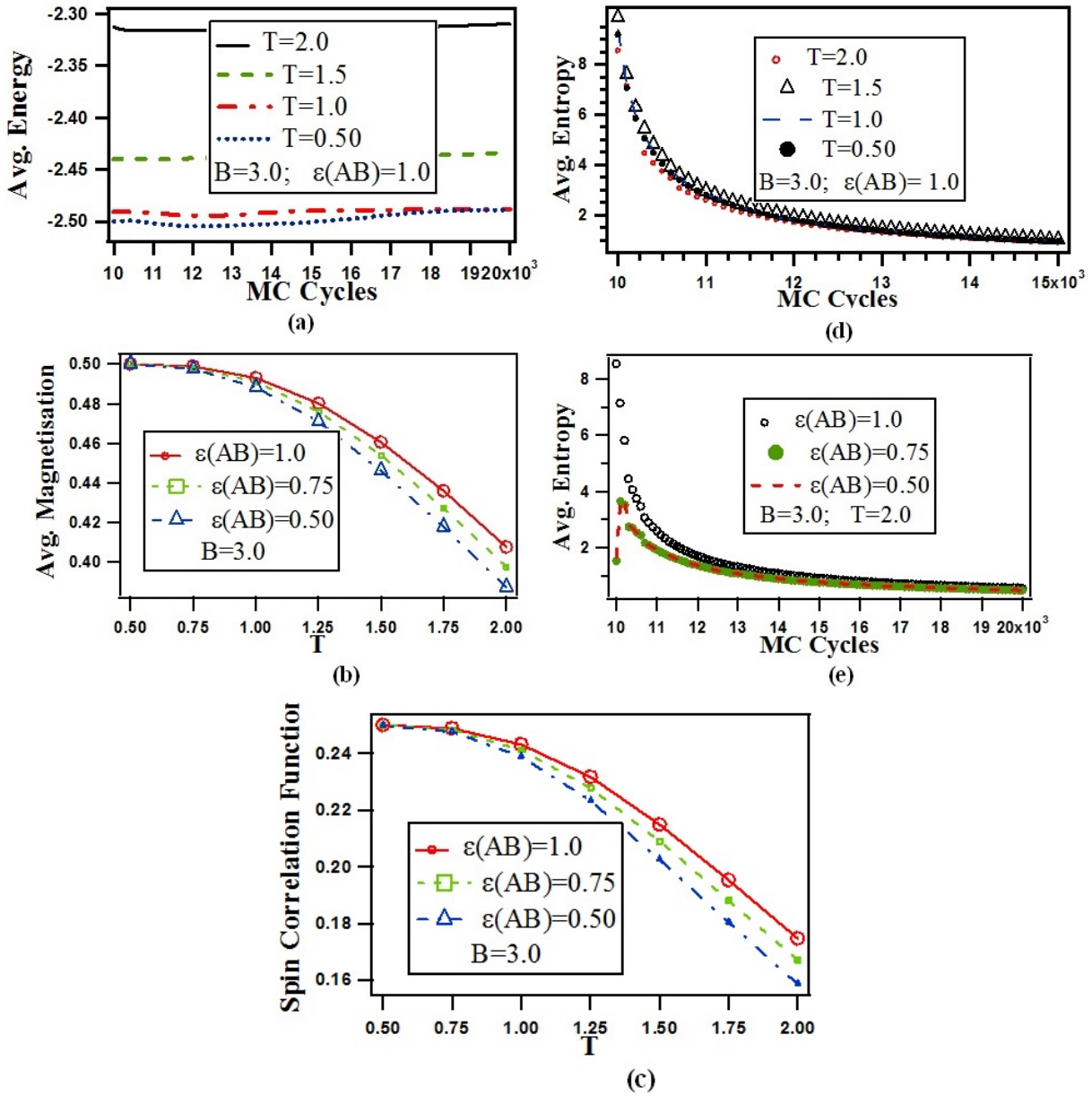


FIG. 2. Shows the (a) Avg. energy variation with temperature; (b) Variation of induced magnetization vs temperature for different spin interactions $\varepsilon_{AB} = 1.0J_0$, $0.75J_0$ & $0.50J_0$; (c) Spin correlation function vs temperature for different spin interactions $\varepsilon_{AB} = 1.0J_0$, $0.75J_0$; (d) Avg. entropy vs temperature and (e) Avg. entropy vs spin interactions ε_{AB} at $kT = 2.0J_0$ for different run cycles. In all cases, the applied external magnetic field is taken as $B = 3.0J_0/\mu_B$. The data are produced after sampling for 20 K cycles starting from 10 K cycles at an interval of 100 cycles. All cases studied here are for non-conserved ferromagnetic film

cause the avg entropy at higher $kT = 2.0J_0$ is observed to be lower than that of $kT = 1.50J_0$, $1.0J_0$ & $0.50J_0$. In general, the entropy or spin disorder must increase at higher temperatures. The lower entropy at relatively higher $kT = 2.0J_0$ can be explained on the basis of a super paramagnetic behavior for the film in which the spin-spin correlation gets weakened to the extent

that the spin starts following the applied external magnetic field irrespective of the interactions with neighboring spins. For relatively easy mixing of spin up i.e. type A and spin down i.e. type B, the spin correlations seems to increase, resulting in a better organization of spins, thus lowering the entropy of the systems as shown in Fig. 2(d). For $\varepsilon(AB) = 0.75J_0$ & $0.50J_0$, the entropy first increases for first 1000 MC Cycles and then decreases with subsequent cycles. The relatively very high values of avg. entropy for $\varepsilon(AB) = 1.0J_0$ at $kT = 2.0J_0$ also supports that at this temperature the film's behavior becomes super paramagnetic. Here, J_0/k is chosen to be unity in all the experiments; i.e. $J_0 = 1.0$. Here, the average energy, temperature and external magnetic field are expressed in units of J_0 , J_0/k_B and J_0/μ_B respectively but are taken to be unity numerically in all the figures of the paper but not shown. Interested readers may determine the exact numerical values provided that they appropriately chose the units of J_0 , k_B and μ_B which are taken to be unity in all the cases of study here. This paper is intended to be a qualitative and phenomenological study of the subject and henceforth omitted from the discussion.

Similar avg. energy sampling has been done at $kT = 1.0J_0$ for $\varepsilon(AB) = 1.0J_0$, $0.75J_0$ & $0.50J_0$. The relative ease of mixing the two types of spins weaken the ferroic behavior of spins, resulting in slightly higher avg. energy values, as shown in Fig. 3(a). For all the three cases of $\varepsilon(AB) = 1.0J_0$, $0.75J_0$ & $0.50J_0$ at $kT = 1.0J_0$ a negative slope is observed in the respective avg. energy values for first few thousand odd MC Cycles which indicate the presence of a minima. The variations are at the third decimal place and are insignificant for indication of any new physical process.

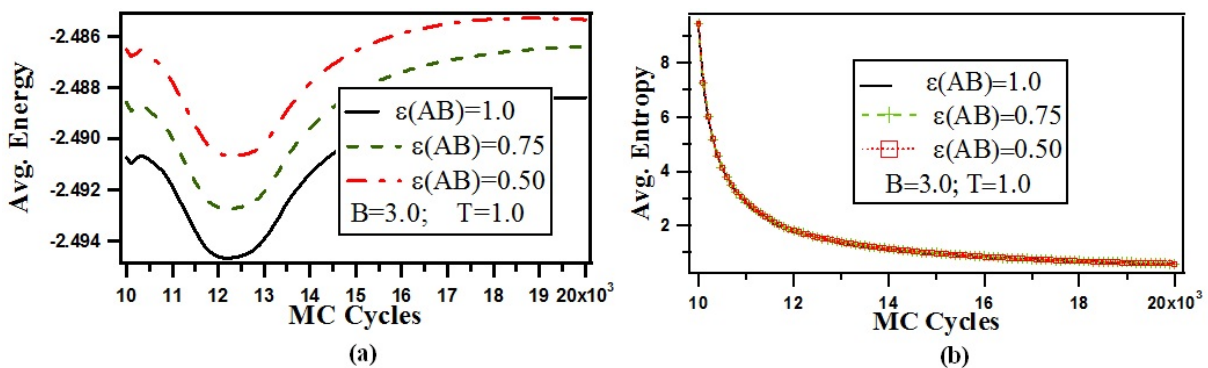


FIG. 3. Shows (a) Avg. free energy vs spin interactions at different run cycles; (b) Avg. entropy vs spin interactions at different run cycles at $B = 3.0J_0/\mu_B$ and $kT = 1.0J_0$ for non-conserved ferromagnetic case. All data are produced after sampling for 20 K cycles starting from 10 K cycles at an interval of 100 cycles. The lines are to aid visualization

The corresponding avg., entropies are plotted in Fig. 3(b). Initially, decreasing energy values were observed for first 10000 – 12000 MC Cycles for $T = 1.0$, as shown in Fig. 3(a). Though the corresponding avg. entropy (depicted in Fig. 3(b)) shows more or less the same values for all three studied cases: $\varepsilon(AB) = 1.0J_0$, $0.75J_0$ & $0.50J_0$ for the same number of cycles run, but the change in entropy (–ve) (i.e. ordering of spins decreases entropy) increases the Helmholtz free energy $\Delta F = \Delta U - T\Delta S$ for a constant internal energy. This can be accounted for on the basis of an energy increase because of homogeneous mixing of up and down spins [7]. Phase separation occurs at relatively lower temperature, which is energetically more favorable and shows a minima in free energy. The remarkable thing to note here is that all the plots of avg. entropy yields entropy values approaching 0, which indicates that after a

long run of several cycles, equilibrium is achieved and the existing microstates have probability close to 1.0. The free energy vs MC Cycles and entropy vs MC Cycles for anti-ferromagnetic cases are as shown in Fig. 4(a) and Fig. 4(b) respectively. The effect of temperature on spin correlation of opposite spins in this case is similar to that of the same type of spins in the ferromagnetic case. The average magnetization and spin correlation function are plotted against temperature in Fig. 5(a) and Fig. 5(b) respectively. These are found to be in agreement with qualitative intuition discussed in this paper.

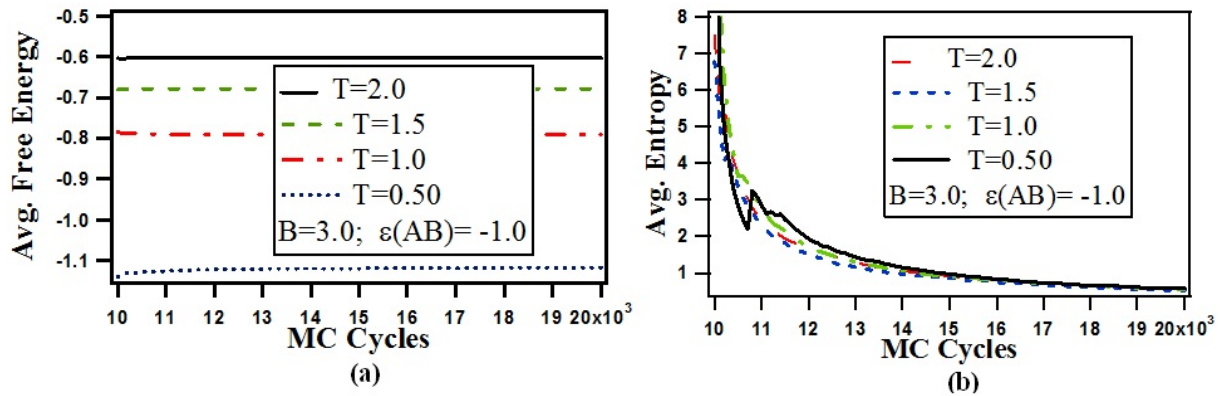


FIG. 4. Shows (a) Avg. free energy vs temperature at different run cycles; (b) Avg. entropy vs temperature at different run cycles at $B = 3.0J_0/\mu_B$ for non-conserved anti-ferromagnetic case. All data are produced after sampling for 20 K cycles starting from 10 K cycles at an interval of 100 cycles. The lines are to assist in visualization

The ferromagnetic transition temperatures for $\epsilon(AB) = 1.0J_0$, $0.75J_0$ & $0.50J_0$ are respectively noted as $k_B T = 0.44J_0$, $0.39J_0$ & $0.33J_0$ respectively. The spin correlation function diverges at the transition temperatures. The lines are to aid visualization.

The conserved spin case is shown for ferromagnetic case with spin up and spin down ratio 1 : 1 in Figs. 6(a), 6(b), 6(c) and 6(d). The conserved spin case for anti-ferromagnetic case with a 1 : 1 spin up and spin down ratio is shown in Figs. 6(a) & 6(b). The large drop at lower temperature near $kT = 0.50J_0$ in average energy values indicates a spontaneous ordering in both cases (dominantly in case of ferromagnetism). The spin-spin correlation first increases at lower temperatures and then falls after definite temperatures (i.e. the temperature where the spontaneous ordering switches off Fig. 8(a)). The two regimes shows two distinct and opposite behaviors. For the anti-ferromagnetic case, the converse is true but interestingly for $\epsilon(AB) = -0.50J_0$ with $\epsilon(AA) = \epsilon(BB) = -1.0J_0$ the spin-spin correlation alters the trend to match with that of the ferromagnetic case. Fig. 6(c) shows a change in the trend of average energy values for conserved ferromagnetic case for $\epsilon(AB) = 1.0J_0$ & $\epsilon(AB) = 0.75J_0$ at weak external magnetic field of $B = 0.50J_0/\mu_B$ in films [18].

Even though the spin-spin correlation for like and opposite spins is high (i.e. $\epsilon(AB) = 1.0J_0$, that should enhance the coarsening of similar spins), the average energy values obtained are low (-ve values) in comparison to that of $\epsilon(AB) = 0.75J_0$ which allows for relatively easier coarsening of similar spins). This type of change can be explained on the basis of domain stress which depends on the domain energy. The formation of domains in presence of an external magnetic field deforms the film, creating an anisotropy directed by the external magnetic field. The magnetoelastic energy seems to play an important role. Z. Malek and W. Schiipel et al. have proposed a hypothesis regarding the uni-axial anisotropic effect about the easy axis (i.e. perpendicular to the direction of the applied magnetic field) produced in

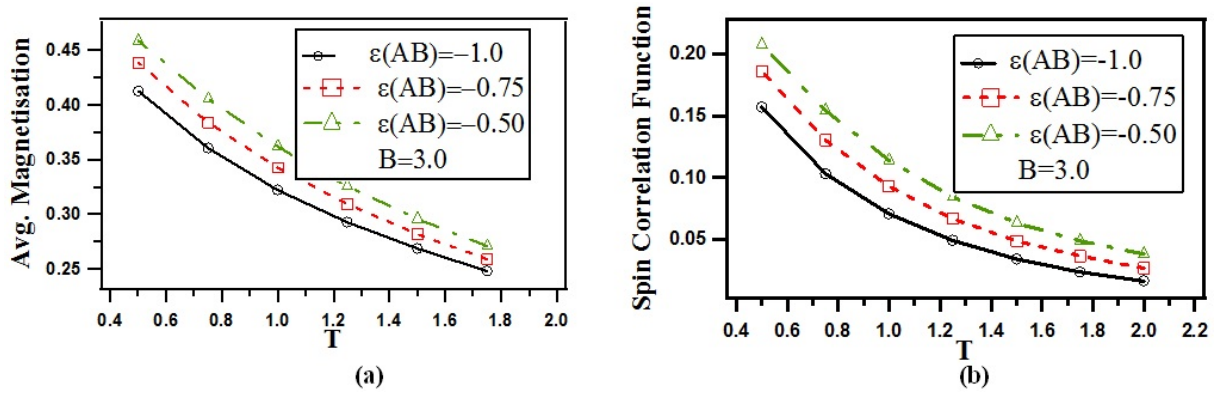


FIG. 5. Shows (a) Avg. magnetization vs temperature for different spin interactions & (b) Spin correlation function vs temperature for different spin interactions at $B = 3.0J_0/\mu_B$. All data are produced after sampling for 20 K cycles starting from 10 K cycles at an interval of 100 cycles. All cases studied here are for non-conserved anti-ferromagnetic film. The lines are to aid visualization

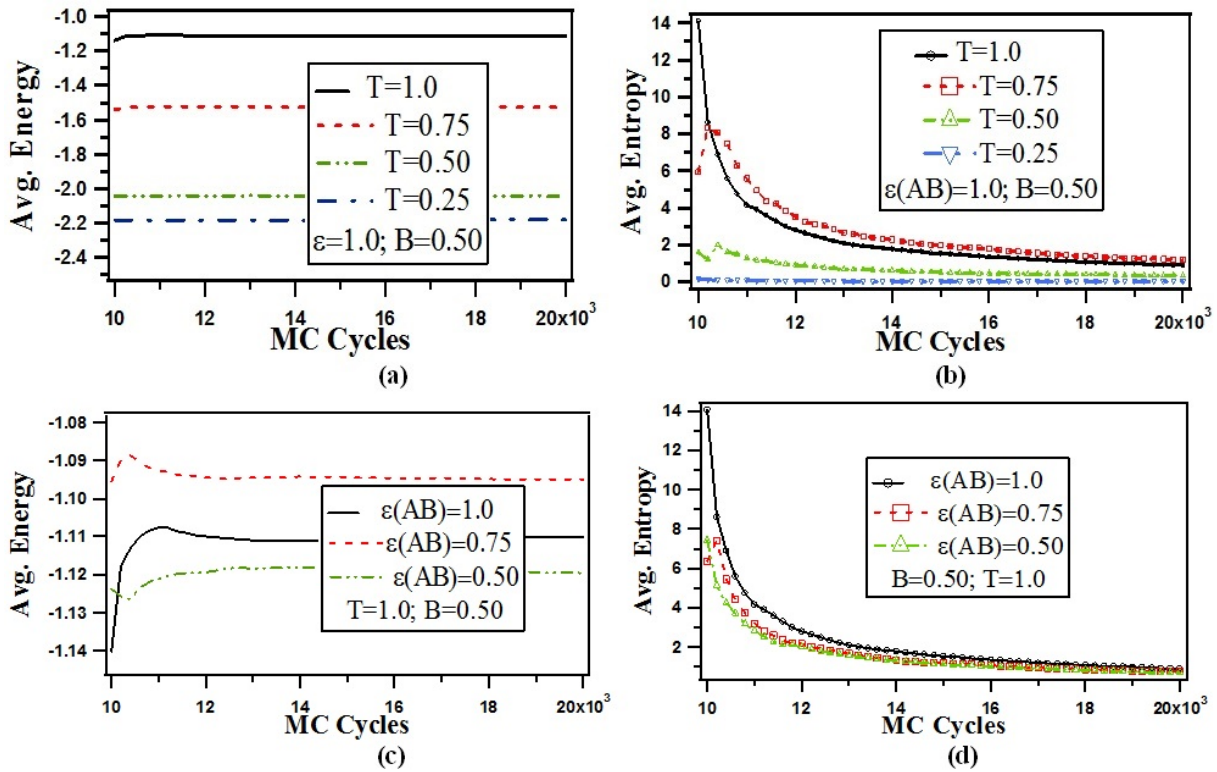


FIG. 6. Shows (a) Avg. energy vs MC Cycles at different T ; (b) Avg. energy vs MC Cycles at different $\epsilon(AB)$; (c) Avg. entropy vs MC Cycles at different T ; (d) Avg. entropy vs MC Cycles at different $\epsilon(AB)$ for different run cycles at a relatively weak magnetic field $B = 0.50J_0/\mu_B$ for conserved binary mixture with composition $A : B :: 50 : 50$. All data are produced after sampling for 20 K cycles starting from 10 K cycles at an interval of 100 cycles. All cases studied here are for conserved spin ferromagnetic film. The lines are to aid visualization

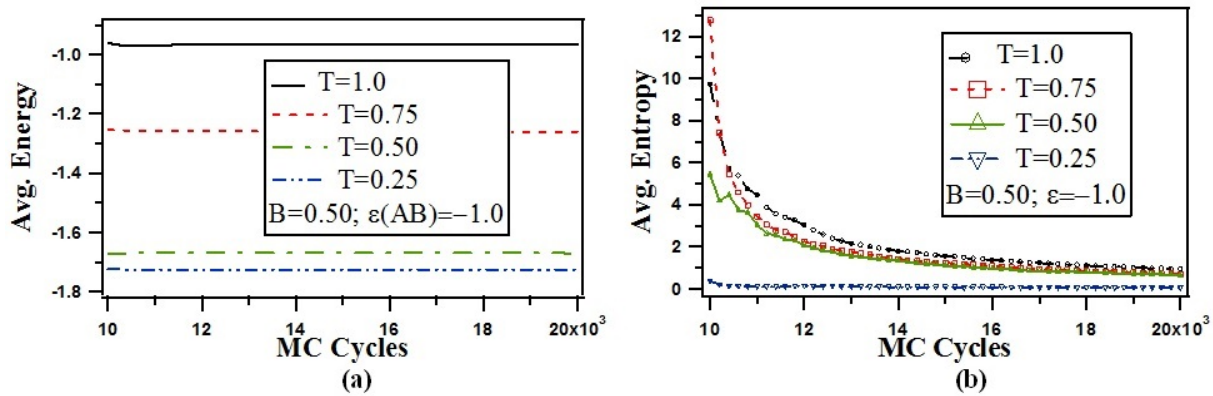


FIG. 7. Shows (a) Avg. energy vs temperature & (b) Spin correlation function vs temperature for different run cycles at a relatively weak magnetic field $B = 0.50J_0/\mu_B$ for conserved binary mixture with composition $A : B :: 50 : 50$. All data are produced after sampling for 20 K cycles starting from 10 K cycles at an interval of 100 cycles. All cases studied here are for conserved anti-ferromagnetic film. The lines are to aid visualization

ferromagnetic thin films [18]. Only weak field is taken in closer proximity to real systems. Constraint of spin conservation cannot be really permissible with higher strength of magnetic fields.

The lowest energy magnetization texture depends on the shape of the domain formed [19]. At relatively lower temperatures, the spin ordering attains equilibrium quickly within 10 K MC cycles and large changes in entropy are not observed with run cycles because of the reduced mobility for the spins, which is temperature-dependent. The simulation data below $kT = 0.30J_0$ may not be reliable, because of the apparent presence of freezing type of behavior, which means that quantum mechanical treatment may be required in order to draw any meaningful conclusions. Fig. 7 shows (a) avg. energy vs temperature and (b) spin correlation function vs temperature for different run cycles at a relatively weak magnetic field $B = 0.50J_0/\mu_B$ for conserved binary mixture with composition $A : B :: 50 : 50$. All data are produced after sampling for 20 K cycles starting from 10 K cycles at an interval of 100 cycles. All cases studied here are for conserved anti-ferromagnetic film. These curves support the effect of temperature on average energy and entropy of the system as discussed in the earlier cases of studies. Fig. 8(a) and Fig. 8(b) respectively shows the spin correlation functions for conserved ferromagnetic and conserved anti-ferromagnetic cases respectively. The ferromagnetic case shows a maximum near the spontaneous transition temperatures and decreases when away from it. This is in agreement with theory. The anti-ferromagnetic case shows a negative effect. The figures show interesting interplay of exchange interactions depending on temperature.

The *spontaneous magnetization* is observed in the absence of an external magnetic field i.e. $B = 0.0J_0/\mu_B$ for non-conserved binary mixture ferromagnetic film as shown in Fig. 9 and Fig. 10. All data are produced after sampling for 20 K cycles starting from 10 K cycles at an interval of 100 cycles. The spontaneous ferromagnetic transition temperatures for $\epsilon(AB) = 1.0J_0, 0.75J_0$ & $0.50J_0$ are respectively noted as $k_B T = 0.44, 0.39$ and 0.33 . The spin correlation function diverges at these transition temperatures, which can be understood as theoretical evidence in support of the spontaneous magnetization observation. The micrographs for conserved ferro- and anti-ferromagnetic films are shown in Figs. 11(a) and 11(b) respectively. The micrographs for non-conserved ferro- and anti-ferromagnetic films are shown in Figs. 12(a)

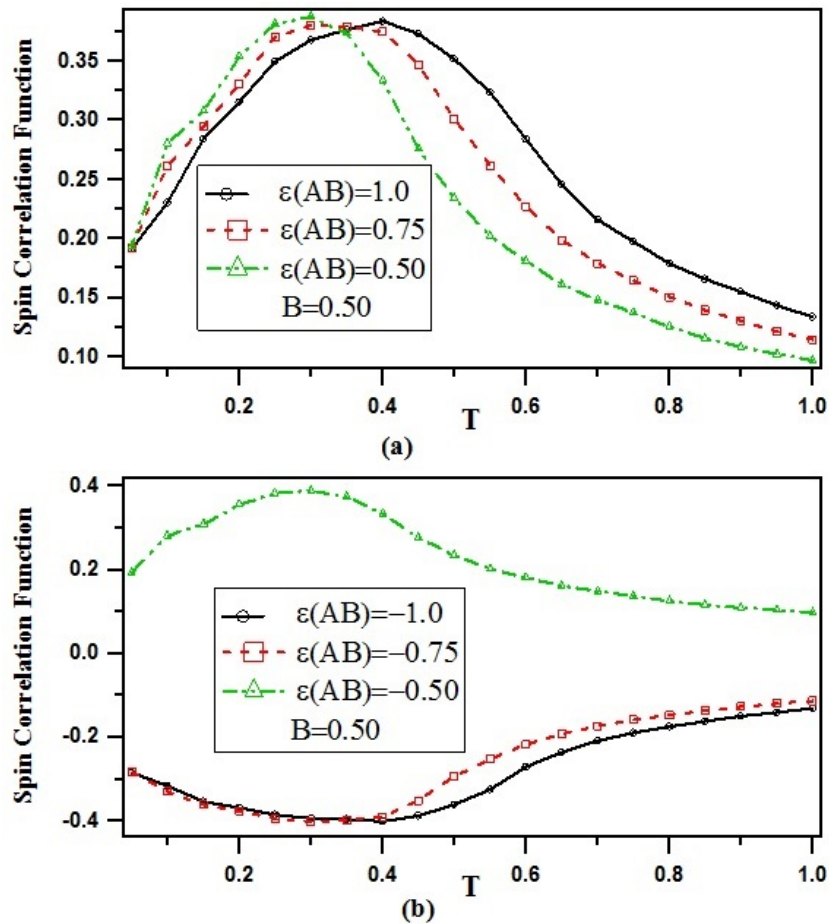


FIG. 8. Shows (a) Spin correlation function vs T for different $\varepsilon(AB) = 1.0J_0$, $0.75J_0$ & $0.50J_0$ for conserved ferromagnetic film; (b) Spin correlation function vs T for different $\varepsilon(AB) = -1.0J_0$, $-0.75J_0$ & $-0.50J_0$ for conserved anti-ferromagnetic film at a relatively weak magnetic field $B = 0.50J_0/\mu_B$. All data are produced after sampling for 20 K cycles starting from 10 K cycles at an interval of 100 cycles. The lines are to aid visualization

and 12(b) respectively. Fig. 12(b) clearly indicates a well-defined domain formation, hinting at the presence of an anisotropic effect, even at an external magnetic field $B = 0.0J_0/\mu_B$ because of the fact that the system is kept below the spontaneous transition temperature. The ferromagnetic to paramagnetic transitions are not very sharp, but the range of the spin-spin interaction can be said to decay gradually. Even at higher temperatures, as $kT = 2.0J_0$, the opposite spin pair correlation function Fig. 14 supports the formation of tiny domains with spin transport from one domain to another whereas for lower temperatures, below $kT = 1.0J_0$, the presence of a majority of $+1/2$ spins diminishes the effect. Tiny domain walls have lower energy surrounded by opposite spins and seem to be energetically preferred. This quasi nature of spin-spin interaction with temperature is also supported by the corresponding ensemble average of entropies. The simulation for the ensemble average of entropy is repeated with 50 K MC Cycles in which the data is sampled after every 100 MC Cycles starting from 30 K MC Cycles in order to ensure that no aging effects are present. This is shown in Fig. 13. These results were found to be in very good quantitative agreement with Fig. 2(d) with only 20 K MC Cycles. Fig. 15 shows the magnetic susceptibility vs temperature. Doing so helps to study the underlying

physical phenomena in three cases of magnetization i.e. ferromagnetic, anti-ferromagnetic and paramagnetic. Spontaneous magnetization is observed below a critical temperature T_c known as the Curie temperature. The ferromagnetic material becomes paramagnetic above the Curie temperature. In the case of anti-ferromagnetic material, the magnetic susceptibility χ initially increases with temperature and after attaining a critical temperature, χ decreases Fig. 15. The critical temperature is called the Neel temperature. Spin up and spin down pairs try to remain intact at lower temperatures. The magnetic induction is strong but negative. Hence the magnetization in external field is small at lower temperatures. With increase in temperature, the spin-spin interaction becomes small and hence χ increases [20]. Above a certain high temperature, known as the Neel temperature, the spins gradually become free and the material becomes paramagnetic and χ decreases with temperature.

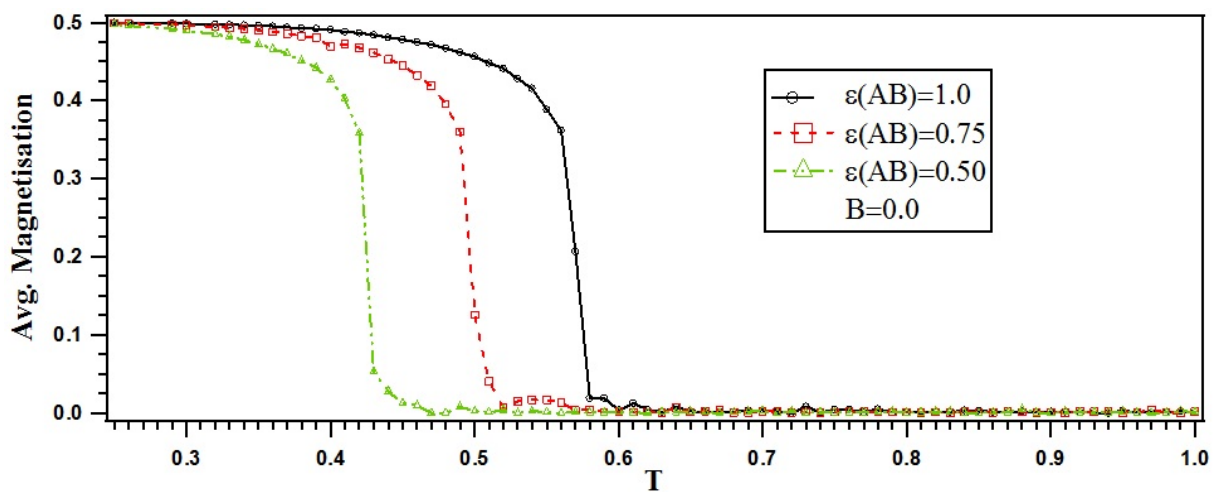


FIG. 9. Shows the spontaneous magnetization in the absence of an external magnetic field i.e. $B = 0.0J_0/\mu_B$ for non-conserved binary mixture with initial composition $A : B :: 50 : 50$ i.e. random binary mixture. All data are produced after sampling for 20 K cycles starting from 10 K cycles at an interval of 100 cycles. All cases studied here are for non-conserved ferromagnetic film. The spontaneous ferromagnetic transition temperatures for $\varepsilon(AB) = 1.0J_0$, $0.75J_0$ & $0.50J_0$ are observed as $k_B T = 0.44J_0$, $0.39J_0$ & $0.33J_0$ (i.e. nearly 96 % magnetizations are observed at these temperatures) respectively at $B = 0.0J_0/\mu_B$ (i.e. absence of any external magnetic field). The lines are to aid visualization

4. Conclusion

This paper deals with the numerical results for the simulation of magnetization in 2D thin films, highlighting the competitiveness of ensemble free energy and entropy averages. Though, many experimental research papers [21–23] have been published showing the magnetic properties of the binary mixtures, discussions of their thermodynamic properties have been scarce. The simulation techniques are also not used in published and available reports to give insight into this type of interplay between free energy and entropy, especially for spin mixture in the absence or presence of an external field. Though the author observes some finite size effect but it has been found that increasing size to 200×200 does not yield much change. The fluctuations are high at $T = 2.0$, indicating a super paramagnetic type of behavior in our case. The spin fluctuations in 2D thin films may give rise to significant variations

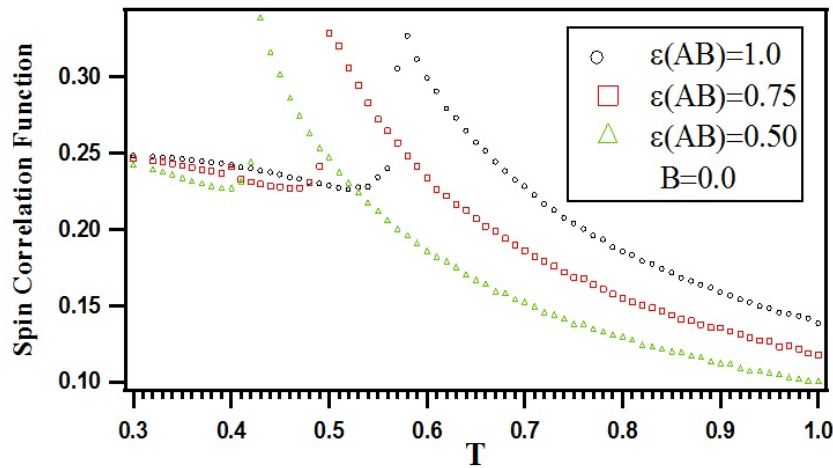


FIG. 10. Confirms the spontaneous magnetization in absence of external magnetic field i.e. $B = 0.0J_0/\mu_B$ for non-conserved binary mixture with initial composition $A : B :: 50 : 50$ i.e. random binary mixture. All data are produced after sampling for 20 K cycles starting from 10 K cycles at an interval of 100 cycles. All cases studied here are for ferromagnetic film

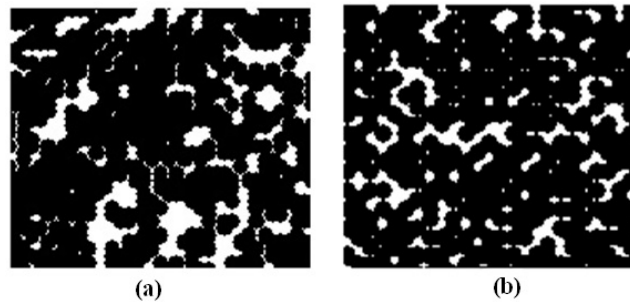


FIG. 11. Shows the (a) micrograph at $kT = 1.0J_0$ for conserved ferromagnetic case and (b) micrograph at $kT = 1.0J_0$ for conserved anti-ferromagnetic case. The configuration data are produced after sampling for 20 K cycles. For ferromagnetic case large circular patches of spin-down component are observed whereas for anti-ferromagnetic case small circular patches of spin-down component are observed with presence of long ridges in the micrograph which is an indication of wetting phenomena as the ridge interface can host spin-up component which is preferred in the anti-ferromagnetic case. Smaller circular drops in large number can better help the system to achieve equilibrium with minimum possible energy, which is opposite to that of the ferromagnetic case

in the magnetic and electrical properties of 2D thin films which may have a wide range of applications. The ferromagnetic to paramagnetic transitions are not very sharp, but the range of the spin-spin interaction can be said to decay gradually. Even at higher temperatures, as $kT = 2.0J_0$, the opposite spin pair correlation function supports the formation of tiny domains with spin transport from one domain to another, whereas for lower temperatures, i.e. below $kT = 1.0J_0$, the presence of majority $+1/2$ spins diminishes the effect. Tiny domain walls have lower energy surrounded by opposite spins and seem to be energetically preferred. This quasi nature of spin-spin interaction with temperature is also supported by the corresponding ensemble average of entropies.



FIG. 12. Shows the (a) micrograph at $kT = 1.0J_0$ for non-conserved ferromagnetic case and (b) micrograph at $kT = 0.45J_0$ for non-conserved ferromagnetic case i.e. below spontaneous transition temperature. The configuration data are produced after sampling for 20 K cycles. The agitated magnetic domains can be observed at $kT = 1.0J_0$ in form of long ridges. At $kT = 0.45J_0$, the well-formed domain reflects spin coarsening, which evolves to form nearly circular domains

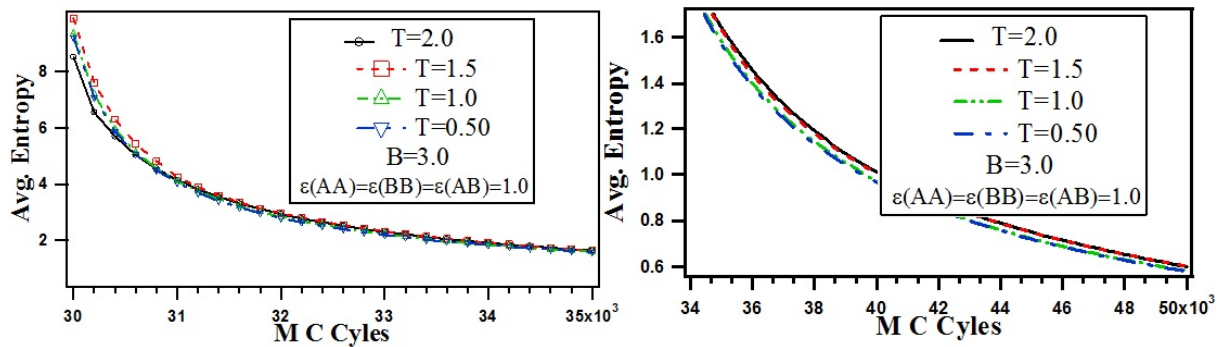


FIG. 13. Shows the avg. entropy vs temperature for the non-conserved ferromagnetic case ϵ_{AB} at $kT = 2.0J_0$ for different run cycles. In all cases, the applied external magnetic field is taken as $B = 3.0J_0/\mu_B$. The data are produced after sampling for 20 K cycles starting from 30 K cycles at an interval of 100 cycles

Acknowledgement

The author is thankful to University Grant Commission, New Delhi, India for its financial support under UGC, MRP Grant No. 42-849/2013(SR).

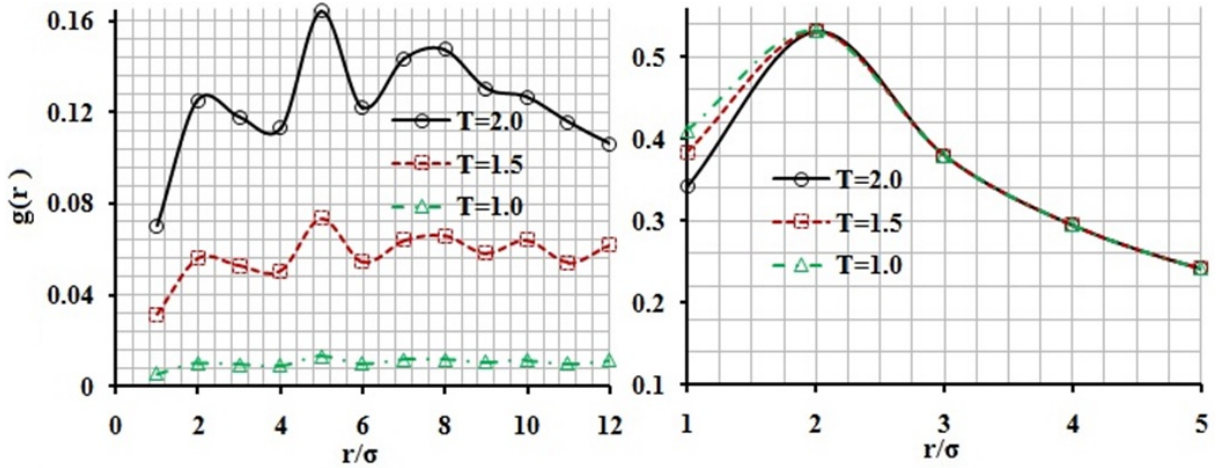


FIG. 14. Shows the pair correlation function $g(r)$ vs distance for opposite spins (left) and for spin up (right) for the non-conserved ferromagnetic case $\varepsilon_{AB} = 1.0J_0$ at $kT = 1.0J_0, 1.5J_0$ & $2.0J_0$. In all cases, the applied external magnetic field is taken as $B = 3.0J_0/\mu$. The data are produced after sampling for 20 K cycles starting from 30 K cycles at an interval of 100 cycles

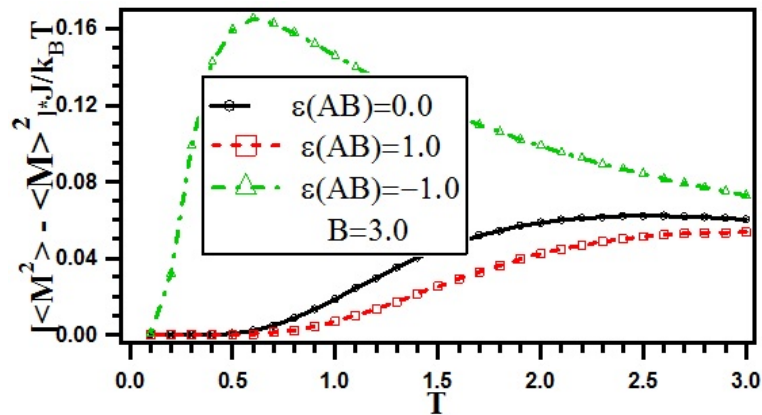


FIG. 15. Shows the magnetic susceptibility vs temperature non-conserved paramagnetic, ferromagnetic & anti-ferromagnetic case respectively with $\varepsilon_{AB} = 0.0J_0, 1.0J_0$ & $-1.0J_0$; $\varepsilon_{AA} = \varepsilon_{BB} = 1.0J_0$. In all case the applied external magnetic field is taken as $B = 3.0J_0/\mu$. The data are produced after sampling for 10 K cycles starting from 10 K cycles at an interval of 100 cycles

References

- [1] C.P. Pooley, F.J. Owens. *Introduction to Nanotechnology*, Wiley India Pvt. Ltd. New Delhi, 2009.
- [2] J. Ramsden. *Nanotechnology: An Introduction, Chapter-2, The nanoscale*, Elsevier, UK, 2011.
- [3] M. Kuno. *Introductory Nanoscience*, Garland Science, Taylor and Francis Gropu, USA, 2012.
- [4] C.W.Shong, S.C.Haur, A.T.S. Wee. *Science at Nanoscale*, Pan Stanford Publishing Pvt. Ltd. 2010, Singapore.
- [5] R.K. Pathria, P.D. Beale. *Statistical Mechanics, 3rd Ed.*, Butterworth-Heinemann, USA, 2011.
- [6] B.K. Tanner. *Introduction to the Physics of Electrons in Solids*, Cambridge University Press, UK, 1995.
- [7] J.D. Fast. *Entropy, 2nd Ed.*, Gordon and Breach Science Publishers Inc., USA, 1968.
- [8] A.K. Saha, S.P. Singh, J.K. Singh, S.K. Kwak. Quasi- 2D and prewetting transitions of square well fluids on a square-well substrate. *Molecular Physics*, 2009, **107** (20), P. 2189–2200.
- [9] S.P. Singh, J.K. Singh, A. Sharma. Adsorption of gas like molecules on self aligned square well fluid channels under confinement of chemically patterned substrates. *Appl. Nanosc.*, 2013, **3**, P. 179–187.

- [10] S.P. Singh, J.K. Singh, A. Sharma. Investigating bridge like structures in a square well binary mixture using NVT Monte Carlo simulation. *Int. J. Nanosc.*, 2011, **10**, (1), P. 329–333.
- [11] S.P. Singh. Spinodal theory: A common rupturing mechanism in spinodal dewetting and surface directed phase separation (some technological aspects and the significance of dipole-quadrupole interaction in spinodal dewetting). *Advances in Cond. Mat. Phys.*, 2011, **2011**, Article ID 526397, 14 pages.
- [12] S.P. Singh. Spatial correlation in 2D and 3D thin films of conserved binary mixtures in presence of wetting of substrates by preferred majority component: Interpretation in real scenario. *Appl. Nanosc.*, 2012, **2**, P. 365–369.
- [13] S.P. Singh. Revisiting 2D lattice based spin flip-flop Ising model: Magnetic properties of a thin film and its temperature dependence. *Eur. J. Phys. Educ.*, 2014, **5** (3).
- [14] S.P. Singh. Dimensions and Trends of Nanotechnology. *ISST J. Appl. Phys.*, 2015, **6** (1), P. 73–77.
- [15] G.H. Wannier. *Elements of solid state theory, Chapter-4, Co-operative phenomena in solids*. Cambridge University Press, UK, 1960.
- [16] H.V. Keer. *Principles of solid state, Chapter-5, Magnetic properties*. New Age International Publishers, New Delhi, 2005.
- [17] J. Marro, R. Toral. Microscopic observations on a kinetic Ising model. *Am. J. Phys.*, 1986, **54** (12), P. 1114–1121.
- [18] V.A. Ignatchenko. Spontaneous magnetization of ferromagnetic thin films. *Soviet Physics JETP*, 1961, **13** (4), P. 863.
- [19] S. Banerjee, M. Widom. Shapes and texture of ferromagnetic liquid droplets. *Brazilian J. Phys.*, 2011, **31** (3), P. 360–365.
- [20] A. Goswami. *Thin film fundamentals, Chapter-12, Magnetic and superconducting film*. New Age International Publishers, New Delhi, 2008.
- [21] A. Sundaresan, R. Bhargavi, et al. Ferromagnetism as a universal feature of nanoparticles of the otherwise nonmagnetic oxides. *Phys. Rev. B*, 2006, **74**, P. 161306(R).
- [22] J.M.D. Coey. High temperature ferromagnetism in dilute magnetic oxides. *J. of Appl. Phys.*, 2005, **97**, 10D313.
- [23] N. Poudyai, G.S. Chaubey, C.-B. Rong, J.P. Liu. Shape control of FePt nanocrystals. *J. Appl. Phys.*, 2009, **105**, 07A749.



NANOSYSTEMS:

PHYSICS, CHEMISTRY, MATHEMATICS

INFORMATION FOR AUTHORS

The journal publishes research articles and reviews, and also short scientific papers (letters) which are unpublished and have not been accepted for publication in other magazines. Articles should be submitted in English. All articles are reviewed, then if necessary come back to the author to completion.

The journal is indexed in Chemical Abstract Service of the American Chemical Society and in Russian Scientific Citation Index.

Author should submit the following materials:

1. Article file in English, containing article title, the initials and the surname of the authors, Institute (University), postal address, the electronic address, the summary, keywords, MSC or PACS index, article text, the list of references.
2. Files with illustrations, files with tables.
3. The covering letter in English containing the article information (article name, MSC or PACS index, keywords, the summary, the literature) and about all authors (the surname, names, the full name of places of work, the mailing address with the postal code, contact phone number with a city code, the electronic address).
4. The expert judgement on possibility of publication of the article in open press (for authors from Russia).

Authors can submit a paper and the corresponding files to the following addresses: nanojournal.ifmo@gmail.com, popov1955@gmail.com.

Text requirements

Articles should be prepared with using of text editors MS Word or LaTeX (preferable). It is necessary to submit a pdf copy. In the name of files the English alphabet is used. The recommended size of short communications (letters) is 4-6 pages, research articles – 6-15 pages, reviews – 30 pages.

Recommendations for text in MS Word:

Formulas should be written using Math Type. Figures and tables with captions should be inserted in the text. Additionally, authors present separate files for all figures and Word files of tables.

Recommendations for text in LaTeX:

Please, use standard LaTeX without macros and additional style files. The list of references should be included in the main LaTeX file. Single LaTeX file of the paper with the corresponding pdf file should be submitted.

References in the article text are given in square brackets. The list of references should be prepared in accordance with the following samples:

- [1] N. Surname. *Book Title*. Nauka Publishing House, Saint Petersburg, 2000, 281 pp.
- [2] N. Surname, N. Surname. Paper title. *Journal Name*, 2000, **1**(5), P. 17-23.
- [3] N. Surname, N. Surname. Lecture title. In: Abstracts/Proceedings of the Conference, Place and Date, P. 17-23, 2000.
- [4] N. Surname, N. Surname. Paper title (2010). URL: <http://books.ifmo.ru/ntv>.
- [5] N. Surname, N. Surname. Patent Name. Patent No. 11111, Bul. No. 33, 5 pp., 2010.
- [6] N. Surname, N. Surname. Thesis Title. Thesis for full doctor degree in math. and physics, Saint Petersburg, 105 pp., 2000.

Requirements to illustrations

Illustrations should be submitted as separate black-and-white files. Formats of files – jpeg, eps, tiff.



NANOSYSTEMS:

PHYSICS, CHEMISTRY, MATHEMATICS

Журнал зарегистрирован

Федеральной службой по надзору в сфере связи, информационных технологий и массовых коммуникаций

(свидетельство ПИ № ФС 77 - 49048 от 22.03.2012 г.)

ISSN 2220-8054

Учредитель: федеральное государственное автономное образовательное учреждение высшего образования

«Санкт-Петербургский национальный исследовательский университет информационных технологий, механики и оптики»

Издатель: федеральное государственное автономное образовательное учреждение высшего образования

«Санкт-Петербургский национальный исследовательский университет информационных технологий, механики и оптики»

Отпечатано в Учреждении «Университетские телекоммуникации»

Адрес: 197101, Санкт-Петербург, Кронверкский пр., 49

Подписка на журнал НФХМ

На второе полугодие 2016 года подписка осуществляется через

ОАО Агентство «Роспечать»

Подписной индекс 57385 в каталоге «Издания органов научно-технической информации»